Hydrides in Zirconium: Microstructure and Micromechanics

Xuewei Li

St Edmund Hall

A thesis submitted for the degree of Doctor of Philosophy in materials

University of Oxford

Supervised by: Prof. Angus Wilkinson, Prof. David Armstrong and Prof. Edmund Tarleton

Hilary Term 2024

ABSTRACT

Zirconium alloys has been extensively used as the commercial cladding and structural materials in water cooled nuclear reactors in the last half century. Nevertheless, the formation of brittle hydrides due to the aqueous corrosion in operation will significantly degrade the performance of the zirconium claddings and limit their lifetime. The volume expansion in the zirconium to hydride transformation makes it more complicated. In order to further clarify the mechanism of hydride-induced degradation of zirconium (usually embrittlement), this project was proposed to deep investigate the microstructure and micromechanics of hydrides in zirconium by advanced materials characterization techniques.

Micro-analysis was performed on δ-hydrides in zirconium by serial sectioning, conventional and high angular resolution electron backscatter diffraction (EBSD). Hydrogen in the lattice is expected to be homogeneous at anneal temperature but grain boundaries are preferential sites for hydride nucleation. Most δ-hydrides follow the orientation relationship of $\{0001\}_\alpha||\{111\}_\delta\langle 11\bar{2}0\rangle_\alpha||\langle 110\rangle_\delta$ (OR1) with their parent grains. The orientation relationship of $\{0001\}_\alpha||\{100\}_\delta$ $\langle 11\bar{2}0\rangle_\alpha||\langle 110\rangle_\delta$ (OR2) is supposed to occur only when OR1 is constrained, e.g. in the surface hydrides. For faster cooling, an intra-granular hydride plate is composed of smaller hydride flakes with the same orientation on its habit plane, while several potential habit planes were observed, including $\{0001\}$, $\{10\bar{1}1\}$, $\{10\bar{1}2\}$ and $\{10\bar{1}7\}$. The hydrides were found to accommodate transformation strain mainly by GNDs. The twin-related structures commonly seen in the inter-granular hydrides and surface hydrides may also be helpful. The accommodation of transformation strain in zirconium is more complicated, involving lattice strain, twinning, dislocations (e.g., GNDs and grain boundary dislocations)

and their movements. The anisotropic local plastic deformation induced by hydride formation is likely to affect hydride nucleation and growth next in return.

The in-situ digital image correlation (DIC) tensile tests were then carried out on the zirconium with and without hydrides in SEM. The formation of hydrides was observed to increase the yield strength of zirconium but presumably reduce the work hardening, and the degree of the effect caused by hydrides is associated with the texture of zirconium matrix. At the microscale, hydrides markedly enhanced strain localization during deformation by obstructing the propagation of slip, preventing the growth of the deformation twins nearby in matrix and the shear along hydride-matrix interfaces. The brittle nature of hydrides is likely to result in stress build up at hydride-matrix interfaces, which may be the preferential sites for micro-voids and/or micro-cracks. This is useful to further understand the ductile-to-brittle transformation with increasing hydride content.

The works reported in this thesis are helpful for optimizing the design and working conditions of commercial zirconium alloys to minimize the detrimental impacts of hydride formation. Meanwhile, they provide nice data for further modelling work to develop reliable models of hydride-induced embrittlement in zirconium.

ACKNOWLEDGEMENNT

It is impossible for me to be here without kind help and support from many people in my DPhil life and I would like to take this chance to thank them.

First, I would like to express my most sincere thanks to my supervisors, Prof. Angus Wilkinson, Prof. David Armstrong and Prof. Edmund Tarleton. They always supported my choices in a comfortable way, whether in academic or personal issues. When I met frustration and even doubted myself, the meeting with them always inspired me to hug life and continue. When I fell in struggle and confusion about the future, they told me that it is common for everyone and helped me find out what I truly want. Thanks again for their patience and supports over the last few years, which helped me grow into a better person.

Many thanks to post-doctors in our groups. They gave me help with both lab and writing work. Dr. Junliang Liu, Dr. Phani Karamched, Dr. Hongbin Yu and Dr Jicheng Gong taught me a lot about microscopies and sample preparation, as well as data analysis and presentation skills, which are quite helpful for me to complete my DPhil project. I would also thank the staff in the microscopy centre, mechanical workshop and furnace lab for their assistant.

I would also like to say thanks to many friends in department for inspiring discussion, help on specific techniques or softwares, as well as the relaxing time we spent together, Dr. Botao Hao, Mr. Donghao Liu, Dr. Yi xiong, Dr. Xiaonan Luo, Dr. Qianyang Zhang, Dr. Ziling Gao, Miss Zhexin Cui, Miss Houzhi Liu and so on.

Finally and most importantly, many thanks to my families for their love, understanding and financial support over the last few years, especially during the pandemic when I was force to stay at home and my progress was quite slow.

PREFACE

The work reported in this thesis was performed by the author independently in the Department of Materials at University of Oxford between October 2018 and April 2024, under the supervision of Prof. Angus J. Wilkinson, Prof. David Armstrong and Prof. Edmund Tarleton. All the work is original, and the work of others included here has been properly referenced or acknowledged. Neither the entire nor any part of thesis has been submitted for any other degree at this university or elsewhere.

The oral presentations have been given in conference are as follows.

1. Micro-analysis of delta-hydrides in pure zirconium by HR-EBSD and TKD, TMS2024, Orlando, 3rd-7th March 2024.
2. An investigation of mechanical behaviours of pure zirconium with and without hydrides using in-situ testing method, TMS2024, Orlando, 3rd-7th March 2024.

TABLE OF CONTENTS

Chapter 1 Introduction

In this chapter, an overview on the background of this thesis will be given. It will start with a brief introduction of nuclear energy in the world today, and then the role of zirconium in the nuclear industry. Lastly, this chapter will end with the objectives of this thesis.

1.1 Nuclear energy

Nuclear energy is a low-carbon energy which can be deployed on a large scale to replace fossil fuels, supplying clean, reliable and affordable electricity to the world. It is an important part of solution to global climate change and the rapidly increasing demand of electricity in modern society. The first commercial nuclear power stations were built up and started operation in 1950s. Now about 440 nuclear power plants are operational in 31 countries and provide about 10% of the world's electricity. The growth of worldwide nuclear electricity production in the last half century is shown in Figure 1.1[1]. Meanwhile about 60 nuclear power reactors are under construction and their total capacity is about 15% of the existing capacity.

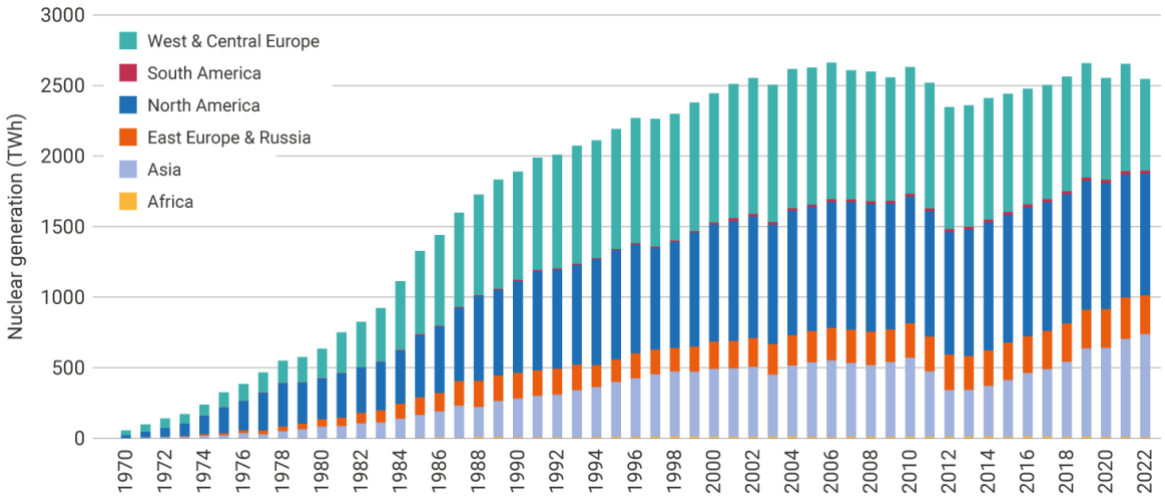

Figure 1.1 Nuclear electricity production in the last 50 years. (Source: World Nuclear Association, IAEA PRIS).[1]

1.2 Zirconium in the nuclear industry

In a nuclear plant, the heat released by the controlled chain reactions of nuclear fuel pellets, most commonly uranium-235, inside the rod claddings warms the surrounding coolant and produces the steam to drive a spin turbine and generate electricity, as show in Figure 1.2[2]. Currently, most operable nuclear reactors in the world are water-cooled, where zirconium alloys are widely used as cladding and structural materials, owing to their low neutron absorption cross-section, high thermal conductivity, reliable mechanical properties and 'adequate' resistance to corrosion at high temperature[3]. The chemical components of the zirconium alloys in nuclear industry are shown in Table 1.1[4] The lifetime and safety of these water-cooled reactors are closely associated with the in-core performance of the zirconium alloy claddings. An example of pressurized water reactor fuel assemblies is shown in Figure 1.3[5].

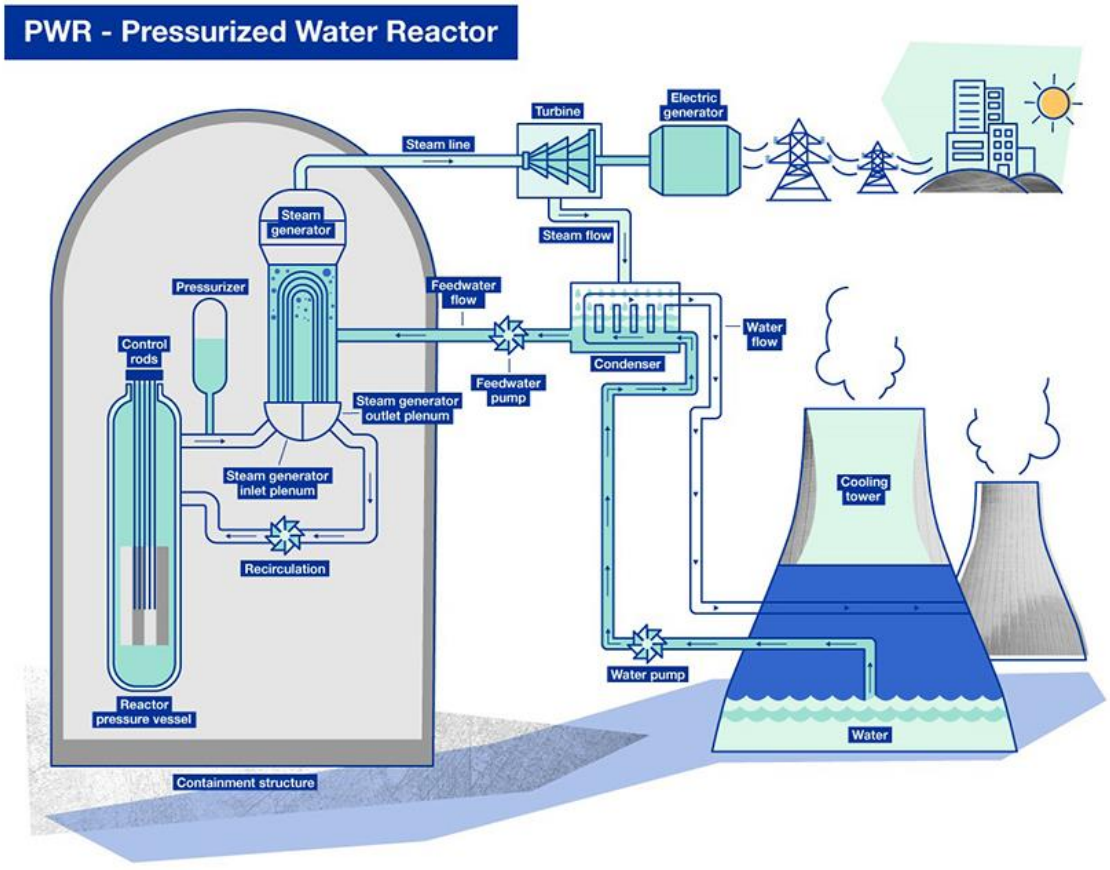

Figure 1.2 A schematic of pressurized water nuclear reactor.[2]

Table 1.1 Chemical composition of the zirconium alloys in nuclear industry.[4]

Name of alloy	Alloying elements (weight %)					Application
	Sn	Fe	Cr	Ni	Nb	
Zircaloy-2	1.50	0.12	0.10	0.05	-	Boiling water reactor, CANDU
Zircaloy-4	1.50	0.20	0.10	-	-	Pressurized water reactor
ZIRLO™	1.02	0.10	-	-	1.01	Pressurized water reactor
M5™	-	0.05	0.02	-	1.00	Pressurized water reactor

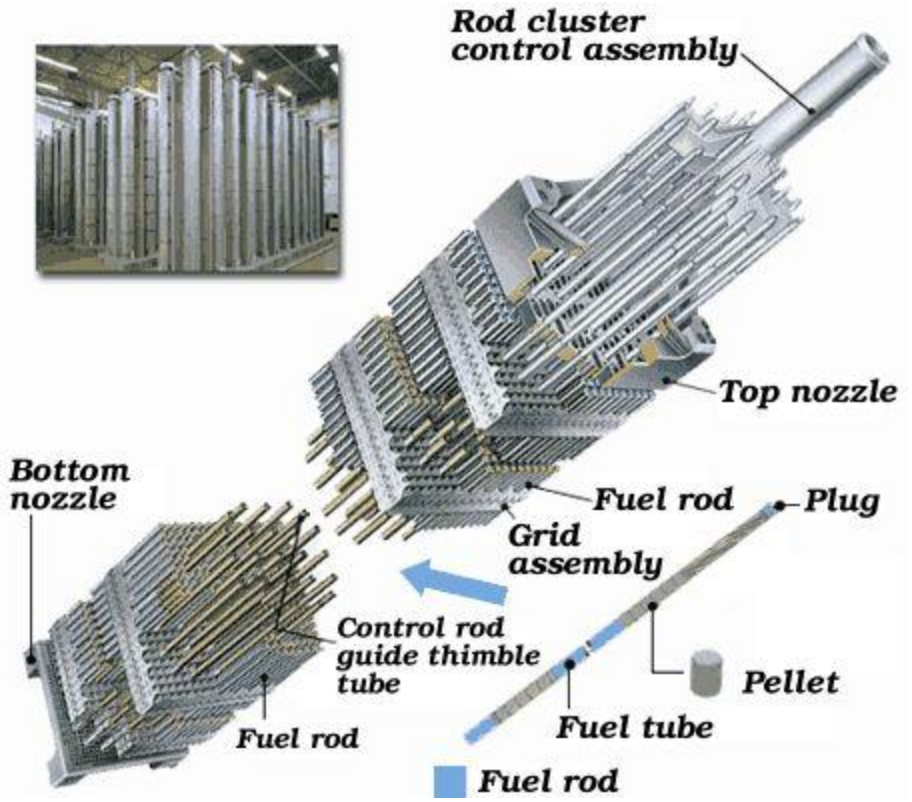

Figure 1.3 An example of pressurized water reactor fuel assemblies.[5]

Although zirconium alloys have successfully served as nuclear fuel claddings since 1950s[6], their performance still suffers from complicated degradation processes in reactor cores, including corrosion, creep, pellet-clad mechanical interaction and departure from nucleate boiling (DNB)[7]. Among them, the aqueous corrosion (or oxidation) of the outer layer of zirconium claddings with coolant water will produce hydrogen[8]. Once the hydrogen concentration exceeds the terminal solid solubility limit in the claddings at the service temperature (commonly around 300-400 ˚C), brittle hydrides precipitate. The formation of

hydrides extensively occurs during both operation period inside nuclear reactors and dry storage stage after usage. It is severely detrimental to the performance of zirconium claddings, including dimensional stability and mechanical properties (e.g. hydride blister on the outer surface, significant reduction in ductility and fracture caused by delayed hydride cracking etc.) [9][10] and limit their service lifetime.

$$Zr + 2H_2O \rightarrow ZrO_2 + H_2$$

$$Zr + xH \rightarrow ZrH_x$$

In addition, although some hydrogen may be from radiolysis of coolant water and moisture contained in the fuel pellets inside claddings, it can be neglected for hydride-induced degradation compared with the source mentioned above[11].

1.3 Objectives

As reviewed in chapter 2, despite various experimental and computational studies performed on the hydrides and hydride-induced degradation in zirconium in the last several decades, many fundamental mechanisms are still ambiguous[12]. This thesis focuses on the systematic investigation of microstructure and micromechanics of hydrides in zirconium in order to give a better understanding of the mechanisms for hydride formation and hydride-induced embrittlement in zirconium.

The microstructure and local deformation induced by hydride formation without external stress are investigated by serial sectioning, conventional and high angular resolution electron backscatter diffraction (EBSD) in chapter 5. This work will reveal the intrinsic characteristics of hydrides in zirconium and the role that transformation stain plays in the hydride nucleation and growth, based on which some measures may be proposed to control the hydride formation in zirconium claddings and minimize its detrimental impacts.

Chapter 6 will explore the effects of hydrides on the local deformation in zirconium during macro-scale deformation by in-situ digital image correlation (DIC) tensile tests in scanning electron microscopy (SEM). This will not only help us clarify how the hydrides lead to ductile-to-brittle transformation in zirconium but also provide input data for further modelling work to develop reliable models to predict the mechanical performance of zirconium claddings during operation and dry storage.

Chapter 2 Literature review

In this chapter, a systematic literature review is performed on the hydrides in zirconium and zirconium alloys, from hydrogen pick up to hydride formation and reorientation, as well as degradation on mechanical properties of matrix. Related computational research is also reviewed, with an emphasis on the work using finite element method (FEM).

2.1 Absorption and solubility of hydrogen in zirconium alloys

The major source of the hydrogen picked up by zirconium alloy claddings in nuclear reactors is the aqueous corrosion, occurring at the interface between water coolant and the rod claddings and generating an oxide layer at the same time. Notably, only part of the hydrogen released by the corrosion reaction above enters zirconium alloy claddings. This hydrogen absorption behavior of zirconium alloy claddings can be measured by the hydrogen pickup fraction (f_H). It is defined as the ratio of the amount of hydrogen absorbed by the cladding to the total amount of hydrogen produced in the corrosion reaction[4], as shown below:

$$f_H = \frac{H_{absorbed}}{H_{generated}}$$

The hydrogen pickup fraction (f_H) varies considerably according to alloying elements, microstructure of matrix, microchemistry and corrosion conditions (e.g. exposure time, corrosion temperature and surface treatment, etc.)[13][14][15]

As shown in the Figure. 2.1[12][14], it is clear that hydrogen content in the zirconium matrix keeps increasing with weight gain. Weight gain represents the degree of the aqueous corrosion and is proportional to the thickness of oxide layer. Theoretically, continuous oxide layer can protect the matrix inside from further oxidation and obstruct hydrogen diffusion toward the

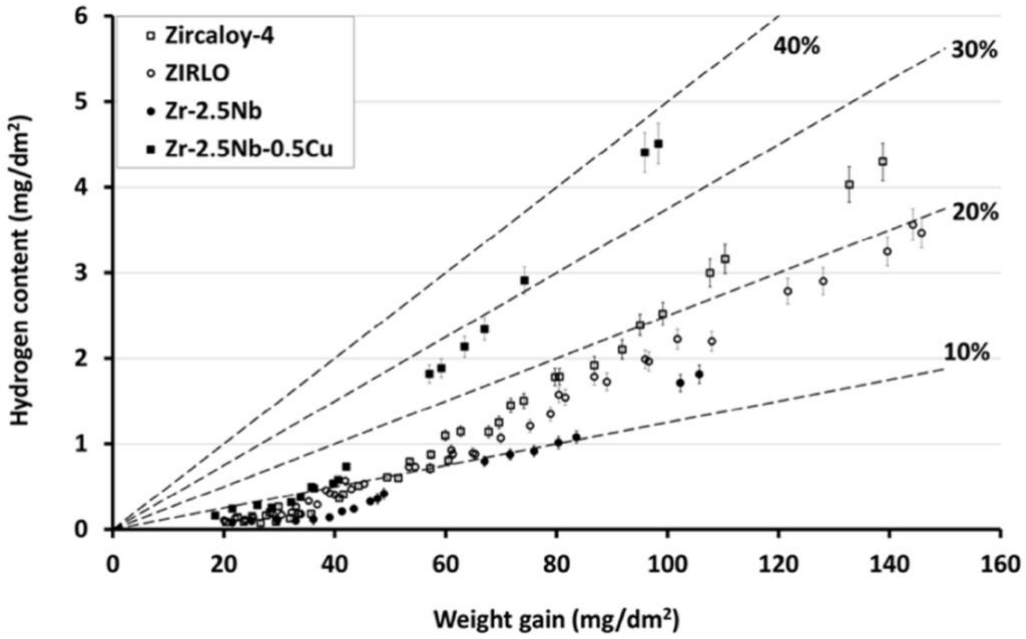

Figure 2.1 Hydrogen content vs weight grain of the aqueous corrosion during autoclave testing of several zirconium alloys in pure water at 360˚C[12][14]. The relationship is non-linear in transitional regime and varies with different composition of zirconium alloys.

matrix. In fact, the generated oxide layer partially dissolves in the normal service conditions in nuclear reactors and micro-cracks appear. These micro-cracks assist oxygen and hydrogen to reach the zirconium matrix, resulting in consistently increasing hydrogen content[16][17][18]. Nevertheless, the hydrogen pickup fraction varies as a non-monotonic function of the weight gain in the oxide transition regime. The effect of alloying elements on the hydrogen pickup fraction of zirconium has also been explored. Copper increases the hydrogen pickup fraction while Niobium decreases this fraction owing to its donor effect in the solid solution[14]. Addition of iron reduces the driving force for hydrogen transport by decreasing the electrical potential gradient in the oxide layer, leading to a lower pickup fraction[15]. In addition, the existence of coarse precipitates of $ZrFe_2$ or $ZrCr_2$ in zirconium alloys can reduce hydrogen absorption as well.

The hydrogen content in the zirconium alloy matrix can be measured by various techniques, divided into destructive and non-destructive methods. The most commonly used destructive

methods are inert gas fusion (IGF) and vacuum hot extraction (VHE), as they are well-established, quick and cheap. However, their precision will decrease when they are used for the specimens with low hydrogen content[19][20]. Many non-destructive methods have also been developed and employed to quantify the hydrogen content. For example, electromagnetic acoustic resonance (EMAR) is proper for in-situ measurement, although its precision is susceptible to oxidation and alloying elements[21]. In addition, some non-destructive methods are based on neutron techniques and perform better at measuring the small amount of hydrogen. Neutron scattering techniques possesses a high sensitivity of 0.4 ppm to hydrogen, and meanwhile offers some phase information inside the sample[22]. Another method is cold neutron prompt gamma activation analysis (CNPGAA), which is able to detect hydrogen of as low as 5 wt. ppm with a precision of ± 2 wt. ppm[23]. It is worth mentioning that a neutron imaging method has been established recently and is capable of quantifying the spatial distribution of hydrogen in zirconium with a precision of about 5 wt. ppm and a spatial resolution of 25 μm approximately[24].

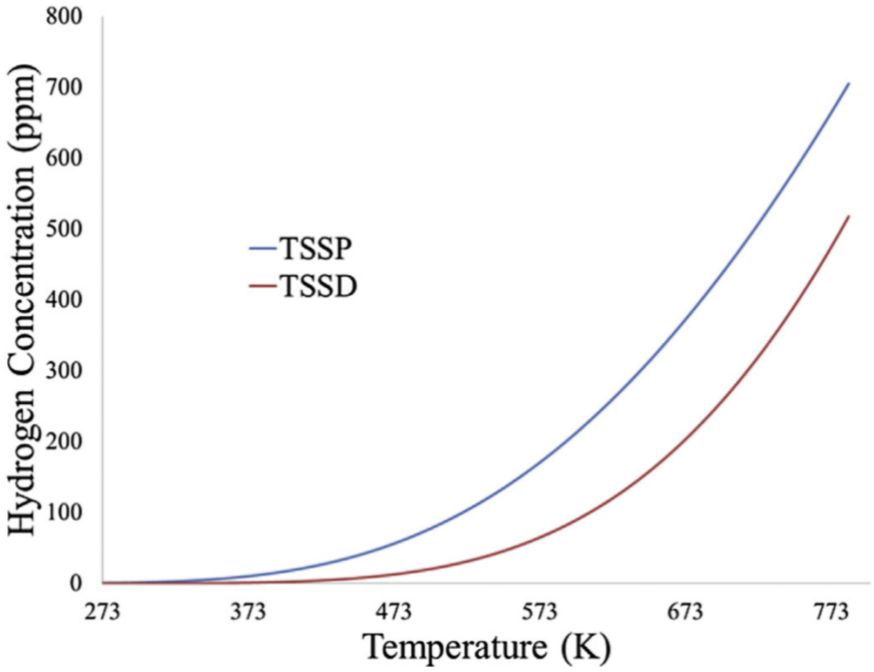

Figure 2.2 Terminal solid solubility (TSS) for precipitation and dissolution of hydrogen in zircaloy-2[3][27]. It agrees with the other experimental work on TSS of hydrogen in zirconium alloys very well.

Once the concentration of hydrogen in zirconium surpasses its terminal solid solubility (TSS) in the given conditions, hydride precipitation occurs. Therefore, many studies have been done on the TSS of hydrogen in zirconium alloys. The most commonly used experimental methods are synchrotron radiation diffraction and differential scanning calorimetry (DSC), which are sensitive to phase transformation. The TSS of hydrogen increases greatly with temperature, from only 10^{-4} at.% at room temperature to about 0.7 at.% at 300 °C and reaching around 5 at.% at elevated temperature[3][25]. At the typical service temperature of ~350°C in a reactor core, it is about 130 ppm by weight (1.16 at.% approximately)[26]. Such small values of the TSS means that hydrogen in zirconium alloys tends to exist as hydride precipitates.

It is noteworthy that the values of TSS for hydride precipitation (TSSP, obtained during cooling process) and for hydride dissolution (TSSD, obtained during heating process) are different. At the same temperature, TSSP is always higher than TSSD and the gap between them increases with temperature, as shown in Figure. 2.2[3][27]. This is called precipitation/dissolution hysteresis in Zr/ZrH_x system, presumably due to the hydride nucleation energy barrier during cooling[28][29]. Once hydride precipitation starts at a certain temperature, it will continue until the hydrogen concentration in the zirconium matrix decreases to the TSSD[28] and lead to pronounced effects on the performance of zirconium alloys. The TSSP is found to vary little with alloying elements, external stress and neutron irradiation [27][29][30][31]. In contrast, it has been observed that addition of chromium and tin increases the TSSD while nickel and iron does not affect the TSSD[32]. Meanwhile, the hydrogen solubility in zirconium and its alloys may be enhanced by neutron irradiation[33][34].

2.2 Hydride phases in zirconium

During the operation of nuclear reactors, zirconium alloys are α-Zr with hexagonal close packed (hcp) structure. Four hydride phases in the zirconium-hydrogen binary system have

Table 2.1 Crystal parameters of hydride phases in zirconium allloys[4].

Phase	x's value in ZrH_x	Crystral structure	Lattice parameters (nm)		Space group
			a	c	
α-Zr matrix	0	Hexagonal	0.3232	0.5147	$P6_3/mmc$
β-Zr matrix	0	Body centered cubic	0.3609	-	*Im3m*
ζ-hydride	0.50	Trigonal	0.3300	1.0290	-
γ-hydride	1.00	Tetragonal	0.4596	0.4969	$P4_2/n$
δ-hydride	1.66	Face centered cubic	0.4781	-	*Fm3m*
ε-hydride	2.00	Teragonal	0.3520	0.4450	*I4/mmm*

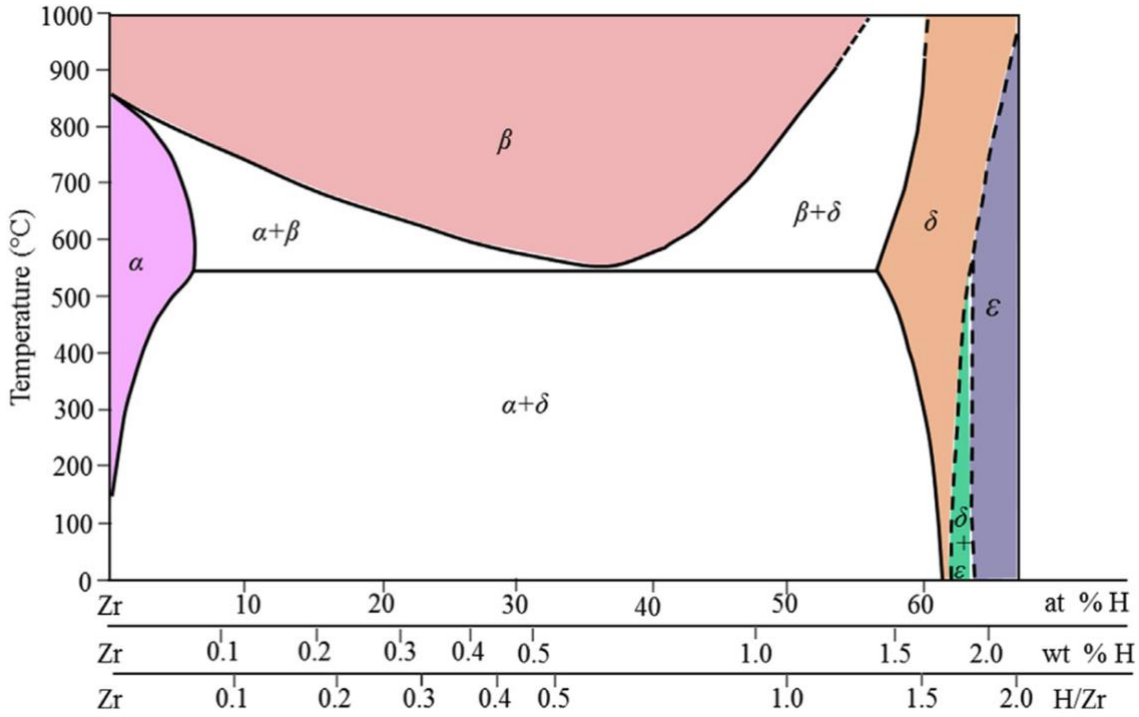

Figure 2.3 The equilibrium phase diagram of zirconium-hydrogen system[4].

already been observed and identified in experiments: ξ-hydride ($ZrH_{0.5}$) with trigonal structure, γ-hydride (ZrH) with face centered tetragonal (fct) structure, δ-hydride ($ZrH_{1.5-1.7}$) with face centered cubic (fcc) structure and ε-hydride (ZrH_2) with face centered tetragonal (fct) structure[4]. In the lattice of the hydrides, except ξ-hydride, hydrogen atoms are considered to occupy tetrahedral interstitial sites with different order and fractions[35]. The crystal parameters of zirconium and these four hydride phases are summarized in Table 2.1[4]. The δ-hydride and ε-hydride are stable phases whereas ξ-hydride and γ-hydride are metastable phases,

as a consequence, excluded in the zirconium-hydrogen phase diagram (as shown in Figure. 2.3[4]). ξ-hydride was newly discovered recently. It is expected to be a precursor for γ- or δ-hydride and may play a critical role in the re-orientation of hydrides[36][37]. In the early stage, there was some controversy on the stability of γ-hydride. Currently, most works reach an agreement that γ-hydride is a metastable phase in zirconium alloys, even though it was observed to be an equilibrium phase in the zirconium with extremely high purity (> 99.9%) in some experimental works[38]. The majority of research work has been done on δ- and γ-hydrides, since they are considered to be most responsible for the embrittlement and fracture of zirconium alloy claddings during both operation and dry storage in the most cases.

All the zirconium hydrides are brittle phases. Their elastic moduli are found to be higher than that of α-Zr matrix[39]. A slight drop in their elastic moduli as the function of temperature is observed by the nanoindentation measurements applied to bulk zirconium hydrides, from ~ 113 GPa to ~110.5 GPa for δ-hydride and from ~ 61 GPa to ~54 GPa for ε-hydride in the temperature regime from room temperature to 300°C[40]. Young's modulus and yield strength of hydride specimens almost stays constant until the stoichiometry ratio ($x = H/Zr$) reaches about 1.5, where δ-hydride becomes the major phase. After that, these mechanical properties start to decrease with rise in hydrogen content and get a minimum for the ε-hydride. The yield strength also diminishes rapidly when temperature increases from ambient temperature to 150 °C[41]. It has been experimentally observed that the hardness of hydrides is much higher compared to that of α-Zr matrix and decrease with increasing hydrogen content[42][43]. The nano-hardness of δ-hydride showed a sharp drop with temperature up to 400°C, from 4.1G Pa to 2.41 GPa. Similarly, the nano-hardness of ε-hydride significantly decreased from 3.06 GPa to 2.19 GPa when temperature was elevated to 300°C[40]. In addition, the thermo-physical properties of these hydrides have been experimentally investigated as well. The heat capacity

of hydrides seems to mainly depend on the vibrational contributions. It is remarkably larger than that of α-Zr matrix and the gap between them widens with temperature elevated. The thermal diffusivity decreased with increasing temperature but appears to be not determined by hydrogen content. The thermal conductivity of δ-hydride, calculated from heat capacity and thermal diffusivity, was slightly smaller than that of α-Zr matrix. The thermal expansion coefficients of hydrides are found to be larger than α-Zr matrix and show an increase with rise in temperature[39].

2.3 Hydride precipitation, morphology and distribution in zirconium alloys

Precipitation of hydrides in zirconium alloys is a martensitic transformation which occurs through simultaneous movements of both zirconium and hydrogen atoms by shearing[44][45]. It is an extremely complicated process and hence affected by various factors involving microstructure (such as texture, grain size etc.), thermal history, hydrogen absorption conditions, hydrogen content and stress state (including both residual and external stress) in α-Zr matrix etc.

A computational study reported that the formation energies of γ-, δ- and ε-hydrides nearly equal to each other and thus the nucleation of a specific hydride phase may be determined by thermal and mechanical treatments[46], which agrees with experimental results to some extent. It has been experimentally observed that the phase of hydride precipitated in α-Zr matrix depends on various factors, including hydrogen concentration, purity of α-Zr matrix, thermal treatment, applied stress, strain rate and cooling rate etc. In general, δ-hydride is usually formed under a high hydrogen concentration and/or a slow cooling rate, while the opposite conditions often result in the formation of more γ-hydrides[47][48]. The amount of oxygen impurities was also found to have influence on which phase of hydrides precipitates. High oxygen concentration

led to the formation of δ-hydride whereas γ-hydride tended to precipitate when the oxygen concentration in α-Zr matrix was low[49]. The hydride rim generated by a long-time electrolyte hydrogen charging on the zircaloy-4 sheet was identified as ε-hydrides[50]. In annealed zircaloy-4 claddings, δ-hydride was predominantly precipitated at the hydrogen concentration up to 1200 wt. ppm. When hydrogen concentration was increased to approximately 3000 wt. ppm, a significant amount of γ-hydride was also observed. The ε-hydrides appeared at even higher hydrogen concentration surpassing about 6000 wt. ppm[51].

Notably, δ-hydride is most commonly observed in experiments. Since the cooling rate of nuclear fuel claddings in service is relative slow, δ-hydride is considered to result in the majority of embrittlement and relevant failure in the real working environment. Nevertheless, the δ to γ hydride transformation still occurs in some occasions. For example, it was reported that δ-hydride could transfer to γ-hydride very slowly at low temperature (below 100°C)[52][53]. Another experimental study showed the precipitation of γ-hydride from the mixture of α-Zr + δ-hydride at 180°C during dehydrogenation at slow cooling rate[54]. This transformation was also observed in hydrogenated zircaloy specimens to which tensile strain

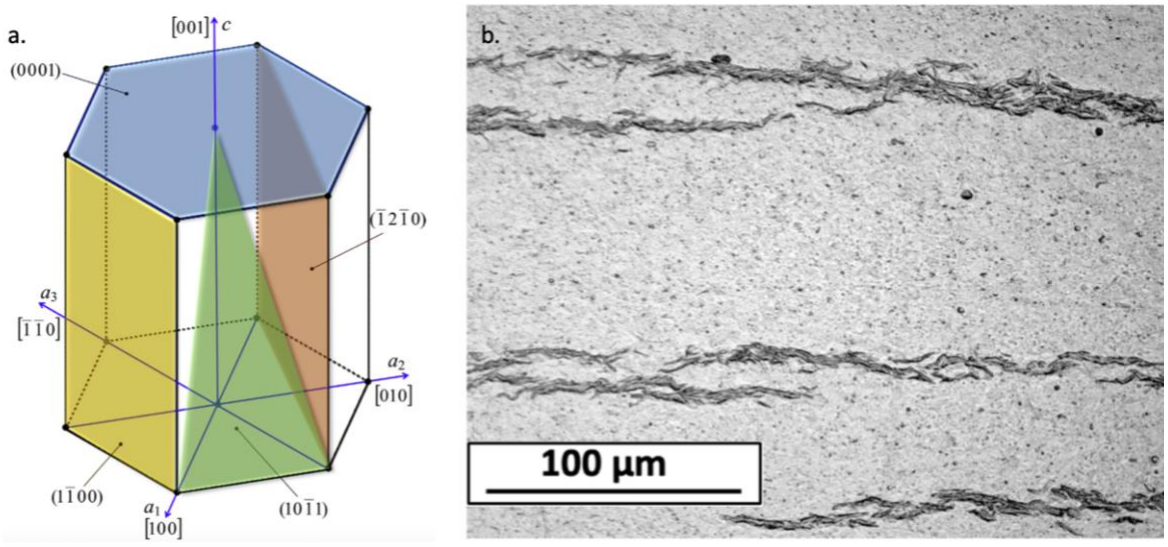

Figure 2.4 a. Some observed habit planes in a hcp unit cell[4] and b. micrograph of a cross section of Zircaloy-4 with hydrides at high magnification[56].

was applied at relatively low rates and can be reversed by annealing the specimens[55]. However, the conditions for δ to γ hydride transformation remain ambiguous.

The δ-hydride tends to precipitates in the form of platelets, while γ-hydride normally appears as needle-like structures with their long axes parallel to the $\langle 11\bar{2}0\rangle$ directions of α-Zr matrix[48]. Furthermore, the mesoscale hydride precipitates observed at low magnification are not isolated hydride grains. They are the mesoscale clusters composed of many nanoscale hydride platelets (or needles) stacking together, as shown in Figure. 24. b[56]. Such morphology is supposed to be mainly determined by the combination of orientation relationship and mechanical interaction between hydrides and matrix, as well as the mobility characteristics of hydrogen in α-Zr matrix.

Table 2.2 The observed crystal orientation relationship between hydrides and α-Zr as well as different hydride phases[4].

Phases	Crystal orientation relationship	Reference
γ-hydride and α-Zr	$(0001)_\alpha//\{111\}_\gamma$, $[11\bar{2}0]_\alpha//[1\bar{1}0]_\gamma$	[47]
δ-hydride and α-Zr	$(0001)_\alpha//\{111\}_\delta$, $[11\bar{2}0]_\alpha//[1\bar{1}0]_\delta$ and $\{10\bar{1}7\}_\alpha//\{111\}_\delta$, $[11\bar{2}0]_\alpha//[1\bar{1}0]_\delta$	[57]
γ-hydride and δ-hydride	$\{100\}_\delta//\{100\}_\gamma$	[62]
ε-hydride and δ-hydride	$(220)_\varepsilon//(220)_\delta$ and $\{111\}_\varepsilon//\{1\bar{1}1\}_\delta$, $\{311\}_\varepsilon//(311)_\delta$	[63]

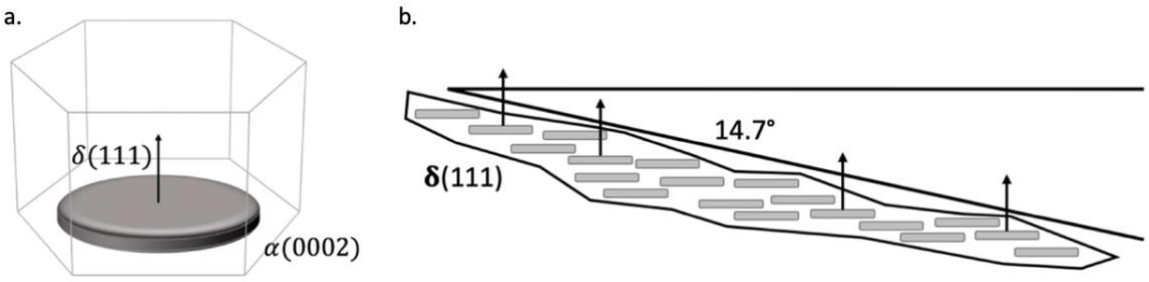

Figure 2.5 a. Schematic diagram of a nanoscale δ-hydride in α-Zr and b. schematic diagram shows how the nanoscale δ-hydrides may stack together to form a mesoscale hydrides[62].

Despite of different crystal structures, both δ- and γ-hydrides grow along the $\langle 11\bar{2}0\rangle$ directions of α-Zr matrix[3]. Dissimilarly, the observed habit planes, crystallographic planes in α-Zr matrix along which hydride precipitation occurs, are quite various. Moreover, the broad side of a δ-hydride platelet is parallel to the corresponding habit plane. γ-hydride was found to have

the habit planes of $\{10\bar{1}0\}$ and $\{10\bar{1}L\}$, where L is equal to 7 approximately[57]. Many habit planes for δ-hydride were reported in literature, including $\{0001\}$, $\{10\bar{1}7\}$, $\{10\bar{1}0\}$ in pure zirconium, $\{10\bar{1}1\}$ and twinning planes of $\{10\bar{1}2\}$, $\{11\bar{2}1\}$ and $\{11\bar{2}2\}$ [48][58][59][60]. Some of these crystallographic planes are shown in Figure. 2.4 a[4]. It was suggested that temperature might influence which crystal planes act as habit planes[61]. Another model proposed based on experimental observation is that the habit plane for nanoscale δ-hydride platelets is $\{0001\}$ while the mesoscale δ-hydride clusters, formed by hydride platelet stacking along the planes 14.7° off the basal plane, exhibiting a habit plane of $\{10\bar{1}7\}$, as shown in Figure. 2.5[62]. The experimental difficulties in identifying the orientation relationship between the hydrides and α-Zr matrix also contributes to such variation in the observation of habit planes. The observed orientation relationships between hydrides and matrix as well as those between the different hydride phases are shown in Table 2.2[4][63][64].

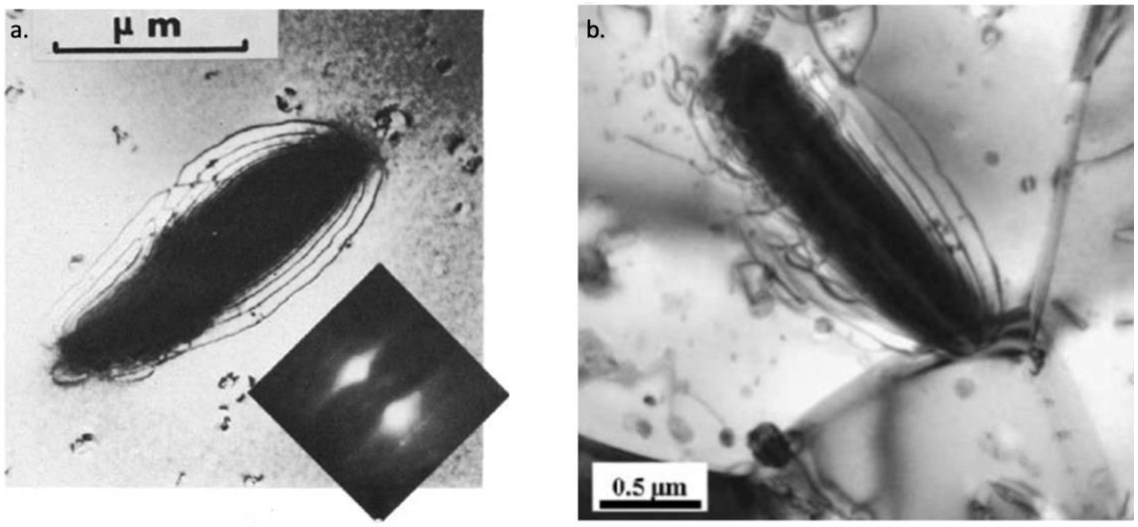

Figure 2.6 The TEM images of dislocation loops around a. an intra-granular nanoscale hydride platelet and b. a nanoscale hydride platelet adjacent to a grain boundary [65][66].

Because of the lower density of hydrides than α-Zr matrix, hydride precipitation leads to local volume expansion, which can be as high as 12.3% and 17.2% for γ- and δ-hydrides respectively[65]. Such expansion induces strains, elastic stress field, and even dislocation loops surrounding the nanoscale hydride precipitates, as shown in Figure. 2.6[65][66]. The misfits

between γ-hydride and α-Zr matrix in $[0001]$, $[11\bar{2}0]$ and $[1\bar{1}00]$ directions were calculated to be 5.70%, 0.551% and 5.64% respectively. The anisotropy in misfits could only encourage the growth of γ-hydride along $[11\bar{2}0]$ direction and thus results in its needle-shaped morphology. For δ-hydride, similar calculation was conducted and showed that the misfits in $[0001]$, $[11\bar{2}0]$ and $[1\bar{1}00]$ directions were 7.2%, 4.58% and 4.58% respectively. Larger misfit in $[0001]$ direction could restrain hydride growth normal to basal plane, while smaller and equal misfits in the other two directions may promote isotropic growth on basal plane, leading to platelet shape of δ-hydride[67]. Furthermore, the diffusion of hydrogen in α-Zr matrix is very sensitive to stress. A stress gradient forces hydrogen to move toward tensile stress concentration region[68]. Therefore, the elastic stress field and dislocation loops around a nanoscale hydride drive hydrogen to assemble and lead to new hydrides precipitate nearby, forming a mesoscale hydride cluster in the shape of plate eventually.

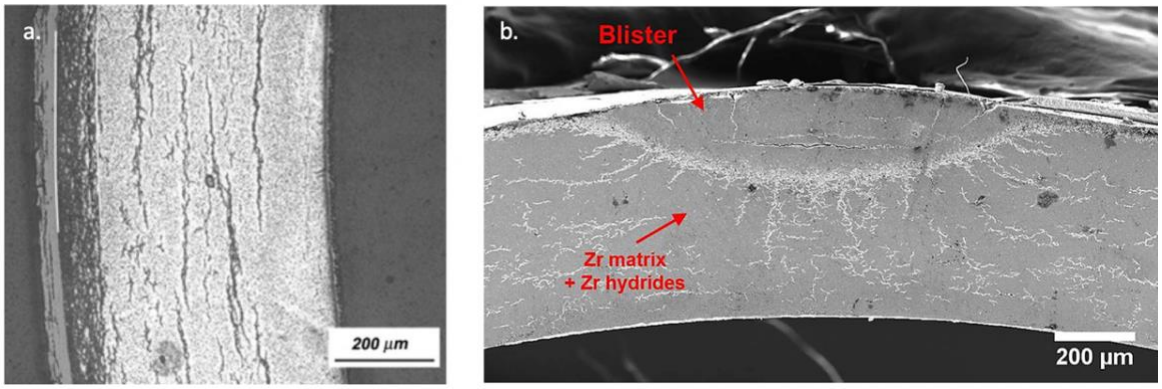

Figure 2.7 The SEM images of a. a hydride rim[70] and b. a hydride blister[71] on the cross section of the zirconium alloy claddings.

Meanwhile, in practice, hydrides are also driven to form at the location with sufficient stress concentration in front of the flaw (such as micro-voids and micro-cracks), even though the hydrogen concentration in the rest parts is still lower than the terminal solubility limit for precipitation[37]. It will significantly degrade the mechanical properties of zirconium alloy claddings. In addition, hydrogen can fairly fast response to temperature gradient and diffuse in the direction of decreasing temperature, leading to higher hydrogen concentration and

preferential precipitation of hydrides in the cold regions. In a nuclear reactor, since the temperature decreases from the inner side to the outer side of the fuel cladding tubes, hydrogen tends to move to the outer side of the tube and then precipitate, usually forming a hydride rim[69], as shown in Figure. 2.7 a.[70]. The hydride rim uniformly covers a relatively large area with the thickness in the range of 50-60 μm. In azimuthal direction, the heterogeneity inside reactor cores, as well as oxide spallation, also can create some regions with relatively lower temperature, where hydride blisters are formed subsequently, as shown in Figure 2.7 b.[71]. Different from hydride rims, a hydride blister only occupies an elliptical-shaped small zoon, but its thickness can be up to half of the cladding thickness. In the axial direction, the accumulation of hydrides is observed in the inter-pellet regions with lower temperature[72][73].

Even though without any temperature and stress gradients, the precipitation of hydrides in α-Zr matrix is still not homogeneous. In the polycrystalline zirconium alloys, hydrides are more likely to precipitate at grain boundaries, especially along the grain boundaries close to the habit planes of hydrides[47][50][74]. However, intra-granular hydrides are dominant in the α-Zr matrix with coarse grains and/or rapid cooling rate[50]. It was also observed that the formation of solute segregation might decrease the grain boundary energy in the matrix and thus diminish hydride precipitation on the grain boundaries[75]. In the zirconium alloys with the presence of β-phase, another favorable site for hydride precipitation is the α-β interface[76]. Additionally, it has been recognized that the texture of α-Zr matrix considerably influences the orientation of hydride precipitates[77]. The zirconium alloy claddings commonly have strong crystallographic texture, where the basal poles of most grains orient close to the radial direction (normal direction for zirconium alloy sheets). As the basal planes of $\{0001\}$ and $\{10\bar{1}7\}$ are the most commonly observed habit planes of the hydrides, the nanoscale hydride platelets precipitate with their normal close to the radial direction, finally forming the mesoscale hydride clusters parallel to the circumferential direction of the claddings, which are called

circumferential hydrides. As shown in Figure 2.7 a.[70], on the cross section of the claddings, these mesoscale hydride clusters appear in the form of long lines, which can be longer than 100 μm and slightly change their orientations while crossing grain boundaries.

2.4 Reorientation of hydrides

It has been shown that externally applied stress has a significant impact on the orientation of mesoscale hydrides. The mesoscale hydrides tend to form along the direction perpendicular to the tensile stress[78]. The reorientation of hydrides in the claddings is often referred to the transformation from circumferential hydrides to radial hydrides. It usually occurs when nuclear fuel rods are transited between wet and dry storage, during which temperature is elevated first, leading to dissolution of hydrides, and then decreased, causing re-precipitation of hydrides. Due to the existence of circumferential stress during the re-precipitation, the new mesoscale hydrides are likely to precipitate along the radial direction and form radial hydrides. Compared to circumferential hydrides, radial hydrides are much more detrimental to the overall mechanical properties of the claddings. Therefore, reorientation of hydrides plays an important role in the degradation of zirconium alloy claddings.

It was observed that such reorientation of hydrides is very pronounced when the claddings were cooled from 300 °C to 200 °C, while less predominant during the cooling process in the lower or higher temperature ranges. Furthermore, longer loading time at a given temperature also can enhance hydride reorientation[79]. It is noteworthy that the reorientation of hydrides occurs only when the applied tensile stress reaches a threshold value. The threshold stress for hydride reorientation has been correlated to various factors. It is found to increase with rise in yield strength of the cladding samples and decrease as temperature is elevated. For example, it was measured to be 90 MPa at 235 °C while 60 MPa at 400 °C[80][81]. Larger tensile stress is

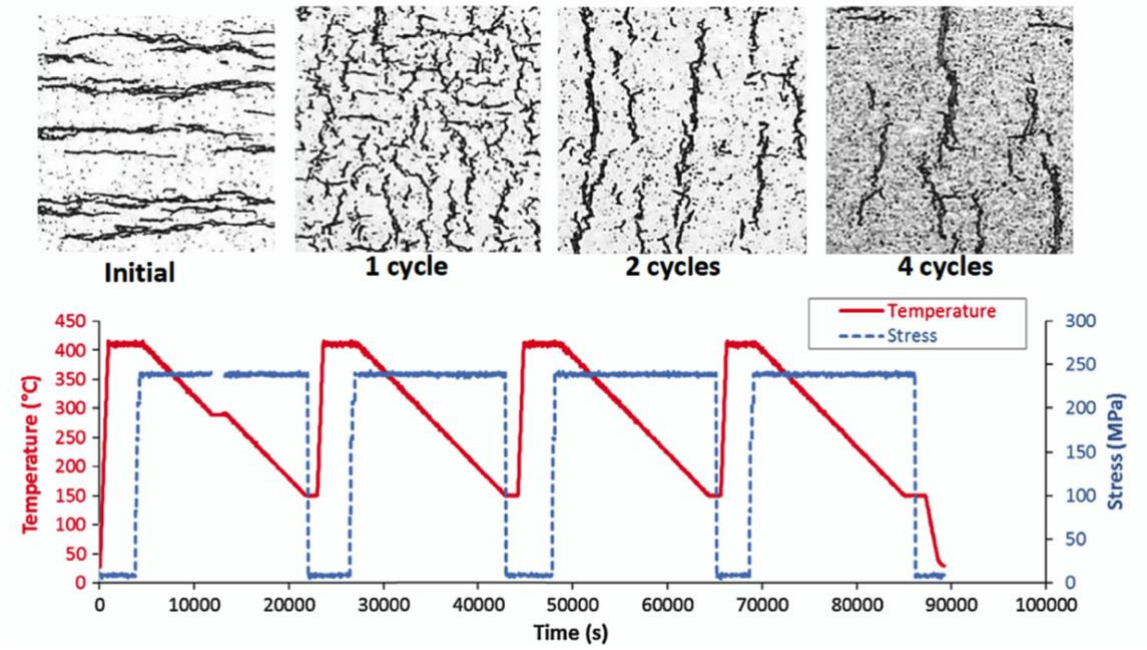

Figure 2.8 The upper four micro-images show the hydrides in the zircaloy-4 samples with 192 wt.ppm hydrogen content after different number of thermal cycles under the applied tensile stress of 230 MPa in the vertical direction. The parameters of thermal-mechanical cycles are shown in the bottom graph[84].

required for the hydride reorientation in the claddings with more hydrogen content[82]. Additionally, some recent experiments showed that the threshold stress was reduced by half when uniaxial tension was changed to be biaxial[83]. However, there is still a lack of a universal model to accurately predict the threshold stress for specific conditions.

The thermal-mechanical cycles have a profound effect on the reorientation of hydrides in zirconium. As shown in Figure 2.8, the area fraction of the radial hydrides to the circumferential hydrides initially, as well as the connectivity and size of hydrides, significantly increase with increasing the number of cycles[84]. There is a memory effect in the hydride reorientation. As mentioned in the section 2.3, the volume expansion during hydride precipitation induces dislocation loops around the nanoscale hydride platelets. Even though initially precipitated hydrides dissolve at higher temperature, these dislocation loops remain and act as heterogeneous nucleation sites during cooling, leading reoriented hydrides to become larger and closer to each other[34].

2.5 Effects of hydrides on the mechanical properties of zirconium

Hydride phases are extremely brittle whether at high or low temperature[85] and hence the precipitation of hydrides has been shown to significantly reduce the ductility of the zirconium alloy claddings, as a result, leading to ductile to brittle transition[86]. The fracture energy shows an abrupt drop, which means ductile to brittle transition, during a decrease in temperature[87][88], as shown in Figure 2.9[87]. Generally, the samples with more hydrogen content exhibits a higher temperature for the transition from ductile to brittle (DBTT). For those with the similar hydrogen concentrations, the DBTT for the samples with radial hydrides is much higher than that for the samples with circumferential hydrides. Uniformly distributed circumferential hydrides might marginally enhance the strength of the claddings and can slightly decrease the ductility at all temperature studied[89][90]. Only at high hydrogen concentrations, can circumferentially oriented hydrides cause ductile to brittle transition in the temperature range from operating temperature to room temperature (approximately 350 °C to

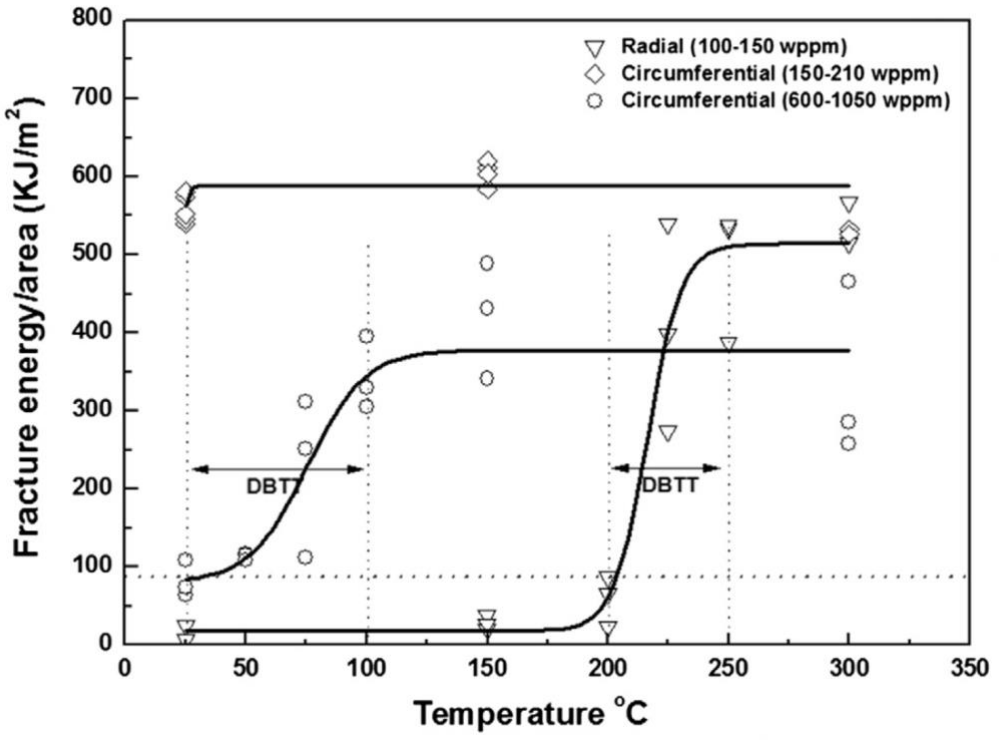

Figure 2.9 The fracture energy of samples with different hydrogen concentrations and orientations of hydrides vs temperature in ring compression tests[87]. Note: ductile to brittle transition temperature (DBTT).

20 °C). Segregated long circumferential hydrides have more detrimental effect on the ductility of the claddings compared to scattered short circumferential hydrides[90]. Although the effect of radial hydrides on the ductility in axial direction is suggested to be insignificant, a small amount of radial hydride can extremely degrade the overall mechanical properties of the claddings in hoop direction[91]. In addition to the hydrogen concentration and the orientation of hydrides, the DBTT also depends on the alloy types and stress at the highest dry storage temperature. For example, the DBTT of high-burnup zircaloy-4 is below 20 °C with hoop stress at 110 MPa, while about 50 °C for the stress of 140 MPa[92].

At high temperatures (operating temperatures for zirconium alloy fuel claddings), the loss of ductility caused by precipitation of circumferential and radial hydrides are relatively small and comparable to each other[93]. Due to the significant improvement in the ductility of the zirconium matrix with temperature increasing, the hydrided claddings usually remain ductile at high temperature[86]. As the zirconium alloy fuel claddings are exposed to corrosive environment and hoop stress, which is lower than the yield stress of the zirconium matrix, at high temperature for a long time in service, creep crack growth is one of the important fracture mechanisms for the fuel claddings[35]. For pure zirconium with hydrogen concentration in the range of 0-185 wt. ppm, a slight increase in creep rate was found with rise in hydrogen concentration. It is also concluded that the dissolved hydrogen increases the creep rate by altering the Young's modulus rather than changing the creep mechanism[94]. For hydrogen concentration ranging from 16 to 756 wt. ppm, it was reported that solute hydrogen greatly accelerated the creep behaviors in the recrystallized zircaloy-4, while diminished the creep rate in the cold-worked stress-relieved zircaloy-4 at 400 °C. The creep rates were decreased by the precipitation of hydrides in the cases of both stress-relieved and recrystallized zircaloy-4[95].

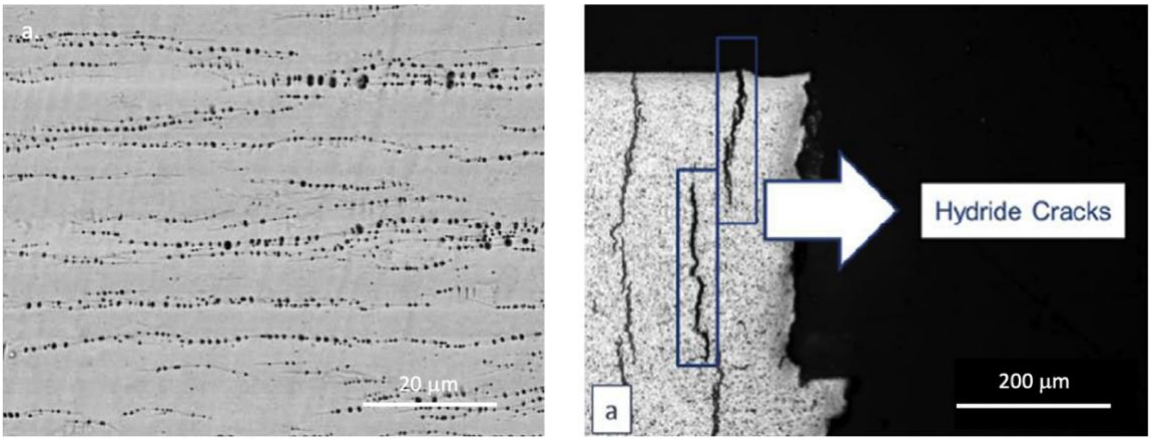

Figure 2.10 a. Voids formed along circumferential hydrides[96] and b. long cracks along radial hydrides[12] in the zirconium alloys after fracture.

At low temperatures, the fracture mechanisms of the zirconium alloy claddings containing circumferential and radial hydrides are totally different. During deformation of the cladding only contain circumferential hydrides, strain can induce the initiation, growth and coalescence of voids on the circumferential hydrides, resulting in a ductile fracture unless the hydrogen concentration is extremely high, as shown in Figure 2.10. a[96]. In contrast, long cracks are likely to form and grow along radial hydrides under load, leading to a brittle fracture, as shown in Figure 2.10. b[12]. When the claddings contain circumferential and radial hydrides simultaneously, fracture is supposed to occur by the combination of these two mechanisms, which is a much more complex process.

It is worth noting that the formation of hydrides under load can cause crack growth through a slow cracking mechanism, called delayed hydride cracking (DHC), even though the fracture toughness of the zirconium matrix is not reached. DHC is an important mechanism for the failure of claddings in the storage stage. The process of DHC is shown in Figure 2.11[4]. The higher tensile stress zone at a crack tip leads to the precipitation of hydride platelets perpendicular to the applied stress, in the plane of crack. These hydrides fracture to extend the crack length once the critical length of them is reached and then new hydrides precipitate at the new tip. This process repeats and causes stable growth of the crack, eventually leading to the

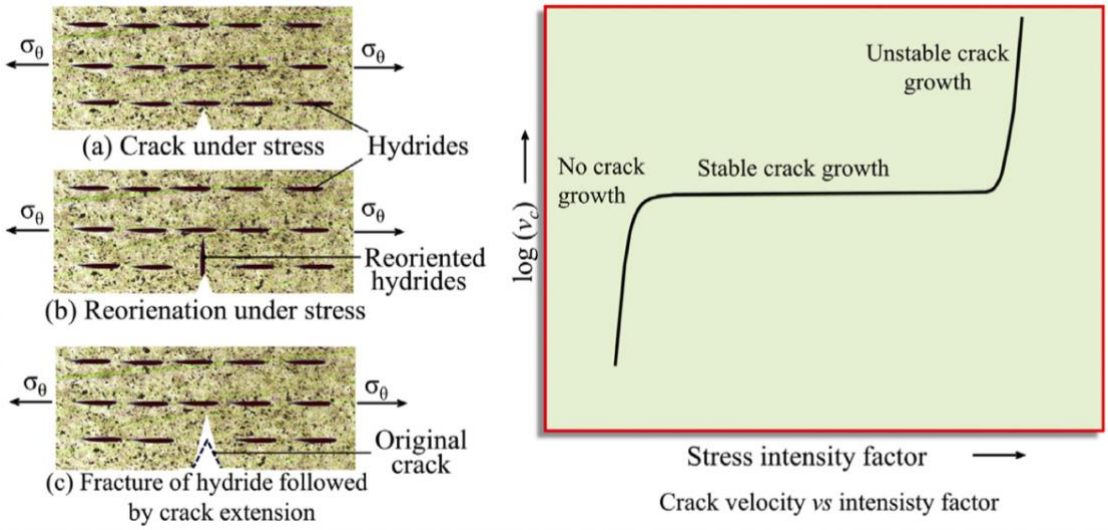

Figure 2.11 Stages during DHC and the relationship between crack velocity and stress intensity factor[4].

failure of claddings[97]. Since it takes some time to reach the critical conditions for hydride fracture at the crack tip, DHC is an intermittent process. The cracking is activated only when the critical intensity factor is surpassed and gradually approaches to the stable state as the crack propagates. For example, when zircaloy-2 cladding tubes with hydrogen concentration ranging from 90 to 130 ppm were tested under tensile hoop stress in the temperature regime of 225-300 °C, the critical stress intensity factor was measured to be in the range of 4-6 MPa $m^{1/2}$[98]. The crack velocity v_c is considered to be greatly controlled by the diffusivity and solubility of hydrogen in zirconium alloys. It was found to be a function of temperature, following Arrhenius relation given by $v_c = v_0 e^{-Q/RT}$, where v_0 is a constant, Q is the activation energy for DHC, R is the gas constant and T represents temperature[99][100]. DHC is able to occur even at room temperature[101]. In addition, it was reported that DHC could be restrained by the existence of remained β phase in α-Zr matrix[102]. Even though extensive investigation has been conducted on DHC in the last few decades, the detailed mechanisms of it are still ambiguous.

In addition, non-uniform distribution of hydrides (e.g., hydride blisters) are more detrimental to the fuel claddings. In the temperature range of 25-300 °C, many cracks nucleate inside and grow through the hydride blisters once the plastic zone underneath the blisters yields, leading

to elastic-plastic fracture at room temperature or ductile failure due to the plastic deformation localization near the blisters at high temperatures. The fracture strain decreases with increasing the depth of the blisters at all the temperatures investigated and it decreases more rapidly with the drop in temperature[103][104].

2.6 Computational study on hydrides in zirconium alloys

The phenomena associated with hydrides in the zirconium alloy fuel claddings during reactor operation and wet/dry storage are extremely complex, influenced by various factors. Due to the limited experiment conditions and methods, too complicated in-situ experiments are unpractical. In order to gain a better understanding of their mechanisms and accurately predict the behaviors of both hydrogen and hydrides in the zirconium claddings, a series of models based on various methods have been developed to study hydrides and relevant phenomena. Most results obtained from them agree with the experimental investigations well.

Atomic scale modelling, such as first principle based density functional theory (DFT) calculations, can provide crucial information about crystal structure and the properties of hydrides at nanoscale, which is quite difficult to be obtained from experiments and can be used for modelling work on hydrides at larger scales. For example, DFT calculations were conducted to approve that the sites occupied by hydrogen atoms in α-Zr matrix are likely to be tetrahedral sites, particularly at low temperatures[46]. In another DFT study, the variations in the free energy from α-Zr matrix to ξ- and γ-hydrides were determined at a few temperatures and showed that hydrogen may firstly precipitate as ξ-hydride, and then transform into γ-hydride, owing to its lower interfacial energy than that of γ-hydride[105].

Phase field method is a powerful and versatile modelling method for microstructure evolution of hydride precipitation and growth at mesoscale, such as the effect of matrix microstructure,

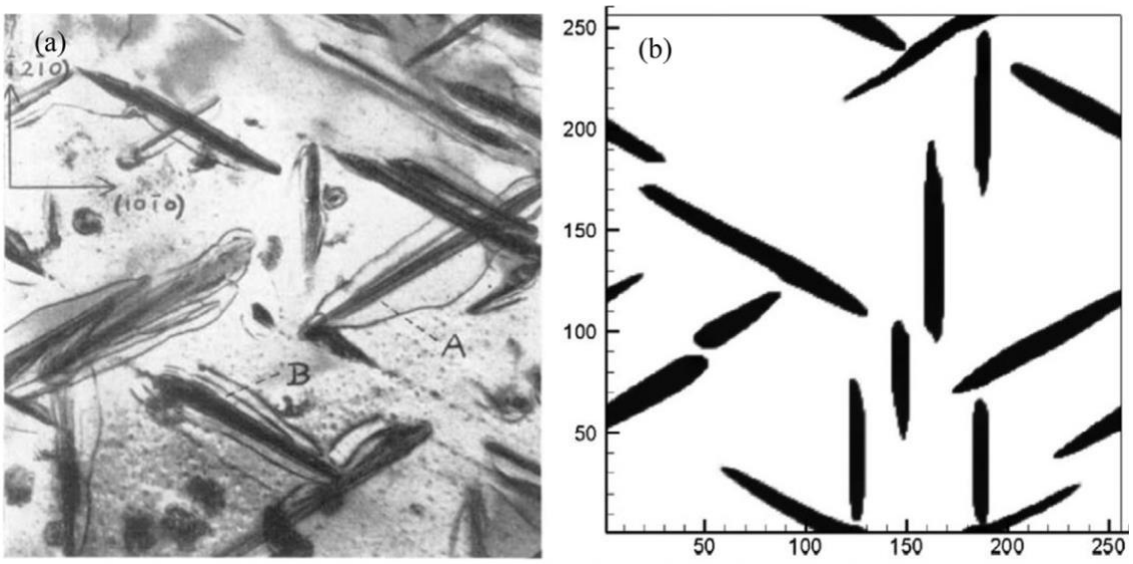

Figure 2.12 (a) TEM observation of γ-hydrides[106] and (b) the results of a quantitative phase field simulation[107]. The side length of both images is about 4μm.

other hydrides, a crack/notch and external stress on the morphology of γ-hydrides. The morphology of γ-hydrides, obtained from a phase field study using a temperature dependent model, is quite similar to that observed under TEM, as shown in Figure 2.12[106][107], even though some key parameters were not considered. At present, quantitative phase field models are being developed by combining the computer coupling of phase diagram and thermochemistry based free energies with a phase field model together. A quantitative phase field model based on free energies of formation has been proposed for α-Zr matrix/ δ-hydride system[108].

The finite element method (FEM) has been widely used for studying the phenomena related to hydride embrittlement. A mesoscale kinetic model based on FEM was developed to investigate the impact of hydrogen content on the creep behavior of zircaloy-4 sheets. In this work, the creep behavior was found to be significantly influenced by the orientation and distribution of hydrides, showing a good agreement with the experimental results in literatures[109]. The outside-in-crack movement with the presence of hydride precipitation was also simulated by using FEM, which showed that longer radial hydride precipitates are more likely to accelerate

the growth of crack[110]. Another model based on de-cohesion crack propagation mechanism was proposed and used to simulate hydride fracture combined with FEM. It revealed that the fracture toughness declined as the parallel stress to crack faces increased[111]. Furthermore, delayed hydride cracking was also studied by a finite element model. It was observed that the precipitation of δ-hydrides can remarkably change the stress distribution near the crack tip and the velocity of cracking was mainly determined by various factors, including temperature, stress intensity factor and material strength etc.[112]

Recently, the internal stress induced by the hydride formation and its effect on the precipitation, growth, and morphology of δ-hydrides in α-Zr matrix were investigated by using discrete dislocation dynamic method on the basis of a Fast Fourier Transform (FFT). This simulation work showed that the stress was relaxed within very small regions (approximately 300nm) surrounding a δ-hydride precipitate and the dislocations released from the hydride-matrix interface can act as nucleation sites for new hydrides[113].

Chapter 3 Techniques and instruments

This chapter gives an overall introduction of the techniques and instruments used for microstructure and micromechanical characterization of hydrides in zirconium in this thesis, including scanning electron microscope (SEM), focus ion beam (FIB), electron backscatter diffraction (EBSD) and digital image correlation (DIC) strain measurements.

3.1 Scanning electron microscope

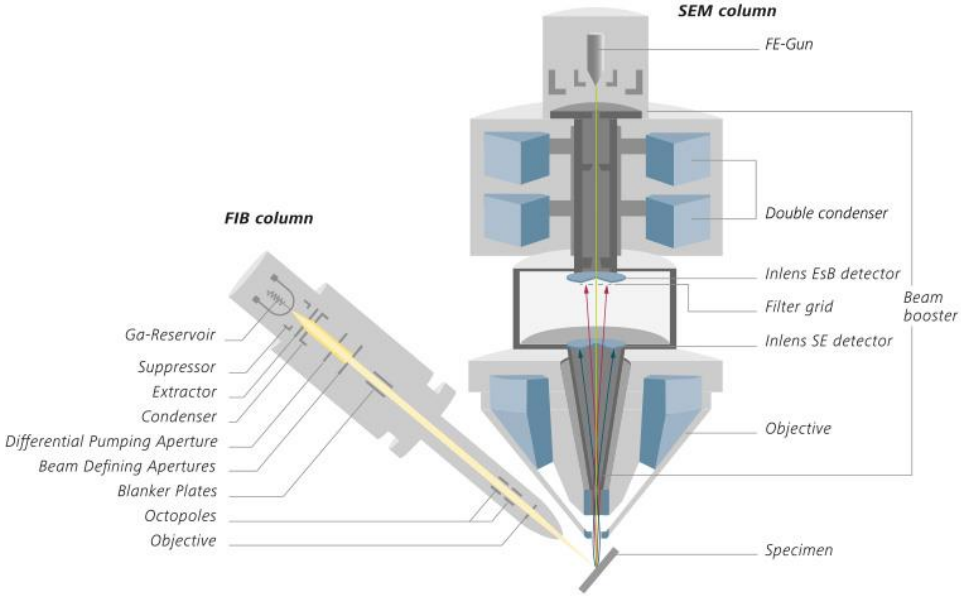

Figure 3.1 Schematic of one of the newest FIB/SEM systems, ZEISS Crossbeam 550 whose predecessor is crossbeam 540 and the FIB-column arranged at an inclination angle of 54°. (This image is provided on https://www.zeiss.com/microscopy/en/products/sem-fib-sem/fib-sem/crossbeam.html/).

A scanning electron microscope (SEM) is a powerful research tool in materials science. It images the small details of materials at high magnifications with an excellent depth of field by scanning the sample surface with a focused electron beam in a raster pattern. The typical spatial resolutions offered by a SEM are between 0.5 and 4 nm. An example of a SEM column with a FIB column beside is shown in Figure 3.1. When the focused electron beam hits the sample

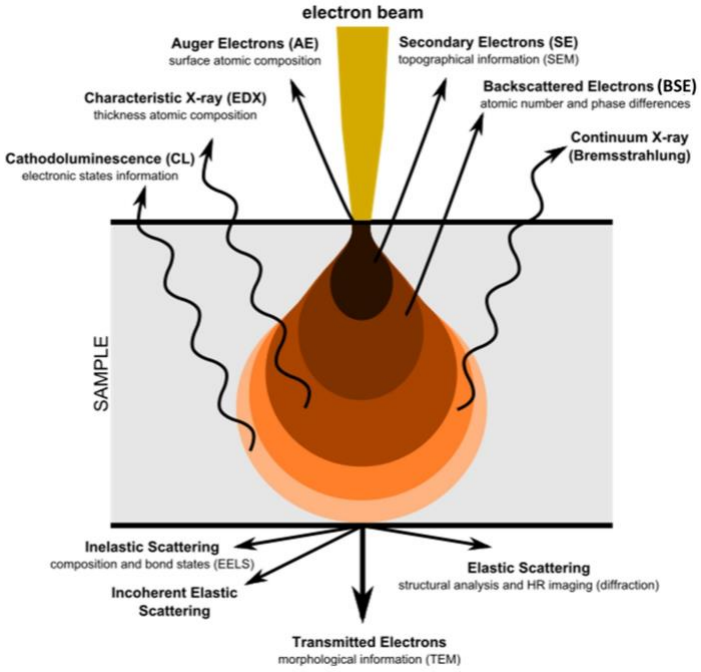

Figure 3.2 Schematic of the interaction between electrons and the sample at and near the sample surface and the different types of signals are generated from different depth zones. (This image is provided by Wikipedia https://en.m.wikipedia.org/wiki/File:Electron_Interaction_with_Matter.svg)

surface, the electrons interact with the atoms and various signals carrying different information are released, as shown in Figure 3.2. The SEM can perform versatile types of analysis by collecting different signals via proper detectors.

For visual inspection of the sample surface, backscattered electrons (BSEs) and secondary electrons (SEs) are commonly used. BSEs come from the elastic interaction between the

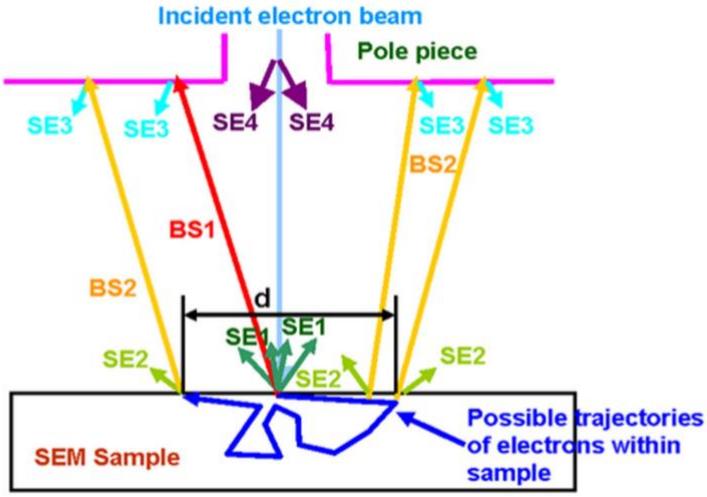

Figure 3.3 Schematic of the generation of the four types of secondary electrons when the electron beam hits the sample surface in a SEM[114]. SE1-SE4 are secondary electrons. BS1 and BS2 are backscattered electrons.

incident electrons and the sample in a deeper zone, while SEs are the result from the inelastic interaction between the electrons and atoms in surface regions. Thus, BSEs imaging are more sensitive to the differences in atomic number, whereas SEs imaging are better at revealing surface topography.

The SEs are further classified into four types according to how they are generated, as shown in Figure 3.3[114]. SE1 and SE2 are used to produce images of the sample surface, while SE3 and SE4 lead to noise for imaging. SE1 are directly generated at the point where the incident electron beam hits the sample surface and provide the highest resolution information. The imaging mode using SE1 is commonly called In-lens mode. SE2 are produced when the BSEs leave the sample surface, sub-microns away from the incident beam. SE2 images also contain information of atomic contrast, but with slightly lower resolution. The In-lens image and SE2 image of a region of interest can be obtained simultaneously. It plays an important role in the chapter 7.

Furthermore, the characteristic x-ray generated from the deeper areas can be used for chemical composition analysis, call energy dispersive x-ray spectroscopy (EDS). However, a hydrogen atom only has one electron in the shell and cannot emit x-ray when the other electrons bombard it. EDS cannot detect the hydrogen in the lattice. The electron backscatter diffraction (EBSD) provides the detailed information of the crystalline structures and orientations, which is one of the crucial techniques in this thesis and will be introduced in detail later in section 3.3.

3.2 Focused ion beam

The focused ion beam (FIB) systems were developed in the 1970s[115][116][117] and then took approximately 20 years to become commercially available[118]. A FIB setup is similar to a SEM, but replacing the electron beam by an ion beam, as shown in Figure 3.1. Most of

modern FIB systems are using liquid metal ion sources (LMIS), especially gallium (Ga^+) ion sources, and the gold and iridium ion sources are also available. Another type of commercial ion sources is plasma ion source of noble gas, such as xenon (Xe^+), which have been used more widely in the recent years. Ga^+ sources produce ion beam with small spot size and high current density, while Xe^+ plasma sources can provide much higher maximum beam current for large volume characterization.

The ion beam then is focused by electrostatic lenses and then hits the sample surface. A small amount of materials is sputtered away from the sample surface in the form of secondary ions or neutral atoms, producing secondary electrons simultaneously. Both secondary ions and secondary electrons can be collected for imaging. The amount of the materials sputtered away is greatly determined by the ion beam current. Low beam currents are used for imaging, while high beam currents for site specific sputtering, in other words, ion milling. Owing to the feature of removing materials, FIB is extensively used as an efficient micro-machining tool.

Another important function of FIB systems is deposition, which is achieved with the assistance of gas injection systems (GIS). The FIB-induced deposition process is demonstrated by a

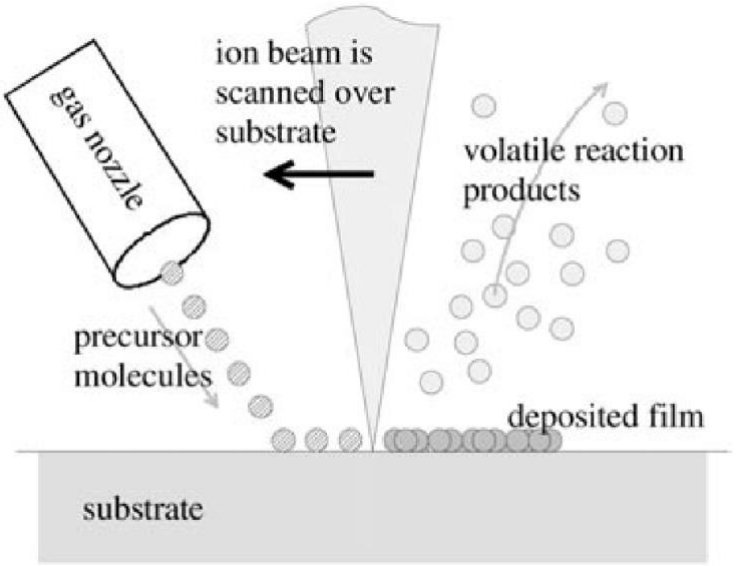

Figure 3.4 Schematic of FIB-induced deposition process [119].

schematic in Figure 3.4[119].When the region of interest is scanned with the focused ion beam, GIS injects the specific precursor gas close to the target area. The precursor gas molecules will be locally decomposed into the almost-pure material and deposit on the sample surface. Pt deposition by FIB was extensively used to protect the region of interest underneath and reduce the curtaining induced during milling.

It should be pointed out that FIB imaging is a destructive process. A FIB system is conventionally incorporated with a SEM to monitor micro-machining process to avoid extra destruction of the sample, which is called a dual-beam platform or FIB/SEM system[118]. A schematic setup of a FIB/SEM system is demonstrated in Figure 3.1. Most FIB/SEM systems are also equipped with GIS and micromanipulators, which enables their more applications in micro-machining and three dimensional (3D) tomography, including better micro-sectioning, serial sectioning and imaging, TEM sample preparation, atom probe tomography (APT) sample preparation, etc.[120][121] Recently EBSD and EDX detectors have been incorporated into some FIB/SEM systems for conventional or 3D microstructure and microchemistry characterization of a specific area or volume[121][122][123]. In this thesis, a Zeiss crossbeam 540 analytical FIB/SEM with Ga^+ source, field emission electron gun and all attachments mentioned above in the David Cockayne Centre for Electron Microscopy (DCCEM, https://www-em.materials.ox.ac.uk/) was used to do micro-sectioning with subsequent EBSD characterization on small hydride blisters and serial sectioning and imaging on redistributed δ-hydrides.

3.2.1 Micro-sectioning

Micro-sectioning with FIB/SEM system is a crucial method for site-specific sub-surface characterization in modern materials characterization. Ion milling with the FIB column is capable of accurately creating cross sections and the SEM column allows for high-resolution

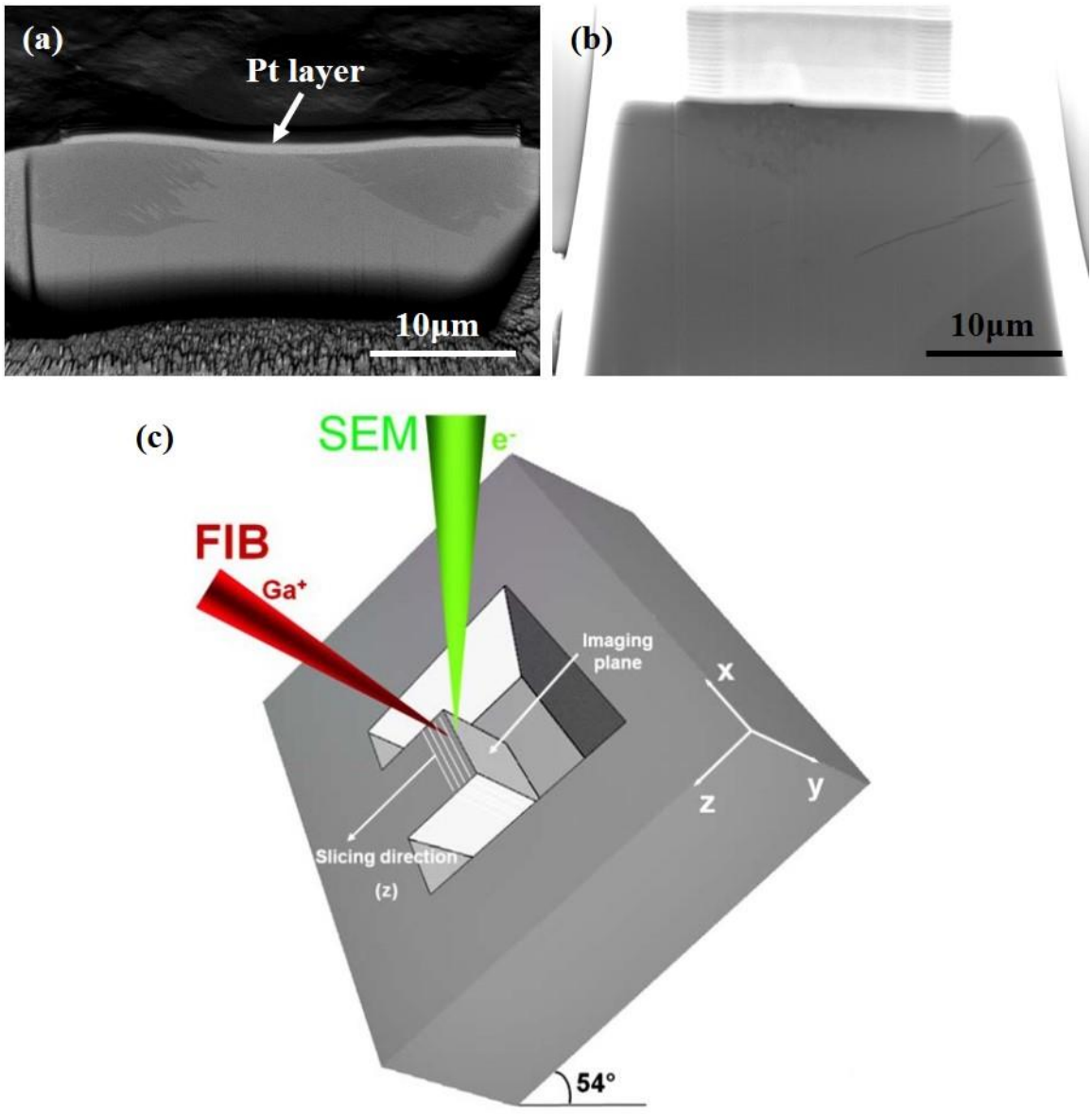

Figure 3.5 (a) Back-scattered (BSE) image of two lens-shaped small hydride blisters on the cross-section prepared by FIB micro-sectioning. (b) Imaging plane of a pure zirconium sample containing redistributed δ-hydrides during serial sectioning and imaging. (c) A schematic of the sample geometry during serial sectioning and imaging[124].

imaging at microscale. A sub-surface characterization of small hydride blisters obtained by 24h electrolytic hydrogen charging by micro-sectioning with FIB/SEM system is shown in Figure 3.5. Before sectioning, a ~1µm thick protective Pt layer was deposited on the two specific blisters interested with the ion beam current of 700pA. A large trench was then milled by a large beam current of 30 nA in front of pre-deposited Pt layer with a 4-5 µm gap between them. The depth of the trench was 25µm, which should be 5 times larger than the depth of interested

features to avoid shadowing during imaging. The finer milling was performed on the exposed cross section to improve its surface conditions for several times, until it is sufficiently defect-free for an adequate SEM imaging quality. The beam current for final milling is 700 pA. The back-scattered (BSE) image, which maximizes the atomic number contrasts, of the well milled cross section (Figure 3.5 (a)) shows the morphology of the small hydride blisters clearly. The ion beam voltage is 30 kV for all deposition and milling steps.

The micro-sectioning was used with EBSD to further study the microstructure and crystallography of small hydride blisters. This process was amended properly to prepare a nice cross section, satisfying the requirements for EBSD characterization. The details will be described in chapter 5.1.1.

3.2.2 Serial sectioning and imaging

Serial sectioning and imaging is developed based on micro-sectioning to acquire information inside a specific volume at microscale by sequential ion milling and SEM imaging. Figure 3.5 (c)[124] is a schematic of the sample geometry during serial sectioning and imaging. After an adequate cross section of the features interested is prepared by micro-sectioning, two large trenches are milled on either side of the pre-deposited Pt layer to avoid shadowing in the later imaging. A thin slice with a constant thickness, which could be as low as a few nanometers, is going to be milled away from the prepared cross section and then high-resolution SEM imaging will be taken on the new cross section. These processes will be repeated until the amount of collected slice images is sufficient to reveal the target features in the slicing direction. The 3D microstructure of the milled volume could be reconstructed from collected serial images by software, for example, Avizo, but it wasn't performed on my samples after a serious consideration. The thickness of slice, ion beam current, imaging mode should be opted carefully according to the conditions of a specific sample and the details will be further

described in chapter 5.2.1 where it was used to characterize the morphology of δ-hydrides in 3D at microscale.

3.3 Electron backscatter diffraction

3.3.1 Conventional electron backscatter diffraction (EBSD)

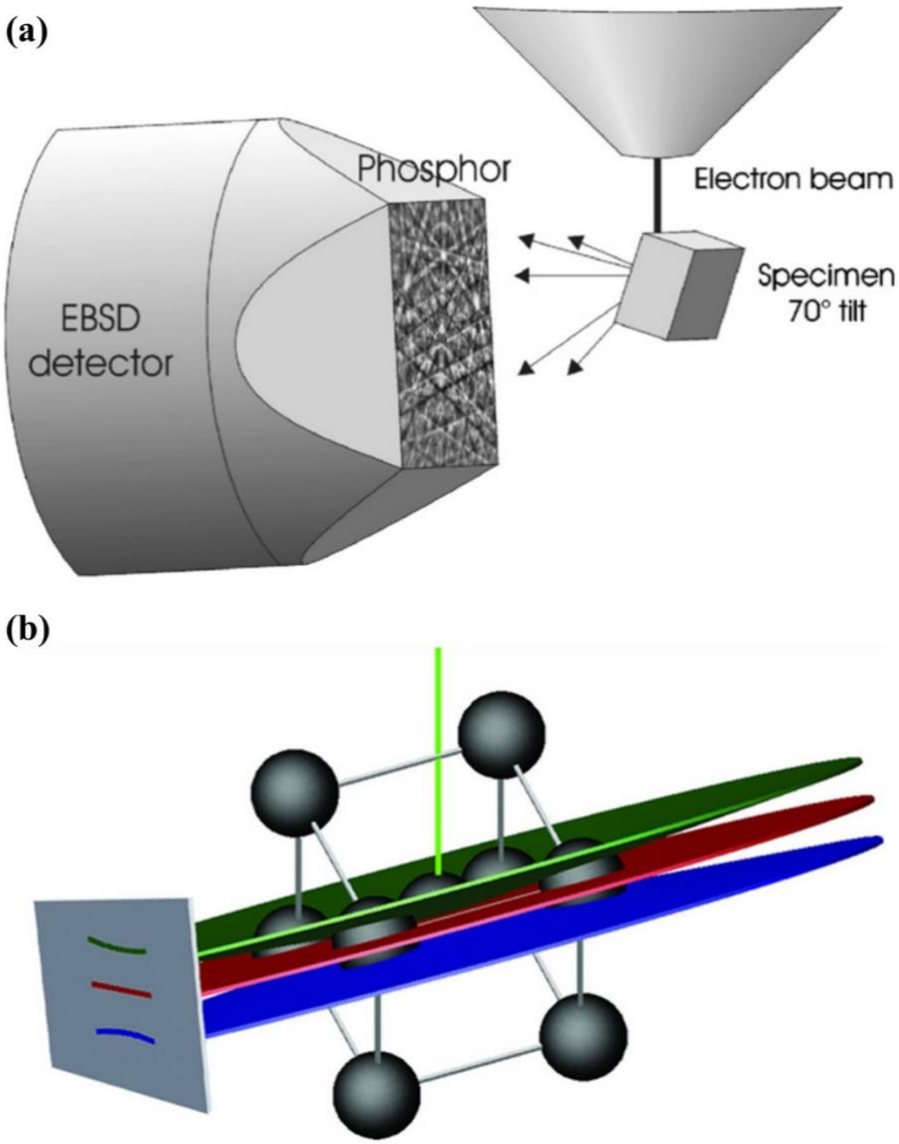

Figure 3.6 (a) Schematic of the commonly used EBSD geometry[125]. (b) The formation of a Kikuchi band in an electron backscatter diffraction pattern (EBSP)[126].

Electron backscatter diffraction (EBSD) is a powerful crystallographic characterization technique, which has been widely used to study the microstructure of the crystalline materials.

It can provide detailed information of grain orientation, grain size and shape, texture, phase distribution, boundaries and interfaces, as well as local deformation. Previous study shows that EBSD is a powerful and reliable technique to discriminate hydrides (i.e. δ- and ε-phases) in zirconium[50] [76] [125][126] [127][128].

In EBSD, a beam of electrons interacts with the crystalline sample which has been tilted to 70˚ from the horizontal. Some of the incoherently and quasi-elastically scattered electrons with the incident angles satisfying the Bragg's law are diffracted by the corresponding atomic lattice planes to form a set of paired large-angle cones, as shown in Figure 3.6[129][130]. The image formed on phosphor screen of the EBSD detector (diffraction pattern) is a gnomonic projection of the diffracted cones. The pairs of lines in the diffraction pattern are called Kikuchi bands.

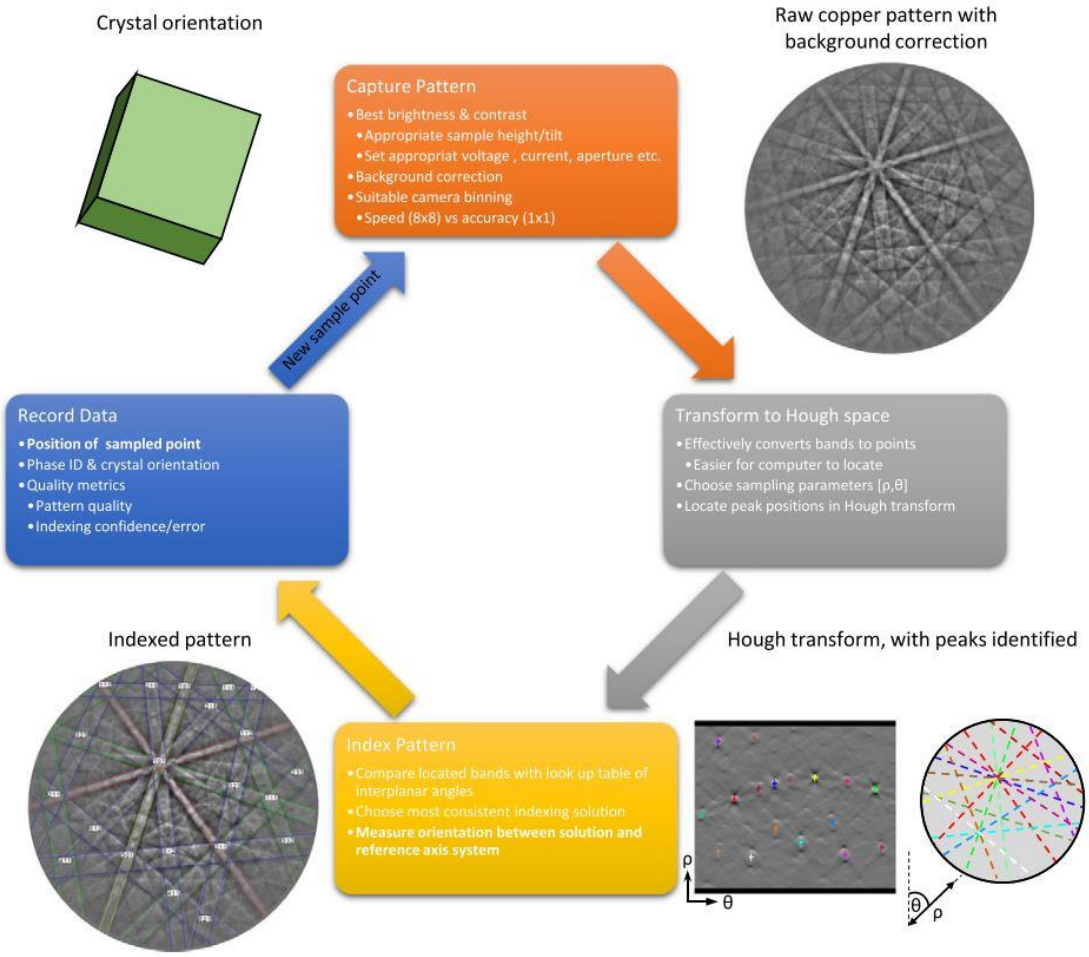

Figure 3.7 Hugh based indexing procedure from pattern capture to determination of crystal structure and orientation during EBSD characterization[132].

The center lines of the Kikuchi bands are the intersections of the corresponding diffracting planes and the phosphor screen. The intersections of the bands represent the zone axes in the crystalline sample. The width of the Kikuchi bands is determined by the spacing of the diffracting planes when the sample-detector distance and the wavelength of the electrons are constant. The diffraction pattern collected by the phosphor screen varies with the crystal structure and orientation of the sample. The collected pattern then recorded by the CCD camera and further indexed to find out the phase and orientation of the sample at this point. When the crystalline sample is raster scanned by the electron beam, the crystal structure and orientation are measured at each point, which enables EBSD to be applied to quantitative characterization of the microstructure in a region of interest. The effective spatial resolution achieved by EBSD technique can be 25-200 nm[131]. In addition, to maximize the diffraction, a flat and relatively 'defect-free' surface of sample is required. The details of sample preparation for EBSD characterization are described in chapter 4.

Now most EBSD analysis are fully automated with high efficiency. The modern commercial EBSD systems index the diffraction patterns based on Hough transformation. The procedure of the Hough based indexing is shown in Figure 3.7[132]. The detected bands in the diffraction pattern are effectively converted to the points in the Hough space, which are easier for computer to locate. The inter-planar angles between the located bands are measured and then compared with those in look-up tables (reflector lists) of the pre-inputted candidate phases, calculated according to kinematic electron diffraction theory. Finally, the most consistent indexing solution is chosen and the angular misfit between the detected and calculated bands (mean angular deviation, MAD) is measured simultaneously to express how well the calculated pattern overlays the measured pattern. In addition, the pattern center, from which a normal vector of the phosphor screen would meet the sample at the interaction volume with the electron beam, and the sample-to-screen distance (also called detector distance) are determined by

calibration procedure in advance. The pattern center is the origin of the coordinate system of diffraction pattern in the Hough transformation and indicates the relative position of the diffraction pattern with reference to the interaction volume in the sample. Accurate knowledge of the pattern center is essential for a precise and correct interpretation of the diffraction pattern and thus a 'Certainty' higher than 90% is required for a successful and confident indexing of the diffraction patterns in this procedure. There are several methods for calibration of the EBSD system now and the typical one is to find the pattern center by correlating the features on the diffraction pattern at different detector distances. Details about the determination of pattern center and calibration procedure can be found in [132][133][134]. The other two parameters associated with the confidence of indexing are minimum number of detected bands and the maximum of angular misfit between the detected bands and the simulated bands. They are usually set as 5 and 2˚ respectively as default for a confident indexing.

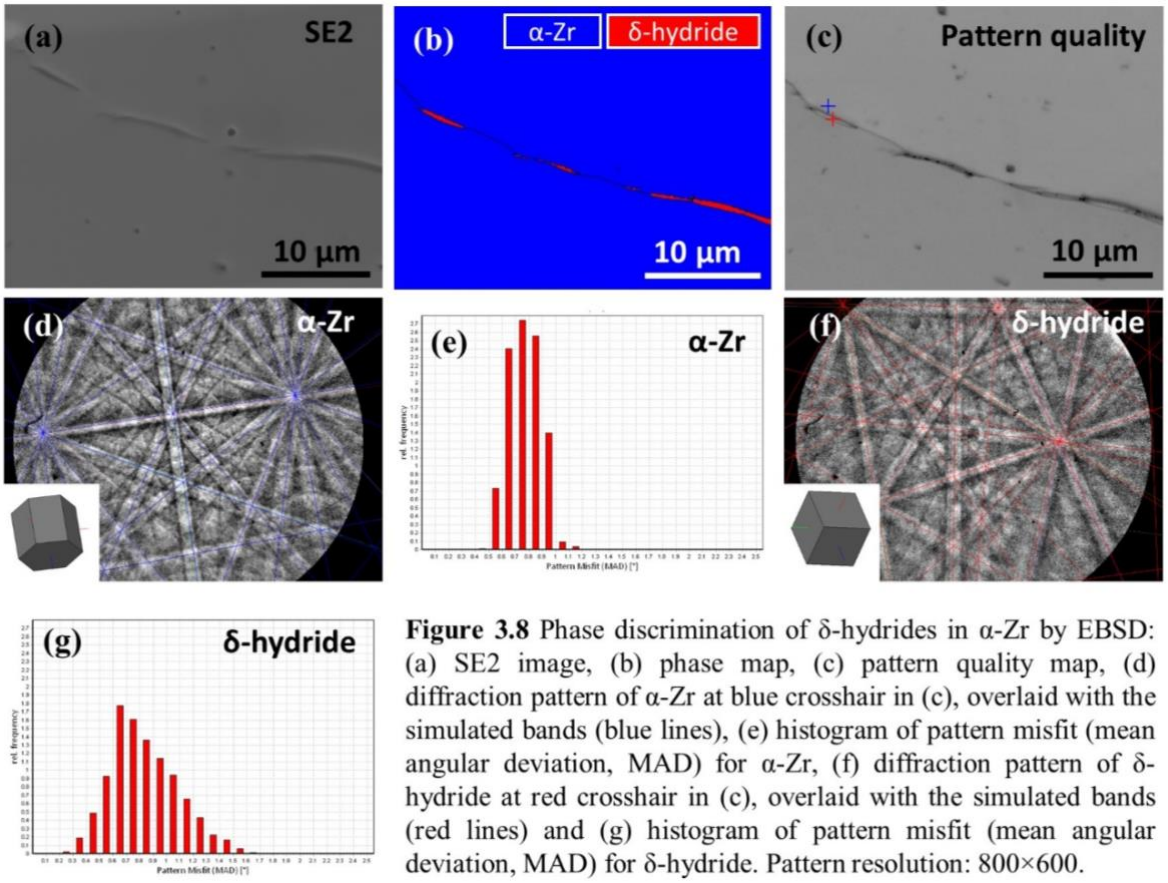

Figure 3.8 Phase discrimination of δ-hydrides in α-Zr by EBSD: (a) SE2 image, (b) phase map, (c) pattern quality map, (d) diffraction pattern of α-Zr at blue crosshair in (c), overlaid with the simulated bands (blue lines), (e) histogram of pattern misfit (mean angular deviation, MAD) for α-Zr, (f) diffraction pattern of δ-hydride at red crosshair in (c), overlaid with the simulated bands (red lines) and (g) histogram of pattern misfit (mean angular deviation, MAD) for δ-hydride. Pattern resolution: 800×600.

One example of the phase discrimination of α-Zr and δ-hydride by EBSD in this thesis is shown in Figure 3.8. The phase distribution well consists with the morphology shown by the SE2 image. Although some δ-hydrides show slightly worse pattern quality than the α-Zr matrix, the pattern quality is still good in general. The diffraction patterns of α-Zr and δ-hydride, overlaid by the simulated bands according to the indexing results, are shown in Figure 3.8 (d) and (f) respectively for examples. The frequency distribution of pattern misfit is indicated by histogram for each phase (Figure 3.8 (e) and (g)). For α-Zr, the pattern misfit is mainly distributed in the range between 0.4˚ and 1.2˚ with the peak at 0.75˚. The pattern misfit in δ-hydrides varies in a larger range from 0.2˚ to 1.6˚ approximately. The peak is located at 0.65˚ with a longer and larger tail to the larger misfit than to the smaller misfit. All the values of pattern misfit are lower than the threshold value of maximum angular misfit of 2˚. The number of indexed bands is larger than 7 in most cases. Therefore, the phase discrimination by EBSD here is fully confident. More details about this example and the related analysis will be described in the chapter 5.2.3.

The angular precision of the misorientation achieved by the Hough based conventional EBSD analysis is 0.1-0.5˚[131] and the sensitivities of the strain and geometrically necessary dislocation (GND) derived from it are ~10^{-3} [135][136] and ~10^{14} m^{-2} respectively , too large to reveal the features of local deformation (such as those induced by nanoindentation) at micro-scale[137]. HR-EBSD technique was developed to measure the local deformation from the diffraction patterns at a much higher sensitivity. Detailed introduction of HR-EBSD technique is given in the next section.

Most of conventional EBSD measurements were performed by using a field emission SEM, Zeiss Merlin-EBSD equipped with a Bruker Quantax EBSD system in the David Cockayne Centre for Electron Microscopy (DCCEM, https://www-em.materials.ox.ac.uk/). The rest

conventional EBSD data was collected by Zeiss crossbeam 540 analytical FIB/SEM with Nordlys Max EBSD system. The details will be given in the corresponding chapters later.

3.3.2 High angular resolution electron backscatter diffraction technique (HR-EBSD)

HR-EBSD technique was developed by Wilkinson et al. [138][139] and further improved in the last decade[140][141][142][143]. The experimental set-up of conventional EBSD is also used to acquire diffraction patterns for HR-EBSD analysis. However, different from conventional EBSD based on Hough transform, HR-EBSD analysis relates the pattern shifts with the lattice shifts to measure deformation states (elastic strains and lattice rotations) in crystalline materials with a high sensitivity of ~10^{-4} [138][139]. The pattern quality is crucial for both resolution and reliability of HR-EBSD results[142][144][145]. High resolution diffraction patterns with no or small binning (usually ≤ 2, determined by the native resolution of detector as well) are essential, which often requires a long exposure time with a moderate probe current (usually ≥ 10 nA) and well-prepared surface.

Once high resolution diffraction patterns are acquired and stored, HR-EBSD analysis is conducted by using xEBSD_v3 codes in Matlab. The pattern shifts are obtained by cross correlating the selected features (i.e. square regions of interest, ROI) on the test patterns with those on the reference pattern in each grain. The point with the highest pattern quality, which means the lowest strain but still may be strain, is auto selected as the reference point in a grain. The measured pattern shifts are then transformed to the lattice displacement gradient tensor, decomposed into elastic strains (symmetric parts) and lattice rotations (asymmetric parts). The strains and rotations calculated by HR-EBSD technique are relative to the reference point in each grain, rather than absolute values. The hydrostatic strain state is not included in the strains derived by the procedure above, as EBSD are not capable of measuring the change in the

Kikuchi band widths due to lattice volume change. In addition, a remapping step, where the test pattern is remapped to be close to the reference pattern by removing the rotation estimated by the initial cross correlation measurement, is included in the algorithm before the elastic strains are extracted, in order to minimize the inaccuracy of measured elastic strains caused by the presence of large rotations[141][146].

The elastic stress tensor is then evaluated from the measured elastic strain tensor by using Hooke's law. Meanwhile, the hydrostatic strain is determined in the process above by applying the plane stress boundary conditions in this step[138]. Reliable stiffness constants for each phases involved, which are essential for the application of Hooke's law, should be inputted into algorithm in advance.

The measured lattice rotations are used to calculate the lattice curvature and then estimate geometrically necessary dislocation (GND) density according to Nye's theory[147]. Theoretically, GND density is related to both elastic strain gradient and lattice curvature, but the contribution of the elastic strain gradient to GND density is considerably smaller than that of lattice curvature in most instances studied by HR-EBSD techniques and thus the former is neglected[137]. HR-EBSD technique measures lattice rotation field in two-dimensional map and only six of nine lattice curvature components are determined. In Nye's theory, the lattice curvature is the sum of distortion gradient generated by each possible type of dislocations. The possible dislocation types are many more than six constrains provided by measured lattice curvature, leading it to be an under-determined problem. Therefore, at each point in the map, an appropriate set of six possible dislocation types is found by using the L1 optimization scheme to minimize the total dislocation line energy[137]. It's a rational solution supported by a physical argument but may not the unique solution. The detailed mathematics of GND analysis from lattice rotation field can be found in [137][148][149]. Different from the

measured elastic strains and lattice rotations with respect to the reference point in each grain, the measured GND density is independent of the reference point. Statistically stored dislocations are not measured. The validation of such GND analysis based on HR-EBSD has been proved by discrete dislocation modelling[150] and it has been experimentally applied on various crystalline materials with different structures[142][148][151][152][153][154].

In order to indicate how successful the HR-EBSD analysis has been performed at each point in the map, two data quality parameters are introduced. The first one is mean angular error (MAE), describing the difference between measured pattern shifts and the predicted pattern shifts according to the best-fit solution of the displacement gradient tensor. Larger MAE values represent lower accuracy. The second is peak height (PH), assessing the quality of cross-correlation matching for pattern shift measurements. It is the geometric mean of peak heights found in cross correlation function for all ROIs in a test or remapped pattern and often normalized against autocorrelation (i.e., bring the peak height of the reference pattern to 1 in each grain). When the value of PH is extremely low, the pattern shift measurements is likely to be failed. In order to obtain reliable results of HR-EBSD analysis, the points with MAE > 0.004 or PH < 0.2 have been removed in this thesis. Detailed information about these two parameters and their threshold selection can be found in the work by Britton et al.[143].

In this thesis, the resolution of diffraction patterns for HR-EBSD analysis was 1600×1200 pixels (i.e., native resolution of the detector) or 800×600 pixels (i.e., binning of 2×2). For each pattern, twenty ROIs were auto selected with one at the center of pattern and the others on a circle at the edge of the pattern. The size of ROIs depended on the pattern resolution, 256×256 pixels for native resolution and 128×128 pixels for those with binning of 2×2. The stiffness constants of α-Zr with hcp structure were taken from Fisher and Renken's work[155]:$C_{11} = 143.4$, $C_{12} = 72.8$, $C_{13} = 65.3$, $C_{33} = 164.8$, $C_{44} = 32.0$ and $C_{66} = 143.4$ in GPa. The

hydride phase studied in this thesis is δ-hydrides with fcc structure in zirconium. There's no bulk of δ-phase zirconium hydrides in nature, and quite few experimental results of their stiffness constants are available in literatures. Therefore, the stiffness constants were taken from density functional theory (DFT) modelling results, even though some discrepancies remain. Three sets of stiffness constants of δ-hydride from DFT modelling works[156][157][158] were chosen to test how much influence of stiffness constants of δ-hydride on HR-EBSD analysis. The testing results showed that the change of HR-EBSD results with the different sets of stiffness constants of δ-hydride was so small to distinguish, whether in magnitude or distribution, and can be neglected. Finally, stiffness constants calculated by Weck et al.[156] were used for all HR-EBSD analysis in this thesis: $C_{11} = 103.0$, $C_{12} = 145.5$ and $C_{13} = 27.1$ in GPa. The predicted atomic model for this set of stiffness constants matches with the crystal structure of δ-hydride used in HR-EBSD analysis in this thesis and has the lowest total energy, although it doesn't completely satisfy the Born criteria for mechanical stability. Meanwhile, the types of dislocations considered for GND calculation should be consistent with the deformation mode and thus varies with different crystal structures. For α-Zr with hcp structure, the possible dislocation types involved in the GND calculation are <a> screw, <a> edge on basal planes, <a> edge on prismatic planes, <a> edge on pyramidal planes, <c+a> screw and <c+a> edge on pyramidal planes. The GNDs in δ-hydrides with fcc structure are considered to be contributed by the dislocations in {111}<110> slip systems, including 6 possible types of pure screw dislocations and 12 possible types of pure edge dislocations. For more information on the GND calculation for hcp structure and fcc structure, see ref. [149] and [151] respectively.

All HR-EBSD were performed by using a field emission SEM, Zeiss Merlin-EBSD equipped with a Bruker Quantax EBSD system in the David Cockayne Centre for Electron Microscopy

(DCCEM, https://www-em.materials.ox.ac.uk/). The details will be given in the corresponding chapters later.

Post-processing of all EBSD data, including mapping of phase distribution, crystal orientation and band contrast (or pattern quality), plotting of pole figures, statistical analysis et al., was performed by using Oxford Instrument HKL_Channel 5 software.

3.4 Digital image correlation strain measurements

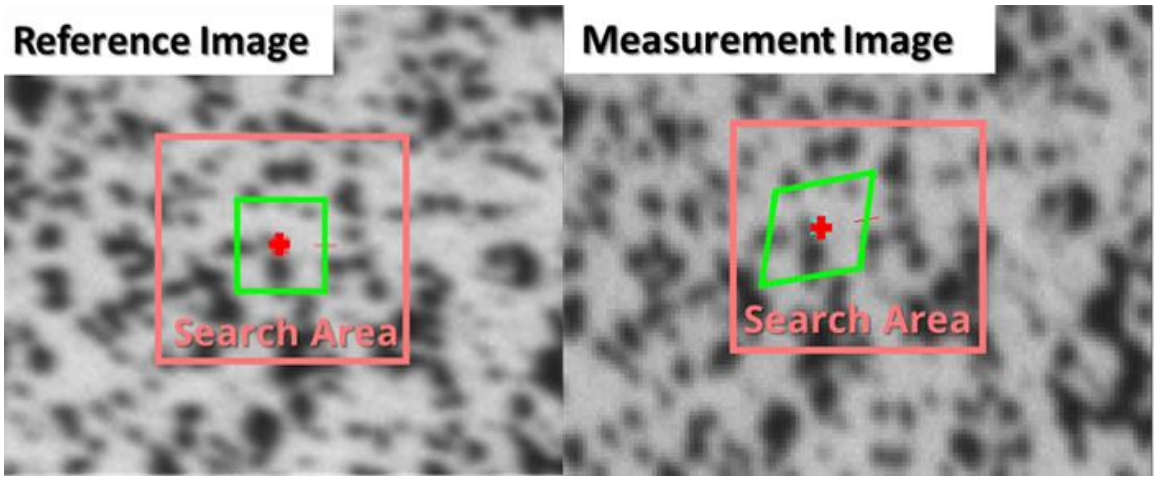

Figure 3.9 A subset on the speckle pattern is tracked in the reference image (undeformed) and a measurement image (deformed)[159].

Digital image correlation (DIC) measures the in-plane strains by comparing the digital images of the deformed sample surface with the reference image, which is usually acquired before deformation. In order to successively correlate the images of the sample surface acquired before and after/during deformation, speckles should be homogeneously applied in a region of interest on the sample surface in advance. The reference image of the speckle pattern is divided into a series of square subsets. The changes in the position and shape of the subsets are tracked in the images of the speckle pattern on the deformed sample surface by using image correlation algorithms and then the strains of each subset are determined, as shown in Figure 3.9[159].

DIC is a non-contact and full-field strain measurement technique which can be applied in various loading conditions. Compared with linear variable differential transformers (LVDTs) and strain gauges, DIC is a much better choice for mechanical testing of the materials with heterogeneous microstructure, as it can provide information of strain distribution in a specific region. Different from HR-EBSD technique which reveals the local deformation accommodated in the lattice, DIC measures the total in-plane strains caused by deformation. DIC also can be used to monitor the strains in a larger region during the deformation, owing to much less image acquiring time than HR-EBSD. Meanwhile, use of SEM for image acquisition enables DIC strain measurements at micro-scale. For the large deformation where the crystal structure is seriously destroyed, DIC is a better choice. However, in the cases without external strain/stress applied (i.e., thermal residual strain and strain induced by second phases), HR-EBSD technique is a powerful method while DIC strain measurements doesn't work. In this thesis, DIC was utilized to characterize the micromechanics of hydrides in zirconium during the in-situ uniaxial tensile tests performed in a SEM chamber. The details will be presented in chapter 6.

Chapter 4 Materials and sample preparation

This chapter give a detailed description of the commercially pure zirconium material used in this work, anneal process for grain-size control, development of a hydride generation method, several sample preparation recipes, and methodologies for EBSD characterization.

4.1 As-received pure zirconium

In order to study intrinsic relation between zirconium hydrides and zirconium matrix, 10 commercially pure zirconium sheets (99.2 wt.%) with the size of $50\ mm \times 50\ mm \times 1\ mm$ were purchased from Goodfellow Cambridge Ltd (https://www.goodfellow.com). The detailed chemical composition is shown in Table 1. These sheets were cut into different size and shape by low/high speed saw or waterjet cutting machine for different purposes, which will be described in the following chapters.

Table 4.1 Chemical Composition of the ordered pure zirconium sheets.

Element	Hf	O	C	Fe	Cr	N	H
Concentration (ppm)	2500	1000	250	200	200	100	10

Due to the anisotropy of their hcp structure, the texture of zirconium alloys has significant influence on their performance in service, including hydride orientation, distribution, morphology, irradiation-induced growth behavior and hydride-induced embrittlement[160][4]. Both of IPF map with respect to the normal of as-received pure zirconium sheets (ND, Figure 4.1 (a)) and pole figures for $\{0001\}_{\alpha-Zr}$, $\{10\bar{1}0\}_{\alpha-Zr}$ and $\{11\bar{2}0\}_{\alpha-Zr}$ planes respectively (Figure 4.1 (b)), acquired by EBSD, show that the as-received pure zirconium sheets has a very strong texture. Most basal poles are located in two small areas on the transverse direction (TD) near to the center. In details, the normal directions of basal planes of most grains are deviated from normal of the sample surface (ND) toward TD by the angles of 0-30° approximately. The preferential orientations for $\{10\bar{1}0\}_{\alpha-Zr}$ and $\{11\bar{2}0\}_{\alpha-Zr}$ planes are not as obvious as those for

basal plane. This is the typical texture for the rolled zirconium sheets. The grains are equiaxed and the grain size is relatively even, which indicate that the sheets were actually annealed and recrystallized after rolling process[161][162]. The average grain size is measured to be 11.9 μm by Bruker ESPRIT software.

4.2 Pre-anneal for grain size control of pure zirconium

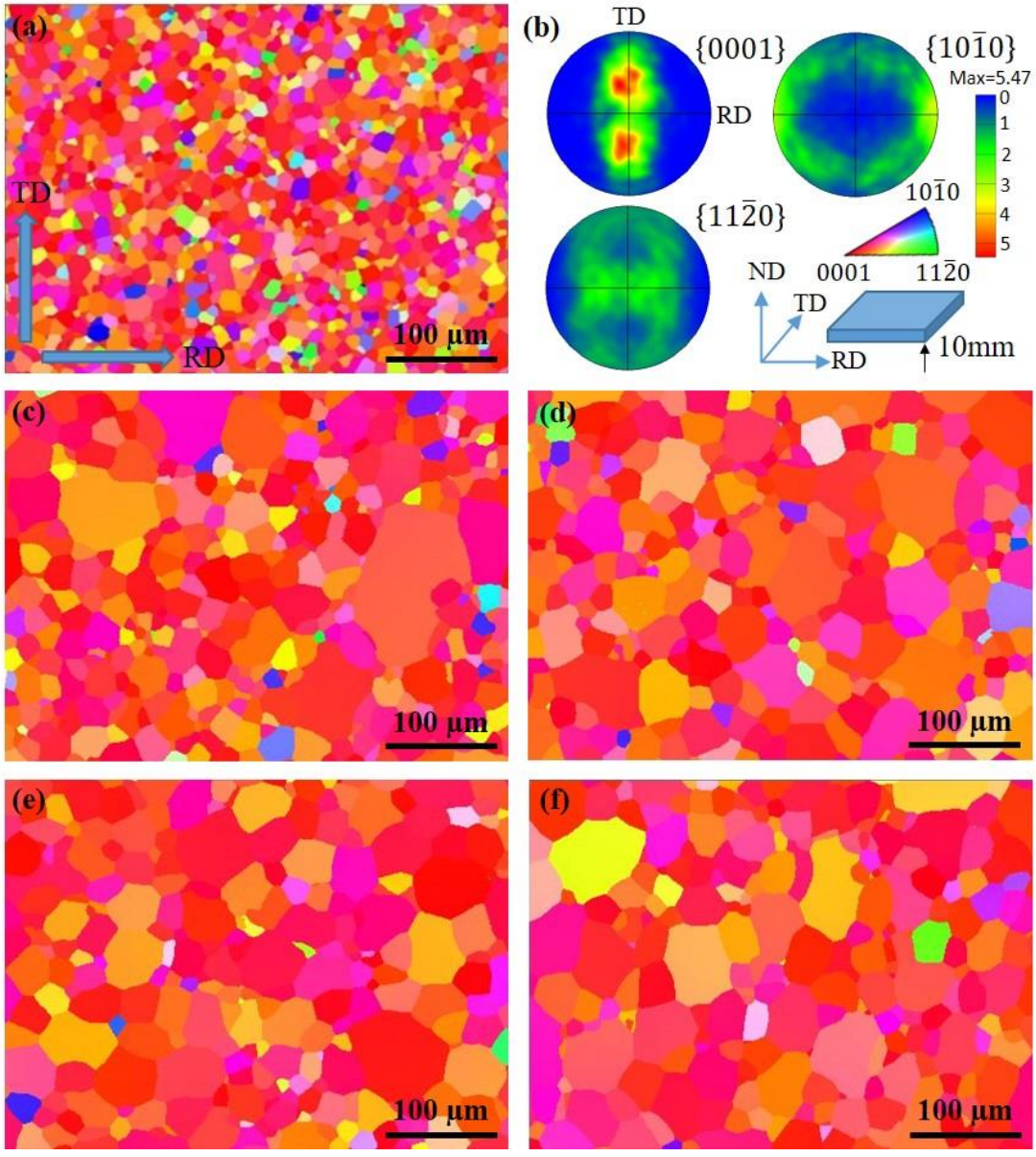

Figure 4.1 Inverse pole figure (IPF) maps with respect to the pure zirconium sheet surface normal of (a) as-received pure zirconium and pure zirconium after anneal at 750 ˚C for (c) 12 h, (d) 24 h, (e) 36 h and (e) 72 h respectively. (b) shows the pole figures for $\{0001\}_{\alpha-Zr}$, $\{10\bar{1}0\}_{\alpha-Zr}$ and $\{11\bar{2}0\}_{\alpha-Zr}$ planes respectively and geometry of the received pure zirconium sheets.

As mentioned in Chapter 2, the distribution, morphology and structure of hydrides in zirconium vary with the grain size of zirconium matrix[50]. In order to study hydrides with different morphology and structure at different sites, it is essential to figure out how to control the grain size of pure zirconium sheets by anneal process firstly. In addition, proper anneal process will reduce defect populations and relieve residual stresses inside zirconium[163].

Table 4.2 Average grain size and median grain size before and after anneal.

Anneal time (h)	0	12	24	36	72
Average grain size (μm)	14.4	84.5	84.4	87.6	96.9
Median grain size (μm)	13.5	60.4	64.1	75.9	77.6

Several received pure zirconium sheets were heated and kept at 750 ˚C for 12 h, 24 h, 36 h and 72 h respectively, and then cooled down to room temperature in a vacuum furnace. 750 ˚C is a commonly used annealing temperature for zirconium alloys in lab[50]. It is just below α/β phase transition temperature for pure zirconium and thus a high rate of grain growth will be achieved without phase change at this temperature. During the whole anneal process, pure zirconium samples are in a quartz tube, which is pumped overnight and refilled by argon (Ar), to avoid oxidation by oxygen in air. As shown in Figure 4.2, both average grain size and median gain size are significantly increased by anneal for only 12 h, from 14.4 μm to 84.5 μm and from 13.5 μm to 60.4 μm respectively. A few grains are larger than 100 μm, which are sufficient large to allow hydride precipitation and growth inside grains and also for micromechanical tests, such as nano-indentation. However, more than half of grains are still smaller than 60 μm. With increase in anneal time from 12 h to 36 h, the average grain size doesn't show an obvious increase, while median grain size is increased to 75.94 μm. After that, although anneal time is doubled to 72 h, average grain size is only increased to 96.9 μm and there is almost no change in median grain size. Considering both time consumption, grain size and its distribution after annealing, 36 h was chosen as the anneal time for experiments that need large-grain zirconium

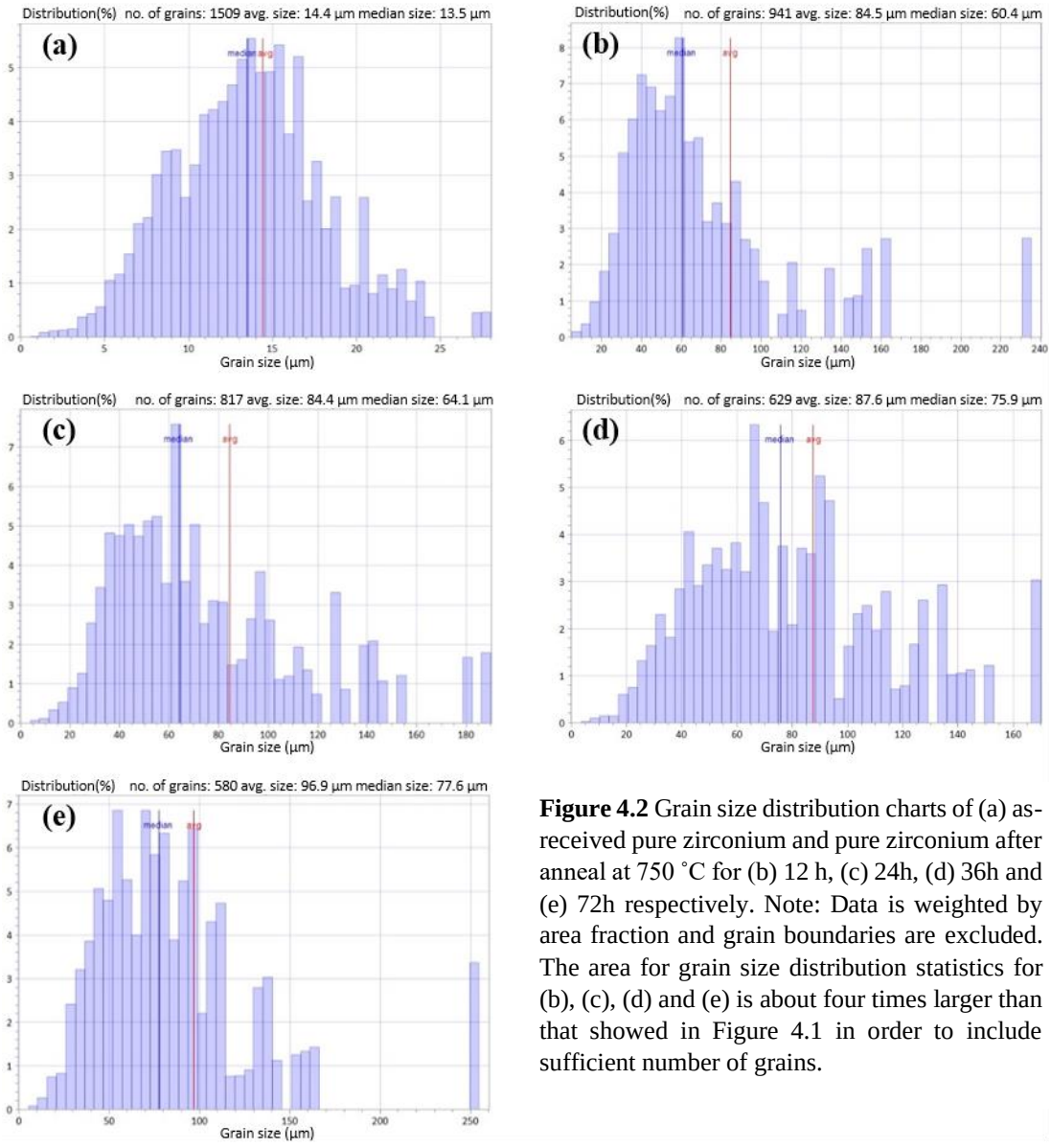

Figure 4.2 Grain size distribution charts of (a) as-received pure zirconium and pure zirconium after anneal at 750 ˚C for (b) 12 h, (c) 24h, (d) 36h and (e) 72h respectively. Note: Data is weighted by area fraction and grain boundaries are excluded. The area for grain size distribution statistics for (b), (c), (d) and (e) is about four times larger than that showed in Figure 4.1 in order to include sufficient number of grains.

in the future. In addition, IPF maps in Figure 4.1 show that pre-anneal doesn't change the texture of pure zirconium samples.

4.3 Basic micro-mechanical properties of pure zirconium

Before generating hydrides inside pure zirconium, it is important to learn the basic mechanical properties of pure zirconium. Nano-indentation tests were carried out on the pure zirconium after 36 h anneal at 750 ˚C to measure its modulus and hardness, and then study its mechanical anisotropy as a function of crystal orientation. The relevant parameters are summarized in Table

Table 4.3 Parameters used in nano-indentation tests on the pure zirconium after 36 h anneal at 750 ˚C.

Depth limit	Strain rate	Harmonic displacement	Frequency	Poisson's ratio
2.0μm	0.05/s	2.0nm	45Hz	0.18

4.3. The radius of plastic zone of a indent on pure zirconium is estimated to be 8-9 μm when the maximum indentation depth is 2 μm, according to the equation given by J. Chen[164]. Figure 4.3 (b) misorientation average map shows that the indentation-induced misorientation is localized within a 15 μm radius around the centers of indenter impressions approximately. In order to avoid the interaction between any two adjacent indents, the interval distance was set to be 50-70 μm in all indentation arrays. All counted indents are kept at least 20 μm away from grain boundaries to avoid the influence of grain boundaries on the measurements. In addition, because of strong texture, it's hard to find grains with high declination angles on the top surface of the pure zirconium sheets, as shown in Figure 4.3 (a). Nanoindentation tests were also carried out on the well-polished cross-section to get sufficient data of the other orientations.

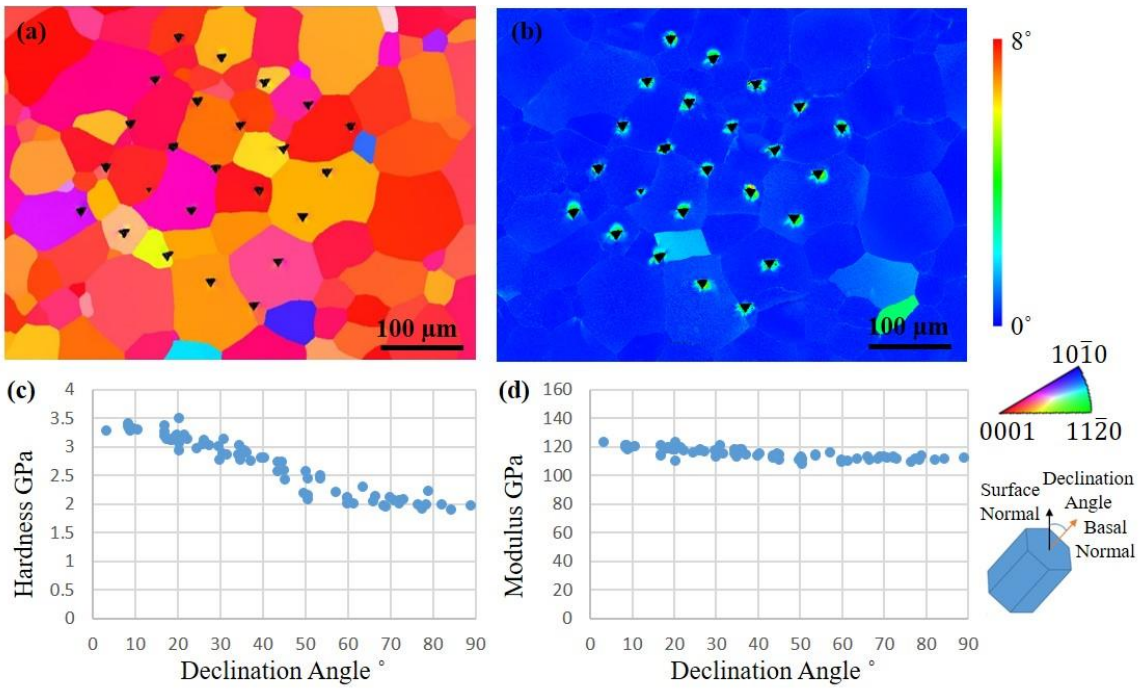

Figure 4.3 (a) Inverse pole figure (IPF) maps of 36h pre-annealed pure zirconium after nano-indentation tests with respect to sample surface normal. (b) Misorientation average map of the same area to (a). Scatter plots of (c) hardness and (d) modulus to the declination angle of the normal direction of basal plane ([0001] direction) to sample surface normal of large-grain pure zirconium after 36h pre-anneal process from nano-indentation tests.

Figure 4.3 (c) and (d) plot hardness and modulus as functions of declination angle of basal plane from the sample top surface respectively. The near basal hardness, when the declination angle is close to zero, is commonly supposed to be the highest hardness in zirconium[163][165][166]. The hardness decreases from about 3.5 GPa to around 2 GPa when declination angle increases from 0˚ to 90˚. It's noteworthy that the decrease in hardness is negligible when declination angle is close to 0˚ or 90˚, in the range of 0˚ to 20˚ or 60˚ to 90˚, while significant drop of hardness is discovered in between. Different from hardness, modulus only shows a slightly decreasing trend with increase in declination angle. The modulus ranges from 125 GPa to 115 GPa. Similar plastic and elastic anisotropy of pure zirconium was also discovered in literatures[167][168].

4.4 Hydride generation

4.4.1 Electrolytic hydrogen charging

Currently, two methods, gaseous hydrogen charging and electrolytic (cathodic) hydrogen charging, are commonly used to generate hydrides in zirconium and its alloys in lab. Gaseous hydrogen charging requires relatively strict lab conditions, including a Sievert-type device, high temperature of 300 ˚C to 450 ˚C, high pressure and high purity hydrogen atmosphere[169][71][9][55][170][125]. Considering the lab conditions in our group, risk

Table 4.4 Details of electrolytic hydrogen charging for zirconium and its alloys in literatures.

Materials	Electrolyte (H_2SO_4 vol.%)	Temperature (˚C)	Current density ($kA \cdot m^{-2}$)	Temperature for post anneal (˚C)	Hydride phase	Ref.
99.2% Zr	0.5	65	1.5	No	δ	[18]
Zircaloy-4	1.0	65 (±5)	2	830	δ	[19]
Zircaloy-4	0.82*	65 (±5)	2	400	ε	[5]
Zircaloy-4	0.67*	70 (±5)	1.5	375	δ	[20]
Zircaloy-4	2.67*	RT	0.8	400	δ	[21]
Zircaloy-2	1.0	70 (±5)	-	200-400	δ	[22]
Zr-Nb-Sn	2.76*	80	2	400	-	[23]

*Converted to vol.% from the other units in the literatures. RT: room temperature.

assessment, expense and charging efficiency, electrolytic hydrogen charging was chosen. In addition, as mentioned in section 1.1, the outer layer of zirconium fuel claddings are hydrided in coolant water rather than gas atmosphere during service. Electrolytic hydrogen charging provides a much more similar environment to working environment of zirconium fuel claddings. The details of electrolytic hydrogen charging for zirconium and its alloys in literatures are shown in Table 4.4[50][171][172][173][174][175][176].

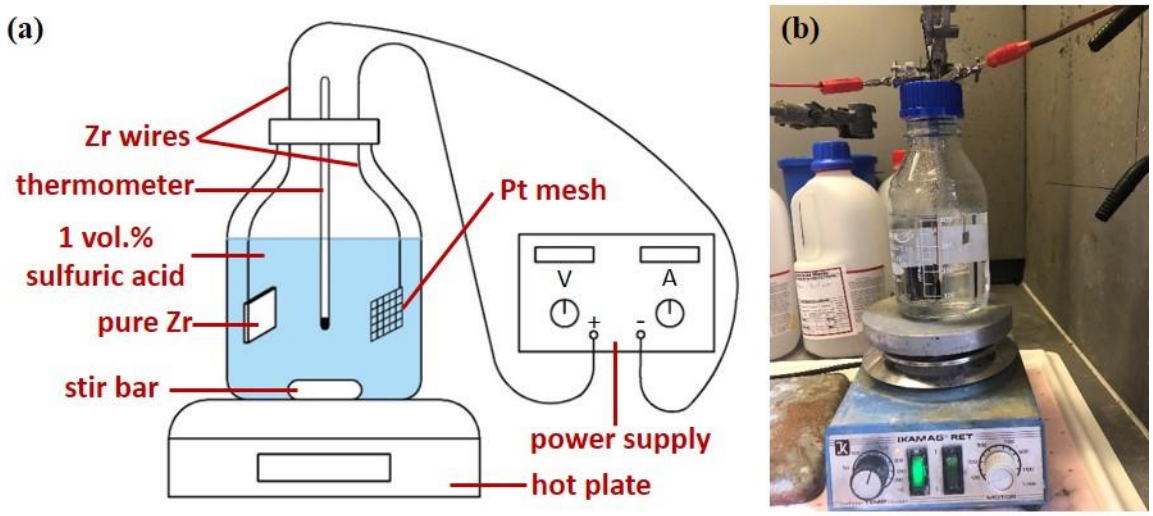

Figure 4.4 (a) Schematic drawing of the experimental setup for electrolytic hydrogen charging. (b) Photo of corresponding equipment setup for electrolytic hydrogen charging.

The experimental setup for hydrogen charging was designed in terms of equipment setup of electrolytic hydrogen charging in literatures and conditions in our lab. Figure 4.4 (a) is the schematic drawing of it. Before charging, one side of the pure zirconium sheet sample was ground and polished, which made it quite easy to tell if hydrides precipitate on the surface by optical microscopy just after charging. The details of grinding and polishing process will be described in the section 4.5. The pure zirconium sample is spot welded with pure zirconium wire and connected to cathode of direct current (DC) power. The voltage for spot welding depends on materials and the total thickness of two ends needed to be welded together. Thicker specimen usually requires higher voltage for the same material. The voltage of 20-30 V was used for spot welding and adjusted with sample thickness. Platinum mesh is also spot welded

with pure zirconium wire and acts as anode, owing to its chemical inertness. The polished side of the pure zirconium sample faces the platinum mesh. The electrolyte is 1 vol. % diluted sulfuric acid. The hot plate is used to keep temperature at 65±5 ˚C and a magnetic stir bar is rotated at 50-60 rpm during the whole charging process. After charging, the sample was cleaned by deionized water.

During electrolytic hydrogen charging, the reaction happening in the solution is electrochemical water splitting indeed. H^+ cations gain electrons and reduce to zero valance state at the pure zirconium cathode. Some of them diffuse into the pure zirconium cathode while the others are then released from the cathode surface as hydrogen gas in the form of bubbles. The hydrogen charging efficiency is determined by various factors, including current density, surface condition, temperature, concentration of H^+ ions in solution (PH values) and potential at the cathode. The amount of H^+ cations reduced back to zero valance state at the cathode per unit area per second greatly depends on current density. The fraction of hydrogen absorbed into zirconium cathode can be estimated according to the Nernst equation for the potential of charge transfer process and the equilibrium state achieved on the cathode surface during the charging, as derived by ref.[177]. The results show that the fraction of hydrogen absorbed into zirconium cathode can be increased by applying a higher temperature, more negative potential or more content of H^+ cations in solution (smaller PH values). The surface condition is not taken into account in the estimation above, but it may influence the absorption of hydrogen via surface roughness.

Diluted sulfuric acid was used as electrolyte to increase the H^+ content and conducting ability of solution without inducing any other cation competitors. Sulfate (SO_4^{-2}) is hard to be oxidized and thus avoid the formation of impurities in the electrolyte during the charging process. The diffusion velocity of hydrogen in pure zirconium at the charging temperature is much lower

than the rate at which hydrogen was produced and absorbed during the charging, and thus hydrogen would accumulate in the superficial layer of the charged samples. Once the local concentration of hydrogen in zirconium just underneath the charged surface exceeds its solid solubility limit, hydrides will precipitate. Because of lower density of the hydride phases, volume expansion happens during zirconium to hydride phase transformation and causes bumps on the charged surface. Charging time greatly determines the total amount of hydrogen charged into zirconium samples, as well as the amount of hydride precipitates. The hydrides formed on the zirconium sample surface is considered to reduce the further hydrogen absorption and diffusion into the sample and decrease the charging efficiency. It is important to choose a rational charging time.

Six samples with one side mechanically polished were charged at a current density of 1.0 kA/m^2 (0.01 mole hydrogen atoms form per meter square per second approximately) for different time to find out a proper charging time for the following study. The voltage changes with the total surface area of the sample. For the pure zirconium sample of 10mm×10mm×1mm, the voltage is ~ 3.9±0.3 V approximately. As shown in Figure 4.5 (a)-(f), only after the charging for 3 h, many tiny 'islands' formed on the pre-polished surface. These 'islands' were identified as δ-hydrides by EBSD. Details will be discussed in the Chapter 5. With charging time increasing, these hydride islands grew up and nearly covered the whole surface after 24 h charging. After that, the depth of hydride islands increases from 7.4 μm to 13.0 μm when charging time was increased to 72 h, as shown in Figure 4.5 (g)-(i). Obvious cracks started to appear on top of hydride islands under optical microscopy after 48 h charging and micro-cracks were found near the top on the cross section of hydride islands obtained by the charging for 72 h. The cracks probably result from stress concentrations caused by volume expansion during zirconium to hydride transformation. Considering the time expense and the number of hydrides required by following study, 24 h was chosen. In addition, less and much smaller hydride islands were

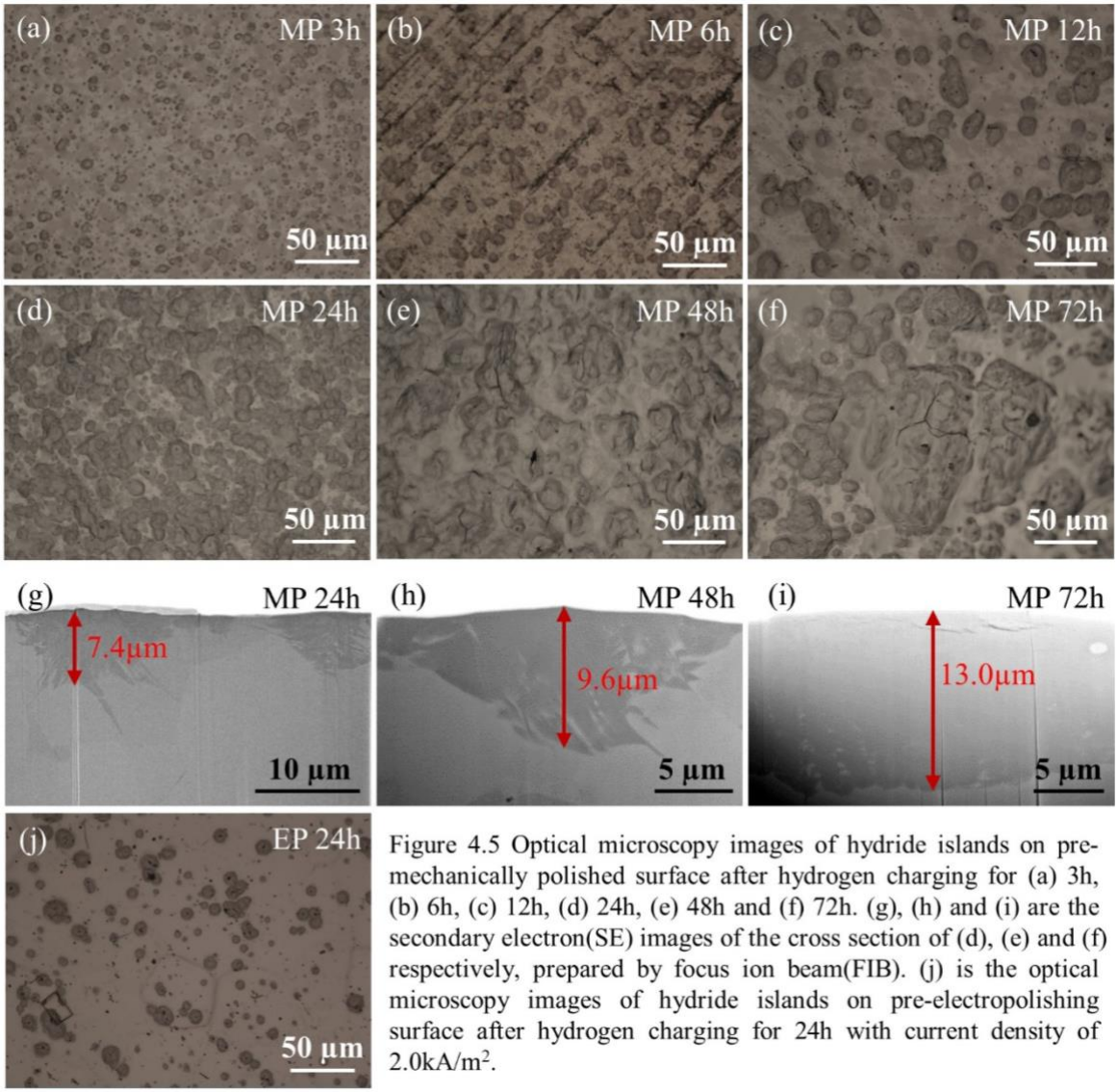

Figure 4.5 Optical microscopy images of hydride islands on pre-mechanically polished surface after hydrogen charging for (a) 3h, (b) 6h, (c) 12h, (d) 24h, (e) 48h and (f) 72h. (g), (h) and (i) are the secondary electron(SE) images of the cross section of (d), (e) and (f) respectively, prepared by focus ion beam(FIB). (j) is the optical microscopy images of hydride islands on pre-electropolishing surface after hydrogen charging for 24h with current density of 2.0kA/m^2.

Note: for a, b, c and d, the diameter of Zr wire used is 1 mm, while 0.5 mm for e, f. However, the voltage is nearly the same for the same current.

found in Figure 4.5 (j), where the sample surface was electro-polished before charging and then charged with current density of 2.0 kA/m^2 (double than all the others) for 24 h. It indicates that lower surface roughness would decrease the charging efficiency even though much higher current density was used.

4.4.2 Re-distribution of hydrides

The surface hydride islands obtained by electrolytic hydrogen charging are more like hydride blisters, which only form at some regions with relatively lower temperature on the zirconium claddings inside nuclear reactor cores[169][71][125]. In most cases without temperature and

stress gradients, hydrides precipitate in the form of hydride strings or lines. Therefore, homogenization annealing was taken to re-distribute hydrides after hydrogen charging.

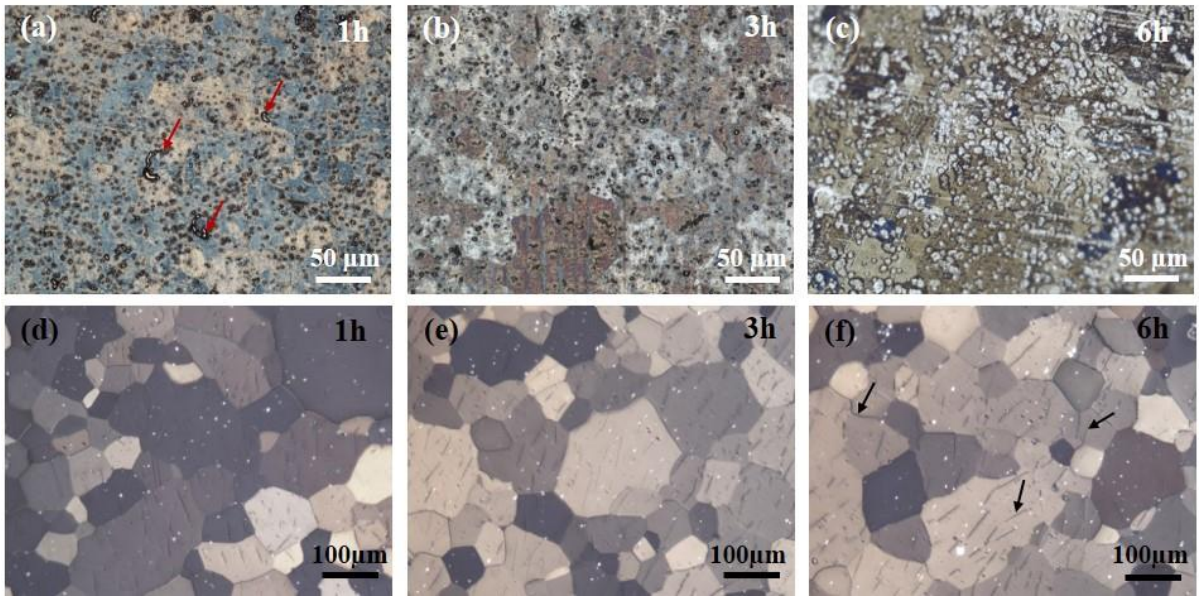

Figure 4.6 Optical microscopy images of the top surface of three 1mm thick pure zirconium plate samples, which were charged for 24h and then annealed at 400 ˚C for (a) 1h, (b) 3h and (c) 6h respectively. (d), (e) and (f) are the polarized light images of the cross section of these three samples, corresponding to (a), (b) and (c) respectively.

24 h charged pure zirconium samples were put in quartz tubes respectively, which is then pumped overnight and refilled by argon (Ar), to avoid oxidation by oxygen in air during the following homogenizing anneal. The tubes containing charged samples were heated to 400 ˚C and kept for 1 h, 3 h and 6 h respectively in a vacuum furnace, and then cooled down to room temperature in air, as the previous studies on hydrides summarize in Table 4.4 show that air-cool-down allow hydrides to precipitate both inside grains and on grain boundaries in zirconium. As shown in Figure 4.6 (a)-(c), with increasing the annealing time from 1 h to 6 h, residual hydrides (pointed by red arrows in Figure 4.6 (a)) on charged surface gradually diminish and completely disappear after 6 h anneal. It means 6 h anneal is sufficient to allow all the surface hydrides completely dissolve into zirconium matrix. Inside charged samples, only an hour anneal allows dissolved hydrogen to diffuse and re-precipitate in the form of

hydride lines homogeneously over the whole sample. The hydride lines become more and thicker when anneal time is increased to 6 h.

The hydrides prepared by the electrolytic hydrogen charging with or without homogenization annealing were then studied by conventional and high angular resolution EBSD in the chapter 5. The results show that they are δ-hydride phase. The distribution, morphology and structure of hydrides in zirconium vary with gain size of zirconium matrix and/or cooling rate[50]. Proper grain size and cooling rate will be chosen in terms of research objectives in the following chapters.

4.5 EBSD specimen preparation

4.5.1 Mechanical grind and polish

Table 4.5 Mechanical grinding and polishing process for zirconium samples.

Surface	Abrasive	Load (N)	Speed (rpm)	Time
Grinding disc	P600 grit SiC with water cooling	*	100	30-120s
Grinding disc	P1200 grit SiC with water cooling	*	100	30-60s
Grinding disc	P2500 grit SiC with water cooling	*	100	30-60s
Grinding disc	P4000 grit SiC with water cooling	*	100	30-60s
Polishing pad CHEM-H	Diluted colloidal silica (1:1) with water	5	20-50	1-1.5h

Note: * means samples were held by hand during grinding process. The first grinding may need longer time to create a flat surface.

Mechanical grind and polish were carried out to obtain a flat mirror surface firstly. The target surface of a sample was ground by grit SiC grinding discs from P600 to P4000 and then polished by diluted colloidal silica (1:1) with a tiny water flow. The details of mechanical grinding and polishing process are summarized in Table 4.5. After that, grains can be distinguished under polarized light optical microscopy, but the color difference between grains is not obvious and the grain boundaries are ambiguous, as shown in Figure 4.8 (a). Furthermore, there was no Kikuchi pattern when EBSD was carried out. That means mechanical grind and

polish is insufficient for preparing a flat and damage free surface required by EBSD. Therefore, electro-polishing was conducted to further remove the residual surface defects.

4.5.2 Electropolishing at low temperature

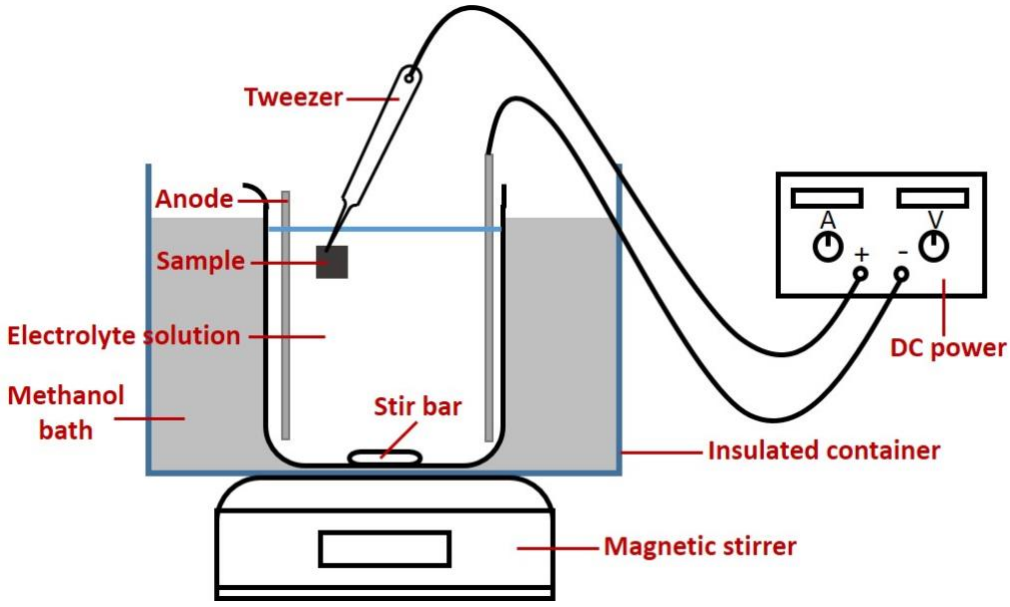

Figure 4.7 Schematic drawing of the experimental setup for electropolishing at low temperature.

The experimental setup for electropolishing at low temperature is shown in Figure 4.7. The electrolyte solution is the mixture of 90 vol. % Methanol + 10 vol. % perchloric acid. Methanol bath and liquid nitrogen was used to create a stable low temperature environment (lower than -30 ˚C) inside the insulated container during the whole electropolishing process. Voltage of 20 V was applied, and the polishing time was controlled within the range of 10 s to 40 s in most cases. The electropolishing time depends on many factors, including materials, temperature, and surface conditions after mechanical polish, etc. It was properly adjusted according to relevant electropolishing experiences. Electropolishing greatly removed residual surface defects after mechanical polish. As shown in Figure 4.8 (b), polarized light optical image of as-received pure zirconium after mechanical polish and electropolishing in order, color difference

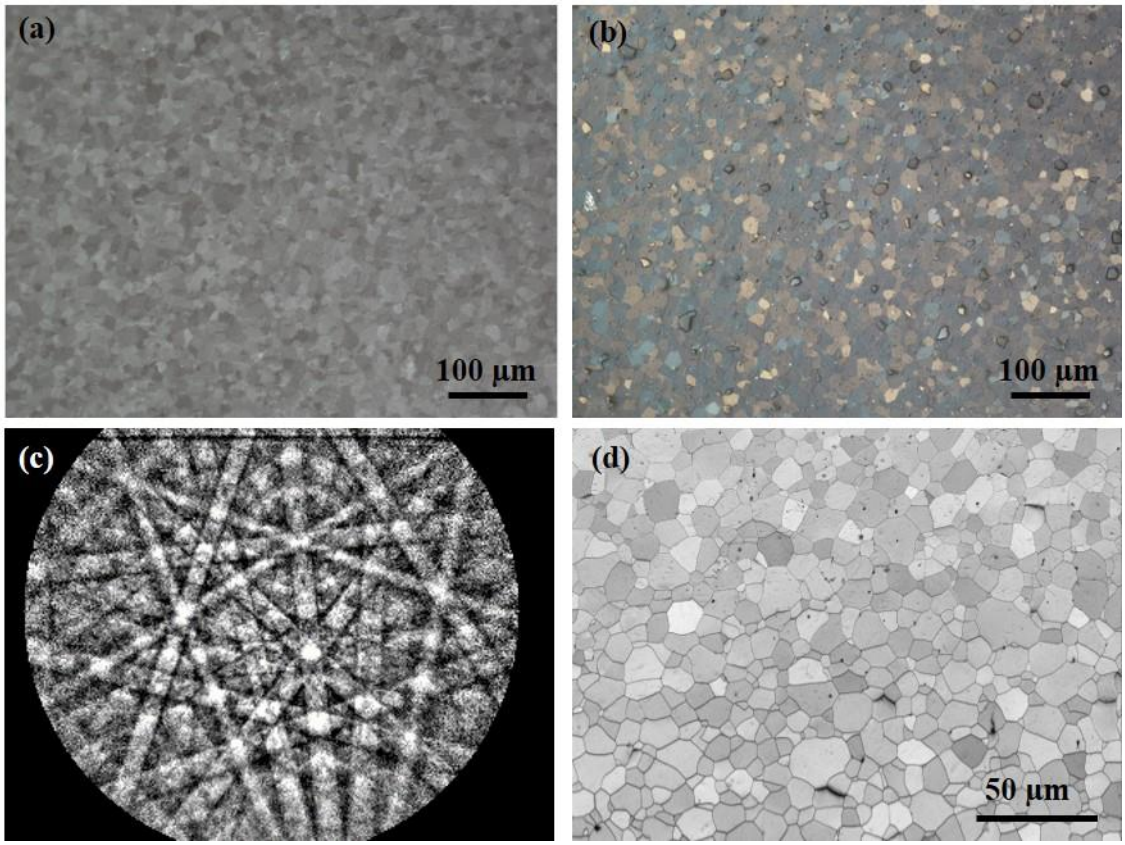

Figure 4.8 Polarized light optical images of as-received pure zirconium (a) only after mechanical polish and (b) after electropolishing. (c) and (d) are Kikuchi pattern with resolution of 400×300 and pattern quality map (more white means higher quality) of as-received pure zirconium after electropolishing, obtained by EBSD scanning.

between grains was significantly improved. At the same time, electropolishing created some tiny pits, but their bad influence on the general EBSD mapping is negligible. Nice Kikuchi patterns were obtained in more than 99% of EBSD mapping area. Examples of Kikuchi pattern and pattern quality map of electropolished as-received pure zirconium are shown in Figure 4.8 (c) and (d).

Chapter 5 Micro-analysis of delta-hydrides in Zirconium by conventional and high angular resolution electron backscatter diffraction

In this chapter, conventional EBSD was used to quantitatively analyze the microstructure of both small surface hydride blisters and more homogeneously distributed hydrides in pure zirconium. High angular resolution electron backscatter diffraction (HR-EBSD) analysis, working via xEBSD matlab package, was performed to further explore the local deformation induced by the formation of hydrides in pure zirconium. All details provided by these two techniques are helpful to further explore the growth mechanism of different hydrides in zirconium and predict their effects on mechanical behaviors of the zirconium matrix.

5.1 Micro-analysis of small surface hydride blisters by EBSD

As mentioned in section 4.4, the target surface was mechanically polished before hydrogen charging to provide a relative flat and clean surface for hydride formation and keep a sufficient charging efficiency simultaneously. However, it's almost impossible to produce a perfectly uniform surface. Not clear, at this point, if the hydrogen absorption is localized, or hydrogen diffuses to preferential sites, or nucleation of the hydride phase is heterogeneous. Later heat treatment gives more clues. Small hydride islands formed on the sample surface, rather than a uniform hydride thin layer. It's quite similar to the formation of macroscopic hydride blisters on the outer surface of zirconium claddings, which are detrimental to the safety and structural integrity of a nuclear reactor core. The small hydride islands, to some extent, represent hydride blister formation in the early stage and will be called as small hydride blisters in this thesis.

Numerous theoretical and experimental studies have been carried out on macroscopic hydride blisters, which are wider than 1 mm[178][179][180][169][71][125]. However, there is a lack of research on hydride blisters in the early stage to further support the proposed formation and growth mechanism. In this section, conventional EBSD characterization, combined with FIB sectioning, has been carried out on the cross section of small hydride blisters formed after 24 h hydrogen charging, which are no more than 50 μm in width or 10 μm in depth. The results reveal the morphology and structure of the small hydride blisters and surrounding zirconium matrix and provide an improved understanding of hydride blister formation and growth.

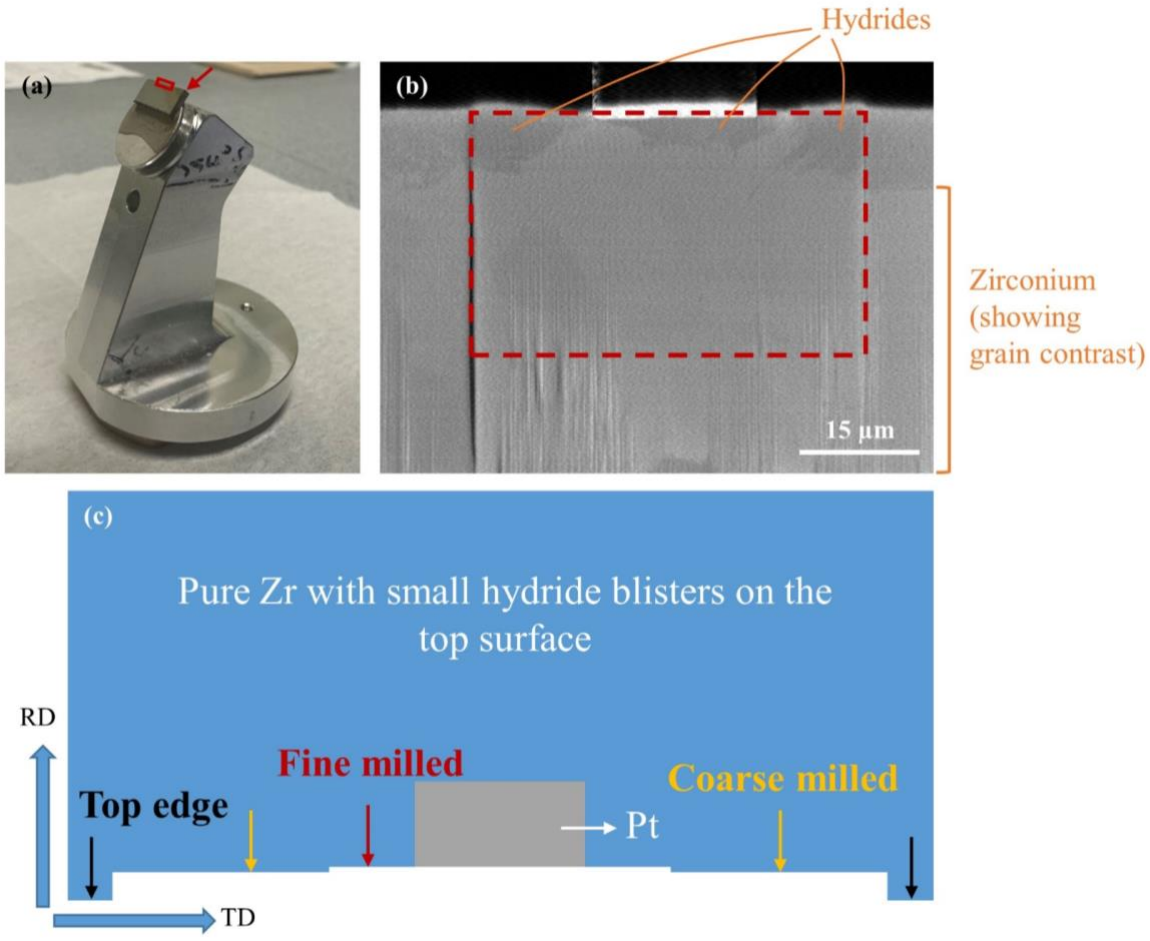

Figure 5.1 (a) Photograph of tilted EBSD holder with hydrogen charged sample stuck on the SEM pin stub by silver dag mounted on it for FIB milling and EBSD characterization by Zeiss crossbeam 540 analytical FIB-SEM. (b) Upright forescatter detector (FSD) image of well-milled cross section area of small hydride blisters produced by 24h hydrogen charging for EBSD characterizations. (c) Schematic drawing of the top view of (b).

5.1.1 Sample preparation by Focused Ion Beam (FIB)

Although electropolishing is sufficient to prepare a nice finish of zirconium plate for EBSD characterization, it will destroy small hydride blisters or even peel them off when used to polish the cross section of 24h hydrogen charged pure zirconium plates. Focus ion beam (FIB) milling was used to prepare a well-milled cross section area of small hydride blisters produced by 24h hydrogen charging. The FIB milling and EBSD characterization were performed on Zeiss crossbeam 540 analytical FIB/SEM in sequence. The FIB milling was carried out with the dual-beam FIB platform using gallium (Ga^+) as the ion source and SmartFIB software. The EBSD data collection was achieved by a Bruker system with the electron beam current of 20 nA and voltage of 20 kV, while the analysis was carried out using Oxford Instruments Aztec software and HKL channel 5 software.

After 24h hydrogen charging, the as-received pure zirconium sample was cleaned by deionized water and dried by dust remover. It was then stuck on a SEM pin stub with silver dag and mounted on 54˚ tilted side of the tilted EBSD holder with one cross section perpendicular to rolling direction upward, as shown in Figure 5.1 (a). Red arrow shows the target cross section perpendicular to rolling direction and the red rectangular on top edge shows the area where FIB milling will be conduct. Figure 5.1 (c) is the schematic drawing of the top view of the well-milled cross section area and shows the configuration of each FIB milling steps. Firstly, a protective platinum layer of about $20\ \mu m \times 20\ \mu m \times 1\ \mu m$ was deposited on the region of interest by Ga^+ ion beam of 700 pA. The long side of platinum layer was parallel to the top edge and the distance between them was about 5~20 μm initially. In order to minimize the shadowing on Kikuchi pattern during EBSD measurements later, both length and depth of coarse milling volume should be around 5 times larger than those of the region of interest under the platinum layer. Meanwhile, the width must be larger than the actual width to be removed

to make sure that the milling will start out of the top edge and gradually mill the target cross section. Two coarse millings were conducted by Ga^+ ion beam with the current of 30 nA and 15 nA in sequence. The first coarse milling volume was set as 95 μm × 15 μm × 50 μm and the second one was 95 μm × 10 μm × 40 μm. After that, final fine milling with the beam current of 1.5 nA was to further polish the cross-section area of interest. The length and depth of fine milling volume was 40 μm and 25 μm respectively. The Ga^+ ion beam voltage of 30 kV was used for all FIB deposition and milling steps. The forescatter electron image of the well-milled cross section of interest is shown in Figure 5.1 (b). The lens-shaped small hydride blisters are easy to be discriminated from zirconium matrix and the red rectangular is the area for EBSD scan next.

5.1.2 Results

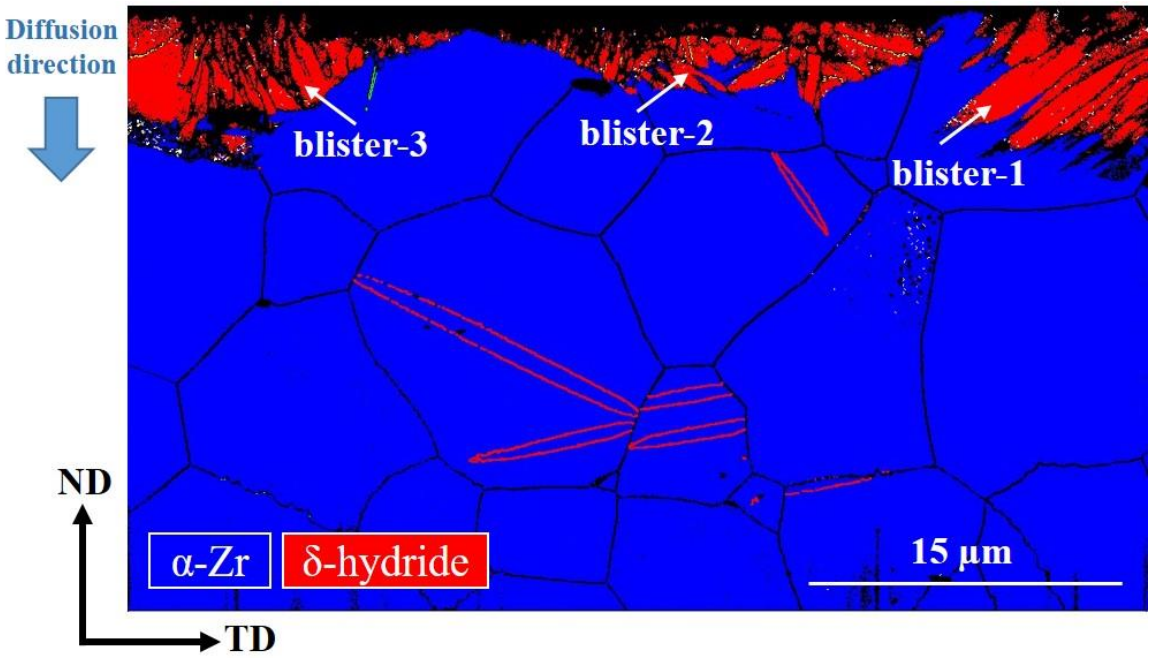

Figure 5.2 Phase and grain boundary map of FIB prepared cross section of small hydride blisters produced by electrolytic hydrogen charging for 24 h. Blue is α-Zr and red is δ-hydrides. Black lines are grain boundaries >2˚. Yellow lines are $\{111\}\langle 11\bar{2}\rangle$ twin boundaries and the misorientation is rotation of 60˚ around $\langle 111\rangle$ in δ-hydride blisters. Red lines are $\{10\bar{1}2\}\langle\bar{1}011\rangle$ (T1) twin boundaries and the misorientation is rotation of 86.28˚ around $\langle 1\bar{2}10\rangle$ in α-Zr. Green lines are $\{11\bar{2}1\}\langle\bar{1}\bar{1}26\rangle$ (T2) twin boundaries and the misorientation is rotation of 38.87˚ around $\langle 01\bar{1}0\rangle$ in α-Zr. The maximum deviation angle for last three is 5˚.

Figure 5.2 is the phase and grain boundary map obtained from EBSD of FIB-prepared cross section of three small hydride blisters. The blue region is α-Zr matrix, while the red region is δ-hydride. The hydrogen diffused from top to the bottom of this cross section during hydrogen charging process, as shown by the blue arrow in Figure 5.2. The lath-shaped δ-hydride grains in the blisters show a general growth direction downward. The EBSD results of them will be described separately later, from right to left (blister-1 to blister-3). The presence of some twins in the α-Zr below the hydride blisters is noted.

5.1.2.1 Small hydride blister-1

As shown in Figure 5.3 (a) and (b), small hydride blister-1 formed inside a parent grain α-Zr-1. The blister consists of many lath-shaped δ-hydride grains, which stack up and grow along a $\langle 11\bar{2}0 \rangle$ direction of α-Zr-1. Three orientation variants of δ-hydrides are found in small hydride blister-1 and represented δ-hydride-1, -2 and -3 respectively, marked by white arrows in Figure 5.3 (b), orientation map (IPFX). In order to distinguish δ-hydrides in the orientations of δ-hydride-1 and -2, which are all in the similar purple colors in the orientation map, the former is enclosed by white lines. Note that there is a smaller δ-hydride-1 grain originating from small hydride blister-2 on the left, rather than small hydride blister-1.

Figure 5.3 (c) shows the pole figures of α-Zr-1, α-Zr-2 and δ-hydrides related to small hydride blister-1. The projected poles of α-Zr-1 is much more dispersed than those of α-Zr-2 underneath, which means the misorientaion inside α-Zr-1 is much greater. It may be caused by volume expansion during zirconium to δ-hydride transformation to some extent. It is also true for the parent α-Zr grains for the other two small hydride blisters.

Poles marked by black triangles are parallel crystallographic planes and those marked by black circles or squares are parallel crystallographic directions. The pole figures shows that δ-hydride-1 and -2 follow the commonly observed orientation relationship of $\{0001\}_\alpha || \{111\}_\delta$

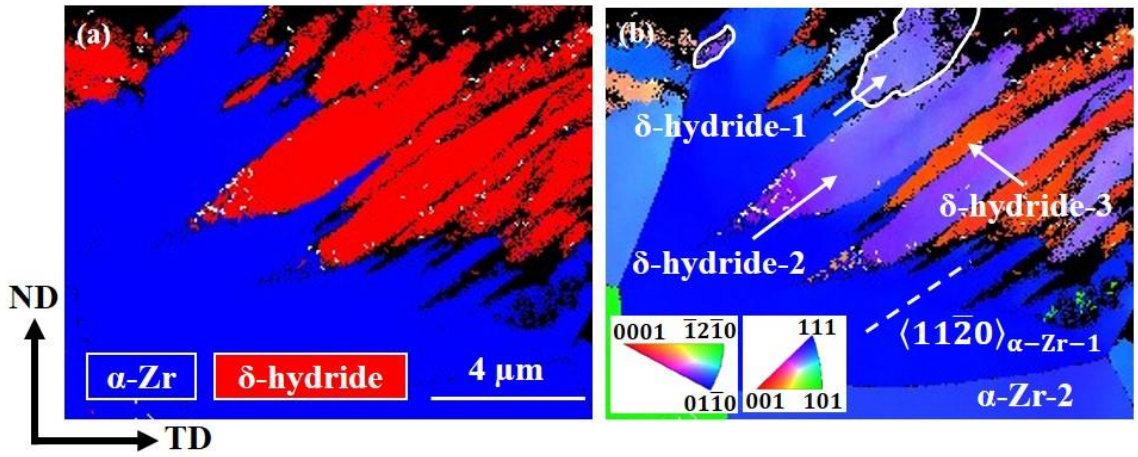

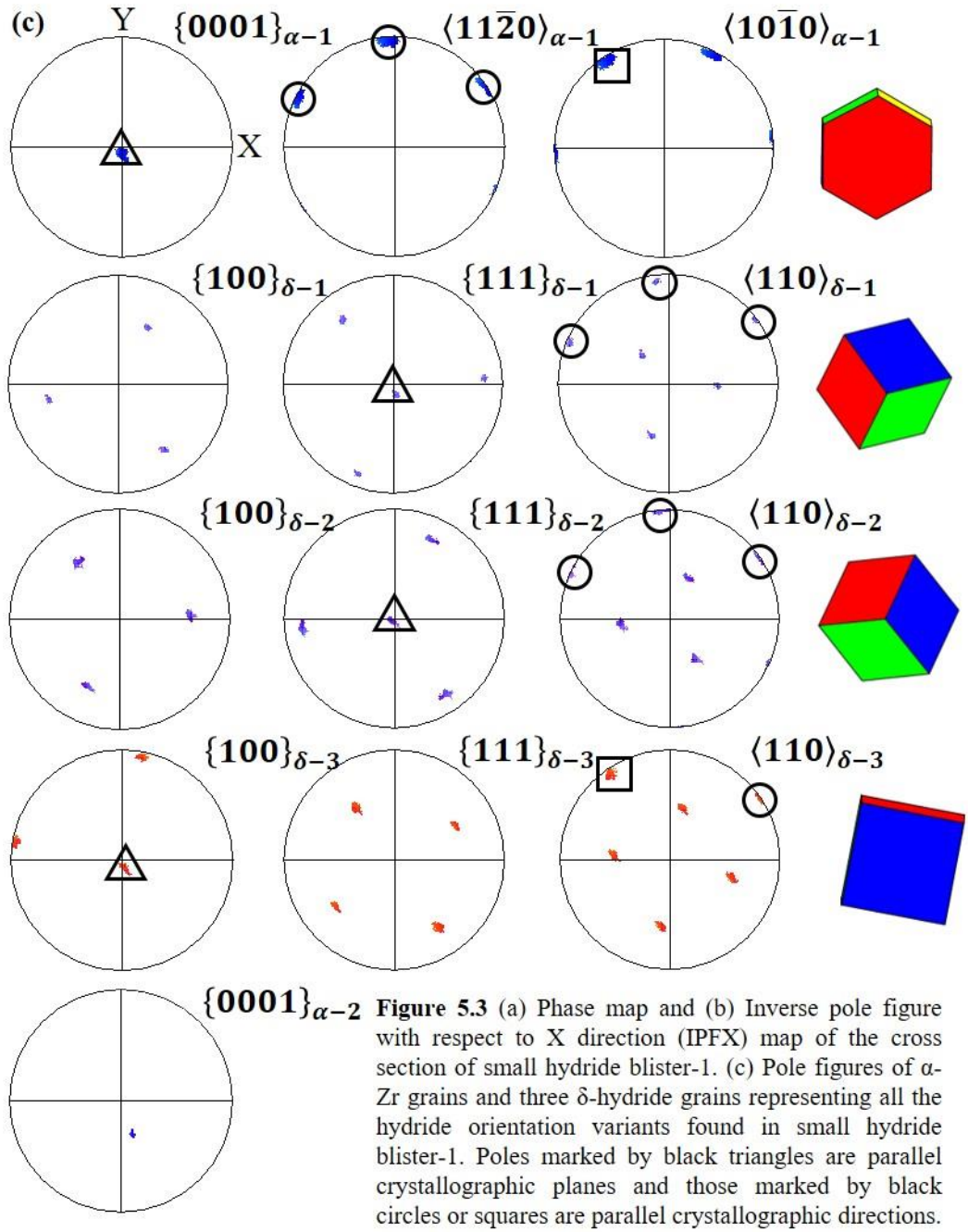

Figure 5.3 (a) Phase map and (b) Inverse pole figure with respect to X direction (IPFX) map of the cross section of small hydride blister-1. (c) Pole figures of α-Zr grains and three δ-hydride grains representing all the hydride orientation variants found in small hydride blister-1. Poles marked by black triangles are parallel crystallographic planes and those marked by black circles or squares are parallel crystallographic directions.

$\langle 11\bar{2}0\rangle_\alpha||\langle 110\rangle_\delta$ with α-Zr-1, which will be called OR1 in this study. Meanwhile, these two δ-hydride orientation variants share one of $\{111\}$ planes and three of $\langle 110\rangle$ directions, which coincides with $\{111\}\langle 11\bar{2}\rangle$ twins, primary twinning type in fcc structures[181]. The misorientation angle between $\{111\}\langle 11\bar{2}\rangle$ twins is a rotation of 60° around $\langle 111\rangle$ direction. However, the interface between δ-hydride-1 and -2 is not shown as twin boundaries in Figure 5.2. The misorientation angle between them is almost 60° but the rotation axes is $\langle \bar{3}4\bar{3}\rangle$, slightly deviated from $\langle 111\rangle$. It is probably caused by large misorientation inside α-Zr-1 grain and/or compression from surrounding δ-hydride grains, induced by volume expansion during zirconium to δ-hydride transformation. The δ-hydride-3 follows a different orientation relationship of $\{0001\}_\alpha||\{100\}_\delta$ $\langle 11\bar{2}0\rangle_\alpha||\langle 110\rangle_\delta$ with α-Zr-1, which was observed less frequently and will be called as OR2 in this thesis. In OR2, one of $\langle 11\bar{2}0\rangle_\alpha$ directions is parallel to a $\langle 110\rangle_\delta$ direction and one of $\langle 10\bar{1}0\rangle_\alpha$ directions is parallel to another $\langle 110\rangle_\delta$ direction. The detailed atomic configuration will be discussed in 5.1.3.1. The δ-hydride-3 grains also forms alternant structure with δ-hydride-1 grains.

5.1.2.2 Small hydride blister-2

Different from small hydride blister-1, blister-2 formed across several α-Zr grains. The EBSD results will be divided into three parts in terms of parent grains and shown from right to left in this section.

As shown in the IPFX map of the cross section of the right part of small hydride blister-2 (Figure 5.4 (b)), only two orientation variants of δ-hydrides exist in α-Zr-1 grain. The δ-hydride grains have lath-shape and form alternant structure. The thickness of each lath is similar. The pole figures in Figure 5.4 (c) indicate that both observed two orientation variants of δ-hydrides follow the OR1 with α-Zr-1 and they are $\{111\}\langle 11\bar{2}\rangle$ twins. The twin plane is the shared $\{111\}$

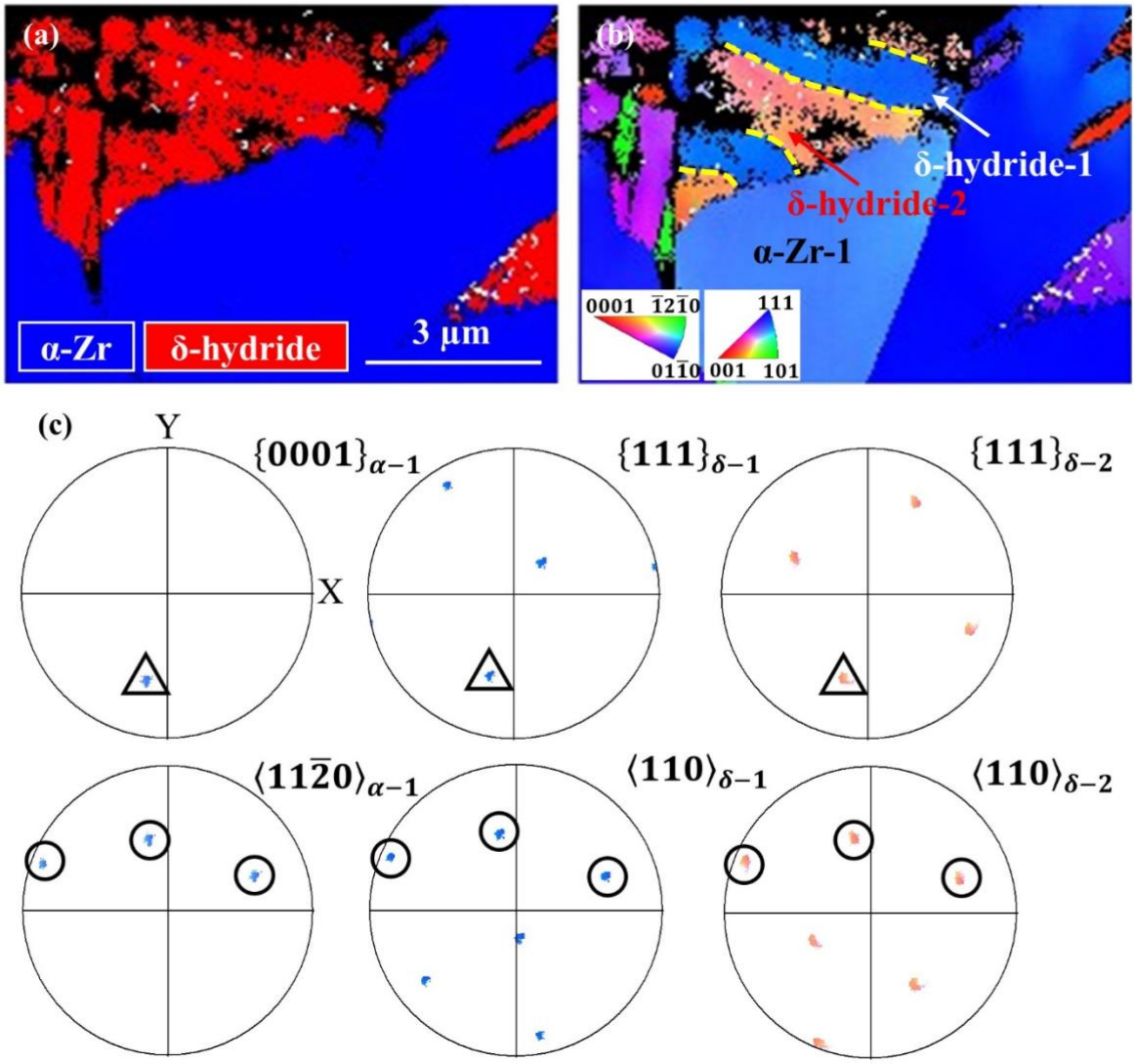

Figure 5.4 (a) Phase map and (b) IPFX map of the cross section of the right part of small hydride blister-2, where yellow dash lines are twinning boundaries of hydrides (the maximum deviation angle is 5˚). (c) Pole figures of parent α-Zr-1 grain and two δ-hydride grains representing the hydride orientations found in small hydride blister-2 in α-Zr-1. Poles marked by black triangles are parallel crystallographic planes and those marked by black circles are parallel crystallographic directions.

plane between δ-hydride-1 and -2, parallel to the basal plane of α-Zr-1. The twinning boundaries are shown by yellow dash lines in Figure 5.4 (b).

In the middle part of small hydride blister-2, δ-hydrides precipitated across two α-Zr parent grains. The white dash line in Figure 5.5 (b), IPFX map of the middle part of small hydride blister-2, is the grain boundary between these two α-Zr parent grains. The top one has almost completely transformed into δ-hydrides, but they were severely damaged by FIB milling.

Therefore, Figure 5.5 (c) only shows the pole figures of α-Zr-2 and the δ-hydrides precipitated inside it.

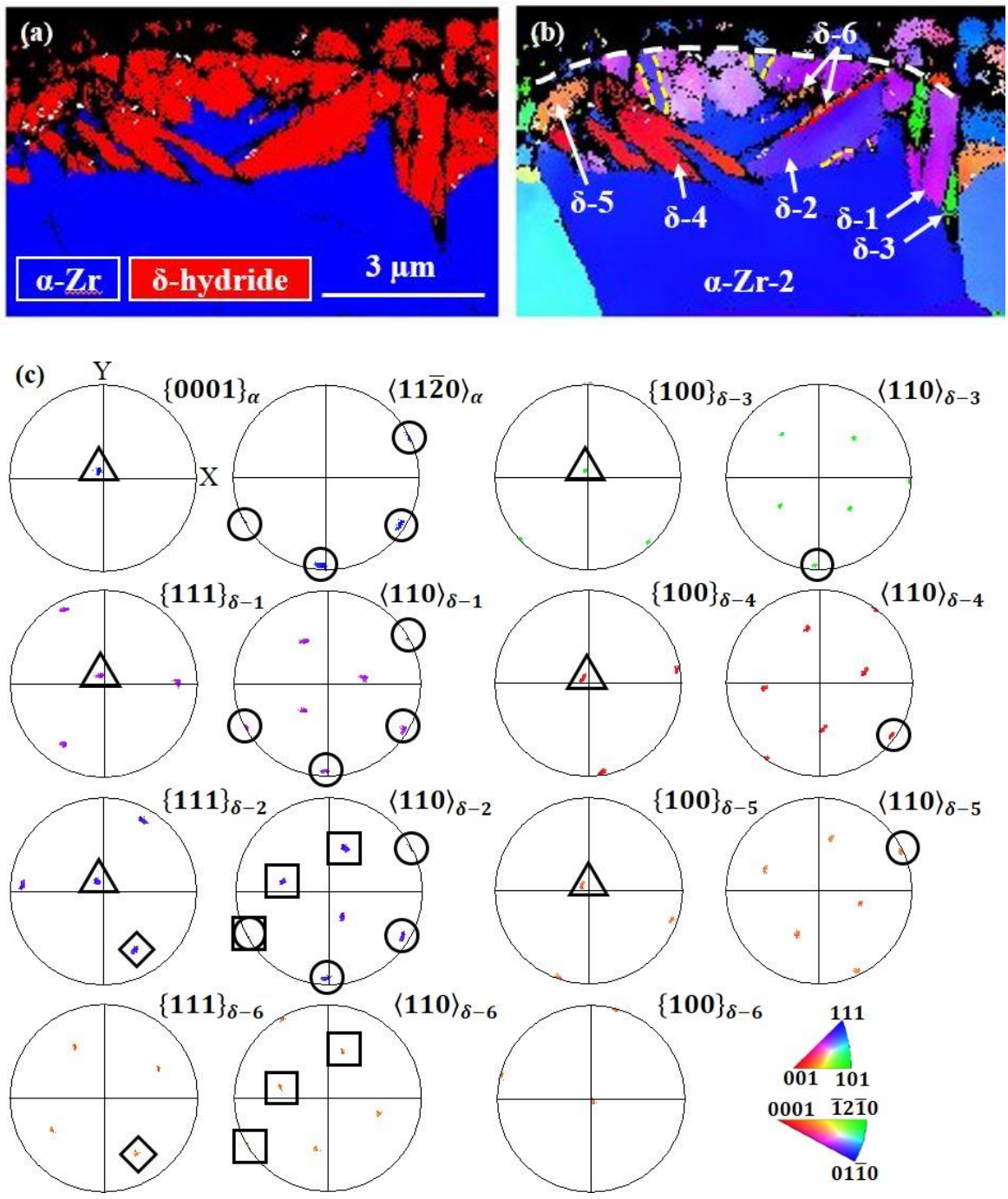

Figure 5.5 (a) Phase map and (b) IPFX map of the cross section of the middle part of small hydride blister-2, where white dash line is the grain boundary of two parent α-Zr grains initially and yellow dash lines are twinning boundaries of δ-hydrides (the maximum deviation angle is 5˚). (c) Pole figures of α-Zr-2 parent grain and six δ-hydride grains, which represent all the hydride orientation variants found in small hydride blister-2 in α-Zr-2. Poles marked by black triangles (or rhombuses) are parallel crystallographic planes and those marked by black circles (or square) are parallel crystallographic directions.

There are six orientation variants of lath-shaped δ-hydrides found in α-Zr-2 in the middle part of small hydride blister-2. The δ-hydride-1 and -2 in the similar purple and pink colors in the IPFX map follow OR1 with α-Zr-2 and $\{111\}\langle 11\bar{2}\rangle$ twinning orientation relationship with each other. Some of these grains form $\{111\}\langle 11\bar{2}\rangle$ twins. The twin plane is one of the $\{111\}$ planes parallel to basal plane of α-Zr-2 and the twin boundaries are shown by yellow dash lines in Figure 5.5 (b). The δ-hydide-3, -4, and -5 follow OR2 with α-Zr-2 and grow in different directions. The δ-hydride-6 can be obtained by small rotation from δ-hydide-5. It has one $\{100\}$ plane close but not completely parallel to basal plane of α-Zr-2. Moreover, it follows $\{111\}\langle 11\bar{2}\rangle$ twinning orientation relationship with δ-hydide-2. Different from δ-hydride-1 and -2, another $\{111\}$ plane of δ-hydide-2 is parallel to a $\{111\}$ plane of δ-hydide-6, but not parallel to the basal plane of α-Zr-2. One of δ-hydide-6 grain forms twins with the adjacent δ-hydide-2 grain and the twin boundary is shown by red dash line in Figure 5.5 (b). Therefore, another potential formation path of δ-hydride-6 is the transformation from δ-hydide-2 by $\{111\}\langle 11\bar{2}\rangle$ twining.

The most of left part of small hydride blister-2 and right part of small hydride blister-3 precipitated in the same parent grain, α-Zr-3, and will be studied together, as shown in Figure 5.6. Only two orientation variants of lath-shaped δ-hydrides are found in α-Zr-3 and the two representative grains of them are marked by white and yellow arrows respectively in Figure 5.6 (b) IPFY map. Both follow OR1 with α-Zr-3 and form alternating structures with each other. Like small hydride blister-1, the orientation relationship between δ-hydride-1 and δ-hydride-2 is close to $\{111\}\langle 11\bar{2}\rangle$ twins, but they rarely exactly form $\{111\}\langle 11\bar{2}\rangle$ twins. It is probably the results of relatively large misorientation inside α-Zr-3 grain and between the neighboring δ-hydride grains, as shown by pole figures in Figure 5.6 (c), presumably induced by the volume expansion during zirconium to δ-hydride transformation.

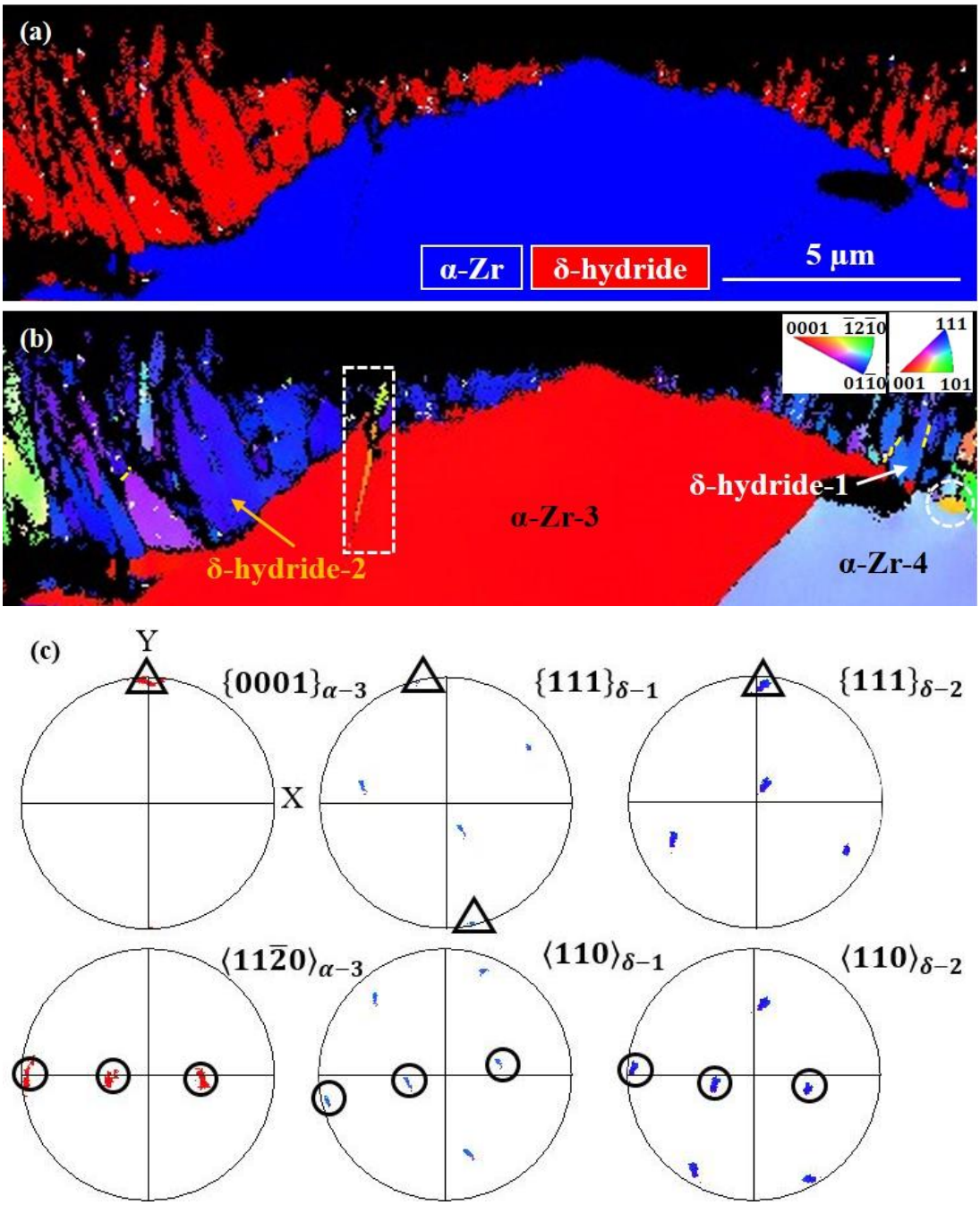

Figure 5.6 (a) Phase map and (b) IPFY map of the cross section of the left part of small hydride blister-2 and left part of small hydride blister-3, where white dash square is a δ-hydride precipitating from a twin of α-Zr-4, yellow dash lines are twin boundaries of δ-hydrides (the maximum deviation angle is 5˚) and white dash circle area represents δ-hydrides precipitating from α-Zr-4. (c) Pole figures of α-Zr-4 parent grain and two δ-hydride grains representing the hydride orientation variants found in small hydride blister-2 and -3 in α-Zr-4. Poles marked by black triangles are parallel crystallographic planes and those marked by black circles are parallel crystallographic directions.

In Figure 5.6 (b), the rectangular area enclosed by white dash lines includes a $\{11\bar{2}1\}\langle\bar{1}\bar{1}26\rangle$ (T2) twin of α-Zr-3. More details about twinning in α-Zr matrix will be present in section 5.1.2.4. The δ-hydride precipitated in it follows OR1 as well. In addition, the yellow δ-hydride,

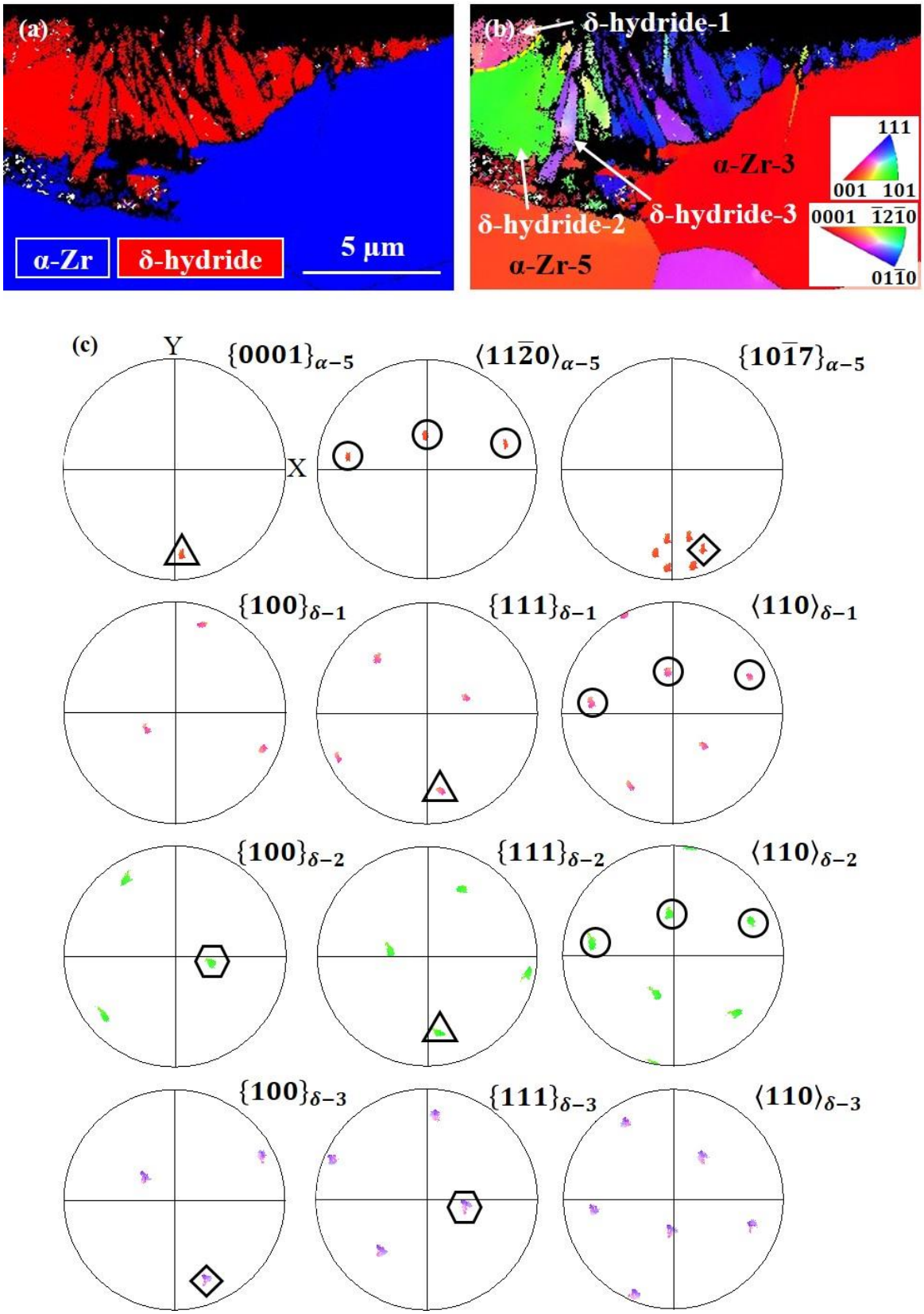

Figure 5.7 (a) Phase map and (b) IPFY map of the cross section of the left part of small hydride blister-3. Yellow dash lines are twin boundaries in small hydride blister-3 (the maximum deviation angle is 5˚). (c) Pole figures of α-Zr-5 and three δ-hydride grains representing the hydride orientation variants found in small hydride blister-3 in α-Zr-5. Poles marked by black triangles (or rhombuses, hexagons) are parallel crystallographic planes and those marked by black circles are parallel crystallographic directions.

enclosed by white dash circle, also follows in OR1 with its parent grain α-Zr-4 at the bottom right.

5.1.2.3 Small hydride blister-3

Figure 5.7 shows phase map, IPFY and pole figures of the left part of small hydride blister-3. This part precipitated within α-Zr-5 and contains three orientation variants of δ-hydrides. The δ-hydride-1 and -2 follow OR1 with α-Zr-5 and form $\{111\}\langle 11\bar{2}\rangle$ twins. The twin plane is one of $\{111\}$ planes parallel to basal plane of α-Zr-5 and the twin boundaries are shown by yellow dash lines in Figure 5.7 (b). The δ-hydride-3, much thinner than δ-hydride-1 and -2, has one of $\{100\}$ planes close to basal plane of α-Zr-5 and parallel to one of $\{10\bar{1}7\}$ planes of α-Zr-5, as marked by diamonds in the pole figures. Furthermore, one of its $\{111\}$ planes is parallel to a $\{100\}$ plane of δ-hydride-1 grains on either side of it. The orientation relationship between δ-hydride-3 and α-Zr-5 deviates from OR2 by 15˚ approximately, presumably associated with different levels of the compression given by δ-hydride-1 grains precipitated on the two sides of it.

5.1.2.4 Twinning in α-Zr matrix

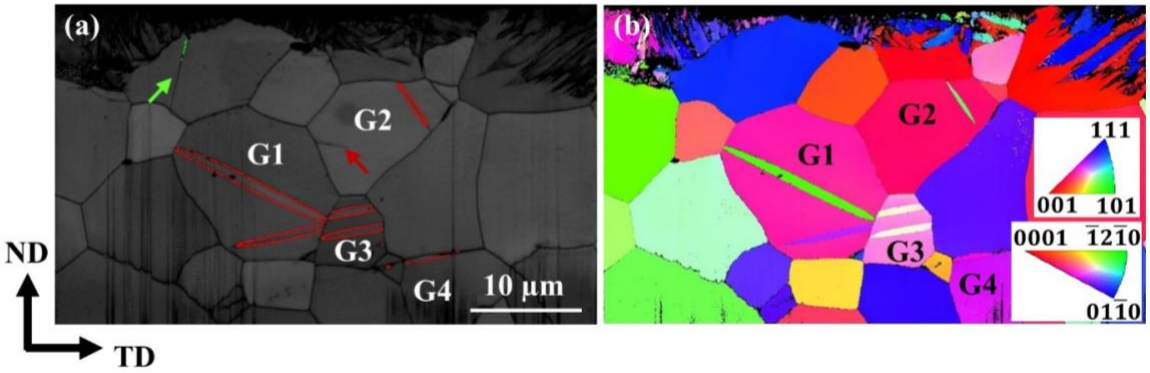

Figure 5.8 (a) Band contrast map and (b) IPFZ map of FIB prepared cross section containing small hydride blisters produced by electrolytic hydrogen charging for 24h. Red lines are T1 twin boundaries and green lines are T2 twin boundaries in α-Zr in (a) with the maximum deviation angle of 5˚.

As shown in Chapter 4, there is no twinning in the pure zirconium received. However, after

hydrogen charging, several twins appeared on the cross section prepared by FIB sectioning. Two types of twins are found in the α-Zr matrix below the small hydride blisters: $\{10\bar{1}2\}\langle\bar{1}011\rangle$ (T1) and $\{11\bar{2}1\}\langle\bar{1}\bar{1}26\rangle$ (T2), of which twin boundaries are shown by red lines and green lines respectively in Figure 5.8 (a).

T1 is the predominant type of twinning in zirconium in most cases[181]. All these twins in the α-Zr matrix underneath the parent grains for small hydride blisters are lens-shaped T1 twins and occupy 1.91% of total α-Zr in area. Two variants of T1 twins appear in G1 while two parallel twins are the same variant of T1 twins in G3. Although only one twin is recognized in G2 in the IPFZ map (Figure 5.8 (b)), another twin nucleation site can be distinguished in the band contrast map (Figure 5.8 (a)), as marked by white arrow. It forms along another $\{10\bar{1}2\}$ plane and is likely to be another variant of T1 twins in G2. In addition, G4 only has a T1 twin forming on the grain boundary rather than inside itself.

Different from T1 twins, only one T2 twin is found inside the parent grain for both small hydride blister-2 and -3. It is extremely thin and tends to be across the whole grain. Some hydrides precipitated inside it, which means it formed before hydride formation.

5.1.3 Discussion

5.1.3.1 Orientation relationship between δ-hydride and α-Zr

The area fractions of δ-hydrides in small blisters following different orientation relationships with α-Zr parent grains are summarized in Table 5.1. Two potential orientation relationships are followed by the formation of small δ-hydride blisters in α-Zr in most cases. First one is $\{0001\}_\alpha||\{111\}_\delta\ \langle11\bar{2}0\rangle_\alpha||\langle110\rangle_\delta$ (OR1). OR1 was observed in all the blisters studied and the area fraction of δ-hydrides obeying it is about 84.1%. OR1 is considered to be primary orientation relationship. 13.4% area of δ-hydrides follow the orientation relationship of

Table 5.1 Area fractions of δ-hydrides in the small blisters following different orientation relationships with α-Zr parent grains.

	Area fraction		
	OR1	OR2	others
Blister-1	74.2%	25.8%	0.0%
Blister-2	85.7%	14.1%	0.0%
Blister-3	93.1%	0.0%	6.9%
Total	84.1%	13.4%	2.6%

$\{0001\}_\alpha||\{100\}_\delta$ $\langle 11\bar{2}0\rangle_\alpha||\langle 110\rangle_\delta$ (OR2). OR2 was only observed in two parent grains with OR1 and never showed up alone. It is considered to be the secondary orientation relationship. The others could be obtained by small rotation or twinning from OR1 or OR2, which is likely to be caused by stress induced by volume expansion during the transformation from hydrogen in zirconium lattice to hydride phase. Therefore, OR1 and OR2 will be further discussed later.

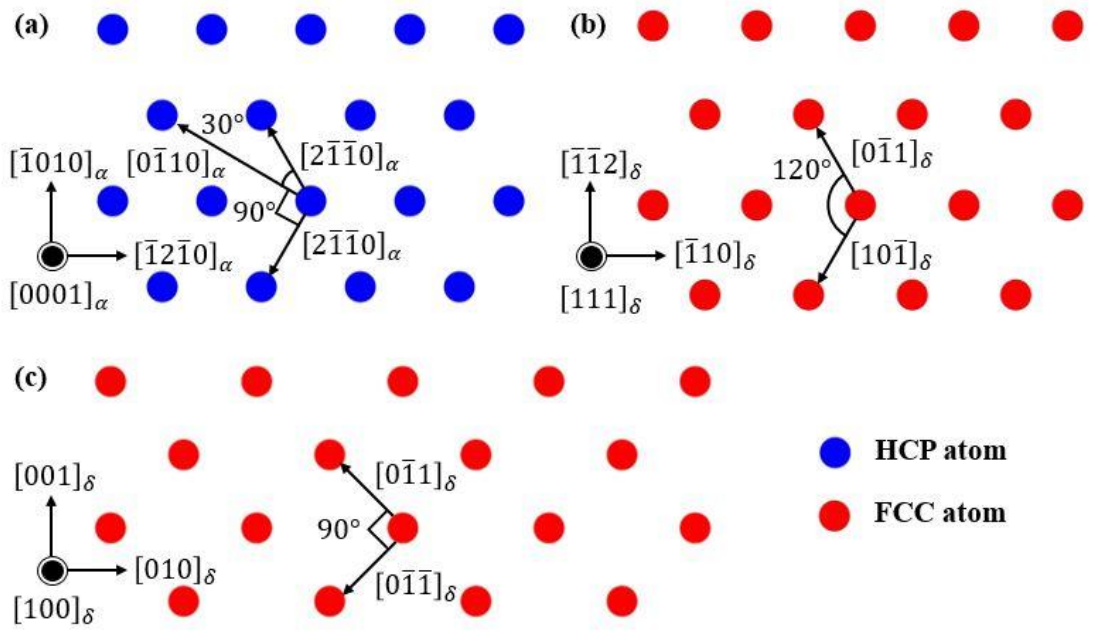

Figure 5.9 Schematics of atomic configuration of (a) $\{0001\}_\alpha$, (b) $\{111\}_\delta$ and (c) $\{100\}_\delta$ planes.

Figure 5.9 shows atomic configuration of basal plane of α-Zr, {111} and {100} planes of δ-hydride phase. The lattice misfits along different directions on these planes for OR1 and OR2 were calculated in terms of lattice parameters used for EBSD characterization in Aztec software

($a_\alpha = 3.231$ Å and $c_\alpha = 5.148$ Å for α-Zr[182], $a_\delta = 4.777$ Å for δ-hydride phase, ICSD[183]). For OR1, both $\{0001\}_\alpha$ and $\{111\}_\delta$ are hexagonal closed packed and thus lattice misfits on them are isotropic, expansions of 4.5% along both $[\bar{1}2\bar{1}0]_\alpha$ and $[\bar{1}010]_\alpha$ directions from α-Zr to δ-hydride phase. Meanwhile, the lattice misfit along $[0001]_\alpha$ direction is 7.2%. These values are in agreement with Carpenter's[67] and Long's[125] measurements and calculations. For OR2, the atomic arrangement of $\{100\}_\delta$ is different from that of $\{0001\}_\alpha$, leading to lower compatibility of δ-hydrides with α-Zr compared to OR1. The expansions of 4.5% along $[\bar{1}2\bar{1}0]_\alpha$ direction and 20.7% along $[\bar{1}010]_\alpha$ direction but compression of 7.2% along $[0001]_\alpha$ direction is required when δ-hydrides precipitate from α-Zr following OR2. These results also agree with Long's measurements and calculations[125]. Higher anisotropic distortion is expected to require more activation energy for hydride precipitation following OR2 compared to OR1. However, the opposite misfits of OR1 and OR2 along $[0001]_\alpha$ could partially mitigate the transformation strain in this direction. It may enable OR2 to become more energetically favorable with the presence of massive δ-hydrides following OR1 and explain the observation of layered structures of δ-hydrides following OR1 and OR2 alternatively in small blister-1 and-2. Therefore, for the localized δ-hydride precipitation in pure zirconium, OR1 is more favorite initially but OR2 still can occur in some specific occasions, especially when OR1 is greatly constrained. In addition, the total volume expansion was then calculated. It is 17.2% and as expect does not change with orientation relationship between δ-hydride and α-Zr[125].

Two twin related orientation variants were often seen within δ-hydrides following OR1 in all small hydride blisters, while orientation variants within δ-hydrides following OR2 are much less commonly observed. Only small hydride blister-2 includes three orientation variants with three different growth directions in δ-hydrides following OR2. It's supposed to be a result of higher symmetry of OR1 than OR2 and different atomic stacking configurations of these two orientation relationships. In addition, the orientation relationship between the δ-hydrides and

α-Zr may affect the structure of small hydride blisters. Jia[184] proposed that the δ-hydride laths with OR1 are parallel to each other but δ-hydride laths with OR2 has three geometric orientations corresponding to their three their variants, in terms of his work on subsurface hydrides in zirconium by XRD and TEM. It may be associated with the twin related structures of two variants following OR1. The twin related structures within δ-hydrides in small hydride blisters will be discussed in detail in next section. These findings consist with the EBSD results of the δ-hydrides in most cases described in 5.1.2. The one exception is in the grain which is not directly exposed at surface where the top and right grain boundaries may influence the geometric orientations of the δ-hydride laths with OR1 (Figure 5.5, middle part of small hydride blister-2).

5.1.3.2 Twin related structures in small hydride blisters

Twin related orientation variants of $\{111\}\langle 11\bar{2}\rangle$ were only found within δ-hydrides following OR1 rather than OR2 in the small hydride blisters studied. The twin plane is parallel to the basal plane of α-Zr parent grain. It's mainly determined by different atomic stacking configurations of δ-hydrides following these two orientation relationships. The stacking of $\{111\}_\delta$ atomic planes follow a sequence of '…ABCABC…' while the atomic stacking sequence of $\{100\}_\delta$ is '…ABABAB…'. Therefore, there is no chance for OR2 to form twin related structures along $\{100\}_\delta$.

Carpenter[185] proposed that the hcp α-Zr to fcc hydride phase transformation is achieved by the successive generation and glide of $\frac{a}{3}\langle 1\bar{1}00\rangle$ partial dislocations on alternate basal planes. Based on that, Wang[186] gave an explanation of the formation of twin related orientation variants within the δ-hydrides following OR1, as shown in Figure 5.10. The Burgers vectors of dislocations required by the formation of a pair of twin related δ-hydrides are opposite on the

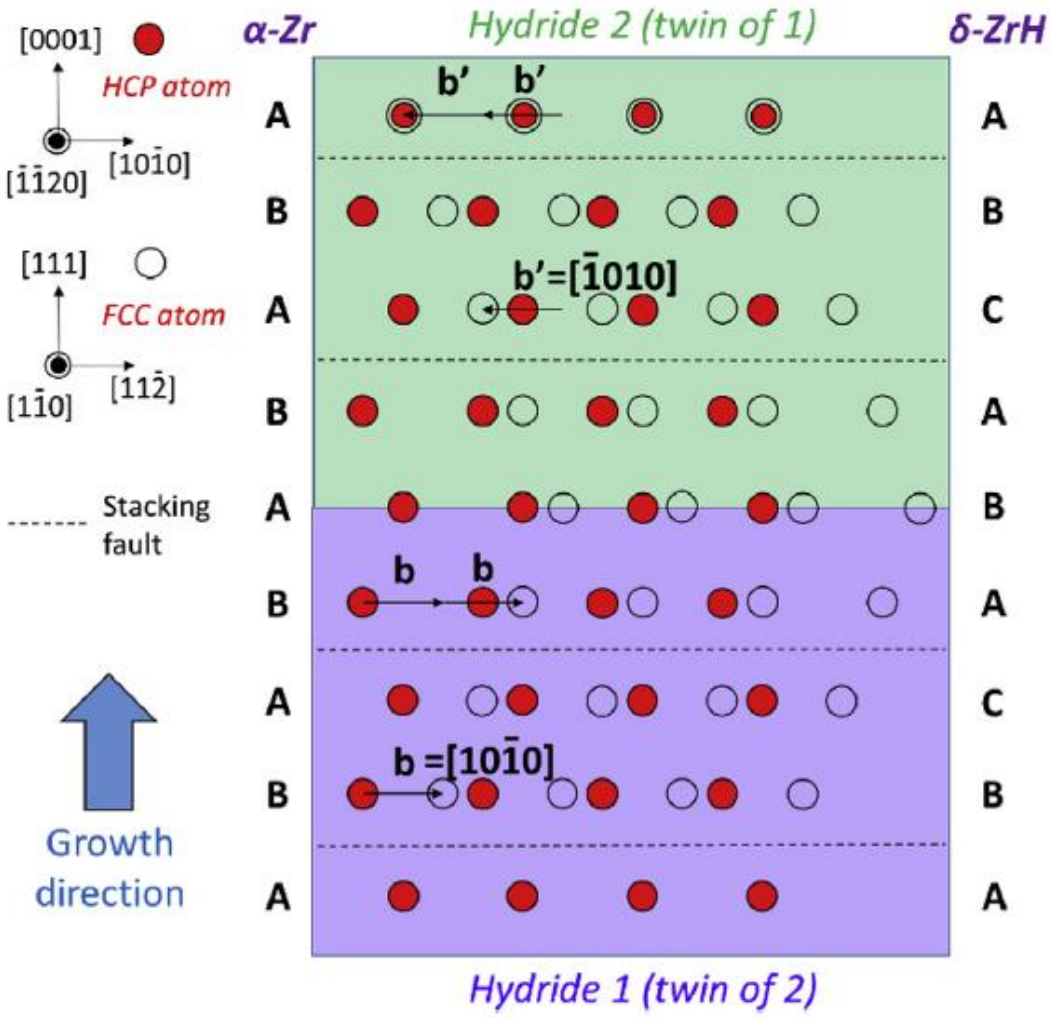

Figure 5.10 Schematic of twin related orientation variants in the δ-hydrides following OR1[178].

twin plane. Therefore, the strain built up along $\{111\}_\delta$ planes can be partially mitigated by the formation of the twin related variants, leading to alternating formation of two twin related variants observed in all small blisters studied. In the right part of the blister-2 (Figure 5.4) and the left part of the blister-3(Figure 5.7), the twin features stack along the hydrogen diffusion direction and the boundaries between these twin features are the corresponding twin planes. It's more likely that these twin features are driven by the mechanism described above. In all the other parts of the blisters in Figure 5.3, 5.5 and 5.6, the hydride laths show the growth direction downward and the boundaries between these twin features are not parallel to the twin planes. It's still possible that the nucleation and growth of them are independent. The

geometrical relation between hydrogen diffusion direction and orientation of a Zr matrix grain may affect the microstructure of a hydride blister.

Another $\{111\}\langle 11\bar{2}\rangle$ twins, δ-hydride-2 and -6, was found in the middle part of small hydride blister-2, as shown in Figure 5.5. The δ-hydride-2 is much thicker than δ-hydride-6. The twin plane is not parallel to the basal plane of parent grain. The boundary between them is straight and parallel to their twin plane. The formation of such twin features is still able to mitigate transformation strain. This will also help with longer range strain field in the Zr matrix too, not just inside δ-hydrides. The δ-hydride-2 follows OR1, while the orientation of δ-hydride-6 is very close to one of the orientation variants following OR2. This, as discussed in last section, can mitigate the transformation strain perpendicular to basal plane. These two factors are able to contribute the formation of such twin structures.

Note that there is probably a balance here. The strain energy is likely reduced by having a finer twinning structure, but this has the penalty of more twin interfaces, which means more interfacial energy.

5.1.3.3 Twinning in zirconium matrix

Twinning in the zirconium matrix underneath the parent grains of small hydride blisters was commonly observed on the FIB-prepared cross sections in the cases studied. Two potential causes for this are proposed first: formation of small hydride blisters and/or FIB-milling. To further figure out the contribution of these two potential causes to such twin formation in α-Zr matrix, EBSD scanning was performed on FIB-milled and electro-polished cross sections of as-received pure zirconium plates, as shown in Figure 5.11. Two T1 twins are found on the FIB-milled cross section near the top surface (no more than 25 μm) and the area fraction of T1 twins is much smaller than that with the presence of small hydride blisters. In contrast, no twin

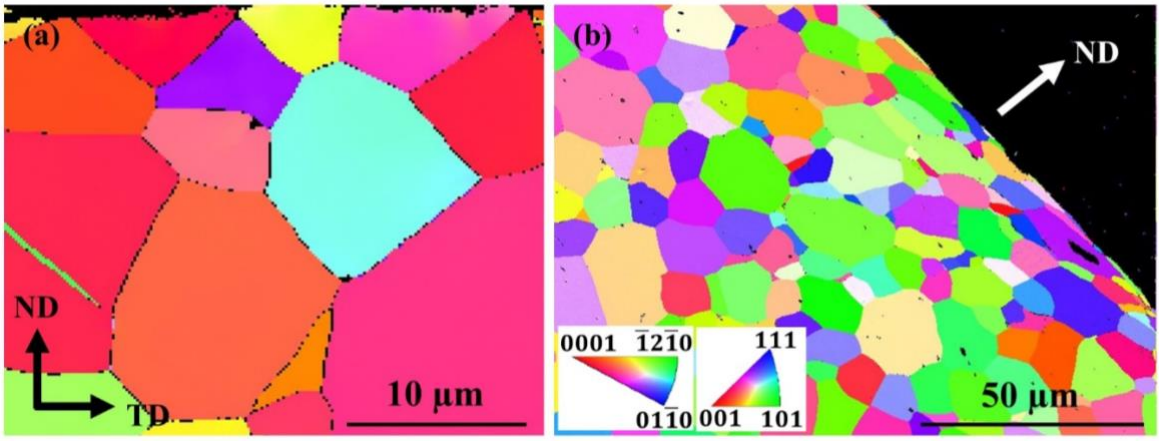

Figure 5.11 IPFY maps of (a) FIB-prepared cross section and (b) electro-polished cross section of as-received pure zirconium plates.

is observed on the electro-polished cross section whether near or far from the top surface, although the top edge of the cross section was etched more during eletropolishing. These indicate that FIB milling may induce T1 twins in pure zirconium and the formation of small hydride blisters may further enhance the formation of T1 twins in α-Zr matrix underneath. Theoretically, the influence of FIB milling, and formation of small hydride blisters decreases with depth increasing. However, much more T1 twins were observed in the α-Zr matrix underneath parent grains of small hydride blister rather than inside the parent grains. The higher concentration of hydrogen in parent grains may contribute to it but still not clear. In addition, all the samples in this chapter were cut from the large pure zirconium plate by high-speed saw, which may cause structural change close to the cutting edge. The FIB-prepared cross section is just 5-20 μm away from the cut edge and a much thicker layer of zirconium, usually tens of microns in my work, was removed from the cut edge during the grinding and polishing process. It is still not sure if the high-speed saw cutting contributes to the twinning structures found in the zirconium matrix.

5.2 Micro-analysis of homogeneously distributed hydrides by conventional and high angular resolution EBSD

Although hydride blisters are extremely detrimental to mechanical properties and structural integrity of zirconium fuel claddings, their formation is unusual and only happens when the hydrogen concentration at a specific site is much higher than the surrounding area due to some external factors. In most cases, individual hydrides were often found to stack or chain together to form larger hydrides along circumferential direction in the claddings. In order to measure the local deformation around such hydrides and explore their growth mechanism, homogenization annealing was performed on the pure zirconium samples after hydrogen charging. This allows the hydride blisters to dissolve into bulk zirconium and re-precipitate in the form of hydride chains or stringers. In terms of lattice misfit distribution between δ-hydrides and α-zirconium matrix, δ-hydrides are supposed to precipitate in the shape of plates after homogenization annealing. However, conventional microscopies only can reveal hydrides in 2D. Therefore, serial sectioning and imaging was used to characterize the morphology of δ-hydrides in 3D. The microstructure and the local deformation, including strain and GNDs, induced by hydride formation were studied by conventional and high angular resolution (HR-) EBSD to provide a better understanding of hydride formation and growth mechanism.

5.2.1 Experiments and methods

5.2.1.1 Materials and sample preparation

The samples studied in this section were cut from the 1mm thick rolled pure zirconium sheets, which were then annealed at 750 ˚C for 36 h to increase the average grain size from ~14 μm to ~87 μm. One of them were thinned to ~0.2 mm by grinding with SiC grinding discs. All

Table 5.2 Summary of samples containing homogeneously distributed δ-hydrides in this section.

	Thickness(mm)	Cooling rate (˚C/min)
Sample-A	1mm	In air
Sample-B	0.2mm	In air
Sample-C	1mm	3

samples were electrolytically charged in 1 vol. % diluted sulphuric acid using the current density of 1.0 kA/m^2 at 65±5 ˚C for 24 h and then annealed at 400 ˚C to homogenized hydrogen in the bulk. One 1mm thick sample was cooled down in furnace to room temperature at the rate of 3 ˚C/min, while the other samples were cooled down in air. Next, one cross section of each sample was ground using SiC grinding discs, mechanically polished with colloidal silica and electropolished in a solution of 90 vol. % methanol + 10 vol. % perchloric acid at a temperature lower than -30 ˚C to prepare a sufficient flat and defect-free surface for subsequent EBSD characterization. The details about sample preparation for EBSD can be found in section 4.5. More details of materials and sample preparation have been described in Chapter 4 and all samples are summarized in Table 5.2.

The morphology and distribution of hydrides greatly depend on the grain size and cooling rate of homogenization annealing when there is almost no change in texture[50]. Precipitation of hydrides on grain boundaries can be promoted by decreasing grain size (i.e. increasing fraction of grain boundaries) and/or slowing cooling rate[50]. In this section, moderate grain size was chosen to allow precipitation of both intra- and inter- granular hydrides, which is defined by the nucleation site. Two cooling rates were applied to prepare hydrides in different sizes, which represent hydrides at different stages of growth.

The hydrides prepared in this section were identified as δ-phase by EBSD and all the hydrides in the following sections refer to δ-hydrides. The general morphology and distribution of them are shown by polarized light images in Figure 5.12. In sample-A and sample-B which were cooled down to room temperature in air, a distinct population of hydrides were observed both inside grains and on grain boundaries. They appear as thin and dark straight-line segments in the polarized light images (Figure 5.12 (a) and (b)). The inter-granular hydride line segments are slightly thicker than intra-granular hydride line segments, but no obvious preferential sites

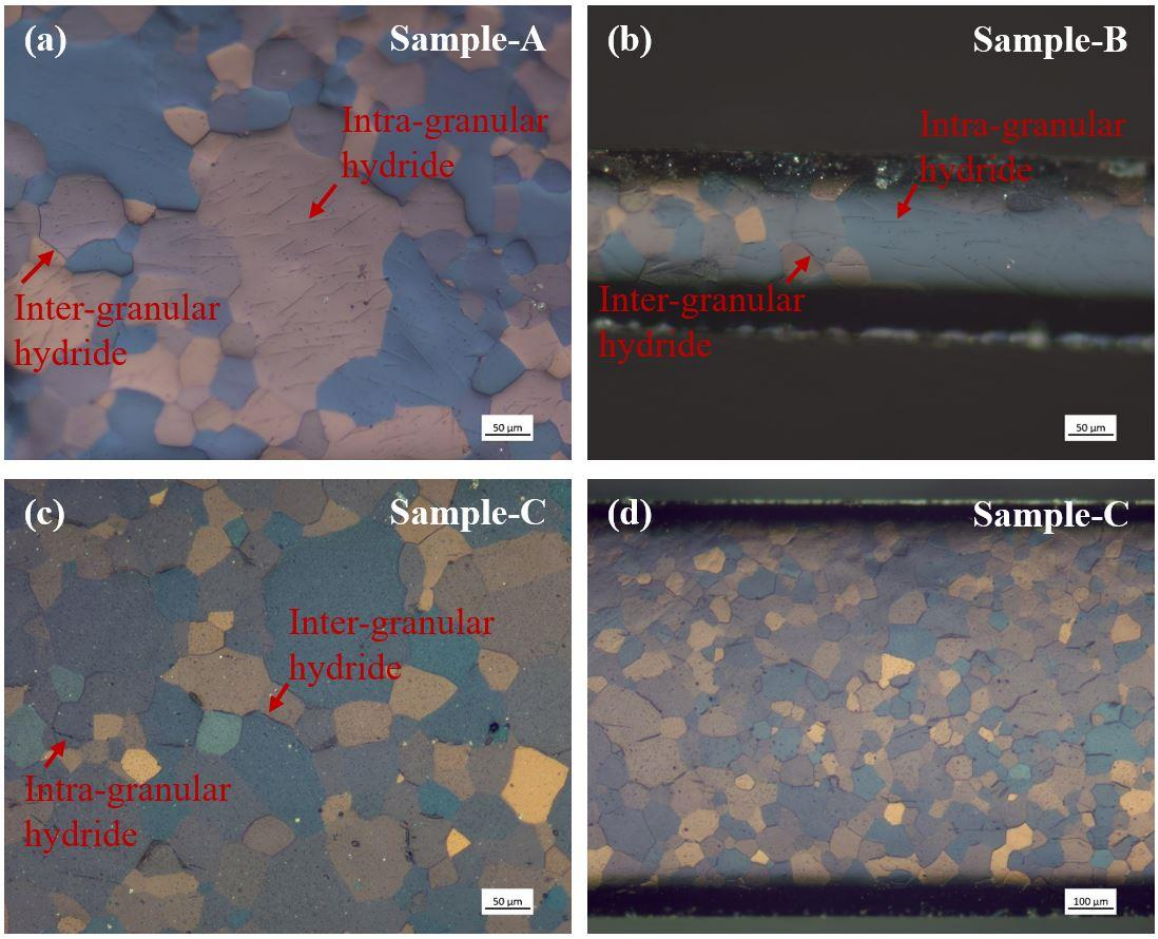

Figure 5.12 Polarized light images of the electro-polished cross sections of (a) sample-A, (b) sample-B, (c) and (d) sample-C after homogenization annealing.

for hydride precipitation are found. Theoretically, the thinner sample allows higher average hydrogen concentration interior in the same conditions. However, there is nearly no visible change in the density of hydrides between sample-A and sample-B. It may be caused by lower hydrogen charging rate and/or more loss of hydrogen of thinner samples during homogenization anneal. In sample-C with a much lower cooling rate of 3 ˚C/min, most hydrides precipitated on grain boundaries and few of intra-granular hydrides were found. All the hydride line segments are much thicker than those in sample-A and –B, especially for inter-granular hydrides. The number of hydrides is much less than those in sample-A and –B. All above indicate that the hydrogen distribution in the lattice at anneal temperature tends to be homogeneous but grain boundaries are preferential sites for hydride nucleation. Hydrogen

presumably prefers to diffuse to nucleated hydrides on grain boundaries to promote their growth when there is sufficient time for hydrogen to diffuse (i.e., decreasing cooling rate) rather than nucleate inside matrix grains. Birch's work shows similar effects of cooling rate[50].

5.2.1.2 Serial sectioning and imaging

Serial sectioning and imaging was performed on the top surface of sample-A by using a Zeiss crossbeam 540 analytical FIB/SEM with a Ga^+ source to study the morphology of δ-hydrides in 3D. Firstly, a protective platinum layer of about $20\ \mu m \times 20\ \mu m \times 1\ \mu m$ was deposited on the region of interest by Ga^+ ion beam of 700 pA. A large trench of $40\ \mu m \times 25\ \mu m \times 30\ \mu m$ was then milled by a large beam current of 30 nA in front of the Pt layer with a 4-5 μm gap between them. The exposed cross section was milled for several times by sequentially finer ion beams of 15 nA, 7 nA, 3 nA and 1.5 nA. Two large trenches of $20\ \mu m \times 40\ \mu m \times 30\ \mu m$ were milled on either side of the square Pt layer by the ion beam of 30nA to avoid shadowing in the imaging later. After that, a SE image and an Inlens image of the newly exposed cross section were captured simultaneously after a 50 nm thick slice was removed from the cross section by the ion beam of 1.5 nA. These imaging and milling steps were repeated for 66 times to collect enough slice images to show the morphology of δ-hydrides in the slicing direction. The imaging resolution was 3027×2304 and the pixel size was ~13 nm. The ion beam voltage of 30 kV was used for all FIB deposition and milling steps. The voltage and current of electron beam for imaging were 20 kV and 7.0 nA respectively. The results will be described in the section 5.2.2.

5.2.1.3 EBSD data acquisition

Conventional and high angular resolution EBSD techniques have been introduced in section 3.3. In this section, all the HR-EBSD and conventional EBSD measurements were performed by using Zeiss Merlin-EBSD equipped with a Bruker Quantax EBSD system.

In this section, all diffraction patterns were acquired with a probe current of 20 nA and a voltage of 20 kV. The conventional EBSD scans were performed with pattern resolution of 400×300 pixels and for most HR-EBSD analysis the patterns were captured at a full resolution of 1600×1200 pixels. The exceptions will be noted in the description of the corresponding figures. The step size varies with the magnification of maps. It may influence the calculated GND density[142] and step size will be included in the description of each EBSD dataset. The parameters for HR-EBSD analysis by using xEBSD_v3 codes can be found in section 3.3.2.

5.2.2 Intra-granular δ-hydrides

Considering intra-granular hydrides were much fewer in the sample-C with cooling rate of 3 ˚C/min than sample-A cooled down in air, sample-A was opted for the characterization of intra-granular δ-hydrides at micro-scale.

5.2.2.1 Serial sectioning results

Figure. 5.13 shows the Inlens images of a series of the cross sections obtained from serial sectioning and imaging performed on sample-A. Figure. 5.13 (a) refers to a general view of the cross section for the following sectioning and imaging. Under the protective Pt layer, the semi-circular region (marked by white dash) is composed of numerous small “blocks” with different contrast. The position, size and shape of this semi-circular region are consistent with small surface hydride blisters discussed in the section 5.1. Meanwhile, these small “blocks” are at the same size scale to the grains in the small surface hydride blisters. It implies the lattice rotation caused by volume expansion during zirconium to hydrides transformation is retained after hydrides dissolve into bulk zirconium. Several intra-granular δ-hydride chains, which appear in a darker contrast than the parent grain, can be found on this cross section. One whole δ-hydride chain is included in the red dashed line rectangle. The area in that rectangle is shown

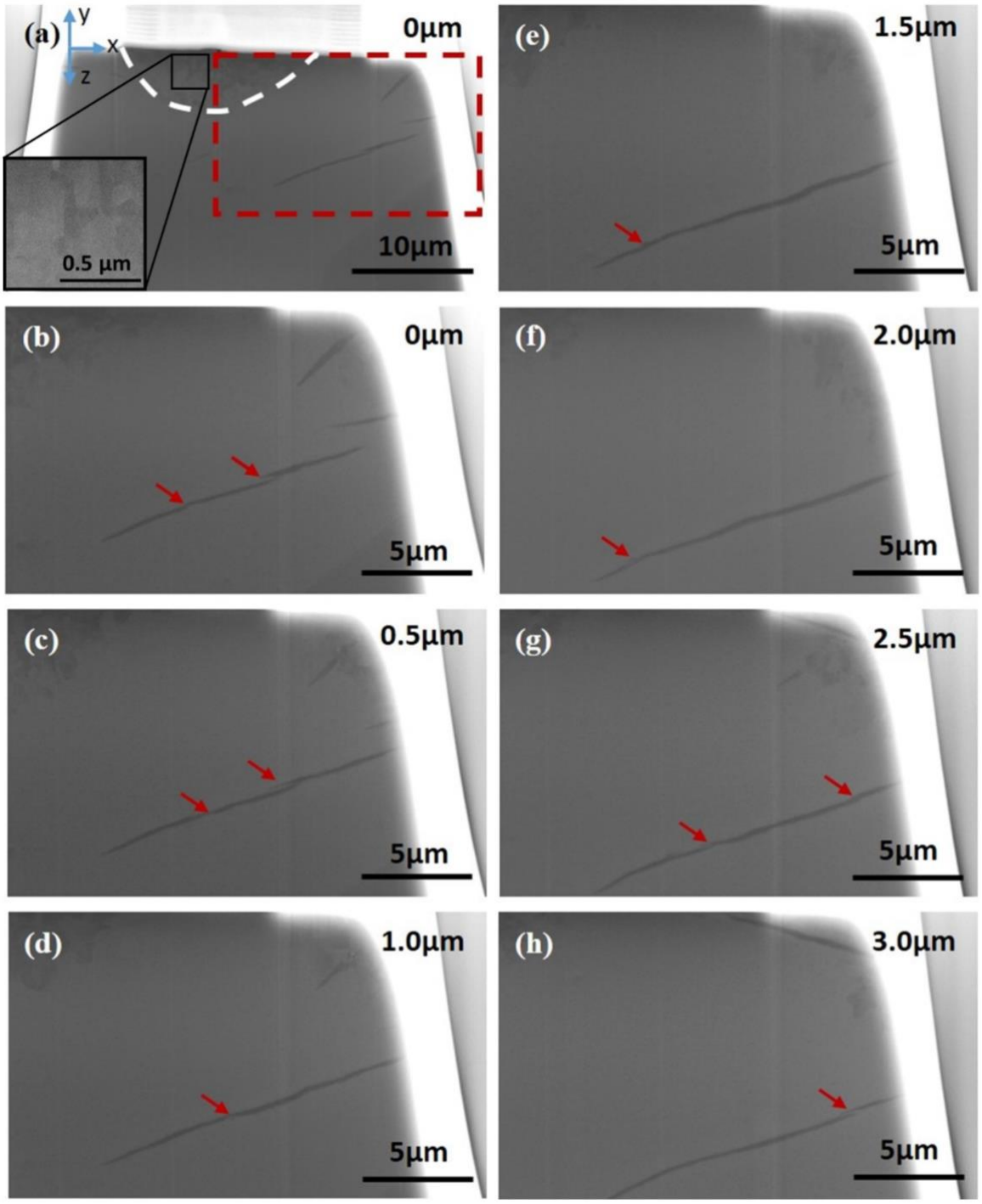

Figure 5.13 A series of eight Inlens images of the cross sections from a serial sectioning experiment performed on sample A. (a) is the general view of the cross section before serial sectioning. (b) is the area in the dashed line rectangle in (a). (c) to (h) are the same area to (b) after different thick slice was removed by FIB during serial sectioning. The depth in the slicing direction (y-direction as shown in (a)) is labelled at top-right on each image and the space internal among the images of (b) to (h) is 500 nm approximately.

at a higher magnification in Figure 5.13 (b) and Figure 5.13 (c) to (h) are the same area to (b) after different thickness was removed by the serial sectioning.

The δ-hydride chain is formed by three hydride plates stacking along the direction nearly parallel to their habit plane, as shown in Figure 5.13 (b). The red arrows point out the places where the adjacent hydride plates overlap or connect with each other. With more slices milled away from the cross section, the length of the hydride chain increases by the formation of new hydride plates at two ends. One small hydride plate appears at the left end of the hydride chain at the depth of 1.5 μm in the slicing direction and another small hydride plate shows up at the right end at the depth of 2.5 μm. Meanwhile, the positions of joints between two adjacent hydride plates are changing. All these implies that the hydride plates stack, or partially overlap each other, along the plane close to their habit plane and then form a much larger "plate", rather than a direction to form a chain in 3D. In addition, the distance between the large hydride plate and the top of the cross section increases with the depth in the slicing direction, which suggests the large hydride plate is not perpendicular to the cross section exposed.

5.2.2.2 Conventional EBSD results

In the extra-large matrix grain in Figure 5.14, the hydride stacks are composed of small hydride plates, which are generally no longer than 15 μm, in the same way shown in 5.2.2.1. The length of these hydride stacks varies from a few microns to dozens of microns, while their thickness is similar, no more than few hundred nanometers, which is also the thickness of the small hydride plates. Furthermore, much shorter small hydride plates are observed at the ends of some hydride stacks. These imply that the intra-granular hydride stacks prefer to grow longer by precipitating small new hydride plate at their tips rather than become thicker during air cool down. The hydride stacks follow several directions, while the angles between them and the trace of basal plane are all in the range of 0˚~20˚ approximately. This suggests there are habit planes for hydride plates and stacks but not only one. Conventional EBSD scans were conducted on the area1, 2 and 3 (red dashed rectangles) in Figure 5.14 to further reveal the

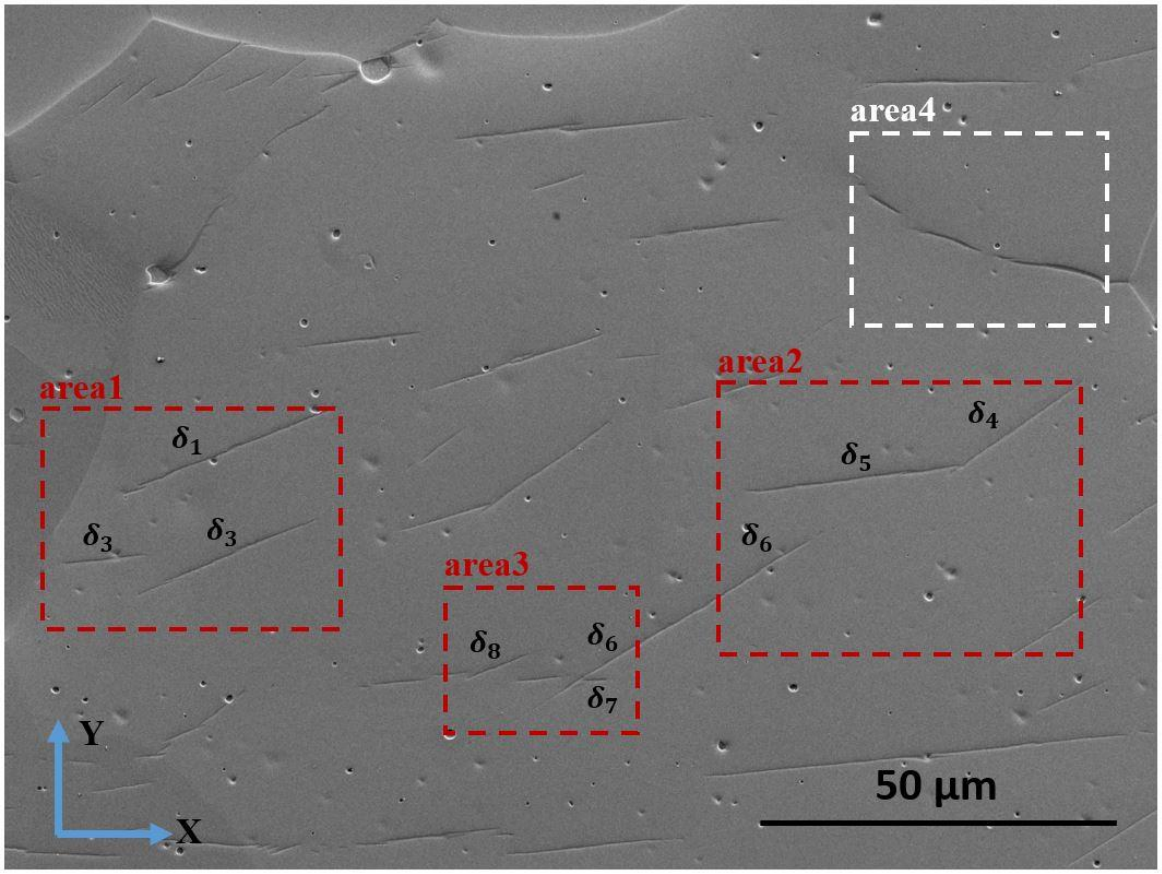

Figure 5.14 Secondary electron (SE2) image of hydrides in pure zirconium (electro-polished cross section of sample A).

precipitation crystallography characteristics of intra-granular δ-hydrides. The results are shown in Figure 5.15. Area4 (white dashed rectangle) includes several inter-granular δ-hydrides for HR-EBSD scanning and will be discussed in 5.2.3.

The step size selected for each conventional EBSD scan mentioned above is about 100 nm, which is in the order of spatial resolution limit of EBSD. Nonetheless, some extremely thin and short hydrides were not successfully identified or distinguished from matrix. In Figure 5.14, eight hydride stacks were successfully identified. All of them follow the commonly observed orientation relationship of $\{0001\}_\alpha||\{111\}_\delta\ \langle 11\bar{2}0\rangle_\alpha||\langle 110\rangle_\delta$ (OR1) with their parent grain α_1 and the average deviation angle is ~ 1.54˚. Meanwhile, two orientation variants of δ-hydrides were found: δ_1, δ_2, δ_6, δ_7 and δ_8 share one orientation variant and δ_3, δ_4 and δ_5

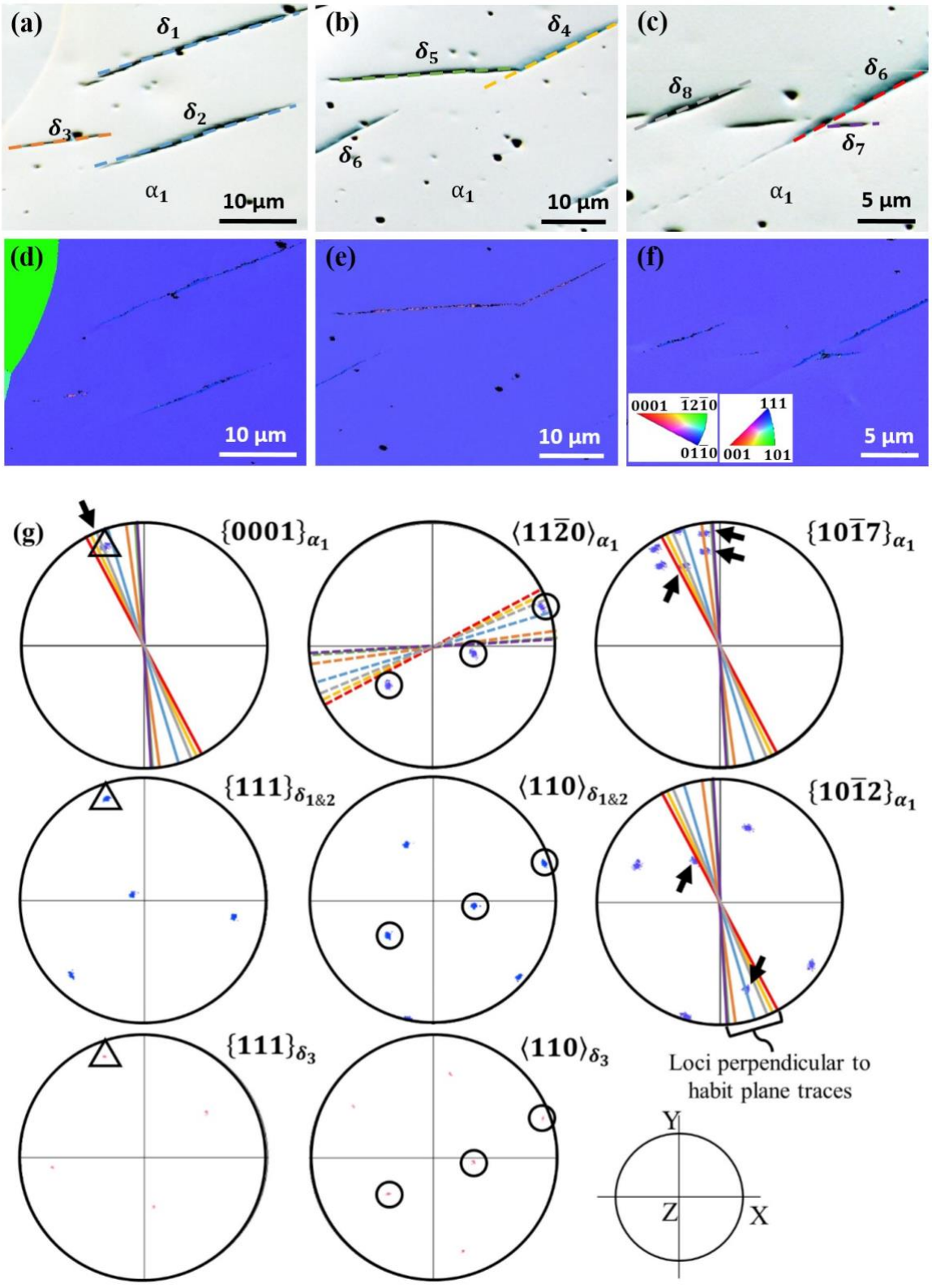

Figure 5.15 Forescattered electron images of (a) area1, (b) area2 and (c) area3 in Figure 5.14, overlaid with the traces of the habit planes of the hydrides (dashed lines in different colours). IPZ maps of (d) area1, (e) area2 and (f) area3 in Figure 5.14. (g) Pole figures of parent grain α_1 with habit plane traces overlaid, hydrides $\delta_{1\&2}$ and δ_3. Step size: 110 nm (area1), 85 nm (area2 and area3). Note the coloured solid lines are the loci perpendicular to the habit plane traces of the hydrides and the planes with their poles past by these loci are the possible habit planes for the hydrides.

follow the other one. The relationship between these two orientation variants is also consistent with $\{111\}\langle 11\bar{2}\rangle$ twins in fcc structures but they were not observed simultaneously in one hydride stack here. The traces of their habit planes are shown by the dashed lines in different colors in (a) to (c). δ_1 and δ_2 are parallel to each other and their traces are shown by the same colour. The traces of δ_4 and δ_6 are quite close to each other and δ_5 is almost the same as that of δ_7. However, these traces only represent the intersection lines of these plate-like hydride stacks and the measured surface. All the planes with the normals perpendicular to these traces are potential habit planes and the loci perpendicular to these traces are shown by corresponding colored solid lines in the pole figures (Figure 5.14 (g)). Basal plane of α_1 is a potential habit plane for δ_8 and $\{10\bar{1}2\}_{\alpha_1}$ is a potential habit plane for δ_1, δ_2, δ_4 and δ_6. $\{10\bar{1}7\}_{\alpha_1}$ is a potential habit plane for all the δ-hydrides identified here.

5.2.2.3 HR-EBSD results

HR-EBSD analysis was conducted to further reveal the microstructure changes and local deformation induced by δ-hydride formation inside α-Zr grains. The morphology of the hydrides in the scanned area is shown by the forescattered electron image (Figure 5.16 (a)). The three intra-granular hydride stacks in the red dashed rectangle will be discussed first and the other hydrides on the grain boundary will be described in the following section.

As shown in the Figure 5.16 (b), the three intra-granular hydride stacks were identified as δ-hydrides and named as δ_1, δ_2 and δ_3 from left to right in order. Although δ_1 impinges on the grain boundary, its morphology is almost the same to δ_2 and δ_3 and thus δ_1 is regarded as an intra-granular hydride. The thin tips of hydrides 1-3 were not distinguished from matrix using EBSD indexing. The three δ-hydride stacks share one orientation and also follow the orientation relationship of $\{0001\}_\alpha||\{111\}_\delta\ \langle 11\bar{2}0\rangle_\alpha||\langle 110\rangle_\delta$ (OR1) with their parent grain α_1. Nonetheless, their habit planes are different. As shown by the habit plane traces on the pole

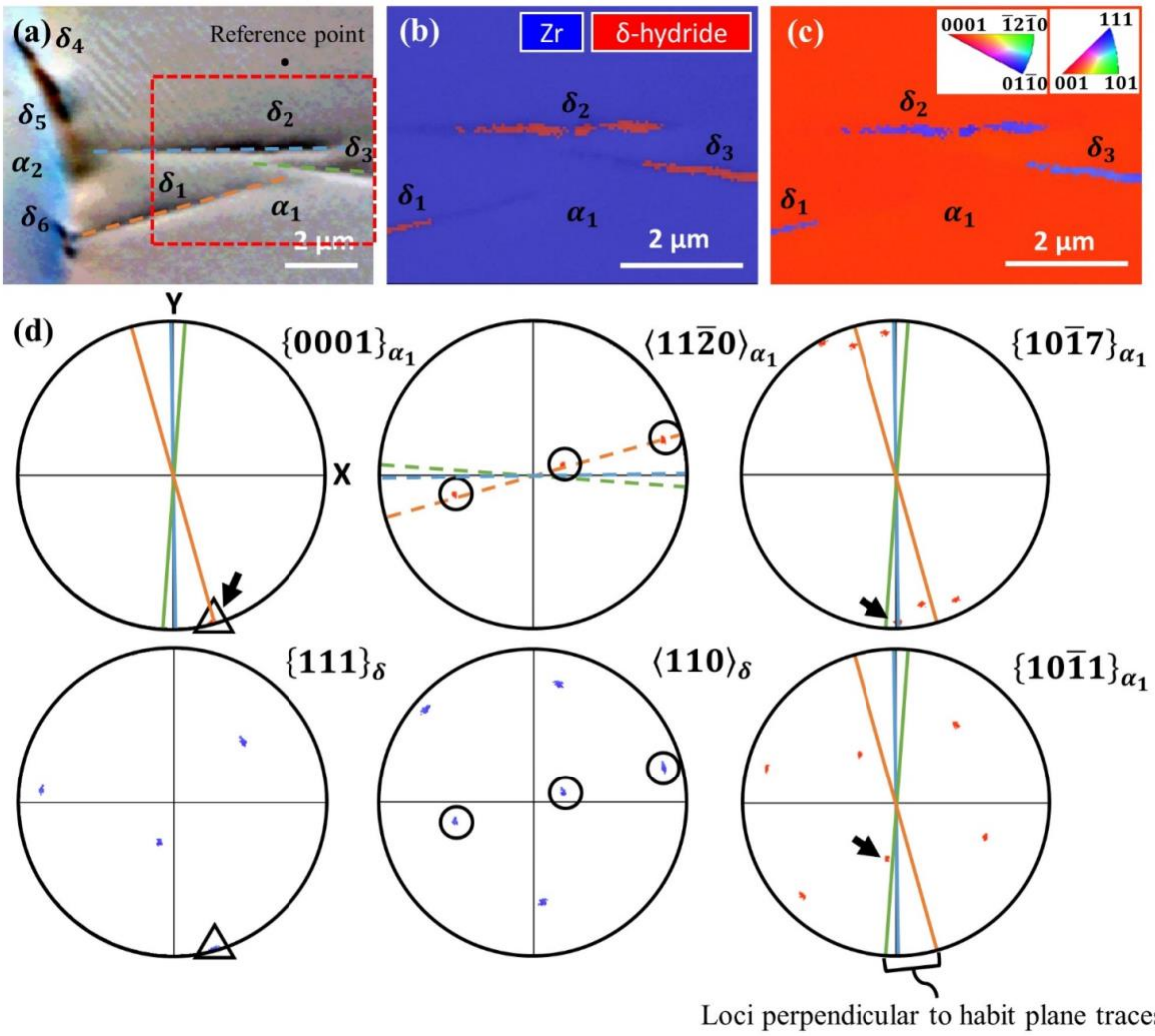

Figure 5.16 (a) Forescattered electron image of the region including both intra- and inter-granular hydrides for HR-EBSD analysis. The intra-granular hydrides in the red dashed rectangle are studied here and the inter-granular hydrides will be discussed in the next section. (b) Phase map overlaid with the pattern quality map, (c) IPFY map and (d) pole figures of parent α-zirconium grain overlaid with habit plane traces and the pole figures of intra-granular δ-hydrides. Pattern resolution: 1600×1200. Step size is 50nm. Note the coloured solid lines are the loci perpendicular to the habit plane traces of the hydrides and the planes with their poles located on these loci are the possible habit planes for the hydrides.

figures of parent grain α_1 in the Figure 5.16 (d), $\{0001\}_{\alpha_1}$, $\{10\bar{1}7\}_{\alpha_1}$ and $\{10\bar{1}1\}_{\alpha_1}$ are the potential habit planes for hydrides δ_1, δ_2 and δ_3 respectively. The deviation angles of the traces of these potential habit planes to the trace of basal plane are within 20˚.

The distribution of GND density is presented by Figure 5.17. The lower bound of the noise error on the GND measurements here is determined by angular resolution for the pattern shift

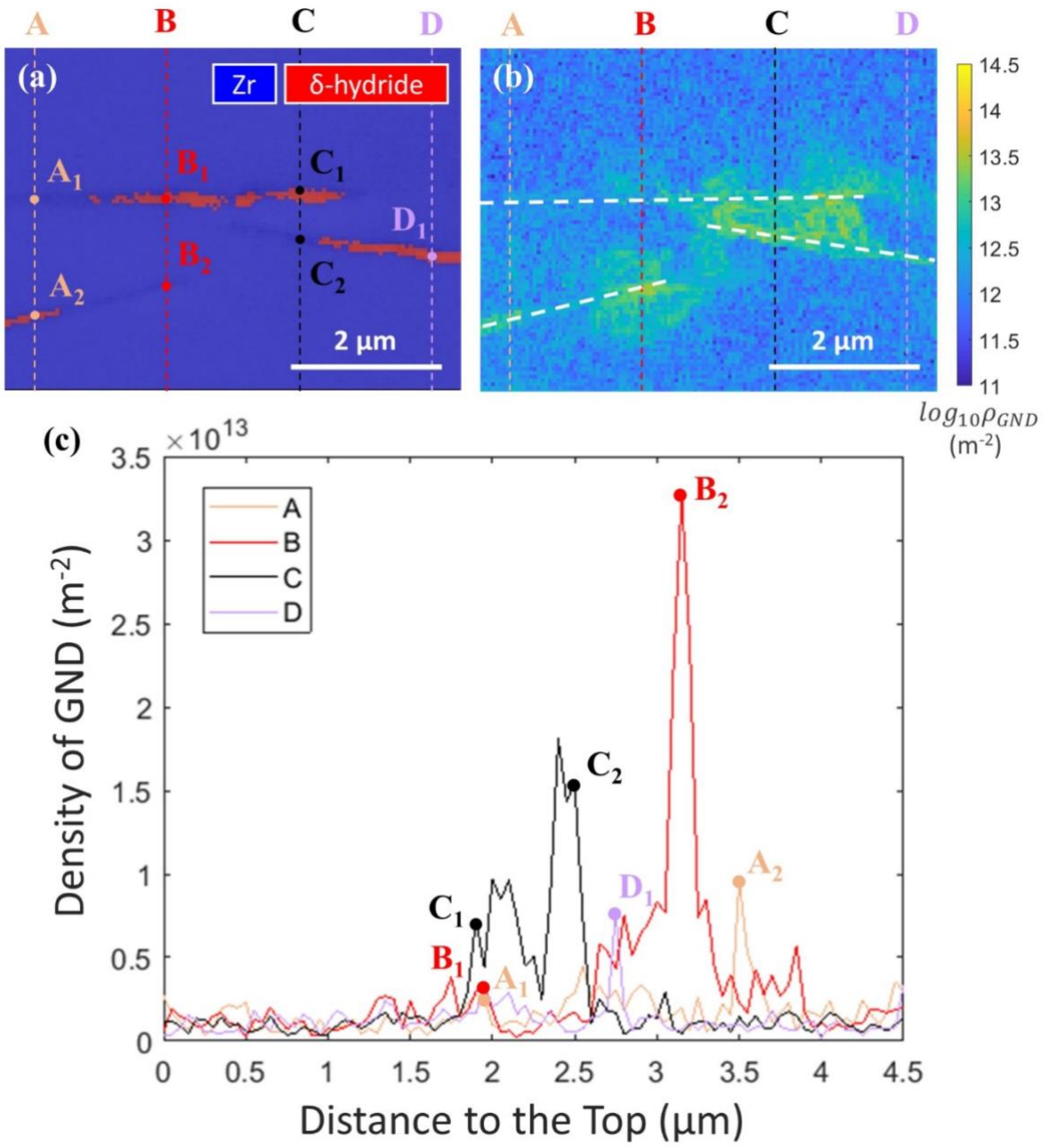

Figure 5.17 (a) Phase map overlaid with the pattern quality map and (b) GND density map, presented as $\log_{10}$ in m^{-2}, of the three hydride stacks in the parent grain α_1. (c) GND density profiles of the four lines shown in (a) and (b). Note the positions of the hydrides are shown by white dashed lines in (b). Pattern resolution: 1600×1200. Step size is 50nm.

measurements $\Delta\theta$ (in radians), Burger's vector length b and step size Δx and can be simply estimated by Eq. (5.1) [137].

$$\Delta\rho = \frac{1}{b}\frac{\Delta\theta}{\Delta x} \tag{5.1}$$

The angular resolution is about 2×10^{-4} rads for the pattern resolution of 1600×1200, measured by Angus in the previous study[137]. The step size of 50nm was used. The Burger's vector length is 3.4068 Å for δ-hydride grains and 2.7990 Å (<a> type dislocations) for α-Zr grains. The estimated noise error of the measured GND density is 1.2×10^{13} m^{-2} for δ-hydride and 1.4×10^{13} m^{-2} for α-Zr grains, which is much higher than the noise floor shown in the GND map. It may be caused by the better angular resolution achieved by the considerable development of EBSD detector in recent years. At the thin tips of hydrides which were not distinguished from the matrix by EBSD indexing, the strain and GNDs were measured as α-Zr matrix. The lower pattern quality presumably rises higher noise error at these points.

Generally, as shown in the GND density map (Figure 5.17 (b)), higher GND density is found close to the hydride positions (white dashed lines) than the matrix far from them. Much higher GND density is found surrounding the tips of δ-hydride stacks (e.g., δ_1), especially on the two sides, and the regions between two δ-hydride tips close to each other (e.g., δ_2 and δ_3). This is likely to trap hydrogen and promote α-Zr to δ-hydride transformation occurring beside the hydride tips next. To give a better quantification of GND density induced by hydride formation, four line profiles shown in different colors are taken along vertical scans in the color map of GND density and the positions of hydrides on the lines are marker by spots in the corresponding color. The spot A_2, B_1, C_1 and D_1 are located at the middle of δ-hydride stacks as successfully identified by EBSD indexing, while spot B_2 and C_2 are located at the tip of δ_1 and δ_3 where the hydrides were not distinguished from the matrix. The GND density at all these positions, as marked by the spots on the line profiles in Figure 5.17 (c), is markedly higher than that in the matrix. There is a span of about 1.3 μm showing higher GND densities around spot B2. The lower GND densities are found on A_1 to A_2 where the hydrides are well separated by matrix. In contrast, the GND densities are notably higher between two hydride stacks especially when they are close together (C_1 to C_2).

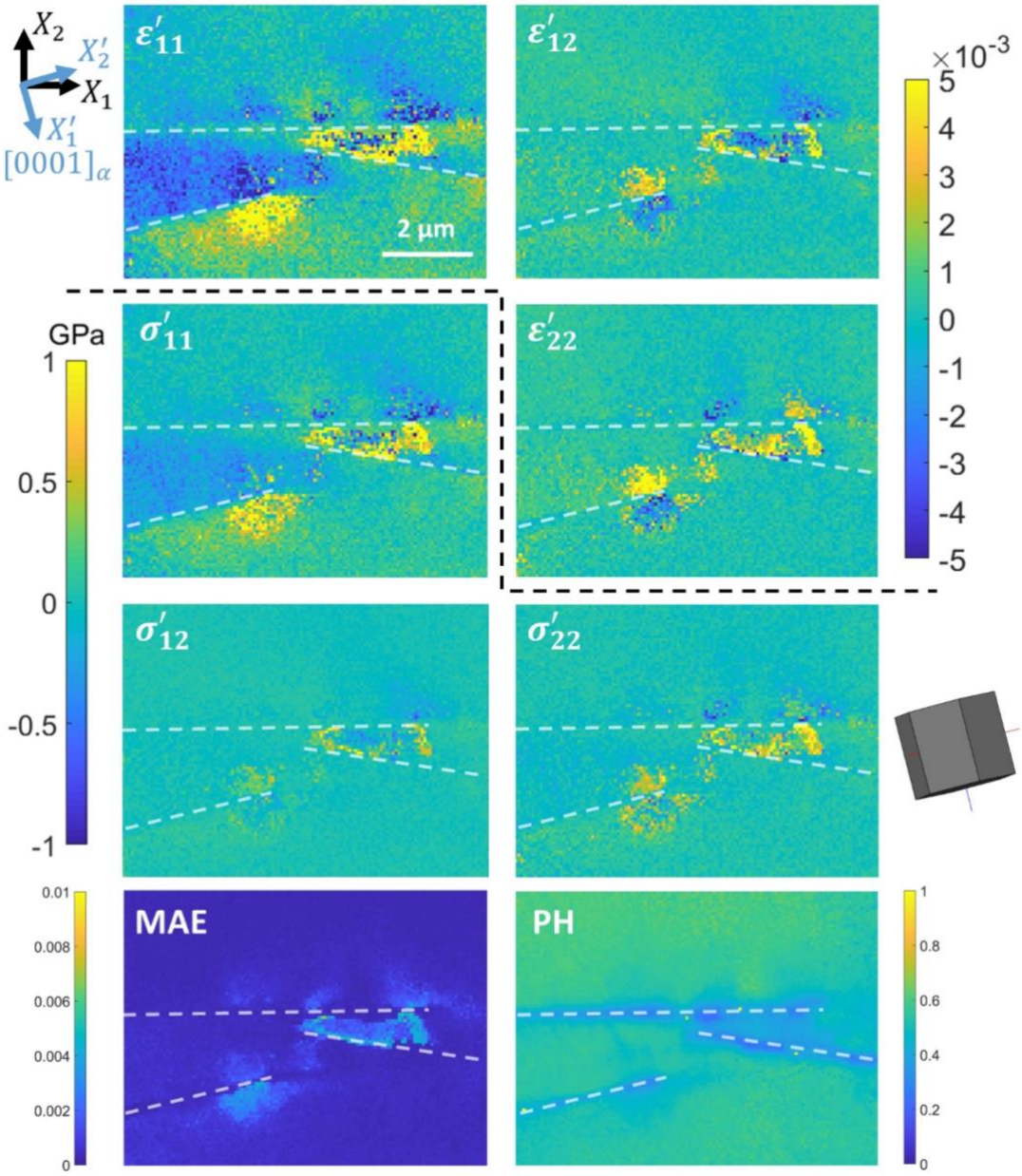

Figure 5.18 In-plane elastic strain (ε_{ij}) and stress (σ_{ij}) tensor components, mean angular error (MAE) map and peak height map (PH) of the three hydride stacks in the parent grain α_1 after a clockwise rotation of 74.56˚from the microscopy reference frame to make X_1 direction parallel to the projection of $[0001]_\alpha$ on the sample surface. Note the positions of the hydrides are shown by white dashed lines. The points with MAE>0.004 or PH<0.2 are filtered.

The in-plane stress and lattice strain components shown in Figure 5.18 indicate that the strain and stress field induced by intra-granular δ-hydride formation are inhomogeneous. Although all six strain/stress components were successfully derived via HR-EBSD calculation, only the in-plane components are discussed in the following work in this chapter, considering that EBSD is a 2D characterization method. As discussed in section 5.3.1.2, the change in the

stacking sequence of atom layers from HCP to FCC during α-Zr to δ-hydride phase transformation is supposed to be achieved by the generation and glide of $\frac{a}{3}\langle 1\bar{1}00\rangle$ partial dislocations on alternate basal planes[185][186]. This generates shear on basal planes, especially along $\langle 1\bar{1}00\rangle$ directions. In this case, the basal plane of the parent grain α_1 is nearly perpendicular to the sample surface. The in-plane strain components were transformed from the original microscopy reference frame to a new frame with X_1' along the projection of the c-axis $[0001]_\alpha$ on the measured surface. This required a rotation by 74.5˚ about the surface normal X_3. In the new reference frame, the in-plane shear components ε_{12}' and σ_{12}' describe the shear strain and stress on the basal plane of the parent grain α_1.

Different from the GND density measured by HR-EBSD analysis, the measured elastic strain and stress components are with respect to the reference point in each grain. In the δ-hydrides successfully identified by EBSD indexing, all the in-plane elastic strain and stress components are relatively low, which may be attributed to their small size. In the parent grain α_1, the selected reference point is quite far from the δ-hydrides and shown by a black spot in Figure 5.16 (a). Similar to GND density, localization of elastic strain and stress are found on the two sides of the hydride tips (e.g., δ_1) and between two δ-hydride stacks close together (e.g., δ_2 and δ_3) for each component. Generally, the distribution patterns are almost the same for the strain and stress components with the same subscripts. As discussed in 5.1.3.1, we expect a larger transformation strain of 7.2% along c-axis, compared to that along a-axis (4.6%). Larger compression stress-strain seen for ε_{11}' in matrix fits this idea. Furthermore, in zirconium, plastic accommodation through movement of <a> type dislocations is easier and could relief σ_{22}' and σ_{12}' stresses. But σ_{11}' would need a component of burger vector along c-axis (i.e., <c+a> dislocations) which are more difficult to activate. Again, seems consistent with observed higher ε_{11}' and σ_{11}'. The ε_{11}' and σ_{11}' are seen to be compressive between δ_1 and δ_2 but tensile below

δ_1. The ε'_{22} and ε'_{12} are localized in much smaller regions on the two sides of the tip of δ_1 and reverse across the hydride. In the region between δ_2 and δ_3, compressive strains are only found in a limited region below δ_2 for ε'_{11} and ε'_{12} and the others are tensile strains. Above the tip of δ_2, similar strain localization to that above δ_1 is observed, where ε'_{11} and ε'_{12} are seen to be compressive and ε_{22} is tensile. It is noted that the tensile shear stress above the tip of δ_1 is generally larger than the compress shear stress underneath it for σ'_{12}.

5.2.2.4 Discussion

All the intra-granular δ-hydride stacks studied by conventional and high resolution EBSD analysis follow the orientation relationship of $\{0001\}_\alpha||\{111\}_\delta\ \langle 11\bar{2}0\rangle_\alpha||\langle 110\rangle_\delta$ with their parent grain and two twin-related orientation variants are observed. Several potential habit planes are found for the precipitation of δ-hydride stacks inside a grain, including$\{0001\}$, $\{10\bar{1}1\}$, $\{10\bar{1}2\}$ and $\{10\bar{1}7\}$, which are consistent with the findings reported in the literature[186][187][74][102]. Liu's work found numerous habit planes of δ-hydrides within 0-25˚ and 70-90˚ off the basal plane of the parent α-Zr grain by using TEM[188]. Different potential habit planes are found for intra-granular δ-hydride stacks sharing one variant and the intra-granular δ-hydride stacks with twin-related variants are able to have the same potential habit planes. These imply that there is no clear correlation between the potential habit planes and orientation variants for intra-granular δ-hydrides. In addition, serial sectioning and imaging could be combined with pre-EBSD scan of the target parent grain on the top surface to further identify the habit planes of δ-hydrides in 3D.

Although the intra-granular δ-hydride stacks have two twin-related variants, the small δ-hydride plates composing an intra-granular δ-hydride stack only share one orientation variant for air cooled down samples. It could be explained by the GND density and in-plane shear stress (σ'_{12}) field surrounding the tip of δ_1 obtained in HR-EBSD analysis to some extent, as

shown in Figure 5.17 (c) and Figure 5.18. Dislocations are preferential sites for hydrogen dissolved in the matrix. The higher GND density above the tip of δ_1 could lead to a higher hydrogen concentration than that under the tip of δ_1, which increases the potential for the precipitation of a new small δ-hydride plate above the tip of δ_1. Furthermore, the sign of the σ'_{12} above the tip of δ_1 is opposite to that under it. As shown by the discussion about the formation of two twin-related variants during α-Zr to δ-hydride transformation in section 5.1.3.2, their motions of Zr atoms along $\langle 1\bar{1}00 \rangle$ directions are opposite. The opposite σ'_{12} above and under the tip of δ_1 may drive the formation of different variants. However, the absolute values of the σ'_{12} above the tip of δ_1 is generally larger than that under the tip, giving larger driving force for the formation of the corresponding variant above the tip. Therefore, it is supposed that a new small δ-hydride plate is likely to precipitate with a specific orientation variant above the tip of δ_1.

5.2.3 Inter-granular δ-hydrides

Different from intra-granular δ-hydrides, the inter-granular δ-hydrides formed at the same cooling rate are much thicker and their morphologies are more various and complex. HR-EBSD analysis is conducted on the several inter-granular δ-hydrides with different morphologies at cooling rates of air cool down and 3˚C/min to study the precipitation characteristics of inter-granular δ-hydrides and the local deformation induce by them.

5.2.3.1 Air cool down

5.2.3.1.1 Type-a

The inter-granular δ-hydrides of type-a are along the grain boundaries and will be presented by two examples with the cooling rate of air cool down from sample-A and -B respectively.

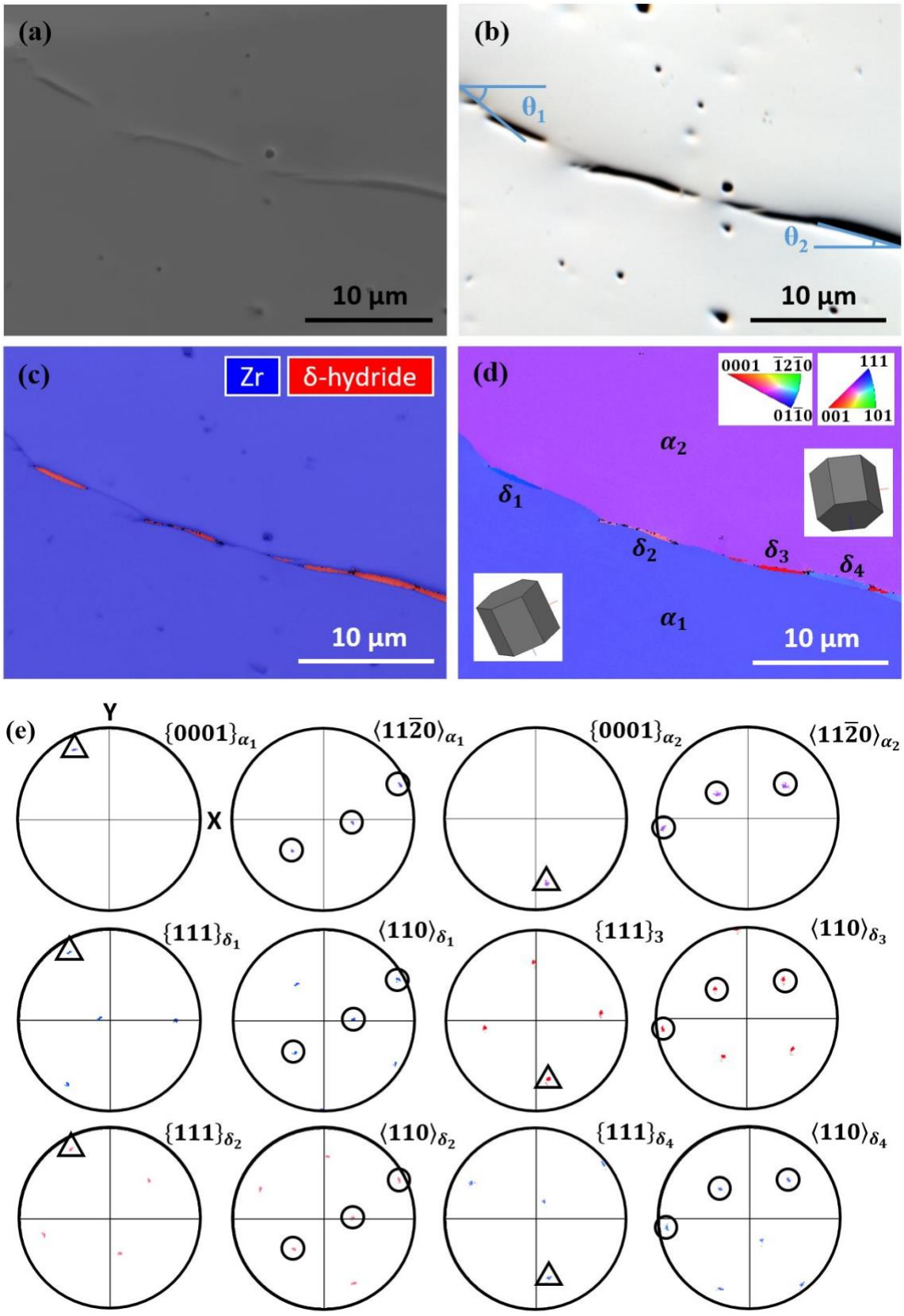

Figure 5.19 (a) Secondary electron (SE2) image, (b) forescattered electron image, (c) phase map overlaid with the pattern quality map, (d) IPFZ map and (d) pole figures of the local area including the δ-hydrides along different sides of one grain boundary in pure zirconium. Pattern resolution: 800×600 Step size: 85 nm. θ_1 and θ_2 are the tilted angle of the grain boundary from the horizontal line on left and right respectively. θ_1 is ~ 40˚ and θ_2 is ~ 16˚.

As shown in Figure 5.19, the δ-hydrides on the grain boundary between α_1 and α_2 are obviously thicker than the intra-granular δ-hydrides discussed in the last section. The maximum thickness reaches almost ~1 μm. The misorientation angle between α_1 and α_2 was measured to be about 48.5˚but the boundary plane varies as the boundary curves across the map. Four orientations of the δ-hydrides are found in the crystal orientation map (Figure 5.19 (d)) and named as δ_1, δ_2, δ_3 and δ_4 from left to right. $\delta_1$and δ_2 appear in two separated hydride packets and the hydride packet of δ_2 has a small tail into α_1. Three small hydride packets share the orientation of δ_3 : the left one has a tail into α_2, the middle one is nearly connected with the hydride packet of δ_4 and the right one is embedded in the hydride packet of δ_4.

The orientation relationship between the δ-hydrides and α-Zr matrix is analyzed by the pole figures in Figure 5.19 (e). δ_1 and δ_2 follow the common orientation relationship of $\{0001\}_\alpha||\{111\}_\delta\ \langle 11\bar{2}0\rangle_\alpha||\langle 110\rangle_\delta$ (OR1) with α_1, while the δ_3 and δ_4 follow the same orientation relationship with α_2. It means that $\delta_1$and δ_2 precipitated from α_1, whereas δ_3 and δ_4 originated from α_2. The side from which the δ-hydrides precipitate on a grain boundary also depends on the spatial relationship between the grain boundary and orientation of the two neighboring α-Zr grains. The average deviation angle of them is ~6.12˚, much larger than that of intra-granular hydrides studied in 5.2.2. It may be attributed to their much larger thickness and the influence of the grain boundary. Meanwhile, $\delta_1$and δ_2 , as well as δ_3 and δ_4, are also consistent with $\{111\}\langle 11\bar{2}\rangle$ twin relationship. The difference is that the two well separated hydride packets of $\delta_1$and δ_2 are supposed to nucleate on the grain boundary independently and the small hydride packet of δ_3 embedded in that of δ_4 may originate from δ_4 by twining.

The results of corresponding HR-EBSD analysis are shown in Figure 5.20. In the GND density map, several spots with high values are found in the matrix grains. Nearly all of them are located at pits induced by electropolishing and supposed to be caused by the lower pattern

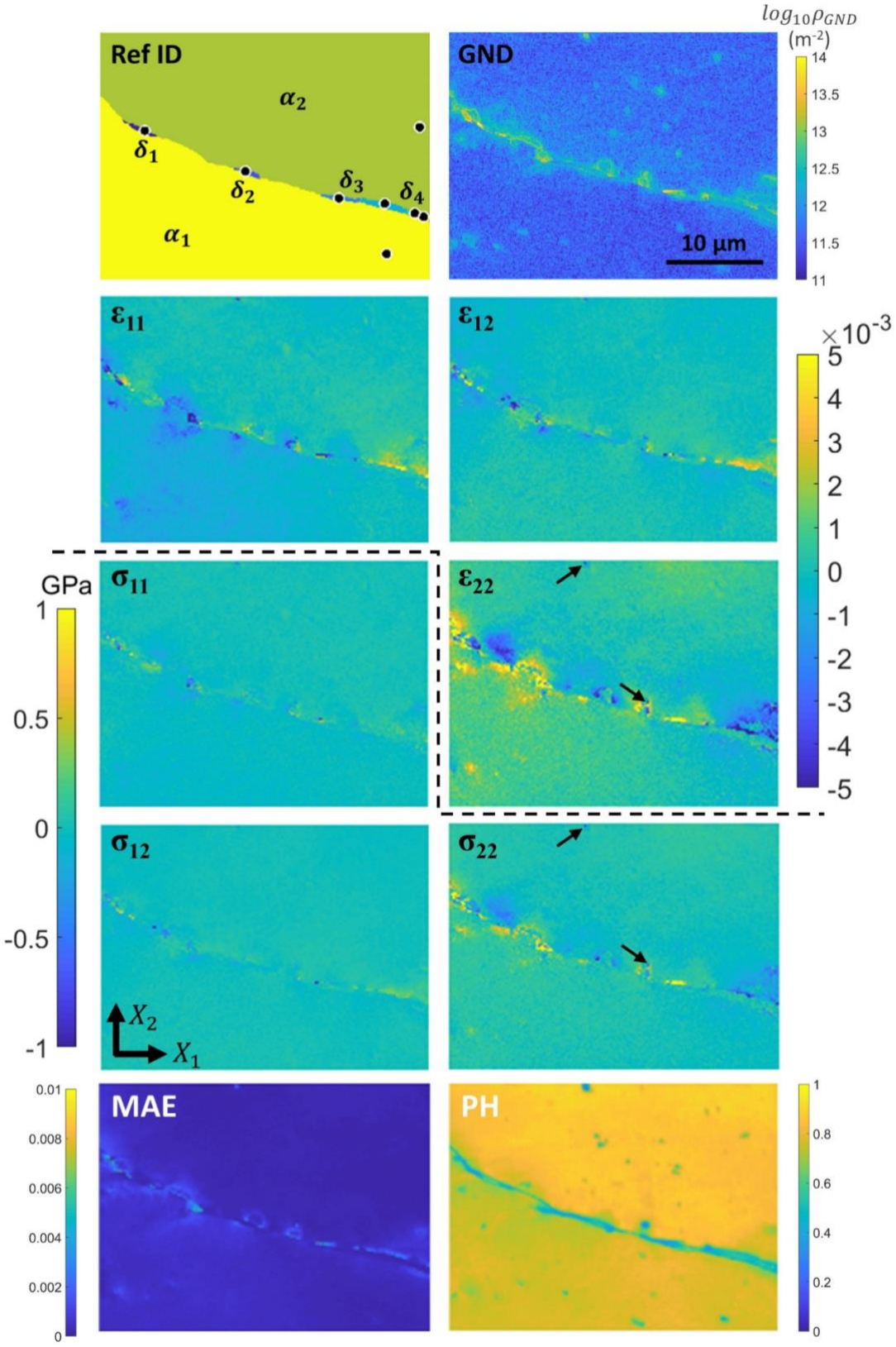

Figure 5.20 Maps of Ref ID where reference points for each grain are marked by black spots, GND density, In-plane elastic strain (ε_{ij}) and stress (σ_{ij}) tensor components, mean angular error (MAE) and peak height (PH) of the local area including the δ-hydrides along different sides of one grain boundary in pure zirconium. Pattern resolution: 800×600 Step size: 85 nm. The points with MAE>0.004 or PH<0.2 are filtered.

quality and inaccurate pattern indexing due to the pits. For the elastic strain and stress maps, the influence of pits is reduced. Only the relatively deep pits lead to apparent high compressive elastic strain and stress, as pointed by black arrows in the ε_{22} and σ_{22} maps.

Generally, the GND density in the matrix grains is no more than ~1.4×10^{12} m^{-2} when the influence of pits is not taken into account. Inside the δ-hydrides along the grain boundary, the GND density is higher, especially at the two tips of the hydride packet of δ_1 with the values of nearly ~1.0×10^{14} m^{-2}. Surrounding these inter-granular δ-hydrides, the relatively high GND density is found beside hydride tips, between the hydride tail and grain boundary and between two hydrides close to each other. The hydride packets of $\delta_1$and δ_2 induces GND density within both α_1 and α_2. A tiny hydride in front of the left tip of hydride packet of δ_1 was not distinguished from α_1 by EBSD indexing. Nonetheless, high GND density is still found between it and δ_1, especially on the side of α_1. Between the hydride packets of $\delta_1$and δ_2, higher GND densities were induced on the side of α_2. For the hydride packet of δ_2, relatively high GND density appears between its tail and grain boundary in α_1. One potential cause may be that the grain boundary blocks the movement of dislocations. Around the right tip of δ_2, GNDs were mainly formed on the side of α_2. The hydride packets of δ_3 and δ_4 induces GND density formation mainly in α_2. The dislocations induced by the tail of δ_3 are like that of δ_2 but in smaller areas. Another high spot of GND density is between $\delta_3$and δ_4. Slightly lower GND density is observed beside the hydride packet of δ_3 embedded in that of δ_3, which indicates that the twinning in δ-hydrides may slightly reduce the GND formation surrounding. In addition, most of the local areas with higher GND density surrounding the inter-granular hydrides show a dislocation loop-like shape.

Like the intra-granular hydrides discussed in the last part, nearly no obvious in-plane elastic strain and stress are found inside δ-hydrides along α_1/α_2 grain boundary, except the two tips of

the hydride packet of δ_1. The distribution of the strain and stress is generally consistent with the distribution of GND density. Meanwhile, the distribution patterns are almost the same for the strain and stress components with the same subscripts and will be described by taking strain components as an example. The ε_{22} is larger than ε_{11} and ε_{12} but the points with compressive ε_{22} usually show tensile for ε_{11} and ε_{12}.

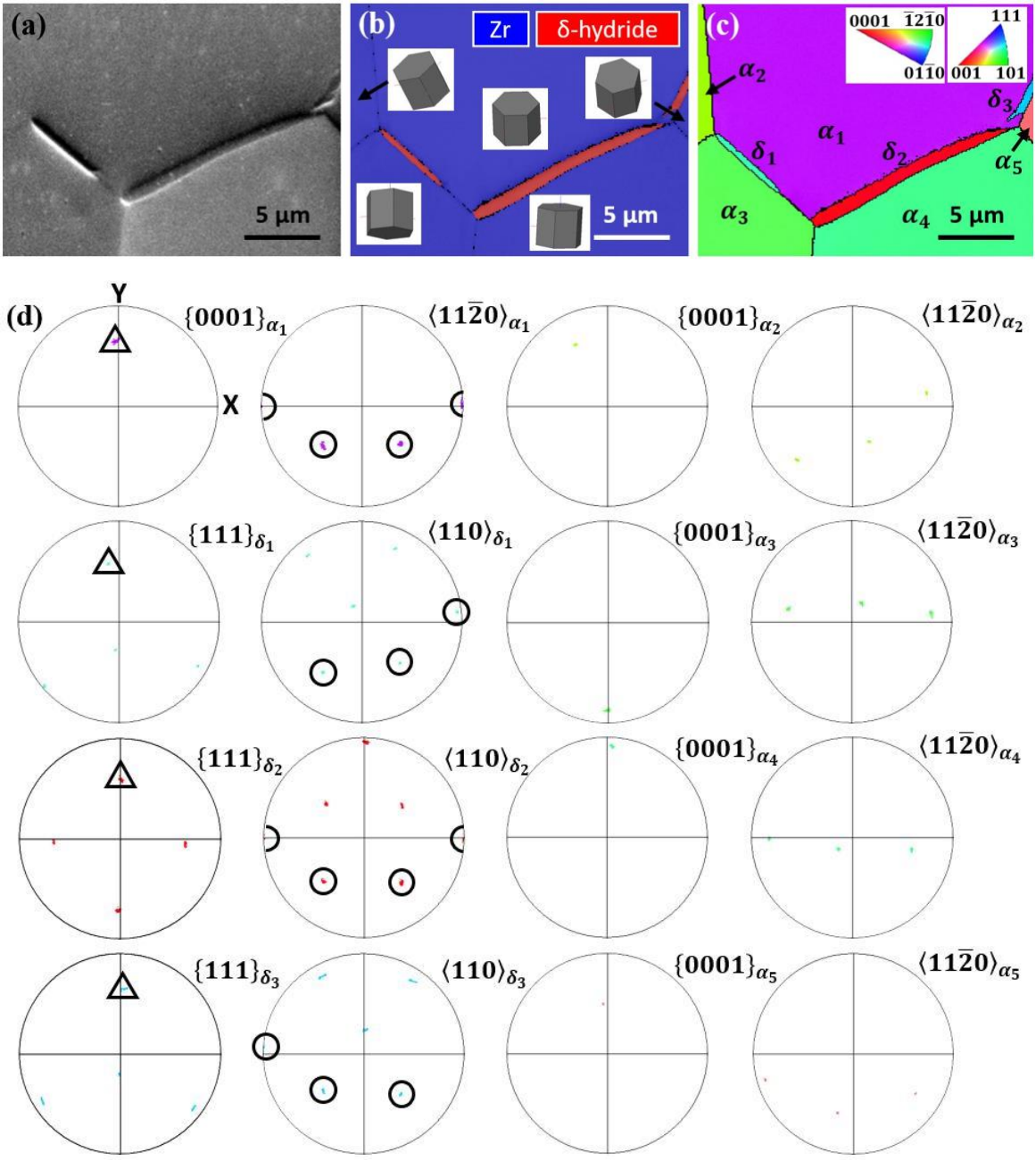

Figure 5.21 (a) Secondary electron image (SE2), (b) phase map overlaid with the pattern quality map, (c) IPFZ map and (d) pole figures of the local area including the δ-hydrides along three different boundaries of a parent grain in pure zirconium. Pattern resolution: 1600×1200 Step size: 100 nm.

Table 5.3 Summary of misorientation angles of α-Zr grain boundaries in Figure 5.21 and Figure 5.23.

Gran Boundary	α_1/α_2	α_1/α_3	α_1/α_4	α_1/α_5	α_2/α_3	α_3/α_4	α_4/α_5
Misorientation Angle (˚)	26.1	54.6	32.1	23.8	54.4	31.2	40.7

The morphology and crystal orientation of the other example where the δ-hydrides form on three different boundaries of a parent grain is shown in Figure 5.21. There are five α-Zr grains in the local area and the misorientation angles of their grain boundaries are summarized in Table 5.3. Three δ-hydride packets are found along the grain boundaries of α_1/α_3, α_1/α_4 and α_1/α_5 respectively. Among them, δ_3 has an obvious small tail into α_1. In addition, δ-hydrides with different morphology are found on the grain boundary of α_2/α_3 and will be discussed in the next part. Theoretically, the grain boundaries with higher misorientation always have higher energy and thus become preferential site for the nucleation of hydrides[189]. However, not all the grain boundaries with δ-hydrides have the highest misorientation angles in the local area studied. The α_1/α_5 with hydrides has a slightly lower misorientation angle than α_1/α_2 without hydrides. However, the direction of α_1/α_2 grain boundary is quite close to the prismatic planes of α_1 and α_2, while the direction of α_1/α_5 grain boundary is much closer to the basal planes of α_1 and α_5. Similarly, no hydrides are found on the α_3/α_4 grain boundary which has almost the same misorientation angle to α_1/α_4 but a direction nearly parallel to the prismatic planes of the bounding grains. For α_4/α_5 with the third high misorientation angle of 40.7˚, its direction is not close to either basal or prismatic planes of the bounding grains. Therefore, the nucleation of δ-hydrides on grain boundaries is determined by various factors, including misorientaion, direction and orientations of the bounding grains.

The pole figures of the inter-granular δ-hydrides and α-Zr in Figure 5.21 (e) show that δ_1, δ_2 and δ_3 follow the most common orientation relationship of $\{0001\}_\alpha||\{111\}_\delta$ $\langle 11\bar{2}0\rangle_\alpha||\langle 110\rangle_\delta$ with α_1 and are supposed to precipitate from α_1. The average deviation angles

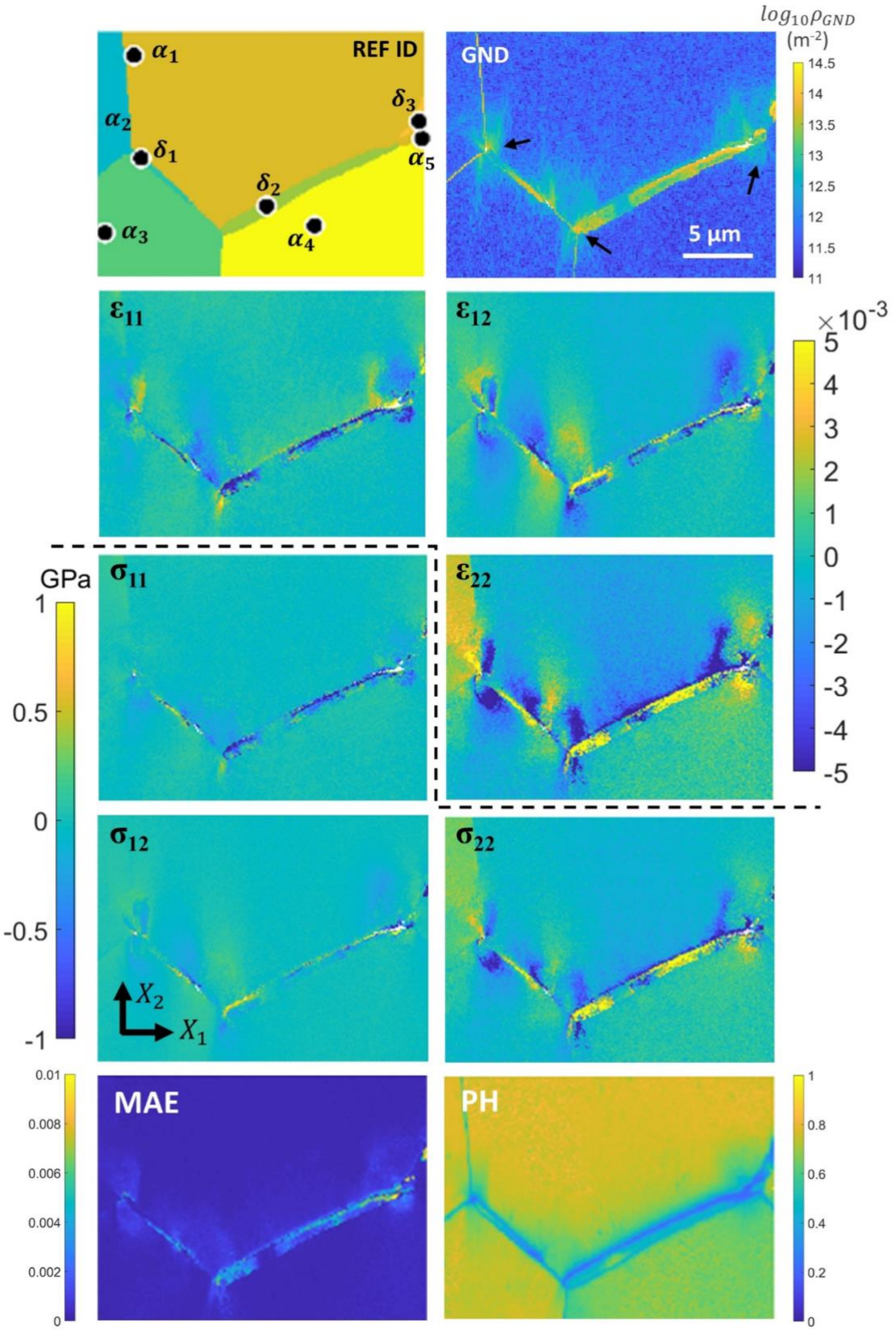

Figure 5.22 Maps of Ref ID where reference points for each grain are marked by black spots, GND density, In-plane elastic strain (ε_{ij}) and stress (σ_{ij}) tensor components, mean angular error (MAE) and peak height (PH) of the local area including the δ-hydrides along three different boundaries of a parent grain in pure zirconium. Note the reference point for α_2 is out of the maps here. Pattern resolution: 1600×1200 Step size: 100 nm. The points with MAE>0.004 or PH<0.2 are filtered.

of them are 8.27˚, 6.48˚ and 4.54˚ respectively, much larger than those of intra-granular hydrides. δ_1 and δ_3 could be regarded as one orientation variant of the δ-hydrides originating from α_I, but their poles of $\{111\}$ planes deviated from the poles of the basal plane of α_I to different direction. The misorientation angle between δ_1 and δ_3 is 13˚ approximately. δ_2 is the twin-related variant for δ_1 and δ_3. The misorientation inside α_I is much lower than the deviation angles above. Meanwhile, the phase interface of the tail of δ_3 into α_I shows lower deviation angles than the other part along the grain boundary. It indicates that the larger deviation from the common orientation relationship may be caused by grain boundaries and the larger misorientation of the grain boundaries is likely to lead to larger deviation.

Figure 5.22 shows the HR-EBSD results of the local area shown Figure 5.21. Generally, the GND density inside the inter-granular δ-hydrides are much higher than that in the α-Zr grains but not uniform. Relatively high GND density is found in the right half of δ_1. More GNDs appear at the end touching the triple junction of grain boundaries and the side of α_I in the δ_2. In δ_3, the small tail and part of body at right show significantly high GND density. Meanwhile, high GND density is found in the area with sunburst appearance surrounding triple junctions of grain boundaries and the right end of δ_1 in the matrix. There are thin layers of slightly higher GND density beside the main body of these inter-granular δ-hydrides in α_I. The distribution of the strain and stress is generally consistent with the distribution of GNDs whether in matrix or hydrides. Meanwhile, the distribution patterns are almost the same for the strain and stress components with the same subscripts.

5.2.3.1.2 Type-b

The inter-granular δ-hydrides of type-b nucleated on grain boundaries and grew into the parent grain interior in the form of large tails extending into the parent grain, blocks aligned with the grain boundary or thin line segments. Three examples will be presented in this section.

The first example includes all three morphologies of type-b, as shown in Figure 5.23. δ_4 and δ_6 are in the shape of large tails extending into α_3 with a specific angle to the grain boundary and share one orientation. The detailed morphology in the SE2 image (Figure 5.23 (b)) shows

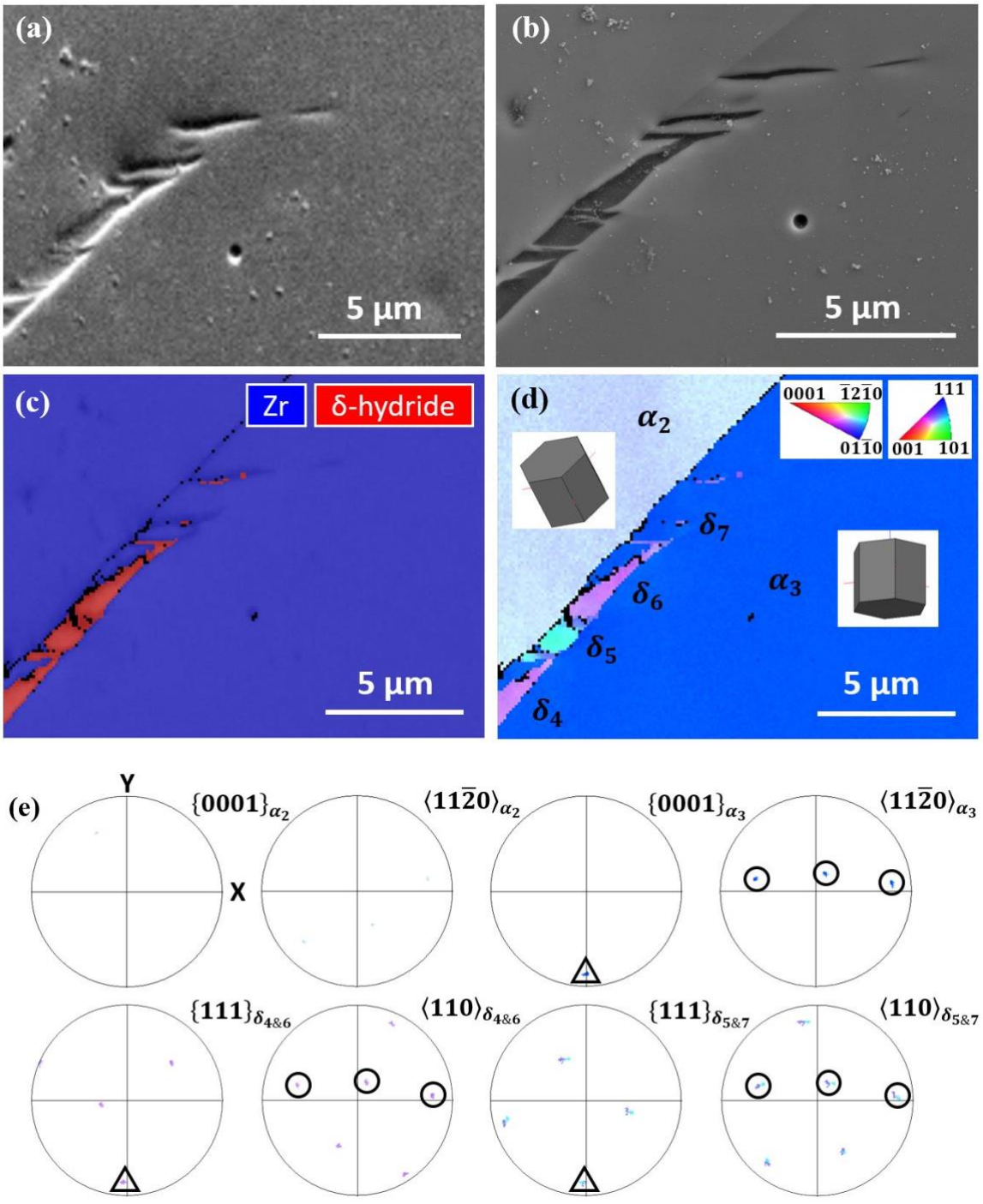

Figure 5.23 (a) Forescattered electron image and (b) secondary electron (SE2) image, (c) phase map overlaid with the pattern quality map, (d) IPFX map and (e) pole figures of the local area including the δ-hydrides nucleated on the grain boundary and grow into their parent grain in the form of large tails, blocks or flacks aligned with the grain boundary in pure zirconium. Pattern resolution: 1600×1200 Step size: 100 nm.

that δ_5 consists of three smaller hydride blocks on the side of α_3, which are parallel to each other and aligned with α_2/α_3 grain boundary. Only one of four hydride line segments like intra-granular hydrides on the top was successfully distinguished from the α_3, which is named as δ_7. Although the colours of δ_5 and δ_7 looks different in the IPFX map, they are still supposed to have the same orientation according to the pole figures (Figure 5.23 (e)). These two observed orientations of δ-hydrides follow the common orientation relationship of $\{0001\}_\alpha||\{111\}_\delta$ $\langle 11\bar{2}0\rangle_\alpha||\langle 110\rangle_\delta$ with α_3 and thus all the δ-hydrides on the α_2/α_3 grain boundary are supposed to transform from α_3. The average deviation angle is 3.21˚, which is larger than that of intra-granular δ-hydrides but smaller than that of type-a inter-granular δ-hydrides. Meanwhile, the relationship between these two orientation variants is consistent with the twin relationship of $\{111\}\langle 11\bar{2}\rangle$. Nonetheless, δ_5 and δ_6 are not connected with each other.

The distributions of GNDs, in-plane strain and stress in the local area including the type-b inter-granular δ-hydrides with three morphologies are presented by Figure 5.24. The density of GNDs in the hydrides is generally higher than that in the α-Zr matrix. δ_5 shows a GND density at the same level of that in δ_6, lower than that in δ_4. It implies that the GNDs caused by the transformation strain in δ-hydrides can be reduced when two variants appear as neighbours. The highest GND density is found at the tip of δ_4. GNDs are also induced along both sides of the δ-hydrides in α_2 and α_3 and between the hydride flakes on the top. The distributions of GNDs surrounding the hydrides are not uniform and vary with the morphologies of the hydrides. Different from GNDs, nearly no strain or stress is found inside the hydrides presumably due to their small size. The distribution patterns of in-plane strain and stress with the same subscripts surrounding the hydrides are almost the same and consistent with the GND map in general. More significant concentrations of in-plane strain and stress are observed between the grain boundary and the roots of the hydride line segments on the top. Furthermore, strain and stress are distributed over a slightly larger area on the side of α_3 than α_2.

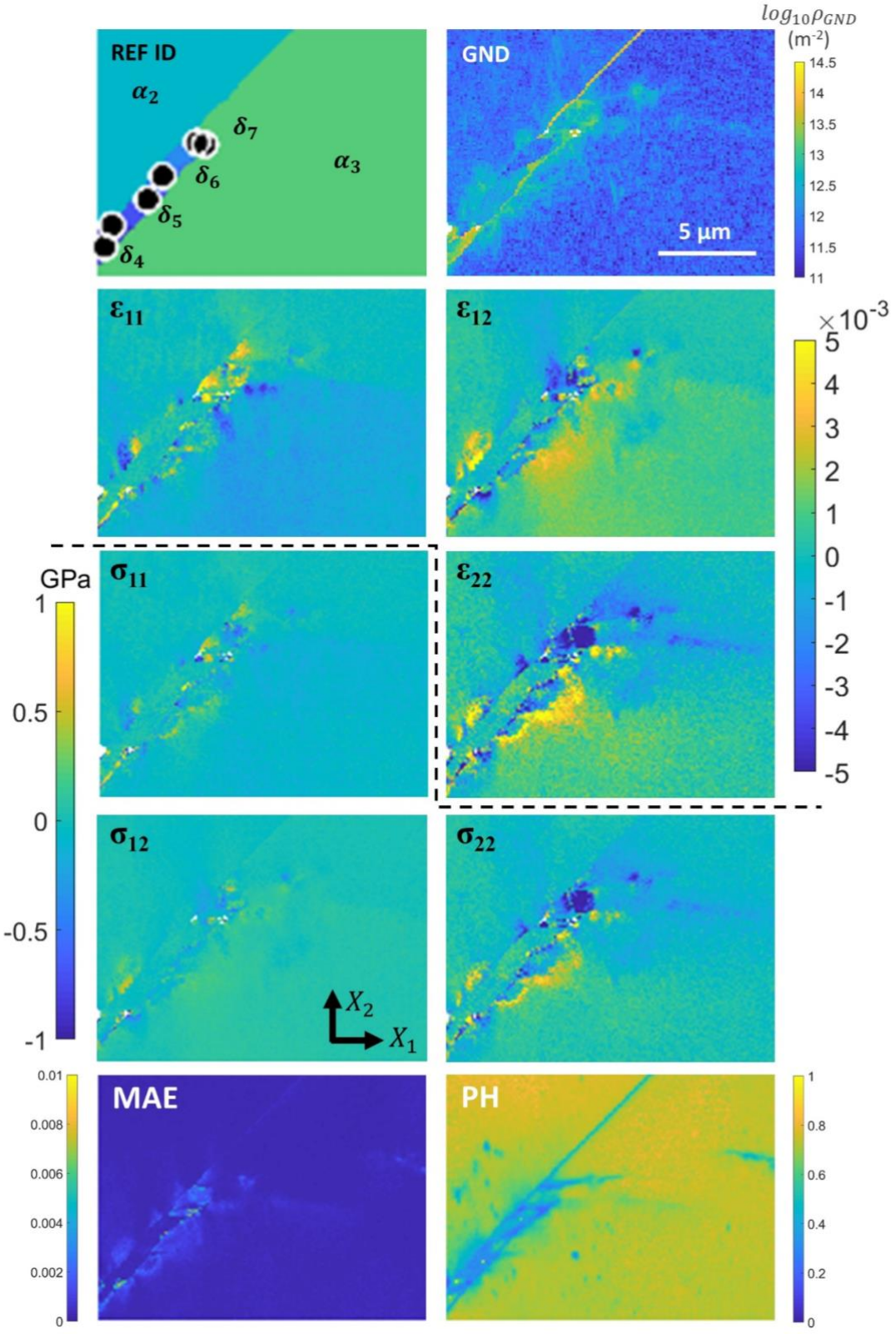

Figure 5.24 Maps of Ref ID where reference points for each grain are marked by black spots (the auto-selected reference points are out of the map shown here and far away from hydrides), GND density, In-plane elastic strain (ε_{ij}) and stress (σ_{ij}) tensor components, mean angular error (MAE) and peak height (PH) of the local area including the δ-hydrides nucleated on the grain boundary and grow into their parent grain in the form of large tails, blocks or flacks aligned with the grain boundary in pure zirconium. The points with MAE>0.004 or PH<0.2 are filtered. Pattern resolution: 1600×1200 Step size: 100 nm.

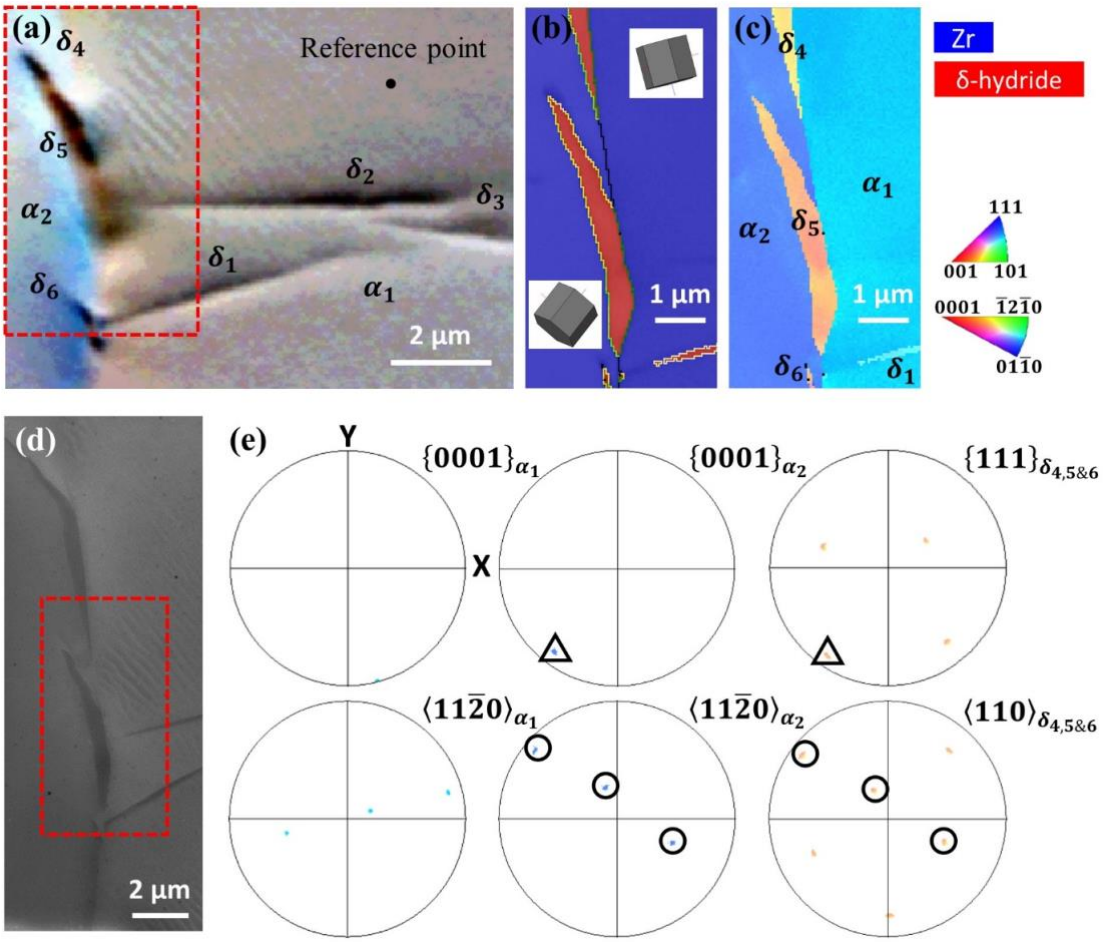

Figure 5.25 (a) Forescattered electron image of the region including both intra- and inter-granular hydrides for HR-EBSD analysis. The inter-granular hydrides in the red dashed rectangle are discussed in this section. (b) Phase map overlaid with the pattern quality map where grain boundaries (>10˚) are shown by black lines and the phase interfaces between δ-hydrides and α-Zr are shown by lines in different colour (white ≤ 3˚ < yellow ≤ 6˚ < lime green ≤ 9˚ < dark green), (c) IPFX map, (d) Inlens image and (e) pole figures of the local area including the type-b inter-granular δ-hydrides in the shape of large tails. Pattern resolution: 1600×1200. Step size is 50nm.

Another example including the type-b inter-granular δ-hydrides in the form of large tails and thin line segments like intra-granular hydrides is introduced in Figure 5.25. δ_4 and δ_5 are the large tails extending into α_2 and the difference is that an intra-granular hydride precipitated in the front of the tip of δ_4 along its extending direction, as shown in Figure 5.25 (d). The angle between δ_4 and the α_2/α_1 grain boundary is slightly larger than that for δ_5. δ_6 is a tiny hydride on α_2/α_1 grain boundary but shows the similar growing trend to δ_4 and δ_5. It could be regarded as the earlier stage of δ_4 and δ_5. In addition, δ_1 precipitated on α_2/α_1 grain boundary and directly grew into α_1 like intra-granular hydrides. The right segment of δ_1 inside α_1 grain was

studied in 5.2.2.3 and the root segment touching the grain boundary will be discussed in this section, although this segment was not distinguished from the matrix by EBSD. The misorientation angle between α_1 and α_2 is 59.62˚. δ_4 ,δ_5 and δ_6 have the same orientation and follow the commonly observed orientation relationship of $\{0001\}_\alpha||\{111\}_\delta\ \langle 11\bar{2}0\rangle_\alpha||\langle 110\rangle_\delta$

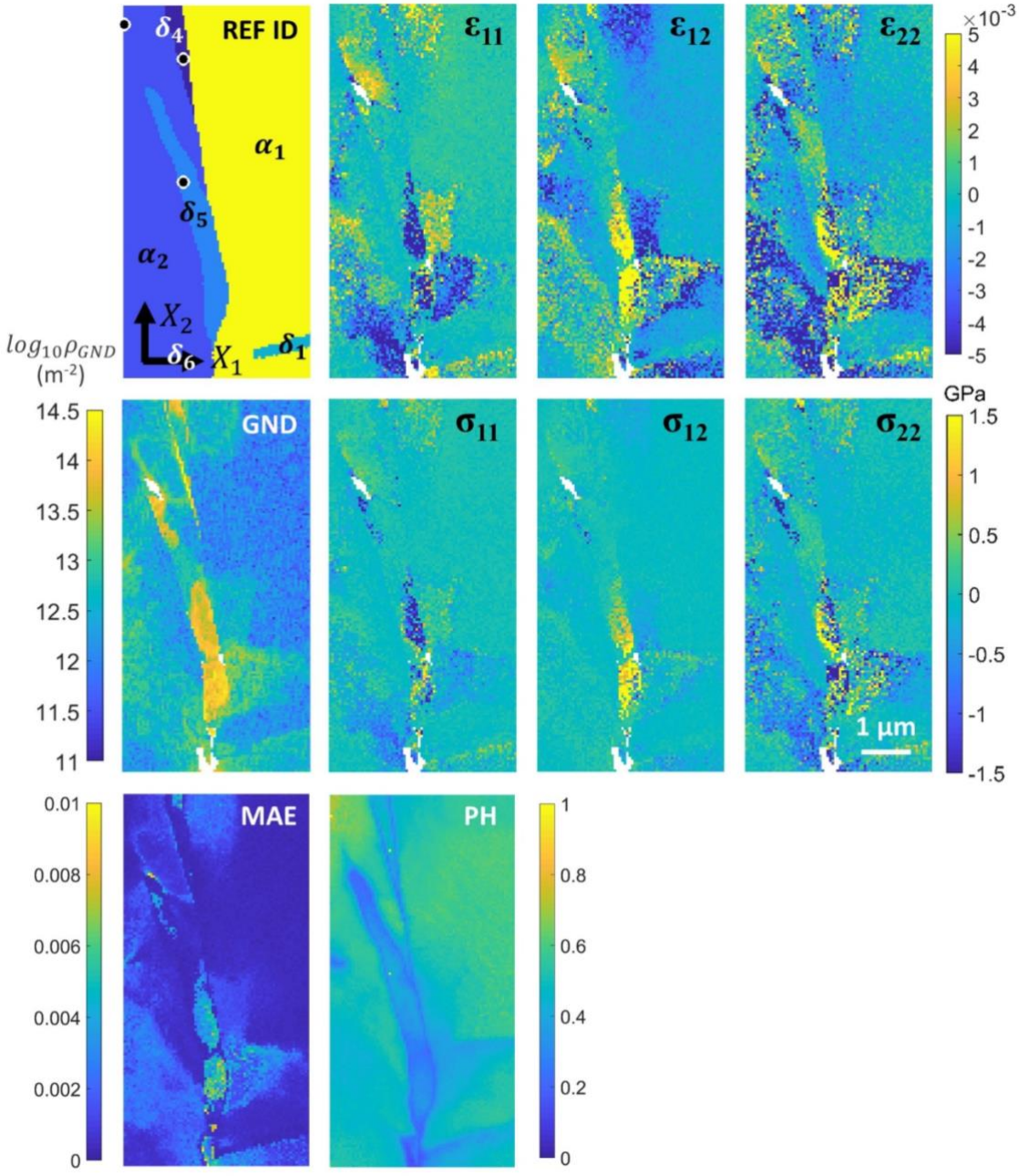

Figure 5.26 Maps of Ref ID where reference points for each grain are marked by black spots, GND density, In-plane elastic strain (ε_{ij}) and stress (σ_{ij}) tensor components, mean angular error (MAE) and peak height (PH) of the local area including the type-b inter-granular δ-hydrides in the shape of large tails in pure zirconium. Pattern resolution: 1600×1200. Step size is 50nm. The points with MAE>0.004 or PH<0.2 are filtered.

with α_2. The average deviation angle is measured to be 3.58˚, slightly larger than the last example including three morphologies of type-b. Meanwhile, the deviation angle for δ_5 gradually decreases from the part along the grain boundary to the tip of the tail, as shown in Figure 5.25 (b).

The HR-EBSD analysis gives the detailed distributions of GND density, in-plane strain and stress in the scanned area, as presented in Figure 5.26. More GNDs are observed inside and surrounding the hydrides. The distributions of GNDs inside δ_4 and δ_5 are not homogeneous. The tip, middle and lower parts of δ_5, as well as the top of δ_4, show the relatively high GND density at the similar level. However, the large MAE values are found at the same parts of δ_4 and δ_5, which is likely to cause some uncertainty of high GND density and strain/stress measured in these parts as well. The middle and lower parts of δ_5 also cause generation of GNDs in the half circle areas along them in α_1. On the side of α_2, slightly high density of GNDs is found surrounding the tips of the tail-shaped hydrides and between them. The density of GNDs inside δ_1 is slightly higher than that in the matrix. The GNDs with the similar density were induce on both sides of the root of δ_1, which may be attributed to the formation of both δ_1 and δ_6. The distributions of in-plane strain and stress agree well with GNDs. The places with higher GND density often show higher strain and stress.

The last example reveals the crystal structures of δ-hydrides penetrate the grain boundary, which is the special case of δ-hydrides nucleating on grain boundary and directly growing into the two neighboring grains simultaneously in the similar morphology of intra-granular δ-hydrides, as shown in Figure 5.27. The misorientation between α_1 and α_2 is 28.3˚ and the angle between their basal plane normals is only 26.6˚. The α_1/α_2 grain boundary looks almost parallel to the basal-plane normal of α_2 and close to that of α_1. It implies the shear on the basal plane may transfer through the grain boundary easily and promote zirconium to δ-hydride phase

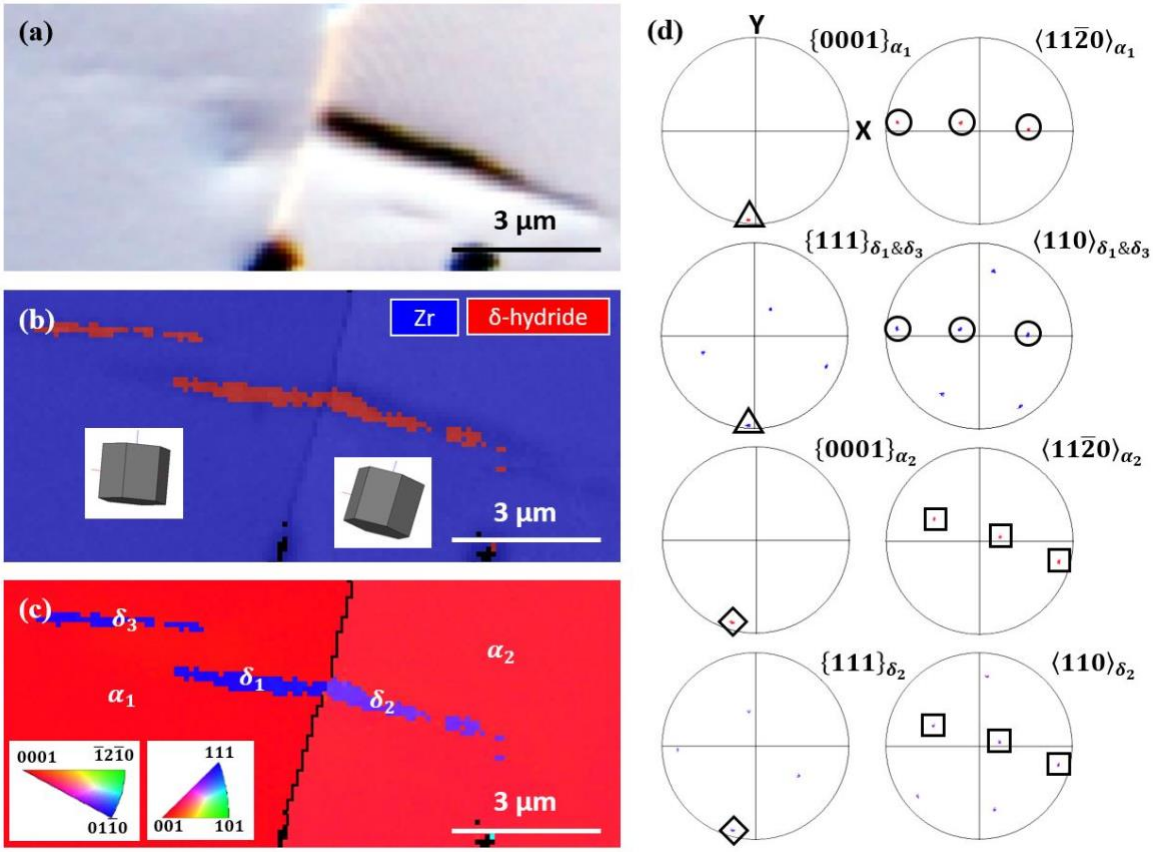

Figure 5.27 (a) Forescattered electron image, (b) phase map overlaid with the pattern quality map, (c) IPFY map and (d) pole figures of the region including the special case of type-b inter-granular δ-hydrides nucleating on grain boundary and directly growing into the two neighboring grains simultaneously in pure zirconium. Pattern resolution: 1600×1200 Step size: 100 nm.

transformation on both sides of the grain boundary. The inter-granular hydride is nearly perpendicular to the α_1/α_2 grain boundary. It is separated into δ_1 and δ_2 by the grain boundary, where they are much thicker than the other tips in α_1 and α_2, as shown by the IPFY map. It suggests that the similar nucleation and growth paths of them are related to the specific grain boundary. δ_3 precipitated on the top side in the front of the tip of δ_1 inside α_1. They have the same orientation, and their habit plane is close to the trace of basal plane of α_1 on the measured surface. Similarly, the habit plane of δ_2 is close to the trace of basal plane of α_2. The orientation relationships between δ_1 and α_1, as well as δ_2 and α_2, satisfy $\{0001\}_\alpha||\{111\}_\delta$ $\langle 11\bar{2}0\rangle_\alpha||\langle 110\rangle_\delta$. It indicates that δ_1 and δ_2 transformed from α_1 and α_2 respectively, which is consistent with their relative locations to the α_1/α_2 grain boundary.

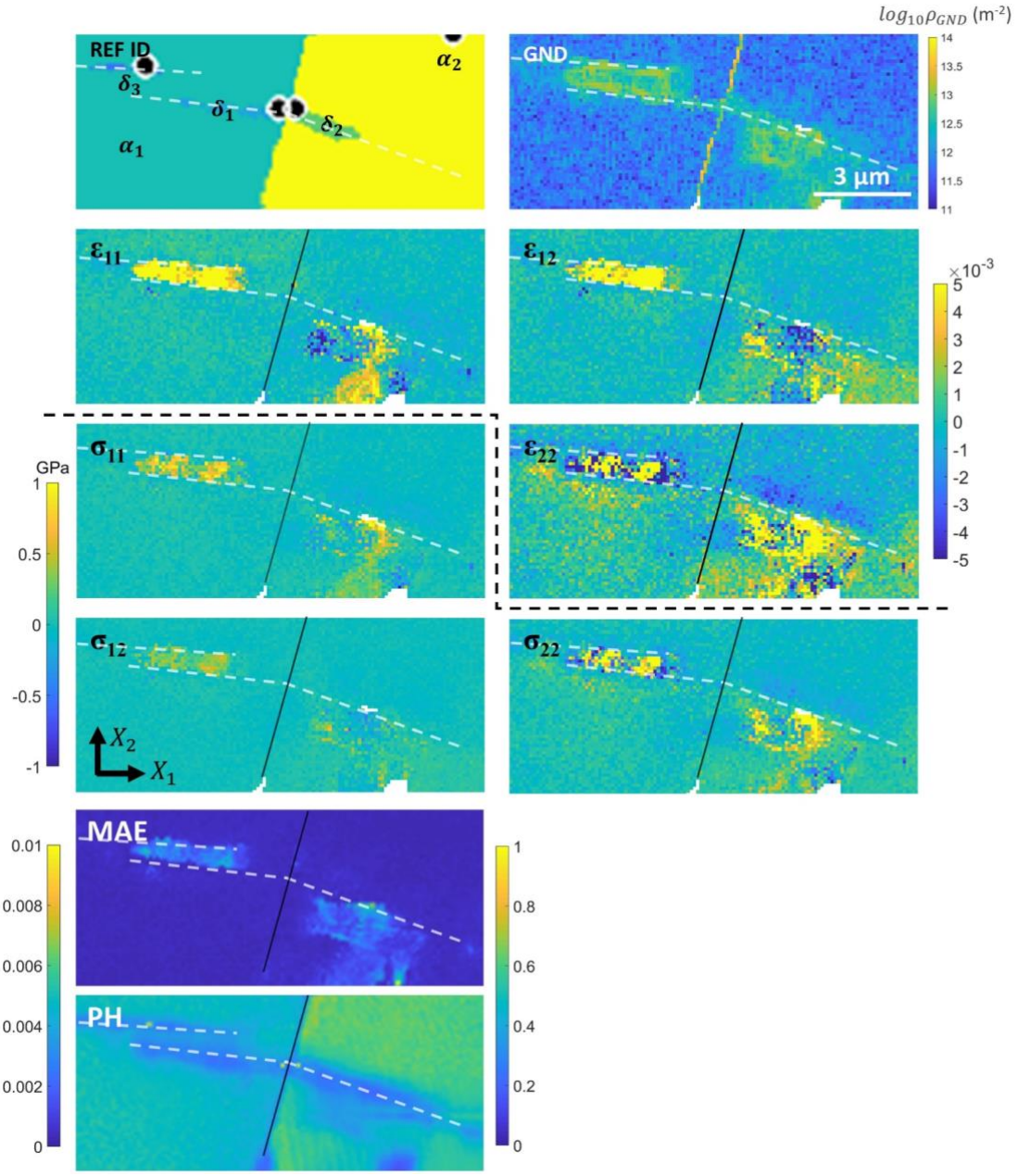

Figure 5.28 Maps of Ref ID where reference points for each grain are marked by black spots (the auto-selected reference points are out of the map and far away from hydrides), GND density, In-plane elastic strain (ε_{ij}) and stress (σ_{ij}) tensor components, mean angular error (MAE) and peak height (PH) of the local area including the special case of type-b inter-granular δ-hydrides nucleating on grain boundary and directly growing into the two neighbouring grains simultaneously in pure zirconium. Pattern resolution: 1600×1200. Step size is 100nm. Note that the positions of hydrides are indicated by white dashed lines and the α_1/α_2 grain boundary is shown by black lines in strain and stress maps. The points with MAE>0.004 or PH<0.2 are filtered.

As shown in Figure 5.28, the distributions of GNDs, in-plane elastic strain and stress in this local area are like those of intra-granular hydrides discussed in the last session, when the influence of the little pits are considered. Localization of higher GND density, strain and stress

is found between hydrides or surrounding their tips. Inside the δ-hydrides, the elastic strain and stress are relatively low, although the GND density is higher than that in the matrix.

5.2.3.2 3˚C/min

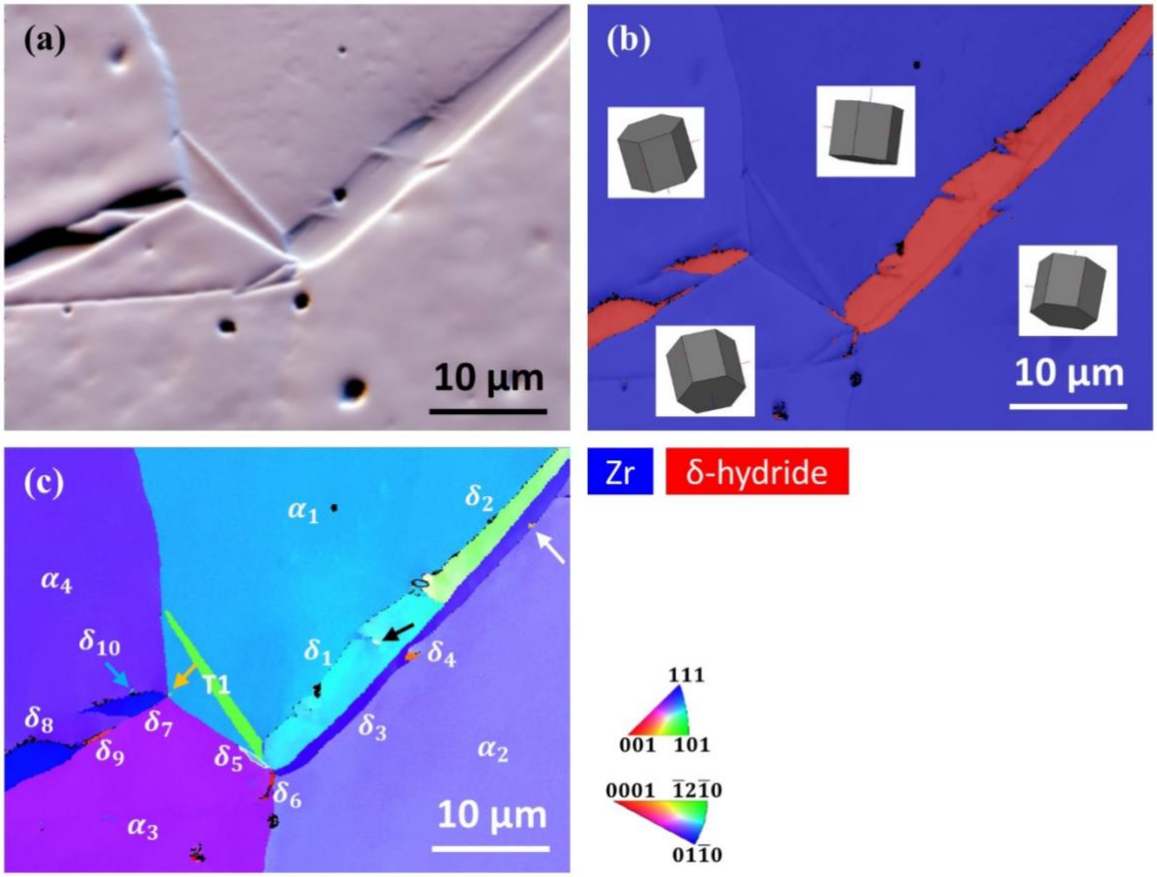

Figure 5.29 (a) Forescattered electron image, (b) phase map overlaid with the pattern quality map, (c) IPFY map of the local region including inter-granular δ-hydrides precipitated at the cooling rate of 3˚C/min in pure zirconium. Pattern resolution: 1600×1200 Step size: 120 nm.

Table 5.4 Summary of misorientation angles of the α-Zr grain boundaries in Figure 5.29.

Gran Boundary	α_1/α_2	α_1/α_3	α_1/α_4	α_2/α_3	α_3/α_4
Misorientation Angle (˚)	25.9	35.9	34.5	25.02	51.66

The inter-granular δ-hydrides precipitated on the two different grain boundaries at the cooling rate of 3˚C/min will be described in this section. As shown in Figure 5.29, they are much thicker than the inter-granular δ-hydrides precipitated during air cool down and show much more

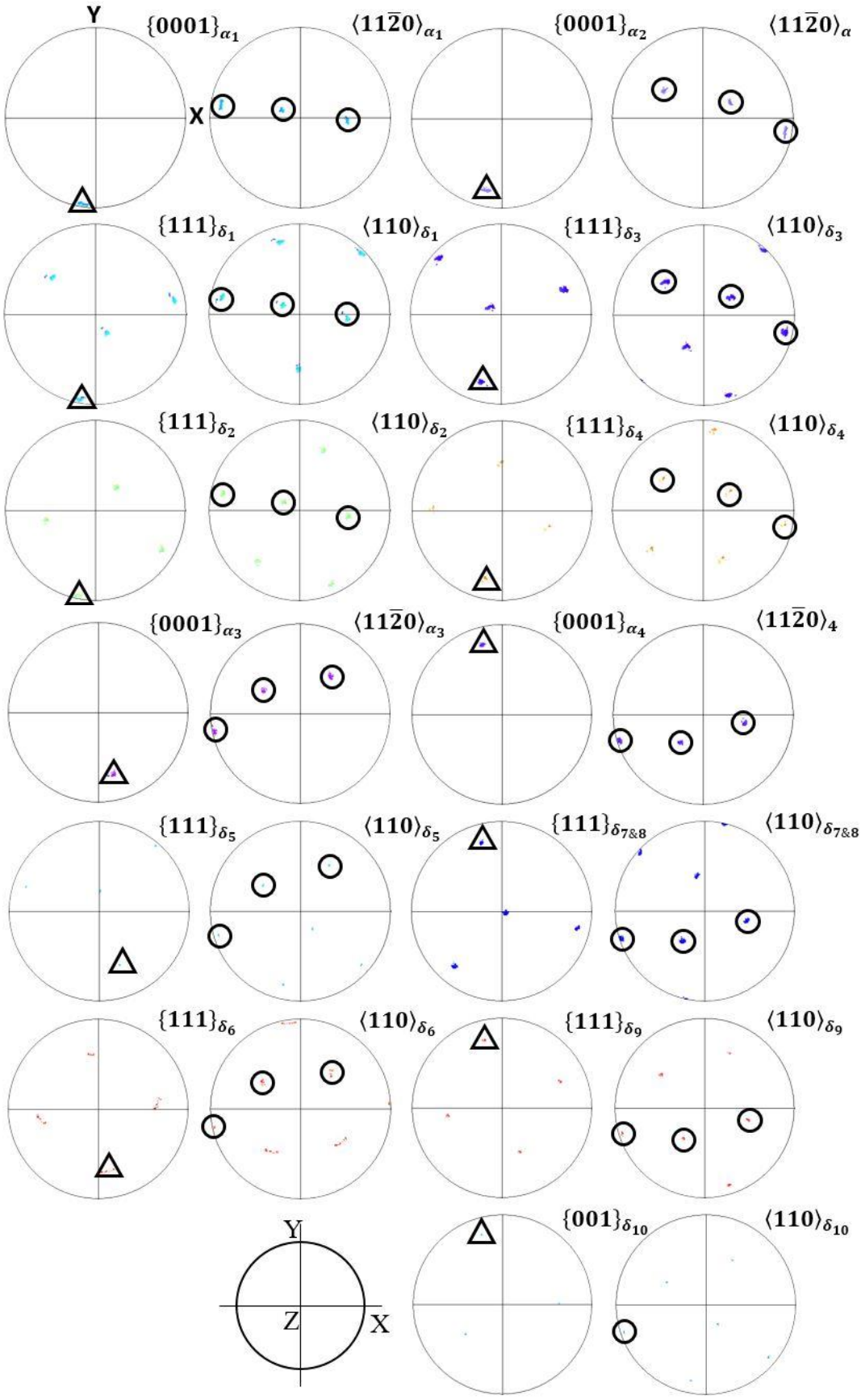

Figure 5.30 Pole figures with respect of the IPFY map of the local region including inter-granular δ-hydrides precipitated at the cooling rate of 3˚C/min in pure zirconium in Figure 5.29.

complicated structures. The detailed orientation relationships of δ-hydride/α-Zr and δ-hydride/δ-hydride are analyzed by the pole figures in Figure 5.30. The misorientation angles of the involved α-Zr grain boundaries are summarized in Table 5.4.

The δ-hydrides precipitated along the two sides of α_1/α_2 grain boundary, as presented by the IPFY map in Figure 5.29. Generally, the δ-hydrides on the side of α_1 is much thicker than those on the side of α_2. On the side of α_1, the large light blue hydride (δ_1) has several small and narrow depressions on the interface with α_1. A small light green hydride is found at the bottom of the one of these depressions, as indicated by the black arrow. Similarly, there is a small light blue hydride (circled by black line) on the interface between the long light green hydride (δ_2) near the δ_1/δ_2 boundary. δ_1 and δ_2 are twin-related structures and follow the orientation relationship of $\{0001\}_\alpha||\{111\}_\delta\ \langle 11\bar{2}0\rangle_\alpha||\langle 110\rangle_\delta$ with α_1. On the other side of α_2, there is a tip with different orientation (δ_4) at the middle of the purple hydride along the grain boundary (δ_3). The orientations of δ_3 and δ_4 satisfy the twin relationship and follow the orientation relationship of $\{0001\}_\alpha||\{111\}_\delta\ \langle 11\bar{2}0\rangle_\alpha||\langle 110\rangle_\delta$ with α_2. A very small yellow hydride (indicated by the white arrow) is observed inside the main body of purple hydride (δ_3). Its orientation is almost the same to that of δ_4 and consistent with the twin relationship with δ_3, which indicate it is likely to transform from δ_3 by twinning.

At the triple joint of α_1, α_2 and α_3, δ_5 (the small light blue hydride cycled by white line) grew along α_1/α_3 grain boundary. δ_6 (the small red hydride) is along α_2/α_3 grain boundary and shows a trend to grow into α_3. δ_5 and δ_6 also follow the most common orientation relationship of $\{0001\}_\alpha||\{111\}_\delta\ \langle 11\bar{2}0\rangle_\alpha||\langle 110\rangle_\delta$ with α_3 and the twin relationship with each other. It implies δ_5 and δ_6 transformed from α_3.

On the α_3/α_4 grain boundary, δ-hydrides only formed on the side of α_4. δ_7 is next to the triple junction of α_1, α_3 and α_4, and in the shape of a tail extending into α_4. δ_8 has the same orientation

with δ_7 but grew along the grain boundary. The lower interface between δ_7 and α_4 is nearly parallel to the top interface between δ_8 and α_4. Another thin red hydride (δ_8) is found between δ_7 and δ_8 along the α_3/α_4 grain boundary. The orientation relationships between these δ-hydrides also agree with $\{0001\}_\alpha||\{111\}_\delta\ \langle 11\bar{2}0\rangle_\alpha||\langle 110\rangle_\delta$ and the two variants follow the twin relationship as well. The tiny blue hydride (δ_{10}, marked by the light blue arrow) follows the orientation relationship of $\{0001\}_\alpha||\{001\}_\delta\ \langle 11\bar{2}0\rangle_\alpha||\langle 110\rangle_\delta$ with α_4, which was found in small hydride blisters as OR2 in 5.1.

Furthermore, two twins found in α_1 satisfy $\{10\bar{1}2\}\langle\bar{1}011\rangle$ (T1). The larger one is through the α_1 grain with one end at the triple junction of α_1, α_2 and α_3. Another one is very tiny and located at the triple junction of α_1, α_3 and α_4. However, before hydrogen charging and homogeneous annealing, there were no twins found in the samples. The formation of these twins might be associated with the hydrides nearby.

The results obtained by the HR-EBSD analysis of the local area above are presented in Figure 5.31, including the maps of GNDs, in-plane elastic strain and stress components. In general, many dislocation tangles are observed inside or surrounding the hydrides, especially for the δ_1. The distribution of GNDs in δ_2 is more localized. The density of GNDs in δ_3 on the side of α_2 is significantly higher than that in δ_1 and δ_2 on the side of α_1. δ_4, small yellow hydride embedded in δ_3 and the small blue hydride on the interface between δ_2 and α_1 show much lower GND density than the hydride next to or surrounding them. It implies the twinning structures in the δ-hydrides is likely to accommodate the transformation strain and reduce the formation of GNDs. Along the hydrides on α_1/α_2 grain boundary, the GNDs were induced in a wider extent in α_1 than α_2. At the triple junction of α_1, α_2 and α_3, more GNDs are distributed along δ_5 and δ_6 or at the end of the large T1 twin next to the triple junction. Relatively high GND densities are also found at the two ends of δ_7 (one is the tip in α_4 and another one is next

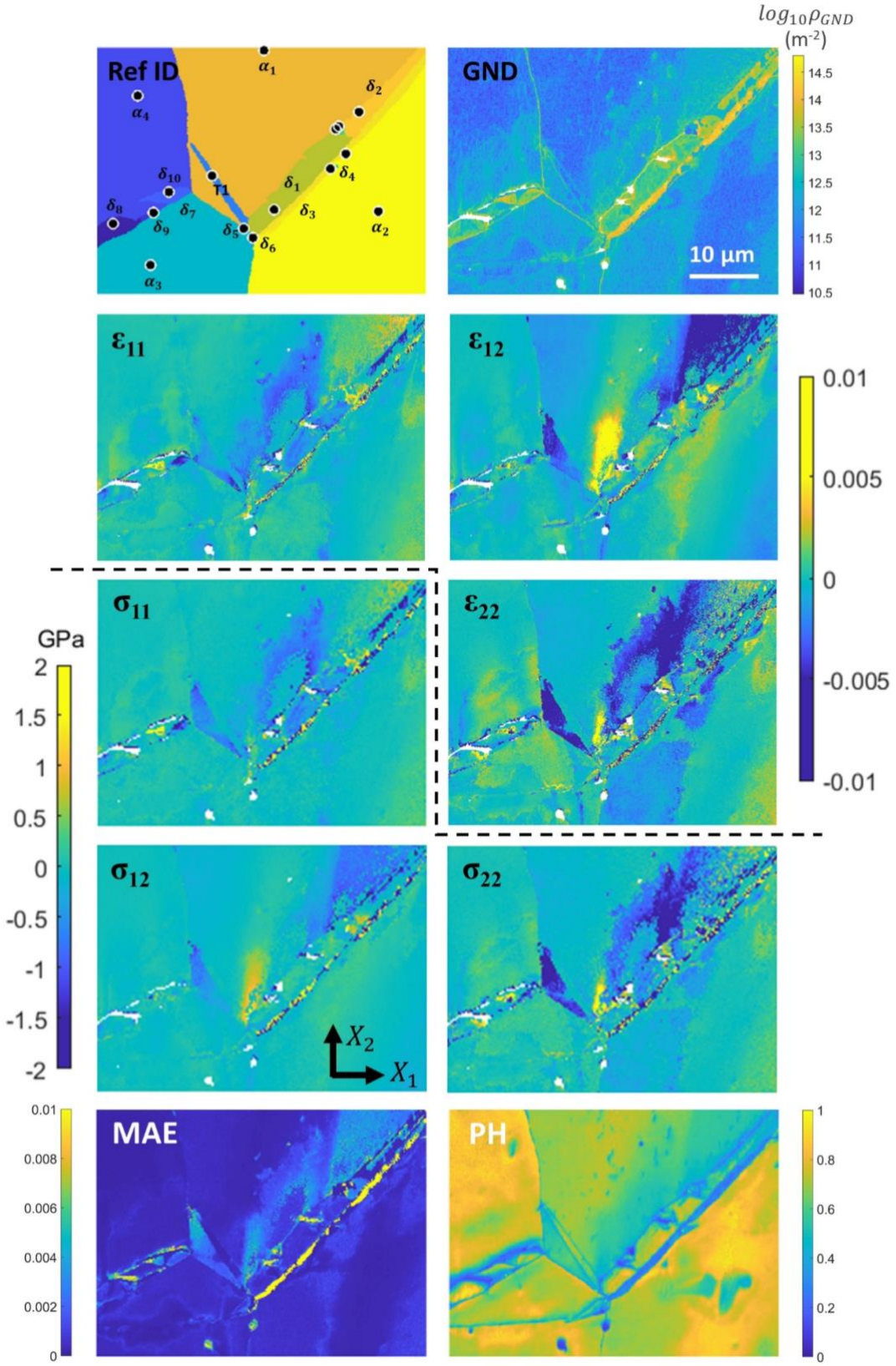

Figure 5.31 Maps of Ref ID where reference points for each grain are marked by black spots), GND density, In-plane elastic strain (ε_{ij}) and stress (σ_{ij}) tensor components, mean angular error (MAE) and peak height (PH) of the local region including inter-granular δ-hydrides precipitated at the cooling rate of 3˚/min in pure zirconium. White represents the MAE > 4×10-3 and PH < 0.2, which means the results are not reliable. Pattern resolution: 1600×1200 Step size: 120 nm. The points with MAE>0.004 or PH<0.2 are filtered.

to the triple junction of α_1, α_3 and α_4). Although the δ-hydrides on α_3/α_4 grain boundary only transformed from α_4, they still induced GNDs on the two sides of the grain boundary, as well as between themselves. Furthermore, GNDs are found to be localized in the triangle formed by α_1/α_3 grain boundary, α_1/α_4 grain boundary and the large T1 twin, while the GND density inside the main body of the large T1 twin is almost as low as that in the matrix without hydrides. It is proposed that the large T1 twin formed later than the hydride precipitation nearby and was caused by the local deformation induced by the hydride formation.

The distributions of in-plane elastic strain and stress components are generally consistent with the distribution of GNDs. More significant strain and stress concentration is observed in the triangle formed by α_1/α_3 grain boundary, α_1/α_4 grain boundary and the large T1 twin, and along the left side of δ_1 and δ_2 in α_1, especially at the intersection of the δ_1 and the large T1 twin.

5.2.3.3 Discussion

Compared to intra-granular hydrides, the nucleation and growth of inter-granular δ-hydrides, as well as the mechanical accommodation of the strain induced by their formation, are much more complicated due to the involvement of grain boundary.

The notable localization of hydrides on grain boundaries at slower cooling rate indicates that grain boundaries are preferential sites for δ-hydride nucleation (Figure 5.12). This can be interpreted by the dislocation-based nucleation model that the α-Zr to δ-hydride transformation is achieved by the successive generation and glide of $\frac{a}{3}\langle 1\bar{1}00\rangle$ partial dislocations on alternate basal planes, which was proposed by Carpenter and described in 5.1.3.2 (Figure 5.10)[185][186]. The hydride nucleation presumably prefers to occur at the features with high energy and/or dislocations having a component of Burgers vector along a-axis, such as grain boundaries. The grain boundaries with higher misorientation are supposed to have higher energy, as shown by the well-known Read-Shockley equation[189]. The grain boundaries close

to basal planes of the neighboring grains may be more likely to have dislocations with a component of their Burgers vectors along a-axis, which can assist hydride nucleation. Similar but more quantitative mechanism based on critical nucleation energy was proposed in literature[75], which supposed that δ-hydrides prefer the grain boundaries lying on the basal planes of the neighboring grains and having high misorientations. The grain boundary plane have more uncertainty and when the orientations of the bonding grains to grain boundaries are not considered, weak correlation was found between hydride precipitation and grain boundary misorientations in previous literature[186][190] at moderately low cooling rate. In my work, the majority of the inter-granular hydrides in the 3˚/min cooled sample are close to be perpendicular to the normal direction, which is also close to the $[0001]_\alpha$ directions of most grains due to the texture. But not all the grain boundaries close to the basal planes were decorated with hydrides. Similar findings were previously reported for hydride precipitation at relatively low cooling rates in the finer grain zircaloy-4 sheet with the similar texture [186][173][191]. Ruth Birch et al.[50] observed longer, thicker but less numerous hydride stringers perpendicular to the normal direction in the zircaloy-4 sheet with the similar texture at further slower cooling rates. During the precipitation of hydrides, the preference for grain boundaries, especially lying close to the basal planes of the bonding grains, is gradually enhanced by slowing the cooling rate.

Like intra-granular hydrides in air cooled samples, inter-granular hydrides follow the orientation relationship of $\{0001\}_\alpha||\{001\}_\delta\ \langle 11\bar{2}0\rangle_\alpha||\langle 110\rangle_\delta$ (OR1) with the matrix grains, even though they precipitated on the grain boundaries of the parent grain with the different neighbour grains (Figure 5.21). This is consistent with a number of previous studies using TEM[60] and EBSD[186][75][58]. In contrast, the corresponding twin-related variants are observed in inter-granular hydrides.

For faster cooling, inter-granular hydrides are thinner and more likely on just one side of grain boundaries. The selection of which side is not simply controlled by grain boundary misorientaion. As the boundary plane changes, the hydrides nucleate and grow on the different side, as shown in Figure 5.19. In terms of the dislocation-based nucleation model, this could be controlled by the nucleation at the localized grain boundary structure. Furthermore, the interplay of differing elastic stiffness on either side of the grain boundary as the grain boundary plane changes can be another factor. Due to the limitation of the 2D EBSD measurements, the three-dimensional grain boundary structure is uncertain in all the examples described in this work. The detailed mechanism is still not clear.

When a hydride forms on one side of a grain boundary, the matrix grain boundary is replaced by two phase interfaces. One with the parent grain always shows larger deviation angles than the interfaces of intra-granular hydrides along the potential habit planes, especially when they are completely along the grain boundary (type-a in air cooled samples), presumably leading to higher phase interface energy. The other interface with the other matrix grain has more uncertainty and usually shows no specific orientation relationship. This presumably results in higher but uncertain interface energy. The competition between the reduction of matrix grain boundary energy and increase of the phase interface energy during the precipitation of inter-granular hydrides may contribute to their morphology. For the hydrides with two orientation variants on the same grain boundary, the different interface structure of them with the other bonding matrix may be responsible for their different morphologies (first example of type-b in air cooled sample, Figure 5.23). More detailed and quantitative study of the hydride-matrix phase interface are still needed.

The inter-granular hydrides can nucleate at multiple points and grow by coalescence into each other (e.g., Figure 5.23 in air cooled sample). This is more common in the slower cooled sample,

where the inter-granular hydrides are thicker, and their precipitation is observed on both sides of a grain boundary (e.g., Figure 5.29). The dislocations formed surrounding the inter-granular hydrides to accommodate transformation strain may contribute to this by promoting the hydride nucleation and growth, according to the dislocation-based nucleation model.

The HR-EBSD results indicate that δ-hydrides accommodate the transformation strain mainly by formation of GNDs, consistent with the previous HR-TEM study in literature[60]. For inter-granular hydrides, twin-related structures is another approach. Wang et al.[186] reported similar twin-related structures in a much thicker intra-granular hydride. This indicate that the twin-related structures are likely to form when transformation strain is accumulated inside hydrides due to thickening.

In zirconium matrix, the accommodation of transformation strain induced by inter-granular hydrides is more complicated. Apart from lattice strain, which could directly accommodate the volume misfit caused by zirconium to hydride transformation, plastic accommodation through GNDs is observed. This agrees with the relevant DDP modelling work in literature[192]. The dislocation distributions of the models and experiments are consistent with each other. Generally, higher GND densities are observed surrounding the tips of the hydrides, consistent with the Birch's findings on the inter-granular hydrides in Zircaloy-4[128]. This suggests that dislocations are presumably involved in zirconium to hydride transformation, supporting the previously proposed dislocation-based nucleation model[185][186] to some extent. As expected, the plastic accommodation through GNDs is anisotropic. The presence of the grain boundary seems complicate this, as different orientations for easier plastic shear modes are present on either side of the grain boundary, leading to different distribution of GNDs on either side of inter-granular hydrides. When hydrides precipitate on either side of a grain boundary, this may contribute to different sizes and morphologies of hydrides on either side. Furthermore,

GND densities in matrix grain decrease with increasing the distance to inter-granular hydrides and their distributions become larger for thicker hydrides (Figure 5.29). This implies that the hydride-interface may be the source of dislocations and the movements of dislocations in matrix are supposed to accommodate transformation strain as well. Meanwhile, when zirconium to hydride transformation occurs on the basal plane close to the grain boundary, the grain boundary dislocation may accommodate shear components too. Lastly, twinning is also occasionally seen in the matrix beside thick inter-granular hydrides (Figure 5.29) to accommodate the transformation strain.

Chapter 6 Micromechanics of delta-hydrides in pure zirconium: *in situ* DIC tensile tests

Hydride formation leads to significant degradation in mechanical properties of zirconium claddings and can even result in fracture through delayed hydrogen cracking (DHC) in operation or long term storage[193][194][10][4][195]. In this chapter, *in situ* digital image correlation (DIC) tensile testing and post-deformation electron backscatter diffraction (EBSD) analysis were used to systematically study the mechanical effects of δ-hydrides in pure zirconium during deformation.

6.1 Experimental details

6.1.1 Tensile specimens

Four dog-bone tensile specimens were cut from the received, rolled, and annealed pure zirconium plates with a thickness of 1mm using water jet cutting. The geometry and dimensions of the dog-bone specimens are shown in Figure 6.1 (a). Considering the strong texture of received pure zirconium plate, as shown in the Figure 6.1 (c) and (d) which was discussed in the section 4.1, the specimens were divided into two groups: one group was produced with loading direction parallel to rolling direction (RD) and the others with loading direction parallel to transverse direction (TD). One of the specimens in each group was electrolytically charged with hydrogen for 24 h, annealed at 400 ˚C for 6 h and then cooled down in air to room temperature. The details of electrolytic hydrogen charging and homogeneous anneal process are described in section 4.4 while the resulting microstructures are described in chapter 5. The details of the dog-bone tensile specimens are summarized in Table 6.1.

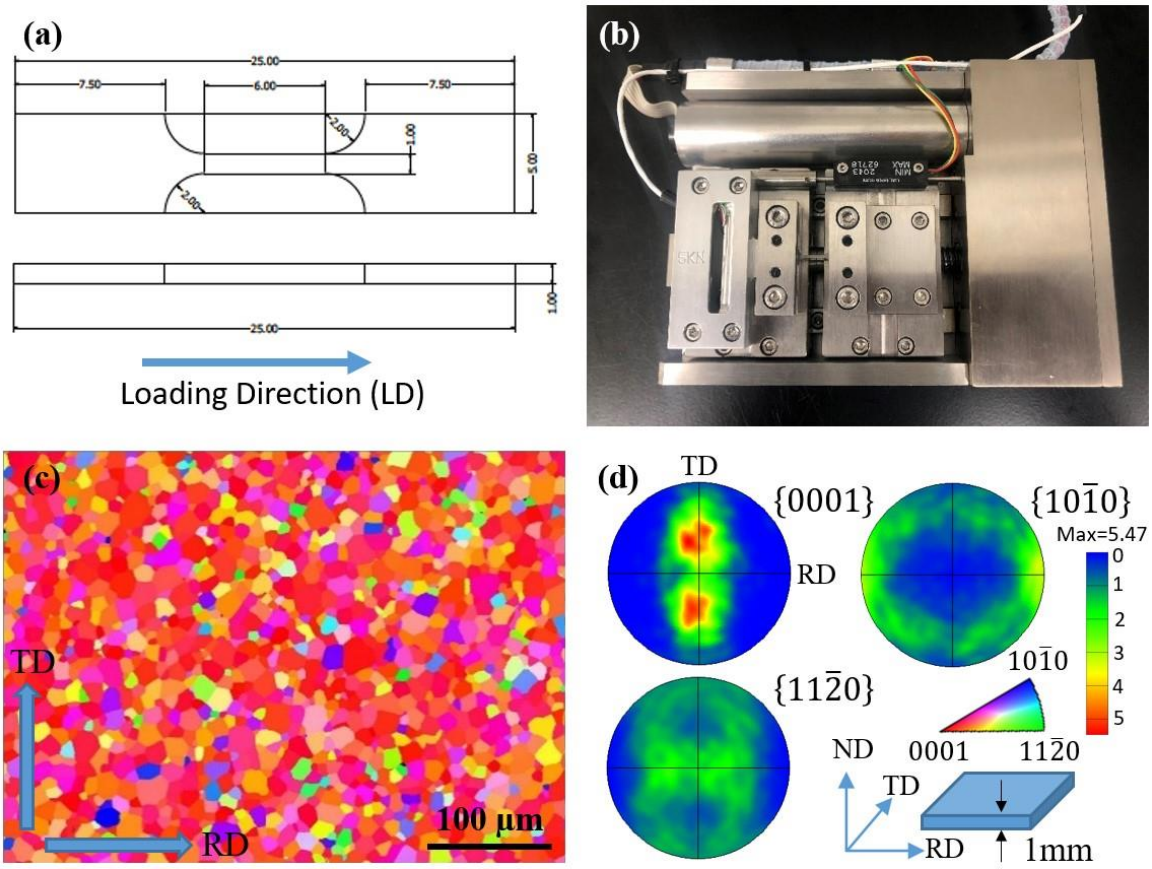

Figure 6.1 (a) Schematic diagram of a dog-bone tensile specimen and (b) photo of a Deben 5kN deformation stage for *in situ* DIC uniaxial tensile testing. (c) IPFZ maps and pole figures of the rolled and annealed pure zirconium plates received.

Table 6.1 summary of the dog-bone tensile specimens

Specimen	Loading direction	Containing hydrides or not
R1	RD	No
R2	RD	Yes
T1	TD	No
T2	TD	Yes

One side of each specimen was ground by SiC grinding discs to P4000 grit, mechanically polished by diluted colloidal silica with water, and then electropolished at low temperature (< -30 ˚C) to allow the following application of DIC pattern and EBSD measurements. Further details of the grinding and polishing process can be found in section 4.5. The thickness of the tensile specimens was measured by a micrometer and the width was measured from SE2 images.

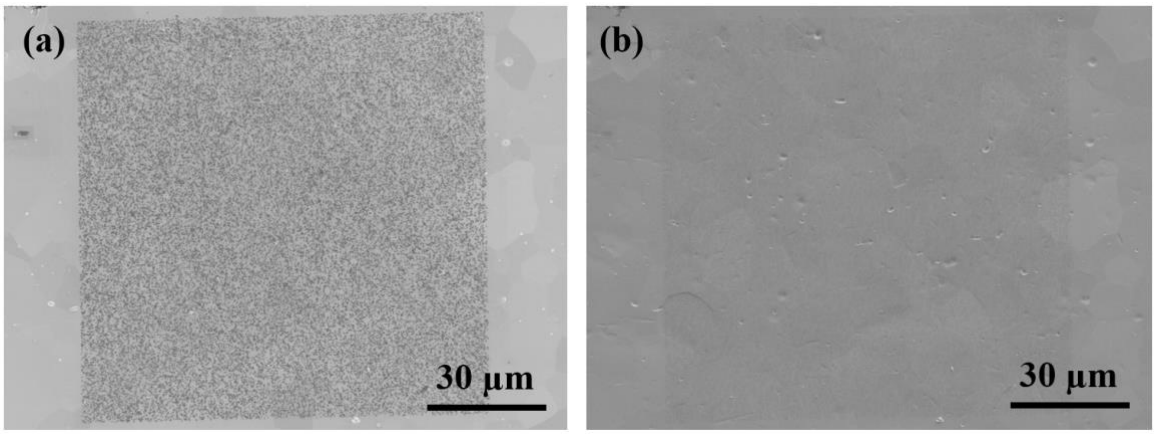

Figure 6.2 (a) In-lens image and (b) SE image of the patterned area on specimen R1 for in situ DIC uniaxial tensile testing before loading.

The speckle patterns for DIC strain measurements were produced by electron beam deposition of platinum (Pt) using Atlas5 software with the beam voltage of 5 kV and current of 100 pA respectively in a FIB. The Zeiss crossbeam 540 analytical FIB/SEM was used to apply the speckle patterns on specimen R2 and T1 and the patterns for specimen R1 and T2 were produced by the Zeiss Auriga FEG FIB/SEM due to the low availability of EMs during the experiments. The Gemini SEM column with the Auriga is the predecessor of that on crossbeam 540 and the size of speckles applied is slightly different. However, its effects on the noise level of measured DIC strain maps are neglectable when the same DIC parameters were applied. The Pt speckle patterns are clearly visible under In-lens imaging (SE1) mode and almost invisible under SE2 imaging mode when proper electron beam voltage and current are chosen, as shown in Figure 6.2. Furthermore, these Pt speckles slightly decrease the quality of Kikuchi patterns, which can be negligible in conventional EBSD analysis but causes some errors in HR-EBSD analysis.

6.1.2 *In situ* DIC tensile testing in SEM chamber

The uniaxial tensile tests were performed using a Deben 5kN deformation stage placed in a field emission gun SEM (Zeiss Merlin-EBSD equipped with a Bruker Quantax EBSD system in David Cockayne Centre for Electron Microscopy). The initial distance between the

crossheads was ~ 10.5 mm and displacement control with the crosshead speed was 0.1 mm/min (elongation rate of ~ 1.59×10^{-4} /s) was used. The largest displacement applied was 5% of the initial distance between the crossheads. In other words, the maximum macroscopic elongation ($\frac{\Delta D}{D_0}$, D_0 initial distance between the crossheads, ΔD increment of the distance between the crossheads) is 5%. It should be noted that the initial distance between crossheads is larger than gauge length of 6 mm and thus the elongation is not the engineering strain of the gauge section. Theoretically, the values of macroscopic elongation here are considered to be slightly smaller than the engineering strain. Images of the patterned area were collected after each 0.5% increment in elongation, as well as before loading and after unloading. The dual channel imaging mode was used with the beam voltage of 5 kV and current of 100 pA. One channel is In-lens to image the speckle patterns for DIC analysis and another is SE2 imaging to record the microstructural changes during deformation. This allows us to establish a rational relation between the deformation strain and microstructural changes. The resolution of the SEM images is 4096 × 3062 pixel^2. The line Int. mode with 6 frames was selected for noise reduction and each image scan took 8.1min. The deformation was paused at fixed displacement for each image collecting. The working distance was controlled in the range of about 12.5 ~ 15 mm to avoid the deformation stage touching the pole pieces or the other detectors in the chamber.

The open-source Ncorr software package[196] was utilized to do DIC analysis with the subset size of 30 pixels and the step size of 3 pixels. The radius of 5 was used for the strain calculation. The corresponding spatial resolution of the measured strain maps is 132~168 nm approximately and will be specified for each specimen.

6.1.3 Pre- and post-deformation EBSD

The carbon contamination caused by an EBSD scan significantly decreases the quality of In-lens images of the speckle patterns for DIC analysis. Thus, the conventional EBSD scans with the diffraction pattern resolution of 400 × 300 pixels were taken on the patterned areas after unloading to provide the crystallography of the microstructure. HR-EBSD scans with the diffraction pattern resolution of 1600 × 1200 and 800 × 600 pixels were performed on as-received pure zirconium and specimen R2 respectively to show the GNDs before the

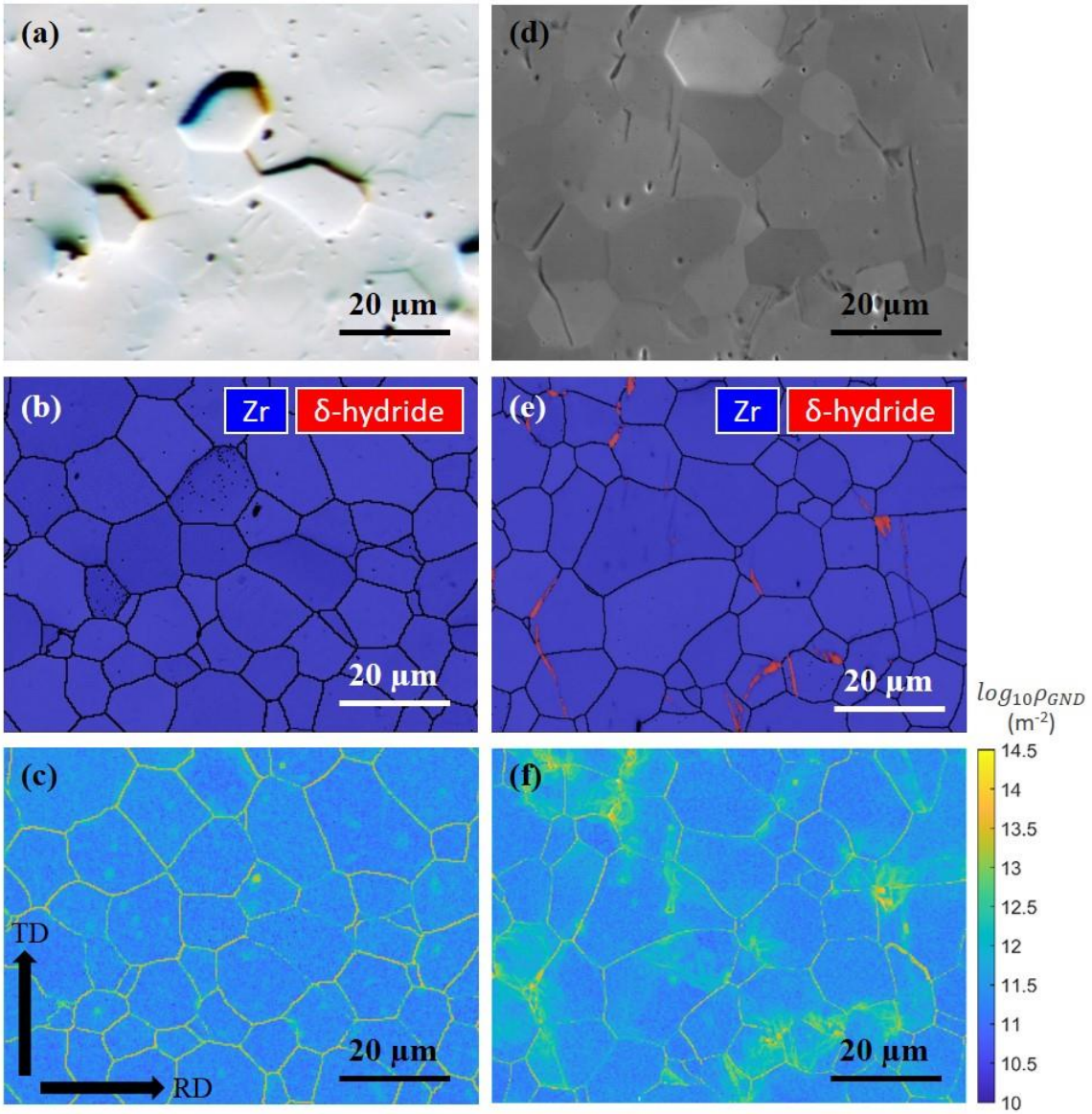

Figure 6.3 (a) Forescattered electron image, (b) phase map overlaid with the pattern quality map and grain boundaries of Zr in black lines (thick line > 10˚ and thin line > 2˚) and (c) geometrically necessary dislocation (GND) density map of as-received pure zirconium. Pattern resolution: 1600×1200. Step size: 300 nm. (d) SE2 image, (e) phase map overlaid with the pattern quality map and grain boundaries of Zr in black lines (thick line > 10˚ and thin line > 2˚) and (f) GND density map of the region of interest after hydriding on specimen R2 before loading. Pattern resolution: 800×600. Step size: 200 nm.

deformation. All the EBSD scans were performed by the same SEM used for *in situ* tensile tests, except the conventional EBSD scan of the patterned area on specimen T2. It was carried out by Zeiss crossbeam 540 analytical FIB/SEM equipped with Nordlys Max EBSD system and the corresponding diffraction pattern binning is 2 × 2. All the diffraction patterns were collected with the electron beam voltage of 20 kV and current of 20 nA.

The HR-EBSD analysis was performed by using xEBSD_v3 codes and the details can be found in section 3.3.2. Figure 6.3 shows the HR-EBSD results of the as-received pure zirconium and specimen R2 containing hydrides before loading. As shown by the GND density map of as-received pure zirconium (Figure 6.3 (c)), the grain boundaries have much higher GND densities. The distribution of GNDs inside grains is generally uniform when the high spots caused by the little pits induced by electropolishing are not considered. The density of GNDs inside grains generally fluctuates at ~1×10^{11} approximately, much lower than the noise error of ~3.6×10^{12}, estimated by equation 5.1. In specimen R2, the hydrides are obviously darker than zirconium matrix in most cases in the SE image. In this chapter, the induced hydrides in the tensile specimen R2 and T2 were identified as δ-hydrides by EBSD and found to follow the most commonly observed orientation relationship of $\{0001\}_\alpha||\{111\}_\delta\ \langle 11\bar{2}0\rangle_\alpha||\langle 110\rangle_\delta$ (OR1) with the matrix as reported in chapter 5. As presented in Figure 6.3 (f), the GND density inside the hydrides is greatly larger than that in the matrix and the highest density of GNDs is found at the tips of some hydrides or the junctions between the hydrides and multiple zirconium grains. The formation of the hydrides also leads to GNDs formation surrounding them in the zirconium grains. Some high spots arising from the little pits still exist. The GND density distribution in specimen R2 is consistent with the HR-EBSD results in Chapter 5.

6.2 Results

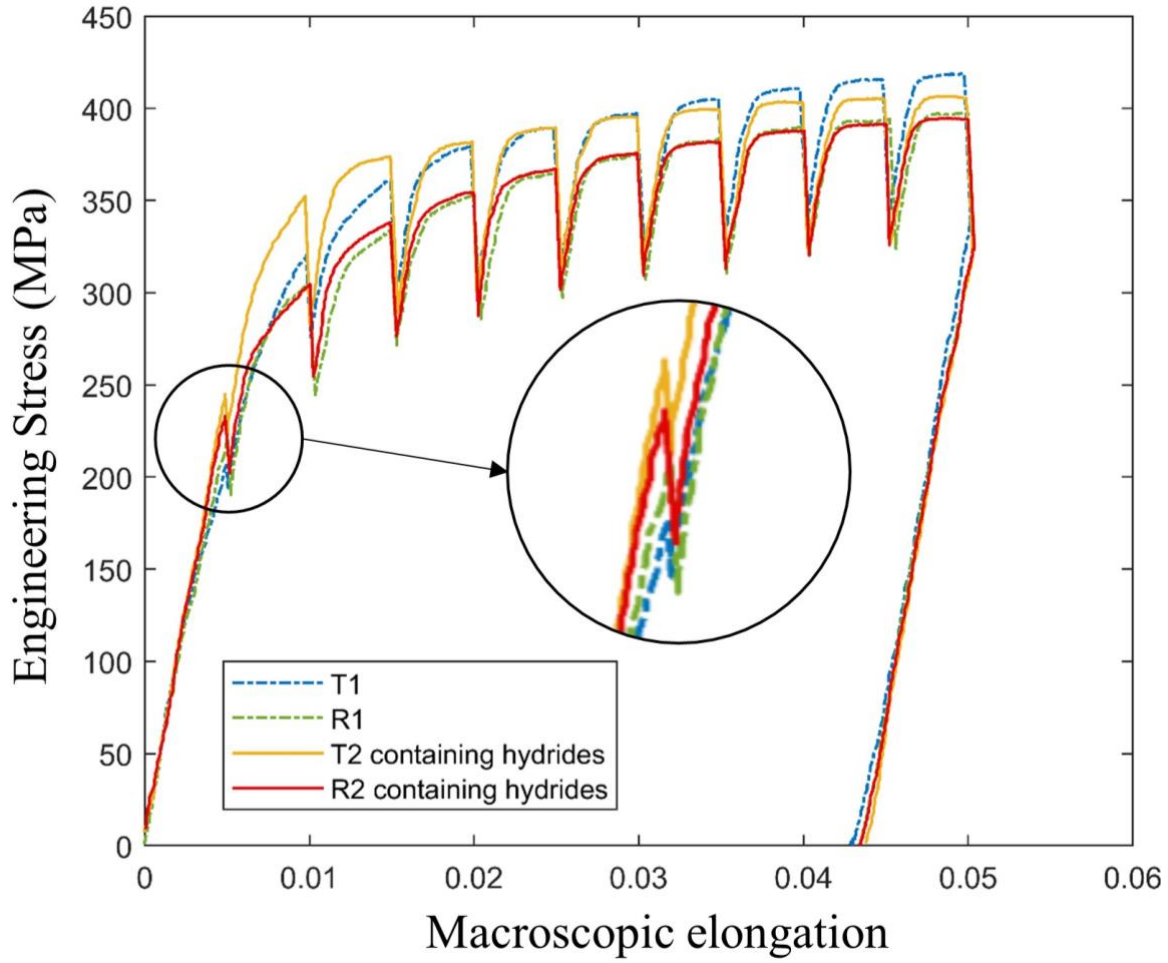

Figure 6.4 Engineering stress – macroscopic elongation curves of the four specimens obtained by *in situ* DIC tensile tests in SEM. Note that the microscopic elongation is obtained from the crosshead movement.

The engineering stress – macroscopic elongation curves of the four specimens are plotted in different colors in Figure 6.4. All four specimens yield slightly before the macroscopic elongation reaches 1.0%. The pure zirconium specimen pulled along the TD (T1, blue dashed line) yielded at a higher stress but showed a slightly weaker hardening than the other pure zirconium specimen pulled along the RD (R1, green dashed line). For the same loading direction, hydrides increased the yield stress but presumably decreased the hardening effect after yield. Similar trend was reported in the literature[197]. The effects of hydrides on the macroscale mechanical response of the specimens with the loading direction parallel to the TD are much more obvious. Furthermore, all four tensile specimens show close agreement on their elastic regime during the initial stage of loading and during unloading. It implies that the elastic

behaviors of the specimens are probably not affected by the loading direction and formation of hydrides. After unloading, the total elongation of the tensile specimens were 4.34% (R1 and R2), 4.29% (T1) and 4.38% (T2) respectively. It means the fraction of plastic deformation varies only very slightly with the loading direction for the typical texture of the rolled zirconium sheet and the hydrides increased the fraction of plastic deformation of the specimens pulled along the TD.

The engineering stress obviously dropped during the image collection, even at the total elongation of only 0.05 where the specimens did not show obvious yield. It suggests that the stress distribution is likely to be heterogeneous in all the specimens, which may lead to partial plastic deformation happening earlier than the obvious yield at macroscale.

Three in-plane strain components (ε_{xx}, ε_{yy} and ε_{xy}, where x is the loading direction) were obtained from the DIC analysis by using Ncorr. In order to demonstrate the local deformation better, effective shear strain was used since most deformation is supposed to be driven by shear at the room temperature[198][199][200]. This also conveniently combines the strain data into a single scaler field. Furthermore, the average uncertainty of the measured effective shear strain was estimated to be no more than 2.9×10^{-3} by conducting the DIC analysis on the two In-lens images of the same speckle pattern acquired before the tensile testing for each specimen.

$$\varepsilon_{eff} = \sqrt{\left(\frac{\varepsilon_{xx} - \varepsilon_{yy}}{2}\right)^2 + \varepsilon_{xy}^2}$$

In general and as expected, the strain was found to be unevenly distributed on all the tensile specimens during both loading and unloading. It also indicates that the distributions of elastic and plastic strain are generally consistent. The details of strain distribution and the changes in the microstructure will be described for each tensile specimens separately using the effective

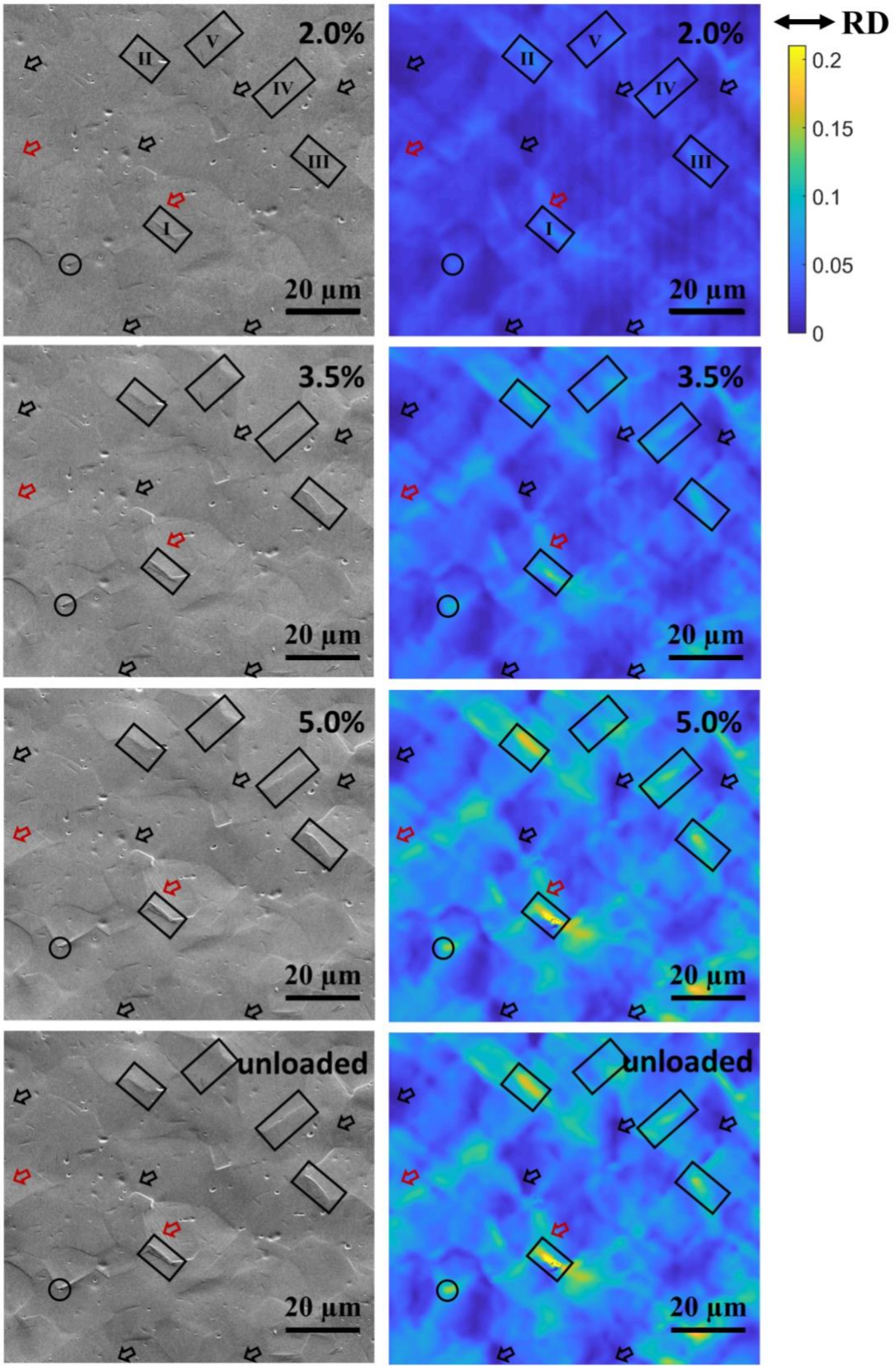

Figure 6.5 SE2 images and the effective shear strain maps of the pure zirconium specimen pulled along the RD (R1) at the macroscopic elongation of 2.0%, 3.5%, 5.0% and after unloading. The spatial resolution of the strain map is 132 nm. The red arrows show high-strain locations with slip bands and the black arrows show the low-strain locations. The boxes show some of the grain boundaries interacting with slip bands and the circle shows a multiple junction of grain boundaries where the strain is strongly localized.

strain maps and the corresponding SE images at the elongation of 2.0%, 3.5% and 5.0%, as well as after unloading.

6.2.1 Specimen-R1

As shown in the effective shear strain maps in Figure 6.5, strong strain localization is seen during the whole deformation process. The values of the strain are positively related to the elongation whereas there seems no change in the strain heterogeneity whether in loading or unloading steps. The heterogeneous distribution of deformation is further quantified by plotting the histograms of the effective shear strain for the maps at each elongation (Figure 6.6 (a)). They are distorted from normal distributions with clear tails to the side of high strain. The mean and distribution range of effective shear strain increase with the elongation. In Figure 6.6 (b), the values of effective shear strain have been normalized by divided by the mean for each map to eliminate the influence of different overall deformation. The four histograms almost perfectly coincide with each other, although the histogram for the elongation of 2.0% shows a small shoulder at ~0.8. The maps of the normalized effective shear strain of all four tensile specimens at the total elongation of 2.0%, 3.5%, 5.0% and after unloading are given in appendix. For the same specimen, the maps at the different total deformation look almost the

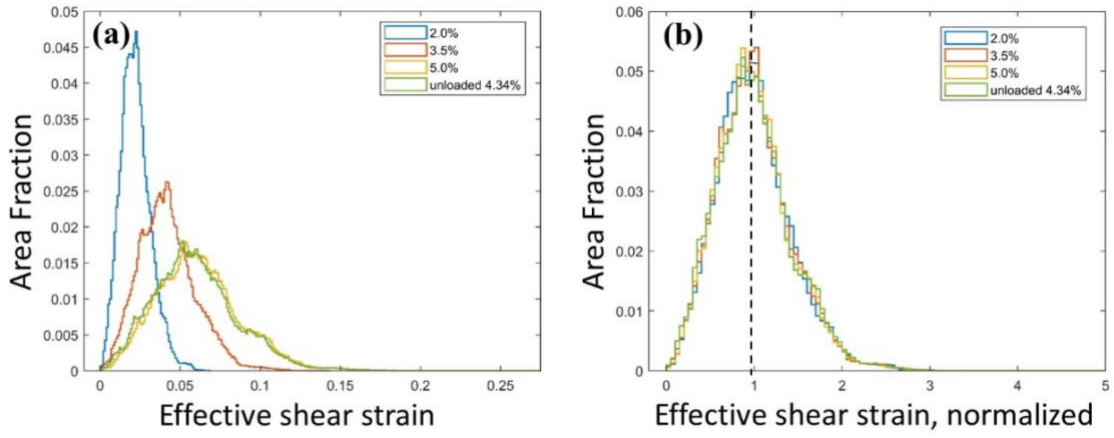

Figure 6.6 Histogram graphs of (a) effective shear strain and (b) effective shear strain normalized by divided by their means for each strain map in Figure 6.5.

same. However, the strip noise is obvious at the elongation of 2.0%, reduced with increasing the total deformation and disappear at the elongation of 3.5% (specimen-R2 and T2) or 5% (specimen-R1 and T1). The stripe noise is suggested to be caused by the microscopy and thus won't increase with deformation. With increasing deformation, the influence of this noise is reduced. The stripe noise presumably contributes to this small misfit between the histograms for the elongation of 2.0% and the other larger elongations. Therefore, it is supposed that the strain heterogeneity has no relation with the magnitude of deformation for R1 or the regime of deformation (i.e., elastic or plastic).

The SE images in Figure 6.5 show that the number of the visible slip bands gradually increase while the flatness of the measured surface decreases as the macroscopic elongation increased from 2.0% to 5.0%. The unloading did not produce visible changes of the microscopic features. These features are mainly due to the plastic deformation. Generally, the slip bands are relatively diffuse. The observed slip bands at the elongation of 2.0% become more clearly visible with the elongation increasing and the strain at the corresponding positions increase as well, as marked by red arrows. The regions with low effective shear strain compared to the surrounding area always keep flat during the whole deformation process (several examples are marked by black arrows). It implies that most plastic deformation occurs by the slip and grain rotation for pure zirconium pulled along the rolling direction.

The Schmid factor map for prismatic slip and IPFX map of the measured area after unloading are shown in Figure 6.7. More than 90% of the measured area has the Schmid factor for prismatic slip larger than 0.4 due to the texture. The orientations of the most slip bands observed in the SE images in Figure 6.5 are found to be consistent with the traces of prismatic slip planes.

The regions with low effective shear strain compared to the surrounding area are always constrained by the neighboring grains with high misorientaion or have a lower Schmid factor,

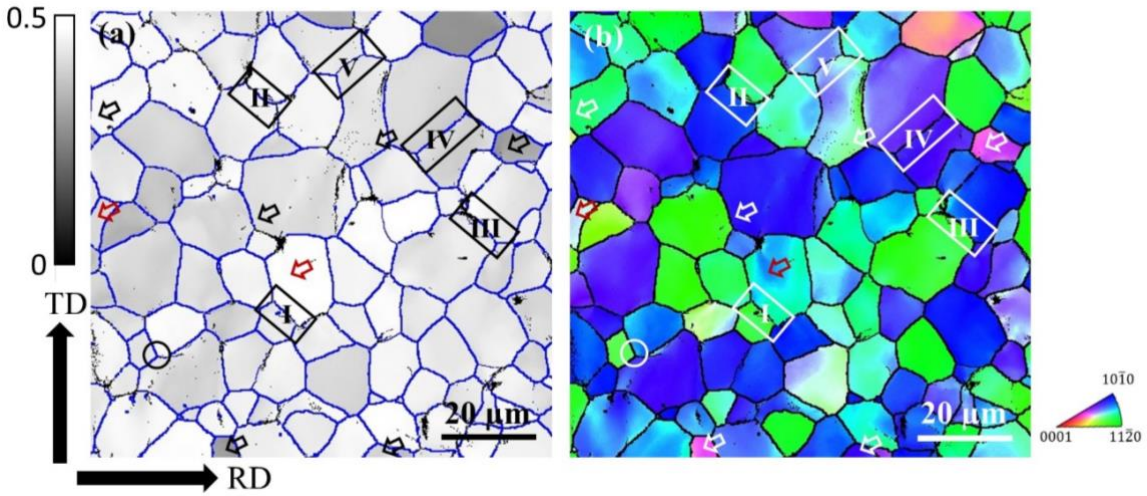

Figure 6.7 (a) Schmid factor map for prismatic slip and (b) IPFX map overlaid with grain boundaries (black lines) of the measured area of R1 after unloading. Same to Figure 6.5: the red arrows show high-strain locations with slip bands and the black (in (a)) or white (in (b)) arrows show the low-strain locations. The boxes show some of the grain boundaries interacting with slip bands and the circle shows a multiple junction of grain boundaries where the strain is strongly localized.

as indicated by the black arrows in Figures 6.5 and 6.7. The strain is greatly localized at the grain boundaries where the slip bands are almost parallel to the grain boundary (boxes I, II and III) or abruptly change their orientations at the grain boundary (box IV). In box labelled V, the slip bands nearly perpendicularly penetrate the grain boundary and have not caused strain localization there. Another preferential sites for the great strain localization are the multiple junctions of the grain boundaries where the misorientation between the active prismatic slip systems of the neighboring grains is relatively large. One example is marked by a circle in Figures 6.5 and 6.7.

6.2.2 Specimen-R2

Figure 6.8 shows the SE images and effective shear strain maps at the selected elongations of R2 containing hydrides. Generally, the surface roughness of R2 seems slightly larger than that of R1 at the same macroscopic elongation. The distribution of effective shear strain and the microscale features of α-Zr matrix without hydrides nearby are like those on the specimen R1. The effective shear strain in the hydrides is much lower than that in the matrix, especially in

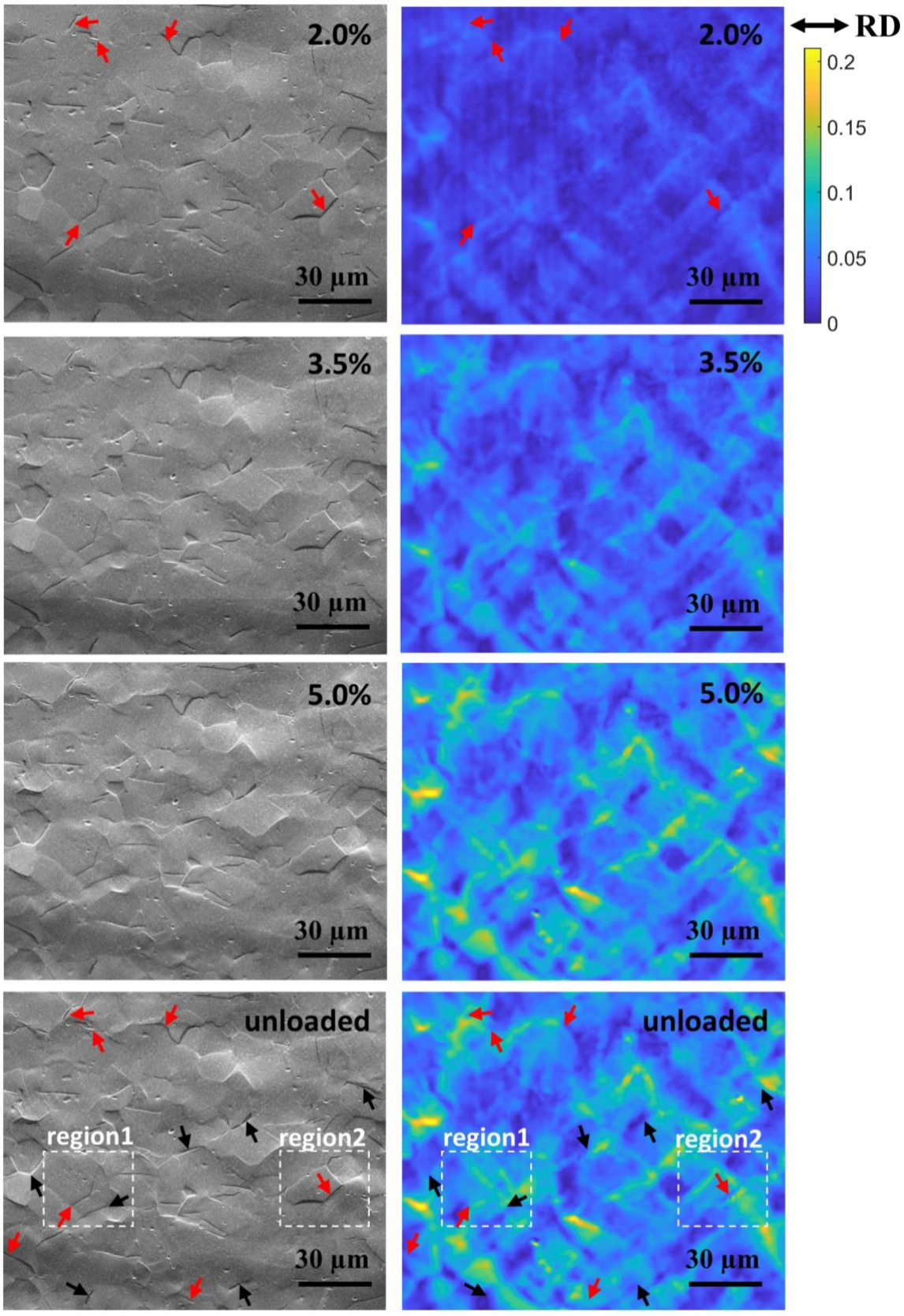

Figure 6.8 SE2 images and the effective shear strain maps of the pure zirconium specimen containing hydrides pulled along the RD (R2) at the macroscopic elongation of 2.0%, 3.5%, 5.0% and after unloading. The spatial resolution of the strain map is 168 nm. The shear traces on the hydride-matrix interfaces are marked by arrows.

the thick inter-granular hydrides, as shown by the arrows in Figure 6.8. It is supported by the finding that few slip bands and rotation are observed inside the hydrides in most cases. In other words, the hydrides are much harder to be deformed than the matrix, consistent with the findings reported in the literature[201]. The more discrete distribution of effective shear strain of R2 is presumably due to the formation of hydrides. Meanwhile, the effective shear strain is often localized at the hydride-matrix interfaces where the slip bands are arrested by the hydrides, in particular for the thick inter-granular hydrides, or local shear of the interfaces happened. The clear shear traces, which seem like micro-cracks, are seen at many of the hydride-matrix interfaces which are almost parallel to the slip bands, even though the localized shear there is not the highest in the whole map. Such hydride-matrix interface shearing firstly appear at the elongation of only 2.0% and then are enhanced by increasing the total deformation, as shown by the red arrows. New hydride-matrix interface shear traces appeared with the total deformation increasing, as shown by the black arrows in the SE2 image and strain map after unloading.

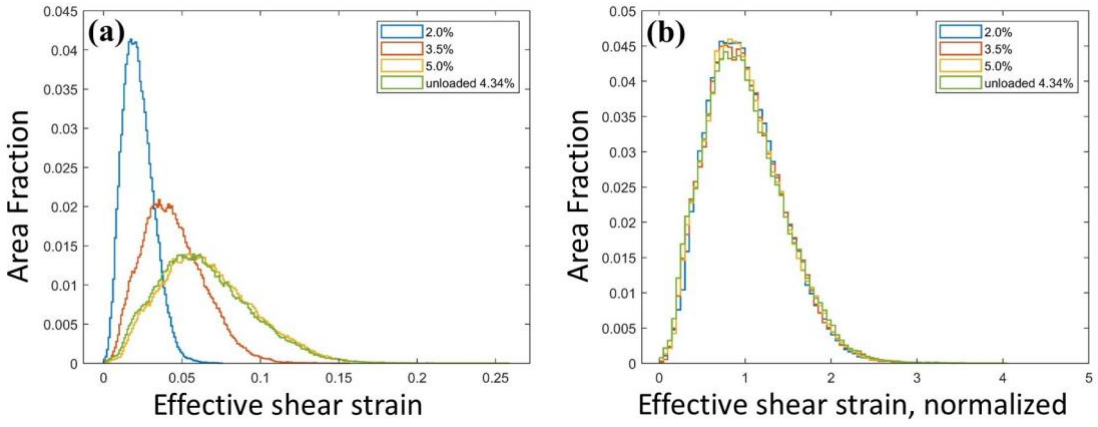

Figure 6.9 Histogram graphs of (a) effective shear strain and (b) effective shear strain normalized by divided by their mean for each strain map in Figure 6.8.

Similarly, the strain heterogeneity does not change with the magnitude of deformation, as shown by the histogram graphs of effective shear strain in Figure 6.9. The histograms of the frequency distribution of normalized effective shear strain matches with each other very well

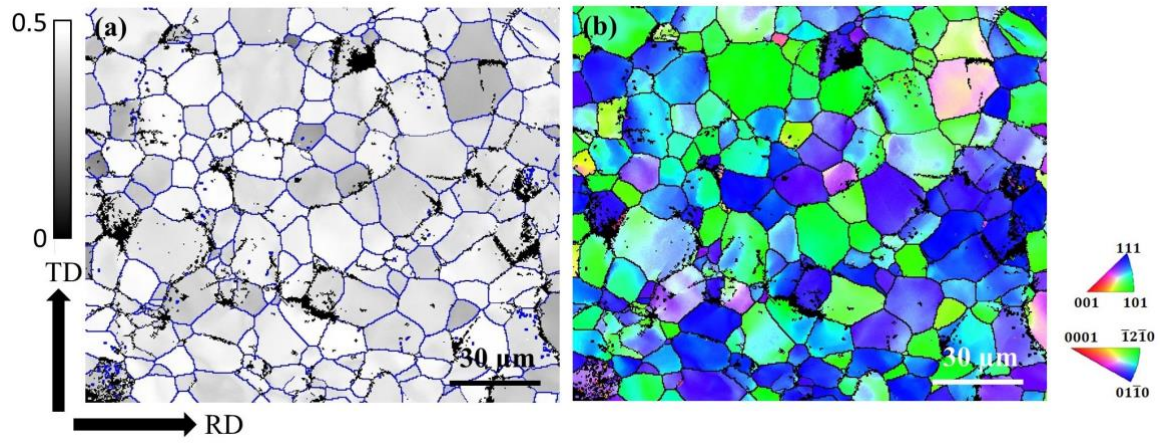

Figure 6.10 (a) Schmid factor map for prismatic slip and (b) IPFX map overlaid with grain boundaries (black lines) of the measured area of specimen R2 after unloading.

and the slightest strip noise is only found in the normalized strain map at the elongation of 2.0% compared with the other specimens (see appendix). The Schmid factor map and the crystal orientation map overlaid with grain boundaries of the measured area of R2 after unloading are shown in Figure 6.10. The δ-hydrides have not been well identified due to the relatively large step size of 0.4 μm used for the EBSD scan. The color gradient found inside the grains in the orientation map further implies that grain rotation and distortion also contribute to the plastic deformation. The slip bands observed in the SE images are identified as prismatic slips by comparison with the slip plane traces.

6.2.3 Specimen-T1

Apart from slip bands, twin-like features (marked by boxes) are observed in the SE images in the Figure 6.11 and identified as the tensile twin $\{10\bar{1}2\}\langle\bar{1}011\rangle$ (T1) by the post-deformation EBSD analysis, as shown in Figure 6.12. Several T1 twins are found at the elongation of 2.0%, as shown in the white boxes. With increasing total deformation, these twins elongate first until they completely penetrate through their parent grains and then gradually thicken. Meanwhile, new T1 twins nucleate as well, as shown by the black rectangles. The twins nucleate at the grain boundaries or multiple junctions of grain boundaries where the effective shear strain is

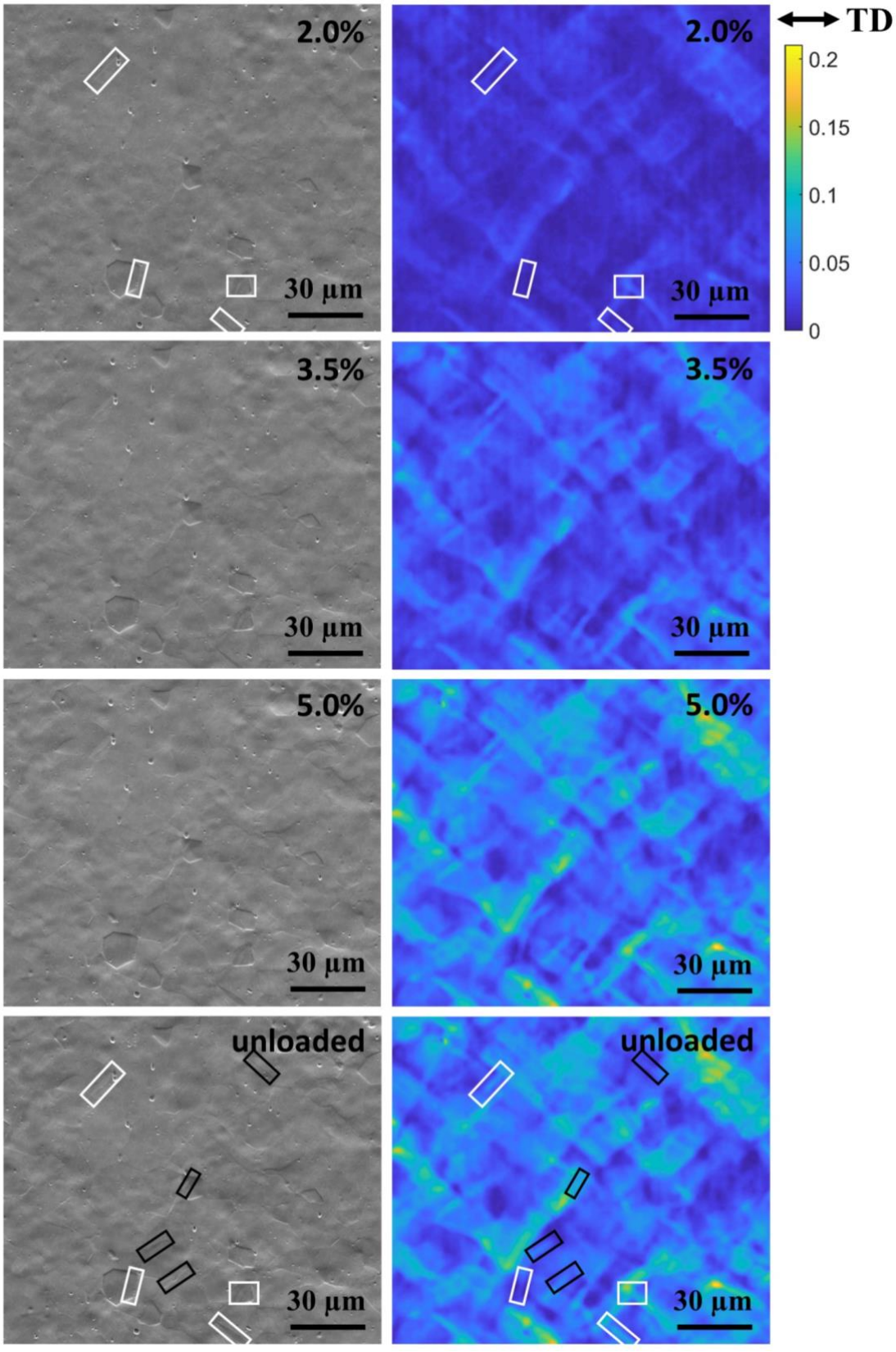

Figure 6.11 SE2 images and the effective shear strain maps of the measured area on the pure zirconium specimen pulled along the TD (T1) at the macroscopic elongation of 2.0%, 3.5%, 5.0% and after unloading. The twins that can be observed from the macroscopic elongation of 2.0% are enclosed by the white rectangles and the other twins are enclosed by the black rectangles in both SE image and the effective shear strain map after loading. The spatial resolution of the strain map is 168 nm.

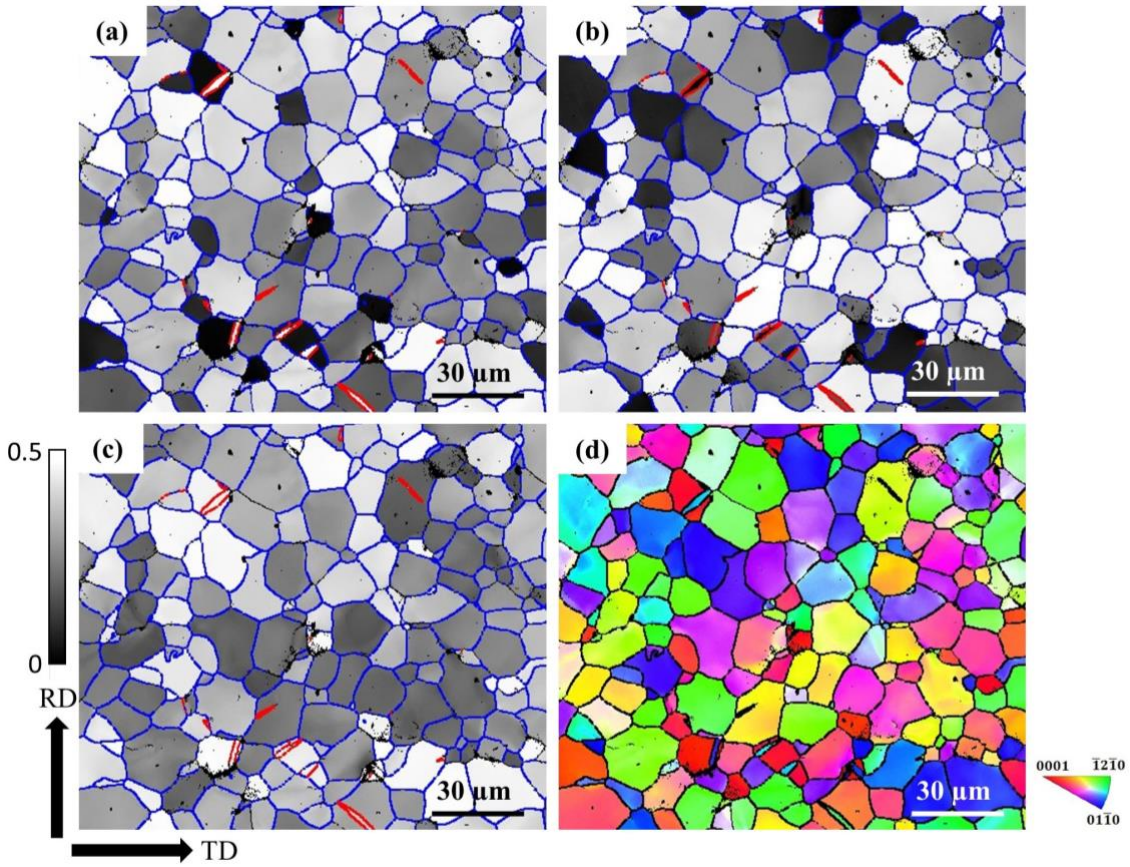

Figure 6.12 Schmid factor map for (a) prismatic slip, (b) basal slip and (c) tensile twin $\{10\bar{1}2\}\langle\bar{1}011\rangle$ (T1) overlaid with the grain boundaries in black lines and T1 twin boundaries in red lines of the measured area on T1 after loading. (d) IPFX map overlaid with grain boundaries in black lines of the measured area on T1 after unloading.

localized. Slip bands or lattice rotation are seldom found in the parent grains of the twins. The effective shear strain is localized inside the twins throughout the deformation, even though it is generally lower than the great localization of shear strain caused by slip. The strain within the twins is homogeneously distributed.

For the polycrystalline structures, the plastic strain caused by twinning can be estimated by the equation of $\varepsilon_{twin} = \sqrt{\frac{1}{2}} s V_t$, where s is the twinning shear and V_t is the volume fraction of twins[202]. The twinning shear of T1 for zirconium is 0.166. In the 2D measurements, the volume fraction is replaced by the area fraction for approximation[203]. After unloading, the area fraction of the T1 twins is 0.50%. The plastic strain from the twinning is calculated to be

6×10^{-4}, which only occupies 1.40% of the macroscopic elongation. It is clear that slip still accommodates most of the plastic deformation in the specimen T1.

It should be pointed out that the grains where the twining happened have the Schmid factors for tensile twin T1 varying from 0.18 to 0.49. Similarly, their Schmid factors for basal slip spread in a large range between 0.14 and 0.49. The Schmid factors of these grains for prismatic slip are relatively low, no more than 0.28. The grains with high Schmid factors for prismatic slip are always found surrounding the parent grains for T1 twining, especially beside the grain boundaries where the twins nucleated. It could be speculated that the nucleation of T1 twining is determined by various factors. It prefers to happen in the grains with low Schmid factor for prismatic slip, high Schmid factor for T1 twining and/or neighboring the grains with high Schmid factors for prismatic slip, corresponding to both slip-independent and slip-induced T1 twins reported by Yang et.[204] .

Compared with the specimens pulled along the rolling direction, fewer slip bands and a flatter measured surface are seen during deformation. Most slip bands observed in the SE images (Figure 6.11) are identified as prismatic slip by the comparison with prismatic slip traces in each grain. The distributions of the Schmid factor for prismatic slip and basal slip seems

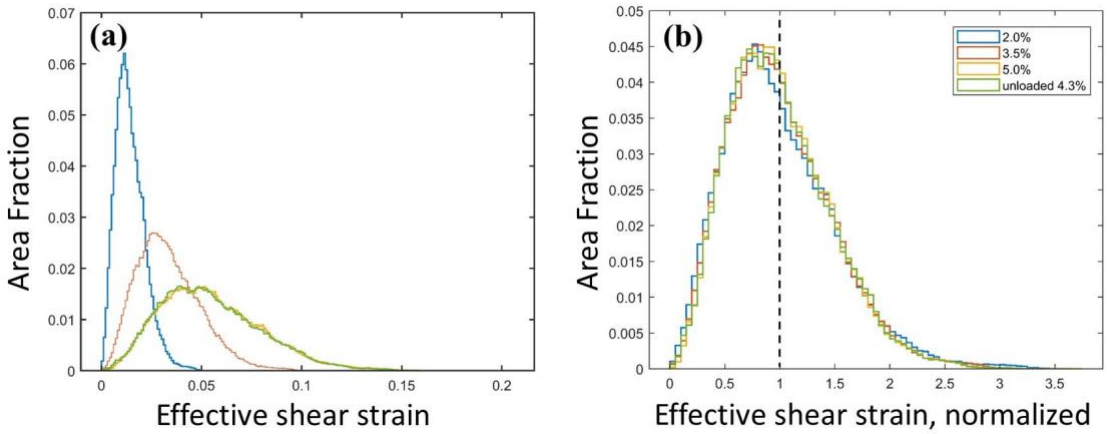

Figure 6.13 Histogram graphs of (a) effective shear strain and (b) effective shear strain normalized by divided by their means for each strain map in Figure 6.11.

analogous due to the change of loading direction. The critical resolved shear stress for prismatic slip is 1.3 lower than that for basal slip in commercially pure zirconium, measured by micro-cantilever tests[163]. To some extent, it could explain why prismatic slip still dominates.

The distribution of the shear is further quantified by plotting the frequency distributions of the effective shear strain for the maps at the selected macroscopic elongations in Figure 6.13. The histograms of the effective shear strain normalized by the means for the maps in Figure 6.11 show that the strain heterogeneity is likely to be not related with the magnitude of deformation for specimen T1. The maps for the normalized strain seem the same and can be found in appendix. Meanwhile, the histogram peaks are not at 1 and show a pronounced deviation towards lower strains.

6.2.4 Specimen-T2

The SE images and effective shear strain maps of the measured area on the specimen containing hydrides and pulled along the TD (T2) are given for the selected elongations in Figure 6.14. Like T1, both twins and slip bands are seen in the matrix during the plastic deformation. The twins are again identified as the tensile twin $\{10\bar{1}2\}\langle\bar{1}011\rangle$ (T1) with the area fraction of 0.85% and most of the slip bands are identified as prismatic slips by the post-deformation EBSD analysis, as shown in the Figure 6.15. The rotation of grains also increases with the deformation. All the twins, slip and grain rotations accommodate the strain. By the method described in the last section 6.2.3, the T1 twinning is estimated to lead to about 2.3% of the macroscopic elongation at the unloaded state. Most of plastic deformation is still accommodated by slip in the matrix for the specimen T2.

The effective shear strain within hydrides is generally lower than that in the matrix surrounding, especially for the thick inter-granular hydrides, which is consistent with their brittleness. Meanwhile, the shear strain is localized at the interfaces of hydrides and matrix. These hydride-

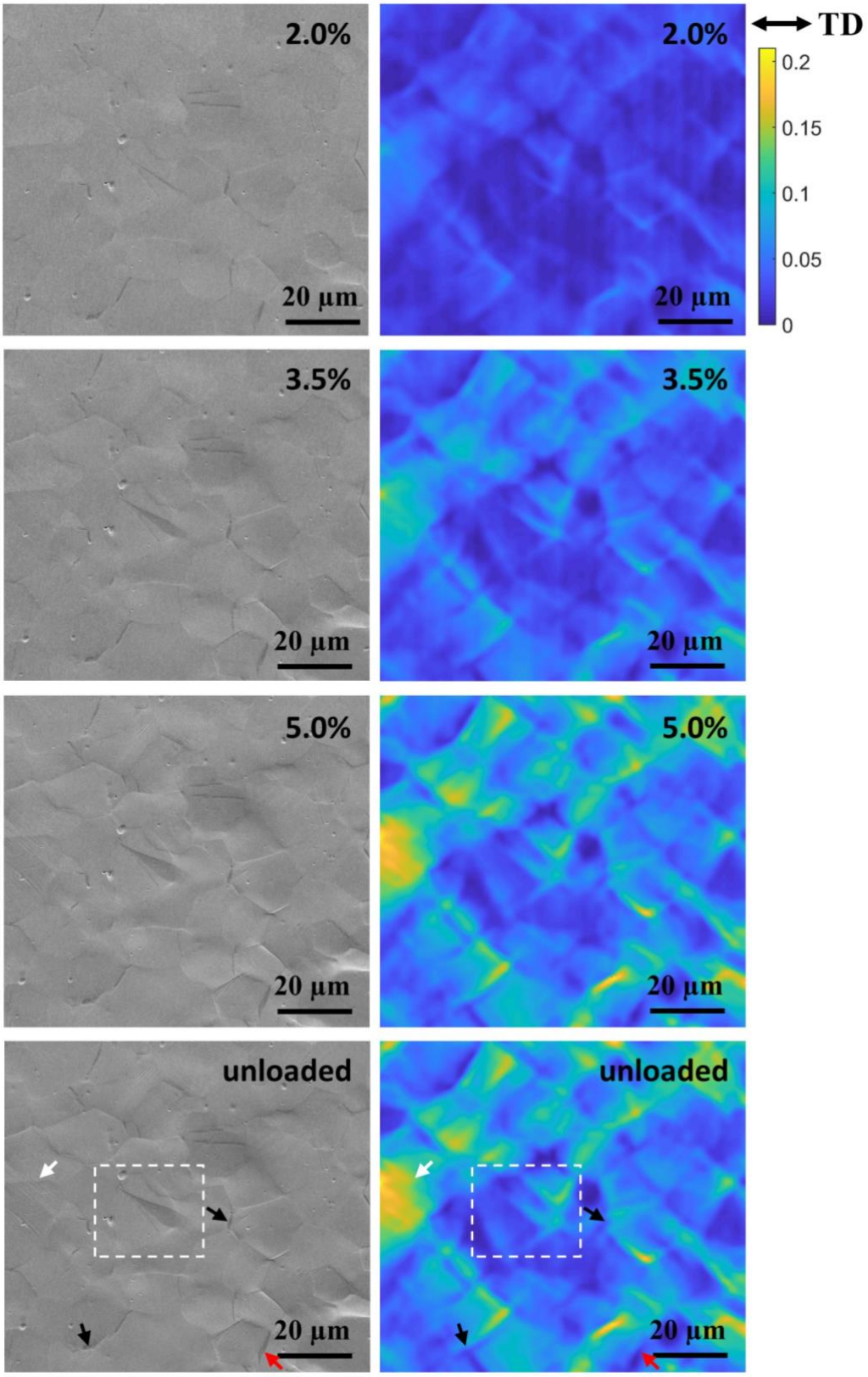

Figure 6.14 SE2 images and the effective shear strain maps of the measured area on the pure zirconium specimen containing hydrides and pulled along the TD (T2) at the macroscopic elongation of 2.0%, 3.5%, 5.0% and after unloading. The twins that can be observed in SE images are enclosed by a white rectangle in both SE image and the effective shear strain map after unloading. The arrows mark the hydride-matrix interfaces arresting the slip bands in the matrix. The spatial resolution of the strain map is 135 nm.

matrix interfaces are observed to arrest the slip bands: stop the propagation of the slip bands at large angles, as shown by black arrows in Figure 6.14, or constrain the slip bands close to parallel to them in limited regions, as shown by the red arrow in Figure 6.14. The hydrides lead to a more discrete distribution of the strain. Moreover, in the regions away from the hydrides, prismatic slip is significantly activated in the grains which are adjacent to each other and almost share a prismatic plane with a high Schmid factor. It results in a remarkable high strain region marked by a white arrow in Figure 6.14 and Figure 6.15, at a level of effective shear strain approximately five times higher than the macroscopic elongation. Nevertheless, there is no

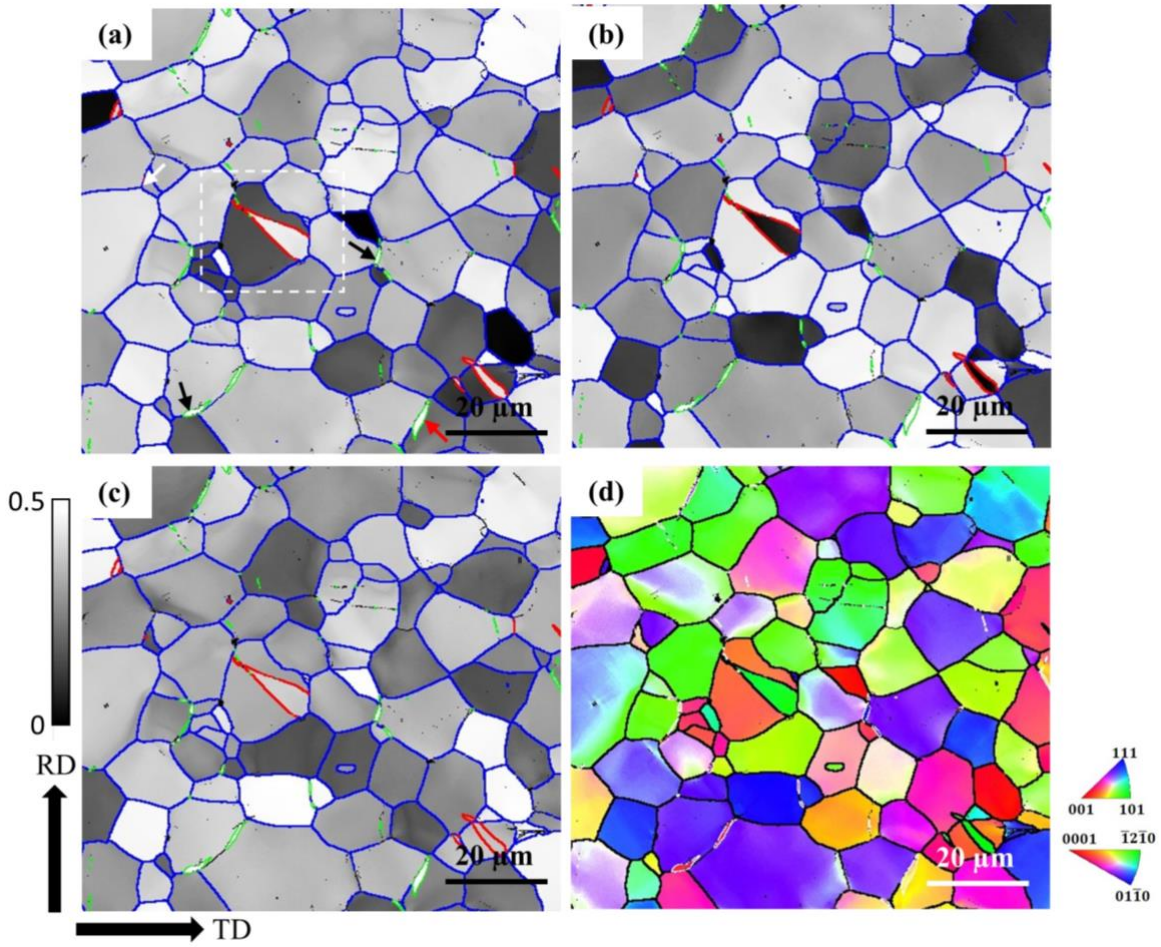

Figure 6.15 Schmid factor map for (a) prismatic slip, (b) basal slip and (c) tensile twin $\{10\bar{1}2\}\langle\bar{1}011\rangle$ (T1) overlaid with the grain boundaries in black lines, T1 twin boundaries in red lines and hydride-matrix interfaces in lime green lines of the measured area on specimen T2 after unloading. (d) IPFX map overlaid with grain boundaries in black lines and hydride-matrix interfaces in white lines of the measured area on specimen T2 after unloading.

strain localization on the grain boundary penetrated by slip bands with an angle of approximately 45° to it in this region.

The Schmid factors of the parent grains for T1 twinning and the grains surrounding them agree with those on specimen T1. The growth of the twins is affected by the hydrides nearby, as shown in the white dashed box in Figure 6.14 and 6.15. Such interaction between hydrides and twinning will be further discussed in section 6.3.

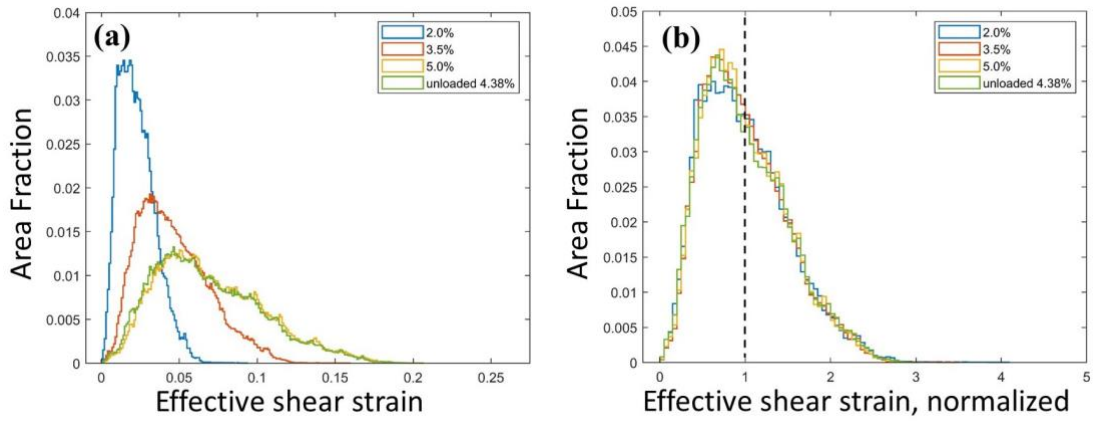

Figure 6.16 Histogram graphs of (a) effective shear strain and (b) effective shear strain normalized by divided by their means for each strain map in Figure 6.14.

The heterogeneity of the deformation is not affected by the magnitude of the elongation. It is supported by the histograms of the effective shear strain normalized by the mean for each strain map in Figure 6.14 (Figure 6.16 (b)). The maps of normalized strain look almost the same at the selected macroscopic elongations, which can be found in appendix. Similar to T1, the peaks of the histograms are located at the left side of 1. The strain distribution of these four tensile specimens will be discussed in depth in the next section.

Different from the other three tensile specimens, small cracks were found on the edges of specimen T2 after unloading, as shown in Figure 6.17. The small cracks seem evenly distributed on the two edges parallel to the loading direction on the top surface and far from

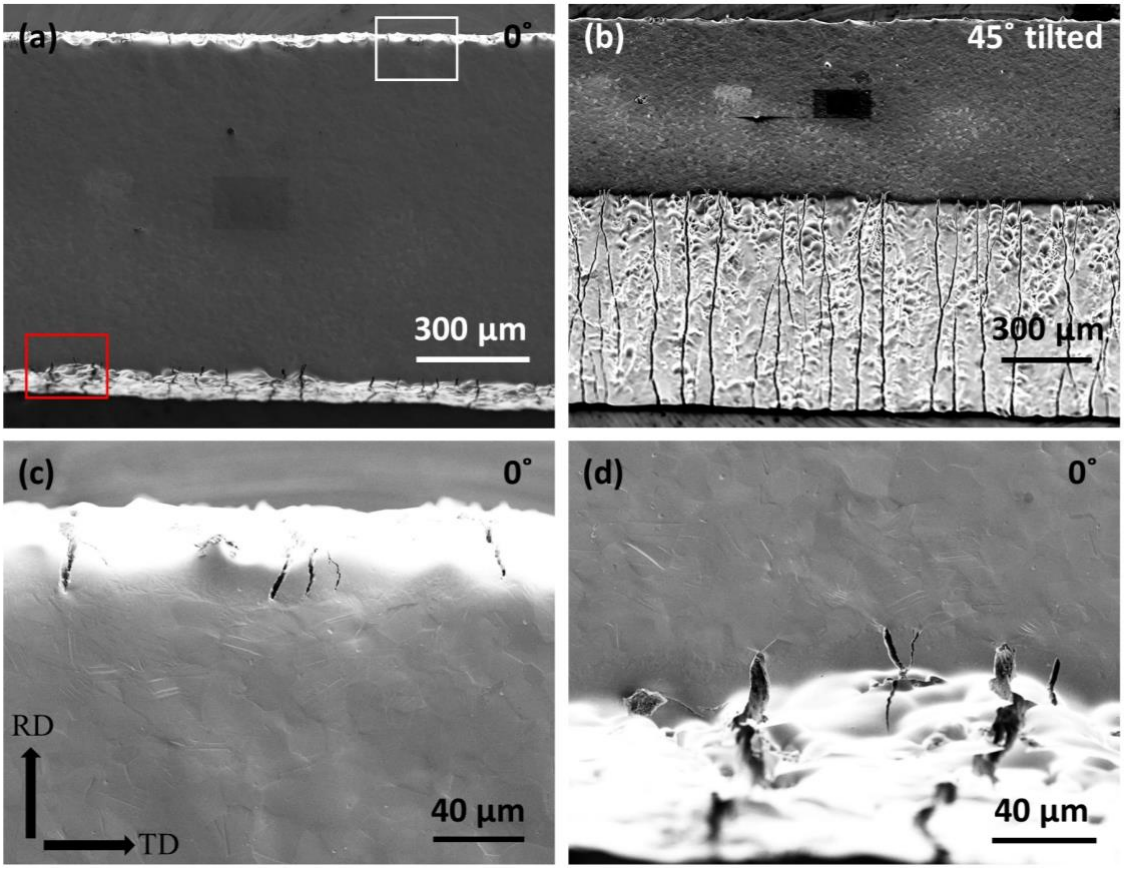

Figure 6.17 (a) SE2 image of the top surface of specimen T2 unloaded at tilted angle of 0˚. (b) SE2 image of specimen T2 unloaded at tilted angle of 45˚. (c) and (d) are the magnified SE2 images of the regions marked by white and red boxes in (a). The loading direction is parallel to TD.

the middle region measured by DIC. The depth of the cracks in the RD into the specimen is no more than 20µm in most cases. Unfortunately, the path of these small cracks cannot be well determined due to low grain orientation contrast at the edges. In order to assess the depth of the small cracks into the thickness (ND), the specimen was tilted to 45˚. The small cracks observed on the edges from the top view penetrate throughout the whole thickness. Some small cracks near to each other join together during this process.

The edges prepared by the waterjet cutting machine are wavy at micro-scale. The stress is usually built up at the sharp features during the deformation and thus the wavy edges may be the preferential sites for stress building-up and cracking. Furthermore, the slip bands observed around the tips of the small cracks are denser and more pronounced than those at the center of

the specimen T2. It is consistent with the finding reported in the literature that high local shear strain give more potential for initiation of ductile fracture in metallic materials[205].

6.3 Discussion

6.3.1 Strain distribution

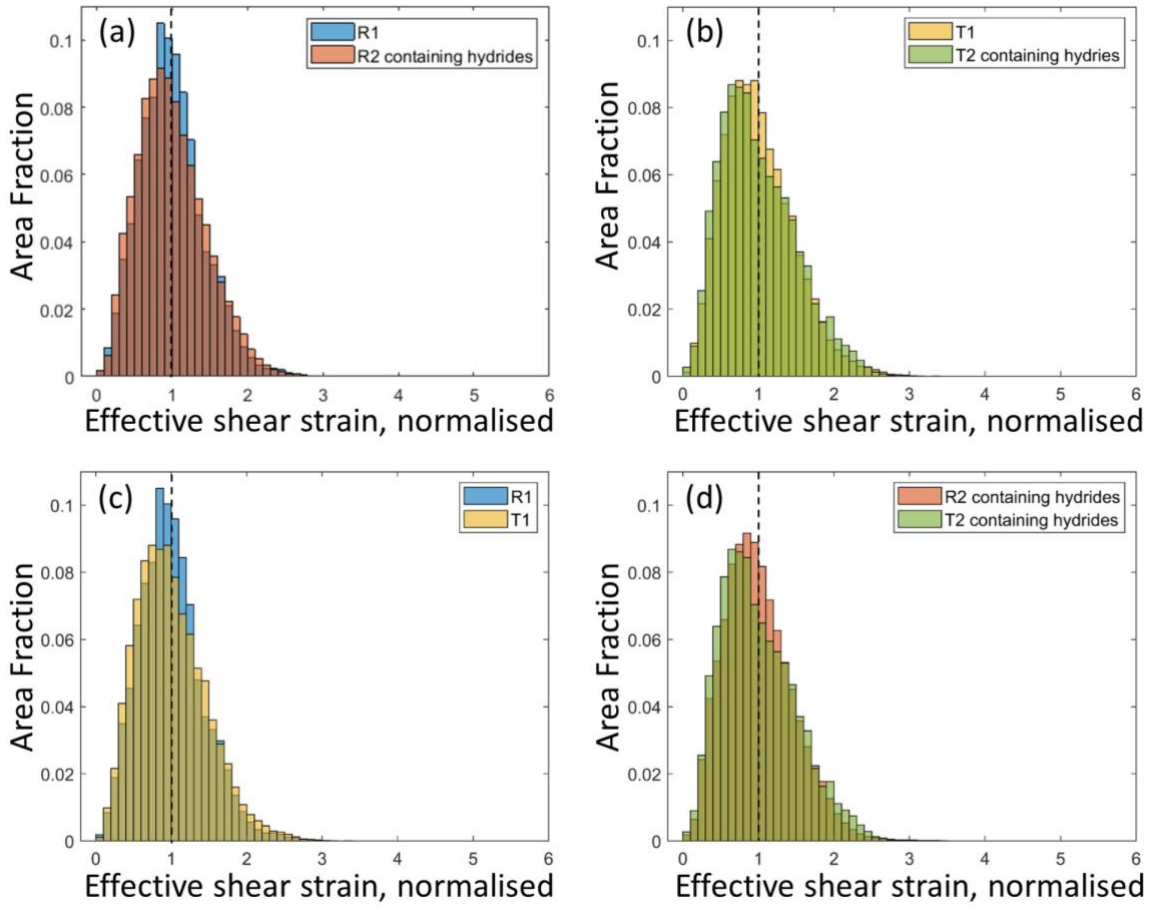

Figure 6.18 Histogram graphs of effective shear strain normalized by divided by their means for the data sets of all four tensile specimens at the macroscopic elongation of 5%.

The comparison of frequency distributions of effective shear strain at the different elongations for each tensile specimen indicates that the strain localization is intrinsically driven by the microstructure during the uniaxial tensile tests. To further clarify the effects produced by texture and hydrides on the strain localization or heterogeneity, the frequency distributions of effective shear strain of the measured region for all four tensile specimens at the macroscopic elongation of 5% are plotted in Figure 6.18. The effective shear strain values are normalized

by their mean for the measured region to eliminate the influence of the different mean values of effective shear strain for each specimen. All the frequency distributions are like skew normal distribution. The highest strain values are nearly three times more than the mean values for all four specimens.

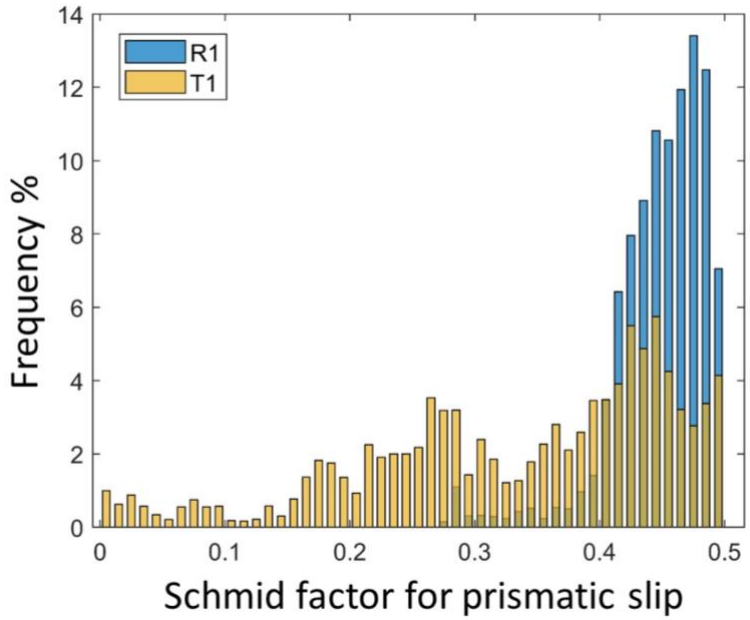

Figure 6.19 Frequency distributions of schmid factor for prismatic slip for the measure areas on the pure zirconium specimens pulled along rolling direction (R1) and transverse direction (T1).

For pure zirconium (Figure 6.18 (c)), the specimen pulled along TD (T1) generally shows higher frequencies than that pulled along RD (R1), when the normalized effective shear strain is higher than 1.3 or lower than 0.9. In between, the frequency of T1 is lower. The strain distribution for T1 is more heterogeneous than R1. This is attributed to the strong texture of the specimens and the anisotropy of hcp crystal structure of zirconium. When the loading direction is changed from RD to TD, the frequencies of the low Schmid factor (< 0.4) for prismatic slip, which has the lowest critical shear stress, significantly increase, as shown in Figure 6.19. As a result, harder grains appear. Some hard grains accommodate shear strain by twinning, which also induces strain localization. Meanwhile, it is supposed to lead to higher yield strength for specimen T1.

The hydrides enhance the strain localization for the specimens pulled along the same direction, whether RD or TD, as shown in Figure 6.18 (a) and (b). For low strains, the frequency of the hydride-containing specimen is higher than specimens without hydrides. The low effective shear strain observed inside the hydrides contributes to this. The hydride-containing specimens also show higher frequencies at high strains. It is supported by the strain localization observed at the hydride-matrix interfaces. Furthermore, the hydrides block the propagation of slip bands and twins, presumably leading strain to be spatially localized more. The interaction between the hydrides and slip, as well as twins, will be discussed in detail in the following sections.

Figure 6.18 (d) gives a comparison between the hydride-containing specimens pulled along the different directions. The frequencies of T2 are higher than those of R2 when the effective shear strain is more than the double of the mean. It is speculated that T2 is more likely to have cracks in the same conditions, which is consistent with the observation of cracks on the edges of T2.

6.3.2 Interaction between hydrides and slip

Two regions in the dashed boxes in the SE image and effective strain map of specimen R2 after unloading in Figure 6.6 are selected for more detailed investigation on the interaction between slip and intra-granular hydrides (region1), as well as inter-granular hydrides (region2) during the deformation.

Figure 6.20 includes the magnified SE images and effective shear strain maps of region1 in Figure 6.6 at the selected elongations, as well as the Schmid factor map for prismatic slip and crystal orientation map overlaid with grain boundaries of this region. In Zr-1, a few slip bands are observed and stopped at the intra-granular hydride (shown by the black arrow) at an elongation of 2.0%. With more deformation applied, these slip bands become more clearly visible and new slip bands progressively form. Meanwhile, the local effective shear strain at the slip bands gradually increases. The slip bands in the bottom left of Zr-1 terminate at the

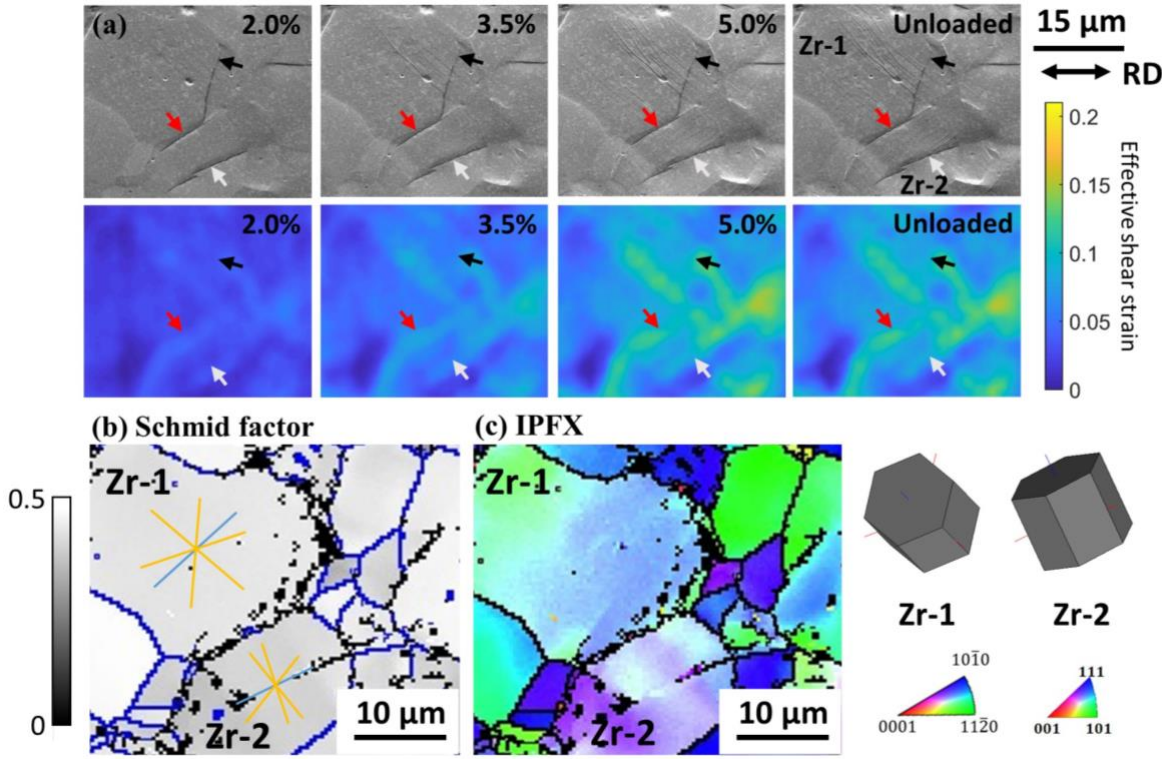

Figure 6.20 (a) Magnified SE2 images and the effective shear strain maps of the region1 in the dashed box in Figure 6.7. (b) Schmid factor map for prismatic slip and (c) IPFX map of the region, overlaid with grain boundaries. The plane traces shown in (b) are in blue for basal planes and yellow for prismatic planes.

grain boundary with Zr-2. The others in the top right of Zr-1 successfully penetrate through the hydride. The orientation of the slip bands slightly changes at the hydride-matrix interfaces. This suggests that the slips in the matrix grain could propagate through the intra-granular hydrides by activating the slip on the plane close to them in the hydrides. The slip bands observed in Zr-1 is due to the activation of a prismatic slip system, as shown by the slip trace analysis. The surface traces of the prismatic and basal planes of Zr-1 and Zr-2 are shown in yellow and blue lines in Figure 6.20 (b).

In Zr-2, there are two sets of hydrides. The hydride-1, shown by the red arrow, is located close to the grain boundary between Zr-1 and -2. The hydride-2 is at the middle of Zr-2, as shown by the white arrow. Slip bands with two different sets of orientations are seen in the region between hydride-1 and -2 from the elongation of 3.5%. They are identified as basal slips and prismatic slips respectively by slip trace analysis. The basal slip bands are parallel to hydride-

1 and the angle between them, and hydride-2 is quite small. Some of them penetrate through hydride-2. The prismatic slip bands terminate at hydride-2 with an angle close to 90˚. All the slip bands are enhanced and intensified with increase of the applied deformation. The hydride-matrix interface shear is only observed between hydride-1 and Zr-2. It has already been enabled at the elongation of 2.0%, earlier than that for the basal slip parallel to them nearby, which implies that the critical resolved shear stress for the shear of the hydride-matrix interface may be lower than that for the basal slips in the matrix and/or the higher stress at the interface caused by the large elastic stiffness difference between the hydride and matrix. The local shear on the hydride-matrix interface also becomes more noticeable upon the further deformation. Similarly, the effective shear strain is localized in the region between hydride-1 and -2. More pronounced accumulation of strain is found along the shear trace on the right-side interface between hydride-1and Zr-2.

The study in chapter 5 shows that the intra-granular δ-hydrides prefer to precipitate along the basal plane or the planes close to the basal plane of the parent grain. The shear of the intra-granular hydride-matrix interface is always accompanied by the basal slips parallel to them in the matrix. The prismatic slip is often obstructed by intra-granular hydrides with a specific angle. The intra-granular hydrides lead to greater strain localization inside the grains when the basal slip is active, compared with the prismatic slip. The observed interactions between the slips and intra-granular hydrides above are in agreement with the findings reported by the compression tests of the zircloy-4 micro-pillars containing intra-granular hydrides[206], indicating that they are intrinsic mechanical behavior regardless of size.

Within α-Zr matrix grains, the slip system is activated when the resolved shear stress exceed the critical value[163]. The slip stops when they reach the hydride-matrix interfaces and some of the slip propagates through the hydrides by triggering slip inside the hydrides with increasing

the applied deformation. It consists with the load transfer between the zirconium matrix and the hydrides, reported by Kerr et.al[201]. Similar slip transfer between the zirconium matrix and δ-hydrides was observed in the compression tests of micro-pillars[206][172]. In other words, the intra-granular hydrides arrest the propagation of slip and localized the strain in a specific region inside the grains. Two factors are proposed to determine whether the slip transfers from the matrix to hydrides happens. One is the stress build up at the hydride-matrix interfaces when the slip is stopped at the hydride-matrix interfaces. As presented in chapter 5, hydride formation induced GNDs around the phase interface in the matrix, which may prevent slip when it gets close to the hydride-matrix interface, presumably leading to stress build-up. Wang et.al[207] observed the build-up of stress and pile-up of GNDs at the hydride-matrix interfaces in the micro-cantilever tests. Another one is the geometric orientation relationship between the active slip systems in the matrix and the potential slip systems in hydrides. Slip may tend to transfer between the matrix and hydrides where the preferential slip systems are closely oriented[206]. Once the slip transfer into the hydride, the stress build-up at the interfaces would be released. The slip may then transfer from the hydride to matrix at the other side via the similar process and finally penetrate the hydride. In addition, deformation twinning of hydrides in zirconium was previously reported[172]. The stress built up at the matrix-hydride interface is also able to result in twinning in hydrides and change the potential slip systems in hydrides to be closely oriented with the activated slip systems in the matrix. At the interfaces where the slip transfer is hard to happen, the build-up stress may lead to micro-cracks/voids there when larger total deformation is applied. EBSD with smaller step size or TKD measurements of the deformed specimen R2 is required to further clarify the slip transfer observed above.

The magnified SE images and effective shear strain maps of the region2 in Figure 6.6 at the selected elongations are shown in Figure 6.21, along with the prismatic Schmid factor map and

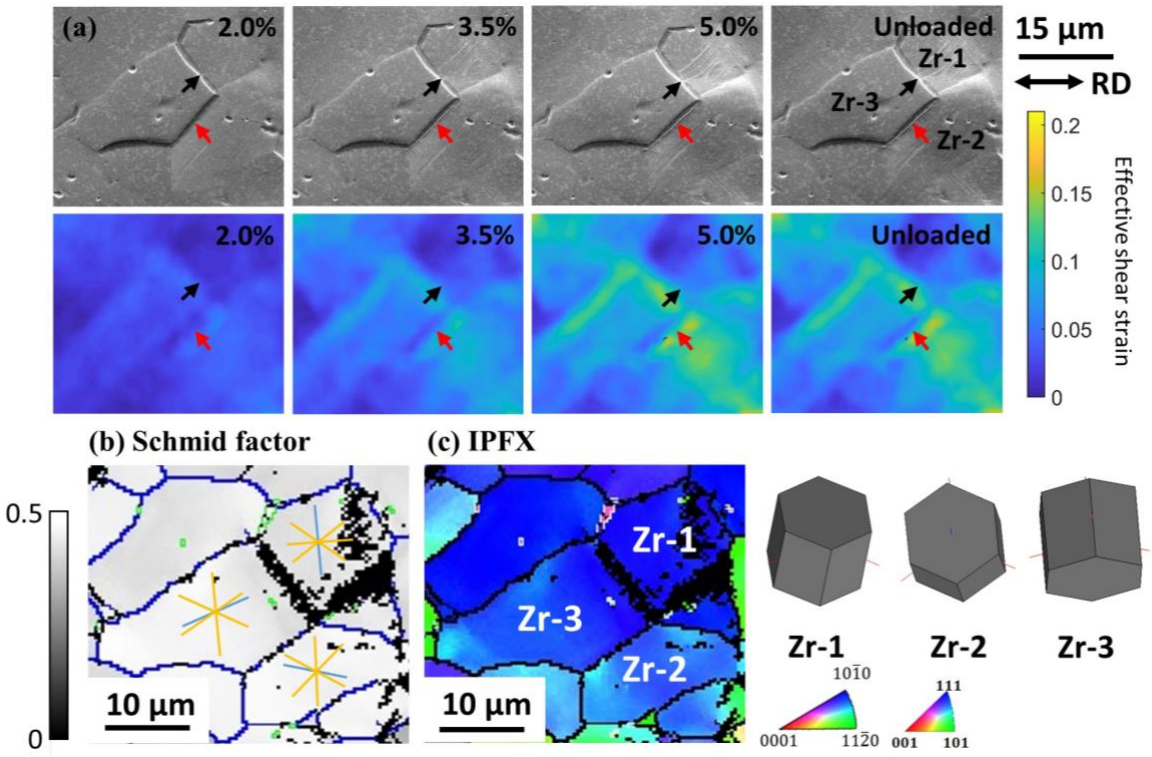

Figure 6.21 (a) Magnified SE2 images and the effective shear strain maps of the region2 in the dashed box in Figure 6.7. (b) Schmid factor map for prismatic slip, overlaid with grain boundaries in blue and phase interfaces in green and (c) IPFX map of the region, overlaid with grain boundaries in black and phase interfaces in white. The plane traces shown in (b) are in blue for basal planes and yellow for prismatic planes.

crystal orientation map (IPFX) overlaid with grain boundaries of this region. The slip trace analysis shows that the slip bands in Zr-1 and Zr-2 are due to the activation of a prismatic slip system.

In Zr-1, the slip bands can be seen from the elongation of 3.5%. They initiate at the top right side and extend toward the bottom left with more deformation applied, until meet the hydride along Zr-1/Zr-3 grain boundary. In the hydrides, no slip bands are observed. It is speculated that the prismatic slip in matrix has not triggered slips in the hydride and the stress is likely to be built up at this hydride-matrix interface.

The prismatic slip bands in Zr-2 are parallel to the hydride along the Zr-2/Zr-3 grain boundary. The shear of the interface between the hydride and Zr-2 is progressively intensified and extends to the hydride-matrix interface in the neighboring grain on the left with increasing macroscopic

deformation. The noticeable strain localization is observed along the interface shear nearby in Zr-2. There is no shear trace on the other side of this inter-granular hydride. It can be assumed that the shear of the hydride-matrix interface may be promoted by slip parallel to them in the neighboring matrix grain. Meanwhile, the interface shear strength for an inter-granular hydride may vary with the neighboring matrix grains.

Although the values of effective shear strain is relatively high, no slip band can be seen in Zr-3, even at the places where the strain is greatly localized almost along the two grain boundaries on the top. Two possible reasons for this are proposed. The first is that the steps caused by slip is too small for SE2 imaging to catch at the magnification and image resolution used. Another one is that the strain here is mainly accommodated by the other plastic deformation mechanisms, such as lattice rotation and the formation of GNDs. It may be clarified by HR-EBSD analysis of this region in the future work.

In general, the mode of interaction between the hydrides and slip is likely to depend on the geometrical relation between them. The loading direction is supposed to influence the activation of the slip systems inside the grains, affecting the interaction between slip and the intra-granular hydrides and then the strain distribution, since the intra-granular hydrides has the preferential habit planes close to basal plane of the parent grain. In the cases studied, most of the active slip in the matrix are prismatic slip and thus the obstruction of slip propagation from the intra-granular hydrides is dominate. The morphology and habit planes of inter-granular hydrides varies with crystal and geometrical orientation relationship of the grain boundaries. The inter-granular hydrides are more likely to be oriented parallel to the active slips and the frequency of shear happening at the inter-granular hydride-matrix interfaces is higher. Furthermore, seldom do slip bands completely penetrate the inter-granular hydrides, probably due to the large misorientation between the hydride and the neighboring grains at the

other side. This is speculated to induce more stress building up at the inter-granular hydride-matrix interfaces where the slip impinges the interfaces, presumably leading to micro-voids at larger macroscopic deformation. The micro-voids were previously observed along the hydride-matrix interface in the micro-cantilever tests[171].

6.3.3 Interaction between hydrides and twinning

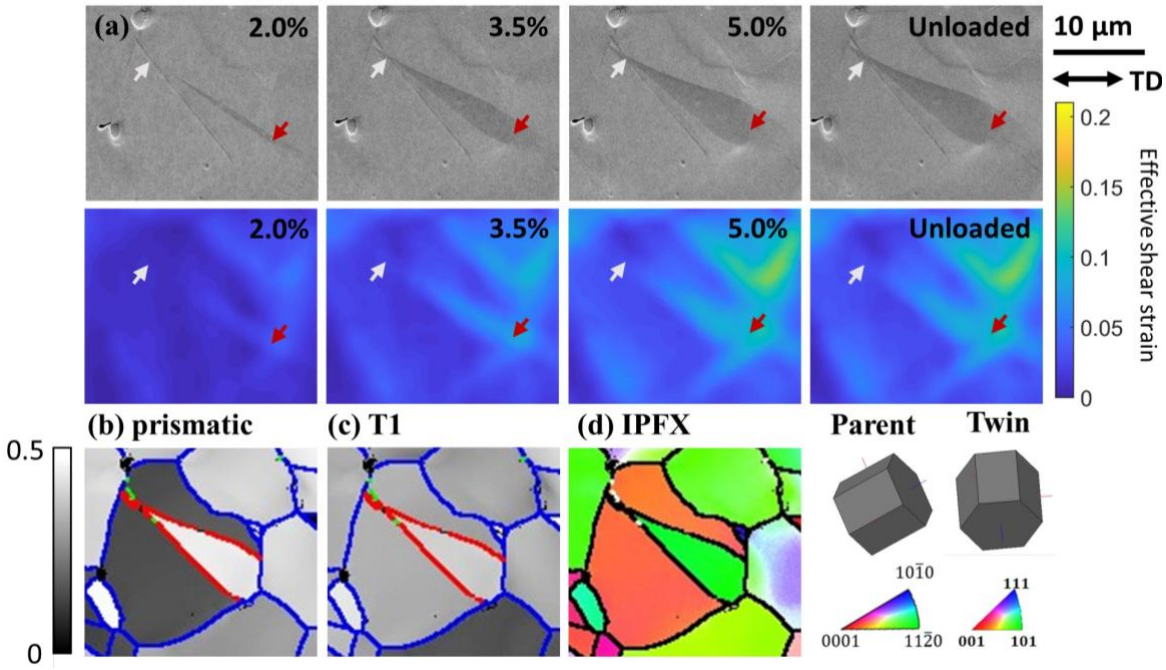

Figure 6.22 (a) Magnified SE2 images and the effective shear strain maps of the region in the dashed box in Figure 6.14. (b) Schmid factor map for prismatic slip, (c) Schmid factor map for the tensile twin $\{10\bar{1}2\}\langle\bar{1}011\rangle$ (T1) and (d) IPFX map of the region, overlaid with grain boundaries. In (b) and (c) twin boundaries are represented by red lines.

Figure 6.22 is taken from the region in the dashed box in Figure 6.14, including the SE2 images and effective shear strain maps at the selected elongations, Schmid factor maps for prismatic slip and T1 twinning and the crystal orientation map. A hydride across the grain at the center where the T1 twining happens during the deformation. In this grain, a twin extends from the bottom right, a triple junction of the matrix grain boundaries, to the top left and penetrates the hydride before the elongation is increased to 3.5%. With further deformation applied, the twin thickens unevenly. The increase in the thickness of the twin seems positively related to the

distance between the twin and hydride. In the top left area where the twin penetrates the hydride, as marked by the white arrow, the twin slightly thickens, while the thickness of the twin far from the hydride at the bottom right corner significantly increases, as marked by the red arrow. The distribution of the effective shear strain generally follows the twinning and strain localization at this multiple junction of the grain boundaries with the twin is pronounced. It implies that the hydride prevents the growth of the twin nearby and then increase the strain localization. After unloading, the shear strain in this twin is around 0.1, close to the characteristic shear strain estimated from the T1 twin shear.

In general, the presence of hydrides is likely to enhance the strain localization during deformation whether the strain is accommodated by slipping or twinning. The much lower strain observed inside hydrides is attributed to their brittle nature. Assumptions about the fracture of the zirconium with hydrides are proposed in terms of the experimental results above. At low hydride content where the hydrides are relatively isolated, the hydrides presumably enhance the strain localization, leading to the ductile fracture at the lower macroscopic deformation. When the hydride content is increased to allow the hydrides to connect with each other, forming hydride network, the micro-voids and/or micro-cracks may be induced by the potential strain/stress built up and the shear on the hydride-matrix interfaces, leading to brittle fracture along the hydrides. This is consistent with the fracture tests of the Zircaloy-4 tensile specimens with different hydride contents, where ductile fracture was observed at low hydride content and a ductile-to-brittle transition was shown when the hydride content reached a specific range[197]. More in-situ fracture tests should be conducted with varying hydride contents to further understand the role that the hydrides play in the failure of zirconium claddings.

Chapter 7 Conclusion and Future work

This thesis reports on the microstructure and micromechanics of δ-hydrides in pure zirconium by advanced microstructure characterization techniques (e.g. serial sectioning, conventional and high angular resolution EBSD) and mechanical testing technique (in-situ DIC tensile testing in SEM), and explored the intrinsic mechanism for hydride nucleation and growth in zirconium, as well as mechanical property degradation induced by hydride formation. The key conclusions are now summarized in this chapter and some suggestions for future work are proposed here.

7.1 Conclusions

Based on the experimental observations reported in previous chapters, the following conclusion can be made:

- The electrolytic hydrogen charging can generate surface hydrides on zirconium, which can be dissolved and re-precipitated in the bulk by a homogenization anneal at 400˚C. Much more localized hydrides were observed on the grain boundaries close to the basal planes of the matrix grains for slower cooling. Hydrogen in the lattice is expected to be homogeneous at anneal temperature but grain boundaries are preferential sites for hydride nucleation. The distribution and morphology of hydrides in zirconium are controlled by many factors, including grain size, texture, cooling rate, etc.

- All hydrides generated in this work are identified as δ-hydrides in α-Zr by EBSD. Most hydrides follow the orientation relationship of $\{0001\}_\alpha||\{111\}_\delta\langle 11\bar{2}0\rangle_\alpha||\langle 110\rangle_\delta$ (OR1) with their parent matrix grains. The orientation relationship of $\{0001\}_\alpha||\{100\}_\delta$ $\langle 11\bar{2}0\rangle_\alpha||\langle 110\rangle_\delta$ (OR2) was only seen in the large inter-granular hydrides at slower cooling rate and surface hydrides composed of many small hydride grains where it just

occupies 13.4%. OR2 is supposed to be the secondary relationship between δ-hydride and α-Zr presumably due to the larger and more anisotropic lattice misfit, which will only occur when OR1 is constrained, e.g. by transformation strain accumulation in strongly localized precipitation. OR1 has two twin-related variants and OR2 has three variants. Meanwhile, the orientation relationship between δ-hydrides and α-Zr has no relation with the nucleation sites (whether inside matrix grains or on the grain boundary).

- For faster cooling, an intra-granular hydride plate is composed of smaller hydride flakes with the same orientation of its habit plane. The potential habit planes for intra-granular δ-hydrides were found to be close to each other and identified as $\{0001\}$, $\{10\bar{1}1\}$, $\{10\bar{1}2\}$ and $\{10\bar{1}7\}$ of the surrounding matrix. This microstructure of intra-granular hydrides is likely related to anisotropy in the accommodation of transformation strain by matrix plasticity, which is revealed by HR-EBSD analysis. The GNDs and higher lattice shear stress-strain on the basal plane surrounding the tip of an intra-granular hydride will promote hydride nucleation there. Different values of GND density and lattice shear stress-strain on the basal plane, as well as the reverse directions of stress-strain on either sides of a hydride tip in the matrix presumably lead to hydride nucleation with a specific orientation variant on one side.

- The nucleation and growth of inter-granular δ-hydrides, as well as the mechanical accommodation of the strain induced by their formation in zirconium, are much more complicated than intra-granular hydrides due to the involvement of grain boundary. The hydride precipitation on grain boundary is suggested to be controlled by grain boundary structure, not only misorientaion but boundary plane. The inter-granular hydrides can nucleate at multiple points and grow by coalescence into each other on some occasions.

The morphology of inter-granular hydrides (completely or partially along grain boundary) may be associated with the competition between the reduction of grain boundary energy and increase of the phase interface energy during growth. Apart from lattice strain and GNDs, grain boundary dislocations and their movement may contribute to the accommodation of transformation strain. The anisotropy of plastic accommodation through GNDs is suggested to be enhanced by grain boundary, as the different orientations lead to different easier plastic shear mode on either side of grain boundary. And in turn, this may affect the growth of hydrides on either side of grain boundary. In addition, twinning was found to accommodate transformation strain in the matrix on some occasions.

- Formation of GNDs is an important approach for δ-hydrides to accommodate transformation strain. Twin-related structures were commonly seen in inter-granular hydrides and surface hydrides, presumably assisting the accommodation of transformation strain as well.

- At the macroscale, the formation of hydrides increases the yield strength of zirconium but presumably reduces the working hardening. For the same hydride content, the degree of effect caused by hydrides varies with loading directions due to the strong texture of zirconium.

- At the microscale, hydrides markedly enhanced strain localization during deformation. The contribution of hydrides to deformation is extremely small due to their brittle nature. Hydrides were found to obstruct the propagation of slip and prevent the growth of the twins nearby to increase strain localization, which may lead to stress build up at the interface where the hydrides interact with slip or twins. Meanwhile, shear was found on some hydride-matrix interfaces usually accompanied with the slip bands parallel to

them in matrix, more frequently observed for inter-granular hydrides. This may be attributed to the higher local stress at the interface caused by the large difference of elastic stiffness between δ-hydrides and α-Zr and/or lower critical shear strength of hydride-matrix interface. The hydride-matrix interface is likely to be the preferential sites for micro-voids and/or micro-cracks with more deformation applied. These should be taken into account for embrittlement induced by hydrides in zirconium.

7.2 Future works

In order to further explore the hydride formation in zirconium and its effects on local deformation, following suggestions for future work can be considered.

- The detailed roles of grain boundary and hydride-matrix interface in hydride precipitation are still not clear due to the uncertainty of them in 2D EBSD measurements. Serial sectioning combined with EBSD or 3D EBSD technique can be helpful to completely show the structures of boundary and interface.

- It would be good to perform TEM and/or TKD measurements on hydrides to further explore the dislocations and their behaviors inside or surrounding hydrides. This would be useful for a better understanding of the interaction between hydrides and matrix.

- The in-situ DIC strain measurements can be further improved to achieve a higher spatial resolution to distinguish the slip bands in effective shear strain map and maybe also expanded to fatigue and creep regimes, and/or thermal cycling. These will give more details of micromechanics of both hydrides and zirconium during various deformation modes.

- The mechanism of the ductile-to-brittle transformation with increasing hydride content can be further studied by mechanical tests of the zirconium with varying hydride contents and larger deformation.

- The role of alloy elements in hydride formation and deformation of zirconium has not been studied in this thesis. More experimental and modelling work is need to be done in this area, which will be very helpful for better alloy design of zirconium.

- Irradiation has not been considered in this thesis but cannot be avoid when zirconium alloys serve as fuel claddings in nuclear reactors. The effects of irradiation on the microstructure and micromechanics of hydrides in zirconium are suggested to be further investigated.

- This thesis provides great experimental data on the microstructure and micromechanics of hydrides in zirconium, which could be the useful input data for modelling work. Further modelling work, e.g. CP-FEM, would be helpful for a better understanding of hydride-induced embrittlement.

Appendix

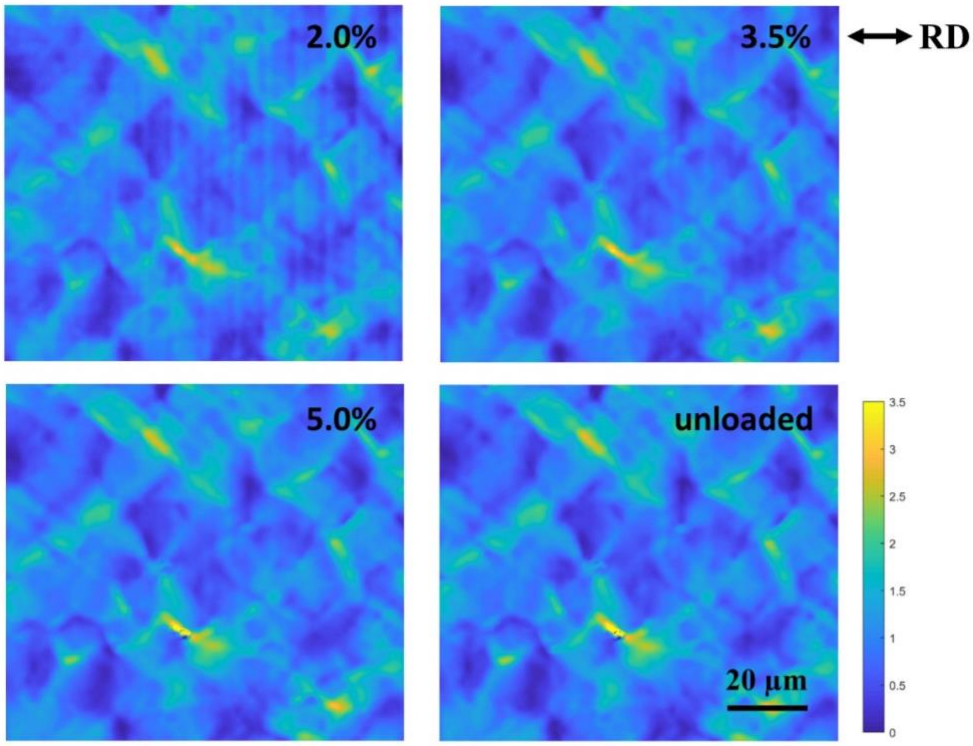

Figure 1 The normalized effective shear strain maps of the measured area on the pure zirconium specimen pulled along the RD (R1) at the macroscopic elongation of 2.0%, 3.5%, 5.0% and after unloading respectively.

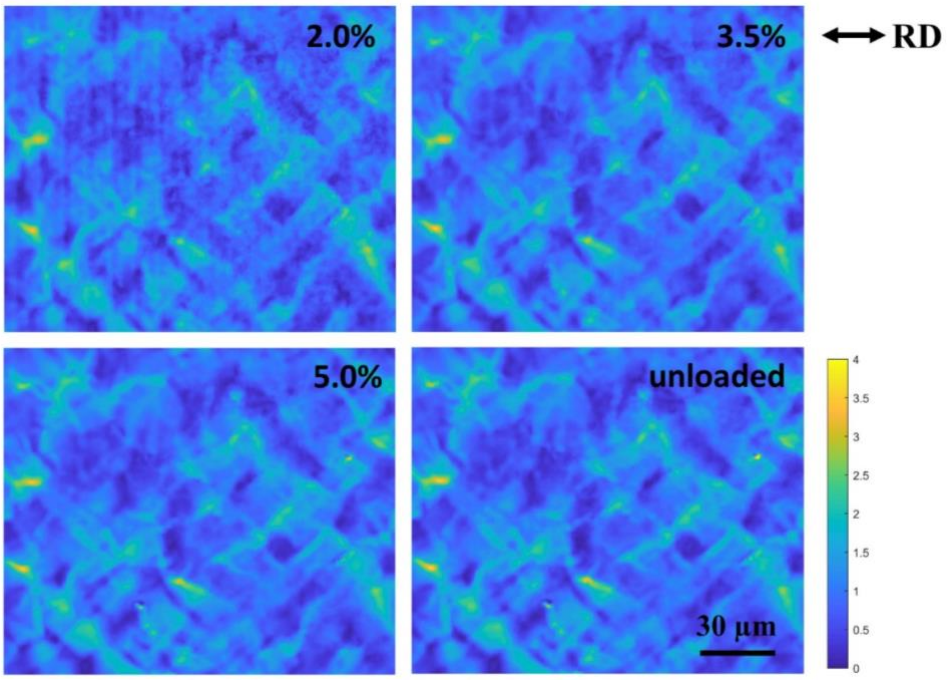

Figure 2 The normalized effective shear strain maps of the measured area on the pure zirconium specimen containing hydrides and pulled along the RD (R2) at the macroscopic elongation of 2.0%, 3.5%, 5.0% and after unloading respectively.

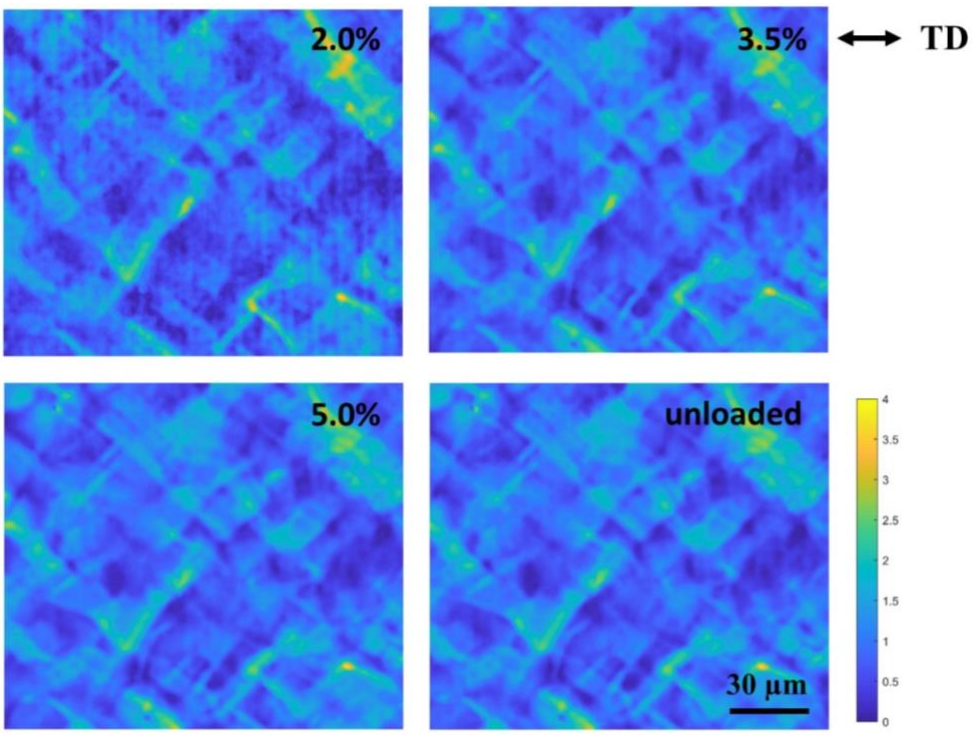

Figure 3 The normalized effective shear strain maps of the measured area on the pure zirconium specimen pulled along the TD (T1) at the macroscopic elongation of 2.0%, 3.5%, 5.0% and after unloading respectively.

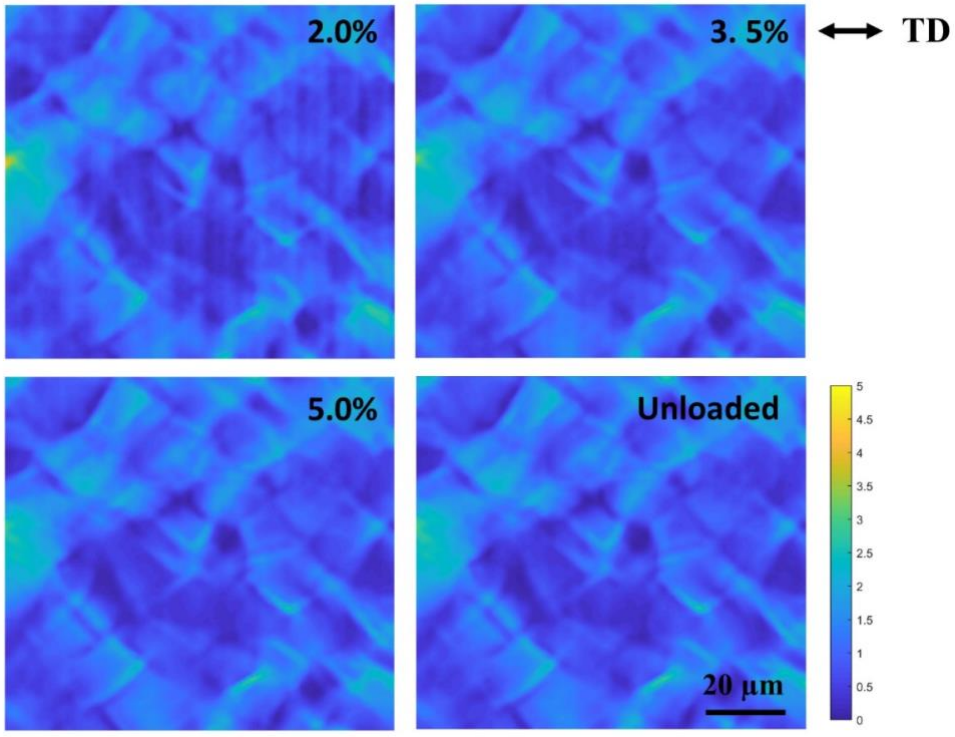

Figure 4 The normalized effective shear strain maps of the measured area on the pure zirconium specimen containing hydrides and pulled along the TD (T2) at the macroscopic elongation of 2.0%, 3.5%, 5.0% and after unloading respectively.

Reference

[1] World Nuclear Association, Nuclear Power in the World Today, (2024). https://world-nuclear.org/information-library/current-and-future-generation/nuclear-power-in-the-world-today.aspx.

[2] A. Galindo, What is Nuclear Energy? The Science of Nuclear Power, (2022). https://www.iaea.org/newscenter/news/what-is-nuclear-energy-the-science-of-nuclear-power.

[3] J. Bair, M. Asle Zaeem, M. Tonks, A review on hydride precipitation in zirconium alloys, J. Nucl. Mater. 466 (2015) 12–20. https://doi.org/10.1016/j.jnucmat.2015.07.014.

[4] S. Suman, M.K. Khan, M. Pathak, R.N. Singh, J.K. Chakravartty, Hydrogen in Zircaloy: Mechanism and its impacts, Int. J. Hydrogen Energy. 40 (2015) 5976–5994. https://doi.org/10.1016/j.ijhydene.2015.03.049.

[5] World Nuclear Association, Nuclear Fuel and its Fabrication, (2019). http://www.world-nuclear.org/information-library/nuclear-fuel-cycle/conversion-enrichment-and-fabrication/fuel-fabrication.aspx.

[6] C.R.F. Azevedo, Selection of fuel cladding material for nuclear fission reactors, Eng. Fail. Anal. 18 (2011) 1943–1962. https://doi.org/10.1016/j.engfailanal.2011.06.010.

[7] T. Alam, M.K. Khan, M. Pathak, K. Ravi, R. Singh, S.K. Gupta, A review on the clad failure studies, Nucl. Eng. Des. 241 (2011) 3658–3677. https://doi.org/10.1016/j.nucengdes.2011.08.009.

[8] H. Stehle, W. Kaden, R. Manzel, External corrosion of cladding in PWRs, Nucl. Eng. Des. 33 (1975) 155–169. https://doi.org/10.1016/0029-5493(75)90020-5.

[9] N.A.P.K. Kumar, Hydride Formation in Zirconium Alloys, McGill University, 2011. https://escholarship.mcgill.ca/concern/theses/1z40kx988.

[10] B. Cox, Environmentally-induced cracking of zirconium alloys - A review, J. Nucl. Mater. 170 (1990) 1–23. https://doi.org/10.1016/0022-3115(90)90321-D.

[11] S. Banerjee, Phase transformation examples from titanium and zirconium alloys, Amsterdam, 2007. https://www.sciencedirect.com/bookseries/pergamon-materials-series/vol/12/suppl/C.

[12] A.T. Motta, L. Capolungo, L.Q. Chen, M.N. Cinbiz, M.R. Daymond, D.A. Koss, E. Lacroix, G. Pastore,

P.C.A. Simon, M.R. Tonks, B.D. Wirth, M.A. Zikry, Hydrogen in zirconium alloys: A review, Elsevier B.V., 2019. https://doi.org/10.1016/j.jnucmat.2019.02.042.

[13] A.T. Motta, A. Couet, R.J. Comstock, Corrosion of Zirconium Alloys Used for Nuclear Fuel Cladding, Annu. Rev. Mater. Res. 45 (2015) 311–343. https://doi.org/10.1146/annurev-matsci-070214-020951.

[14] A. Couet, A.T. Motta, R.J. Comstock, Hydrogen pickup measurements in zirconium alloys: Relation to oxidation kinetics, J. Nucl. Mater. 451 (2014) 1–13. https://doi.org/10.1016/j.jnucmat.2014.03.001.

[15] K. Kakiuchi, N. Itagaki, T. Furuya, A. Miyazaki, Y. Ishii, S. Suzuki, T. Terai, M. Yamawaki, Effect of iron on hydrogen absorption properties of zirconium alloys, J. Phys. Chem. Solids. 66 (2005) 308–311. https://doi.org/10.1016/j.jpcs.2004.06.061.

[16] Y. Nishino, M. Endo, E. Ibe, T. Yasuda, Formation and dissolution of oxide film on zirconium alloys in 288°C pure water under γ-ray irradiation, J. Nucl. Mater. 248 (1997) 292–298. https://doi.org/10.1016/S0022-3115(97)00126-8.

[17] A. Hermann, Thermal behaviour of hydrogen in Zircaloy corrosion layers, J. Nucl. Mater. 302 (2002) 217–219. https://doi.org/10.1016/S0022-3115(02)00811-5.

[18] J.H. Baek, Y.H. Jeong, Breakaway phenomenon of Zr-based alloys during a high-temperature oxidation, J. Nucl. Mater. 372 (2008) 152–159. https://doi.org/10.1016/j.jnucmat.2007.02.011.

[19] GULBRANSEN EA, ANDREW KF, Oxidation Studies on Zirconium Alloys in High-Pressure Liquid Water At 3600C, Electrochem Soc-J. 116 (1969) 659–664. https://doi.org/10.1149/1.2412002.

[20] S. Kass, Hydrogen Pickup in Various Zirconium Alloys during Corrosion Exposure in High-Temperature Water and Steam, J. Electrochem. Soc. 107 (1960) 594. https://doi.org/10.1149/1.2427781.

[21] M. Nakatsuka, S. Ishimoto, Y. Ishii, A. Miyazaki, A New non-destructive technique for hydrogen level assessment in zirconium alloys using emar method, J. Nucl. Sci. Technol. 43 (2006) 1142–1148. https://doi.org/10.1080/18811248.2006.9711206.

[22] L. Bennun, J. Santisteban, J. Díaz-Valdés, J.R. Granada, R.E. Mayer, A neutronic method to determine low hydrogen concentrations in metals, Nucl. Instruments Methods Phys. Res. Sect. B Beam Interact. with Mater. Atoms. 263 (2007) 468–472. https://doi.org/10.1016/j.nimb.2007.07.009.

[23] A. Couet, A.T. Motta, R.J. Comstock, R.L. Paul, Cold neutron prompt gamma activation analysis, a

non-destructive technique for hydrogen level assessment in zirconium alloys, J. Nucl. Mater. 425 (2012) 211–217. https://doi.org/10.1016/j.jnucmat.2011.06.044.

[24] N.L. Buitrago, J.R. Santisteban, A. Tartaglione, J. Marín, L. Barrow, M.R. Daymond, M. Schulz, M. Grosse, A. Tremsin, E. Lehmann, A. Kaestner, J. Kelleher, S. Kabra, Determination of very low concentrations of hydrogen in zirconium alloys by neutron imaging, J. Nucl. Mater. 503 (2018) 98–109. https://doi.org/10.1016/j.jnucmat.2018.02.048.

[25] C.E. Ells, Hydride precipitates in zirconium alloys (A review), J. Nucl. Mater. 28 (1968) 129–151. https://doi.org/10.1016/0022-3115(68)90021-4.

[26] G. Bertolino, G. Meyer, J. Perez Ipiña, In situ crack growth observation and fracture toughness measurement of hydrogen charged Zircaloy-4, J. Nucl. Mater. 322 (2003) 57–65. https://doi.org/10.1016/S0022-3115(03)00305-2.

[27] K. Une, S. Ishimoto, Y. Etoh, K. Ito, K. Ogata, T. Baba, K. Kamimura, Y. Kobayashi, The terminal solid solubility of hydrogen in irradiated Zircaloy-2 and microscopic modeling of hydride behavior, J. Nucl. Mater. 389 (2009) 127–136. https://doi.org/10.1016/j.jnucmat.2009.01.017.

[28] E. Lacroix, A.T. Motta, J.D. Almer, Experimental determination of zirconium hydride precipitation and dissolution in zirconium alloy, J. Nucl. Mater. 509 (2018) 162–167. https://doi.org/10.1016/j.jnucmat.2018.06.038.

[29] M.P. Puls, Effects of Misfit and External Stresses on Terminal Solid Solubility in Hydride-Forming Metals, Perspect Hydrog. Met. (1986) 461–468. https://doi.org/10.1016/b978-0-08-034813-1.50066-8.

[30] G.F. Slattery, The terminal solubility of hydrogen in the zirconium/2 at % chromium/0.16 at % iron alloy, J. Nucl. Mater. 32 (1969) 30–38. https://doi.org/10.1016/0022-3115(69)90139-1.

[31] W.H. Erickson, D. Hardie, The influence of alloying elements on the terminal solubility of hydrogen in α-zirconium, J. Nucl. Mater. 13 (1964) 254–262. https://doi.org/10.1016/0022-3115(64)90046-7.

[32] D. Setoyama, J. Matsunaga, M. Ito, H. Muta, K. Kurosaki, M. Uno, S. Yamanaka, K. Takeda, Y. Ishii, Influence of additive elements on the terminal solid solubility of hydrogen for Zirconium alloy, J. Nucl. Mater. 344 (2005) 291–294. https://doi.org/10.1016/j.jnucmat.2005.04.057.

[33] P. Vizcaíno, A.D. Banchik, J.P. Abriata, Solubility of hydrogen in Zircaloy-4: Irradiation induced

increase and thermal recovery, J. Nucl. Mater. 304 (2002) 96–106. https://doi.org/10.1016/S0022-3115(02)00883-8.

[34] G.J.C. Carpenter, J.F. Watters, An in-situ study of the dissolution of γ-zirconium hydride in zirconium, J. Nucl. Mater. 73 (1978) 190–197. https://doi.org/10.1016/0022-3115(78)90559-7.

[35] S. Suman, M.K. Khan, M. Pathak, R.N. Singh, Effects of hydrogen on thermal creep behaviour of Zircaloy fuel cladding, J. Nucl. Mater. 498 (2018) 20–32. https://doi.org/10.1016/j.jnucmat.2017.10.015.

[36] Z. Zhao, J.P. Morniroli, A. Legris, A. Ambard, Y. Khin, L. Legras, M. Blat-Yrieix, Identification and characterization of a new zirconium hydride, J. Microsc. 232 (2008) 410–421. https://doi.org/10.1111/j.1365-2818.2008.02136.x.

[37] M. Kerr, M.R. Daymond, R.A. Holt, J.D. Almer, S. Stafford, Observation of growth of a precipitate at a stress concentration by synchrotron X-ray diffraction, Scr. Mater. 62 (2010) 341–344. https://doi.org/10.1016/j.scriptamat.2009.10.031.

[38] L. Lanzani, M. Ruch, Comments on the stability of zirconium hydride phases in Zircaloy, J. Nucl. Mater. 324 (2004) 165–176. https://doi.org/10.1016/j.jnucmat.2003.09.013.

[39] S. Yamanaka, K. Yamada, K. Kurosaki, M. Uno, K. Takeda, H. Anada, T. Matsuda, S. Kobayashi, Thermal and mechanical properties of zirconium hydride, J. Alloys Compd. 293–295 (1999) 23–29. https://doi.org/10.1016/S0925-8388(99)00389-8.

[40] M. Nedim Cinbiz, M. Balooch, X. Hu, A. Amroussia, K. Terrani, Nanoindentation study of bulk zirconium hydrides at elevated temperatures, J. Alloys Compd. 726 (2017) 41–48. https://doi.org/10.1016/j.jallcom.2017.07.319.

[41] M.P. Puls, S.Q. Shi, J. Rabier, Experimental studies of mechanical properties of solid zirconium hydrides, J. Nucl. Mater. 336 (2005) 73–80. https://doi.org/10.1016/j.jnucmat.2004.08.016.

[42] M. Kuroda, D. Setoyama, M. Uno, S. Yamanaka, Nanoindentation studies of zirconium hydride, J. Alloys Compd. 368 (2004) 211–214. https://doi.org/10.1016/j.jallcom.2003.08.094.

[43] A. Rico, M.A. Martin-Rengel, J. Ruiz-Hervias, J. Rodriguez, F.J. Gomez-Sanchez, Nanoindentation measurements of the mechanical properties of zirconium matrix and hydrides in unirradiated pre-

hydrided nuclear fuel cladding, J. Nucl. Mater. 452 (2014) 69–76. https://doi.org/10.1016/j.jnucmat.2014.04.045.

[44] R.L. Eadie, C.E. Coleman, Effect of stress on hydride precipitation in zirconium-2.5% niobium and on delayed hydride cracking, Scr. Metall. 23 (1989) 1865–1870. https://doi.org/10.1016/0036-9748(89)90473-0.

[45] G.K. Dey, S. Banerjee, P. Mukhopadhyay, Formation of Gamma Hydride in Alpha and Beta Zirconium Alloys., J. Phys. (Paris), Colloq. 43 (1982). https://doi.org/10.1051/jphyscol:1982446.

[46] C. Domain, R. Besson, A. Legris, Atomic-scale Ab-initio study of the Zr-H system: I. Bulk properties, Acta Mater. 50 (2002) 3513–3526. https://doi.org/10.1016/S1359-6454(02)00173-8.

[47] B. Nath, G.W. Lorimer, N. Ridley, Effect of hydrogen concentration and cooling rate on hydride precipitation in α-zirconium, J. Nucl. Mater. 58 (1975) 153–162. https://doi.org/10.1016/0022-3115(75)90101-4.

[48] J.S. Bradbrook, G.W. Lorimer, N. Ridley, The precipitation of zirconium hydride in zirconium and zircaloy-2, J. Nucl. Mater. 42 (1972) 142–160. https://doi.org/10.1016/0022-3115(72)90021-9.

[49] C.D. Cann, M.P. Puls, E.E. Sexton, W.G. Hutchings, The effect of metallurgical factors on hydride phases in zirconium, J. Nucl. Mater. 126 (1984) 197–205. https://doi.org/10.1016/0022-3115(84)90029-1.

[50] R. Birch, S. Wang, V.S. Tong, T.B. Britton, The effect of cooling rate and grain size on hydride microstructure in Zircaloy-4, J. Nucl. Mater. 513 (2019) 221–225. https://doi.org/10.1016/j.jnucmat.2018.11.011.

[51] R.S. Daum, Y.S. Chu, A.T. Motta, Identification and quantification of hydride phases in Zircaloy-4 cladding using synchrotron X-ray diffraction, J. Nucl. Mater. 392 (2009) 453–463. https://doi.org/10.1016/j.jnucmat.2009.04.004.

[52] Z. Wang, A. Steuwer, N. Liu, T. Maimaitiyili, M. Avdeev, J. Blomqvist, C. Bjerkén, C. Curfs, J.A. Kimpton, J.E. Daniels, Observations of temperature stability of γ-zirconium hydride by high-resolution neutron powder diffraction, J. Alloys Compd. 661 (2016) 55–61. https://doi.org/10.1016/j.jallcom.2015.11.187.

[53] J.H. Root, W.M. Small, D. Khatamian, O.T. Woo, Kinetics of the δ to γ zirconium hydride transformation in Zr-2.5Nb, Acta Mater. 51 (2003) 2041–2053. https://doi.org/10.1016/S1359-6454(03)00004-1.

[54] T. Maimaitiyili, C. Bjerken, A. Steuwer, Z. Wang, J. Daniels, J. Andrieux, J. Blomqvist, O. Zanellato, In situ observation of γ-ZrH formation by X-ray diffraction, J. Alloys Compd. 695 (2017) 3124–3130. https://doi.org/10.1016/j.jallcom.2016.11.337.

[55] A. Steuwer, J.R. Santisteban, M. Preuss, M.J. Peel, T. Buslaps, M. Harada, Evidence of stress-induced hydrogen ordering in zirconium hydrides, Acta Mater. 57 (2009) 145–152. https://doi.org/10.1016/j.actamat.2008.08.061.

[56] M. Cinbiz, A. Motta, D. Koss, M. Billone, Hydride Reorientation in Zircaloy-4 under Different States of Stress as Studied with In Situ X-Ray Diffraction, in: 2018: pp. 1252–1285. https://doi.org/10.1520/STP159720160052.

[57] G.C. Weatherly, The precipitation of γ-hydride plates in zirconium, Acta Metall. 29 (1981) 501–512. https://doi.org/10.1016/0001-6160(81)90074-2.

[58] K. Une, K. Nogita, S. Ishimoto, K. Ogata, Crystallography of zirconium hydrides in recrystallized zircaloy-2 fuel cladding by electron backscatter diffraction, J. Nucl. Sci. Technol. 41 (2004) 731–740. https://doi.org/10.1080/18811248.2004.9715540.

[59] A.E. Kunz, F W and Bibb, HABIT PLANE OF HYDRIDE PRECIPITATION IN ZIRCONIUM AND ZIRCONIUM-URANIUM, Trans. Met. Soc. AIME. 218 (1960). https://www.osti.gov/biblio/4166995.

[60] Z. Wang, U. Garbe, H. Li, Y. Wang, A.J. Studer, G. Sun, R.P. Harrison, X. Liao, M.A. Vicente Alvarez, J.R. Santisteban, C. Kong, Microstructure and texture analysis of δ-hydride precipitation in Zircaloy-4 materials by electron microscopy and neutron diffraction, J. Appl. Crystallogr. 47 (2014) 303–315. https://doi.org/10.1107/S1600576713031956.

[61] R. Singh, P. Ståhle, L. Banks-Sills, M. Ristinmaa, S. Banerjee, Delta-Hydride Habit Plane Determination in Alpha-Zirconium at 298 K by Strain Energy Minimization Technique, Defect Diffus. Forum. 279 (2008) 105–110. https://doi.org/10.4028/www.scientific.net/DDF.279.105.

[62] H.M. Chung, R.S. Daum, J.M. Hiller, M.C. Billone, Characteristics of hydride precipitation and

reorientation in spent-fuel cladding, ASTM Spec. Tech. Publ. (2002) 561–580. https://doi.org/10.1520/stp11406s.

[63] K.G. Barraclough, C.J. Beevers, Some observations on the phase transformations in zirconium hydrides, J. Nucl. Mater. 34 (1970) 125–134. https://doi.org/10.1016/0022-3115(70)90112-1.

[64] M.P. Cassidy, C.M. Wayman, The crystallography of hydride formation in zirconium: II. the δ → ε transformation, Metall. Mater. Trans. A. 11 (1980) 57–67. https://doi.org/10.1007/BF02700438.

[65] Z. Zhao, M. Blat-Yrieix, J.P. Morniroli, A. Legris, L. Thuinet, Y. Kihn, A. Ambard, L. Legras, Characterization of zirconium hydrides and phase field approach to a mesoscopic-scale modeling of their precipitation, ASTM Spec. Tech. Publ. 1505 STP (2009) 29–50. https://doi.org/10.1520/stp48129s.

[66] G.J.C. Carpenter, J.F. Watters, R.W. Gilbert, Dislocations generated by zirconium hydride precipitates in zirconium and some of its alloys, J. Nucl. Mater. 48 (1973) 267–276. https://doi.org/10.1016/0022-3115(73)90023-8.

[67] G.J.C. Carpenter, The dilatational misfit of zirconium hydrides precipitated in zirconium, J. Nucl. Mater. 48 (1973) 264–266. https://doi.org/10.1016/0022-3115(73)90022-6.

[68] Manfred P. Puls, The effect of hydrogen and hydrides on the integrity of zirconium alloy components: delayed hydride cracking, 2012. https://doi.org/10.1007/978-1-4471-4195-2.

[69] R.S. Daum, S. Majumdar, D.W. Bates, A.T. Motta, D.A. Koss, M.C. Billone, On the embrittlement of zircaloy-4 under RIA-relevant conditions, ASTM Spec. Tech. Publ. (2002) 702–718. https://doi.org/10.1520/stp11412s.

[70] M. Billone, Cladding embrittlement during postulated loss-of-coolant accidents (NUREG/CR-6967), (2016). https://www.nrc.gov/reading-rm/doc-collections/nuregs/contract/cr6967/.

[71] S.D. Kim, J.S. Kim, J. Yoon, Phase analysis of hydride blister in zirconium alloy, J. Alloys Compd. 735 (2018) 2007. https://doi.org/10.1016/j.jallcom.2017.11.359.

[72] O. Courty, A.T. Motta, J.D. Hales, Modeling and simulation of hydrogen behavior in Zircaloy-4 fuel cladding, J. Nucl. Mater. 452 (2014) 311–320. https://doi.org/10.1016/j.jnucmat.2014.05.013.

[73] A. Hermann, S.K. Yagnik, D. Gavillet, Effect of Local Hydride Accumulations on Zircaloy Cladding Mechanical Properties, Zircon. Nucl. Ind. 15th Int. Symp. STP1505-EB (2009) 0.

https://doi.org/10.1520/STP48134S.

[74] V.S. Arunachalam, B. Lehtinen, G. Östberg, The orientation of zirconium hydride on grain boundaries in zircaloy-2, J. Nucl. Mater. 21 (1967) 241–248. https://doi.org/10.1016/0022-3115(67)90174-2.

[75] W. Qin, N.A.P. Kiran Kumar, J.A. Szpunar, J. Kozinski, Intergranular δ-hydride nucleation and orientation in zirconium alloys, Acta Mater. 59 (2011) 7010–7021. https://doi.org/10.1016/j.actamat.2011.07.054.

[76] K. V. Mani Krishna, D. Srivastava, G.K. Dey, V. Hiwarkar, I. Samajdar, S. Banerjee, Role of grain/phase boundary nature on the formation of hydrides in Zr-2.5%Nb alloy, J. Nucl. Mater. 414 (2011) 270–275. https://doi.org/10.1016/j.jnucmat.2011.04.003.

[77] E. Schelzke, Hydridorientierung in zircaloy-rohren in abhängigkeit von verformung, textur und spannungen, J. Nucl. Mater. 30 (1969) 324–336. https://doi.org/https://doi.org/10.1016/0022-3115(69)90249-9.

[78] M.P. Puls, Fracture initiation at hydrides in zirconium, Metall. Trans. A. 22 (1991) 2327–2337. https://doi.org/10.1007/BF02664999.

[79] S.I. Hong, K.W. Lee, Stress-induced reorientation of hydrides and mechanical properties of Zircaloy-4 cladding tubes, J. Nucl. Mater. 340 (2005) 203–208. https://doi.org/10.1016/j.jnucmat.2004.11.014.

[80] J.S. Kim, Y.J. Kim, D.H. Kook, Y.S. Kim, A study on hydride reorientation of Zircaloy-4 cladding tube under stress, J. Nucl. Mater. 456 (2015) 246–252. https://doi.org/10.1016/j.jnucmat.2014.09.032.

[81] R.N. Singh, R. Kishore, S.S. Singh, T.K. Sinha, B.P. Kashyap, Stress-reorientation of hydrides and hydride embrittlement of Zr-2.5 wt% Nb pressure tube alloy, J. Nucl. Mater. 325 (2004) 26–33. https://doi.org/10.1016/j.jnucmat.2003.10.009.

[82] J. Desquines, D. Drouan, M. Billone, M.P. Puls, P. March, S. Fourgeaud, C. Getrey, V. Elbaz, M. Philippe, Influence of temperature and hydrogen content on stress-induced radial hydride precipitation in Zircaloy-4 cladding, J. Nucl. Mater. 453 (2014) 131–150. https://doi.org/10.1016/j.jnucmat.2014.06.049.

[83] M.N. Cinbiz, D.A. Koss, A.T. Motta, The influence of stress state on the reorientation of hydrides in a zirconium alloy, J. Nucl. Mater. 477 (2016) 157–164. https://doi.org/10.1016/j.jnucmat.2016.05.013.

[84] K.B. Colas, A.T. Motta, M.R. Daymond, J.D. Almer, Effect of thermo-mechanical cycling on zirconium hydride reorientation studied in situ with synchrotron X-ray diffraction, J. Nucl. Mater. 440 (2013) 586–595. https://doi.org/10.1016/j.jnucmat.2013.04.047.

[85] L.A. Simpson, C.D. Cann, Fracture toughness of zirconium hydride and its influence on the crack resistance of zirconium alloys, J. Nucl. Mater. 87 (1979) 303–316. https://doi.org/10.1016/0022-3115(79)90567-1.

[86] J.H. Huang, C.S. Ho, Effect of hydrogen gas on the mechanical properties of a zirconium alloy, Mater. Chem. Phys. 38 (1994) 138–145. https://doi.org/10.1016/0254-0584(94)90003-5.

[87] J.S. Kim, T.H. Kim, D.H. Kook, Y.S. Kim, Effects of hydride morphology on the embrittlement of Zircaloy-4 cladding, J. Nucl. Mater. 456 (2015) 235–245. https://doi.org/10.1016/j.jnucmat.2014.09.025.

[88] G. Bertolino, G. Meyer, J. Perez Ipiña, Effects of hydrogen content and temperature on fracture toughness of Zircaloy-4, J. Nucl. Mater. 320 (2003) 272–279. https://doi.org/10.1016/S0022-3115(03)00193-4.

[89] H.H. Hsu, M.F. Chiang, Y.C. Chen, The influence of hydride on fracture toughness of recrystallized Zircaloy-4 cladding, J. Nucl. Mater. 447 (2014) 56–62. https://doi.org/10.1016/j.jnucmat.2013.12.028.

[90] S.I. Hong, K.W. Lee, K.T. Kim, Effect of the circumferential hydrides on the deformation and fracture of Zircaloy cladding tubes, J. Nucl. Mater. 303 (2002) 169–176. https://doi.org/10.1016/S0022-3115(02)00814-0.

[91] H.C. Chu, S.K. Wu, K.F. Chien, R.C. Kuo, Effect of radial hydrides on the axial and hoop mechanical properties of Zircaloy-4 cladding, J. Nucl. Mater. 362 (2007) 93–103. https://doi.org/10.1016/j.jnucmat.2006.11.008.

[92] M.C. Billone, T.A. Burtseva, R.E. Einziger, Ductile-to-brittle transition temperature for high-burnup cladding alloys exposed to simulated drying-storage conditions, J. Nucl. Mater. 433 (2013) 431–448. https://doi.org/10.1016/j.jnucmat.2012.10.002.

[93] H.H. Hsu, L.W. Tsay, Effect of hydride orientation on fracture toughness of Zircaloy-4 cladding, J. Nucl. Mater. 408 (2011) 67–72. https://doi.org/10.1016/j.jnucmat.2010.10.068.

[94] D. Setoyama, S. Yamanaka, Indentation creep study of zirconium hydrogen solid solution, J. Alloys Compd. 379 (2004) 193–197. https://doi.org/10.1016/j.jallcom.2004.02.035.

[95] Y. Il Jung, Y.N. Seol, B.K. Choi, J.Y. Park, Thermal creep of Zircaloy-4 tubes containing corrosion-induced hydrogen, J. Nucl. Mater. 419 (2011) 213–216. https://doi.org/10.1016/j.jnucmat.2011.08.047.

[96] M. Le Saux, J. Besson, S. Carassou, C. Poussard, X. Averty, Behavior and failure of uniformly hydrided Zircaloy-4 fuel claddings between 25 °C and 480 °C under various stress states, including RIA loading conditions, Eng. Fail. Anal. 17 (2010) 683–700. https://doi.org/10.1016/j.engfailanal.2009.07.001.

[97] C.D. Cann, E.E. Sexton, An Electron Optical Study of Hydride Precipitation and Growth At Crack Tips in Zirconium, Acta Metall. 28 (1980) 1215–1221. https://doi.org/10.1016/0001-6160(80)90076-0.

[98] T. Kubo, Y. Kobayashi, H. Uchikoshi, Measurements of delayed hydride cracking propagation rate in the radial direction of Zircaloy-2 cladding tubes, J. Nucl. Mater. 427 (2012) 18–29. https://doi.org/10.1016/j.jnucmat.2012.04.012.

[99] G.A. McRae, C.E. Coleman, B.W. Leitch, The first step for delayed hydride cracking in zirconium alloys, J. Nucl. Mater. 396 (2010) 130–143. https://doi.org/10.1016/j.jnucmat.2009.08.019.

[100] R.N. Singh, N. Kumar, R. Kishore, S. Roychaudhury, T.K. Sinha, B.P. Kashyap, Delayed hydride cracking in Zr-2.5 Nb pressure tube material, J. Nucl. Mater. 304 (2002) 189–203. https://doi.org/10.1016/S0022-3115(02)00880-2.

[101] C.J. Ells, C. E., Simpson, Hydrogen in Metals, Metals Park, 1974.

[102] V. Perovic, G.C. Weatherly, C.J. Simpson, HYDRIDE PRECIPITATION IN alpha / beta ZIRCONIUM ALLOYS, Perspect Hydrog. Met. 31 (1986) 469–479.

[103] A. Hellouin de Menibus, Q. Auzoux, P. Mongabure, V. Macdonald, T. Le Jolu, J. Besson, J. Crepin, Fracture of Zircaloy-4 cladding tubes with or without hydride blisters in uniaxial to plane strain conditions with standard and optimized expansion due to compression tests, Mater. Sci. Eng. A. 604 (2014) 57–66. https://doi.org/10.1016/j.msea.2014.02.075.

[104] O.N. Pierron, D.A. Koss, A.T. Motta, K.S. Chan, The influence of hydride blisters on the fracture of Zircaloy-4, J. Nucl. Mater. 322 (2003) 21–35. https://doi.org/10.1016/S0022-3115(03)00299-X.

[105] L. Thuinet, R. Besson, Ab initio study of competitive hydride formation in zirconium alloys,

Intermetallics. 20 (2012) 24–32. https://doi.org/10.1016/j.intermet.2011.08.005.

[106] J.E. Bailey, Electron microscope observations on the precipitation of zirconium hydride in zirconium, Acta Metall. 11 (1963) 267–280. https://doi.org/10.1016/0001-6160(63)90182-2.

[107] S.Q. Shi, Z. Xiao, A quantitative phase field model for hydride precipitation in zirconium alloys: Part I. Development of quantitative free energy functional, J. Nucl. Mater. 459 (2015) 323–329. https://doi.org/10.1016/j.jnucmat.2014.03.013.

[108] A.M. Jokisaari, K. Thornton, General method for incorporating CALPHAD free energies of mixing into phase field models: Application to the α-zirconium/δ-hydride system, Calphad Comput. Coupling Phase Diagrams Thermochem. 51 (2015) 334–343. https://doi.org/10.1016/j.calphad.2015.10.011.

[109] V. Mallipudi, S. Valance, J. Bertsch, Meso-scale analysis of the creep behavior of hydrogenated Zircaloy-4, Mech. Mater. 51 (2012) 15–28. https://doi.org/10.1016/j.mechmat.2012.03.003.

[110] C.C. Tseng, M.H. Sun, C.K. Chao, Hydride effect on crack instability of Zircaloy cladding, Nucl. Eng. Des. 270 (2014) 427–435. https://doi.org/10.1016/j.nucengdes.2014.01.013.

[111] A.G. Varias, A.R. Massih, Temperature and constraint effects on hydride fracture in zirconium alloys, Eng. Fract. Mech. 65 (2000) 29–54. https://doi.org/10.1016/s0013-7944(99)00107-1.

[112] T. Kubo, Y. Kobayashi, Effects of δ-hydride precipitation at a crack tip on crack propagation in delayed hydride cracking of Zircaloy-2, J. Nucl. Mater. 439 (2013) 202–211. https://doi.org/10.1016/j.jnucmat.2013.04.015.

[113] H. Tummala, L. Capolungo, C.N. Tomé, Quantifying the stress state in the vicinity of a δ-hydride in α-zirconium, J. Nucl. Mater. 511 (2018) 406–416. https://doi.org/10.1016/j.jnucmat.2018.08.050.

[114] Yougui Liao, Practical Electron Microscopy and Database, 2006. www.globalsino.com/EM/.

[115] W. Escovitz, T. Fox, R. Levi-Setti, Scanning transmission ion microscope with a field ion source, Proc Natl Acad Sci U S A. 72(5) (1975) 1826–1828. https://doi.org/10.1073/pnas.72.5.1826.

[116] J.H. Orloff, L.W. Swanson, Study of a Field-Ionization Source for Microprobe Applications., J Vac Sci Technol. 12 (1975) 1209–1213. https://doi.org/10.1116/1.568497.

[117] R.L. Seliger, J.W. Ward, V. Wang, R.L. Kubena, A high-intensity scanning ion probe with

submicrometer spot size, Appl. Phys. Lett. 34 (1979) 310–312.

[118] R.J. Young, M. V Moore, Dual-Beam (FIB-SEM) Systems, in: L.A. Giannuzzi, F.A. Stevie (Eds.), Introd. to Focus. Ion Beams Instrumentation, Theory, Tech. Pract., Springer US, Boston, MA, 2005: pp. 247–268. https://doi.org/10.1007/0-387-23313-X_12.

[119] S. Reyntjens, R. Puers, Focused ion beam induced deposition: fabrication of three-dimensional microstructures and Young's modulus of the deposited material, J. Micromechanics Microengineering. 10 (2000) 181–188. https://doi.org/10.1088/0960-1317/10/2/314.

[120] M. Sezen, Focused Ion Beams (FIB) — Novel Methodologies and Recent Applications for Multidisciplinary Sciences, in: M. Janecek, R. Kral (Eds.), Mod. Electron Microsc. Phys. Life Sci., IntechOpen, Rijeka, 2016. https://doi.org/10.5772/61634.

[121] C. Kong, S. Cheong, R.D. Tilley, 2.15 - Recent Development in Focused Ion Beam Nanofabrication, in: D.L. Andrews, R.H. Lipson, T. Nann (Eds.), Compr. Nanosci. Nanotechnol. (Second Ed., Second Edi, Academic Press, Oxford, 2019: pp. 327–356. https://doi.org/https://doi.org/10.1016/B978-0-12-803581-8.10432-1.

[122] P.J. Konijnenberg, S. Zaefferer, D. Raabe, Assessment of geometrically necessary dislocation levels derived by 3D EBSD, Acta Mater. 99 (2015) 402–414. https://doi.org/10.1016/j.actamat.2015.06.051.

[123] C. Gillen, A. Garner, A. Plowman, C.P. Race, T. Lowe, C. Jones, K.L. Moore, P. Frankel, Advanced 3D characterisation of iodine induced stress corrosion cracks in zirconium alloys, Mater. Charact. 141 (2018) 348–361. https://doi.org/10.1016/j.matchar.2018.04.034.

[124] H. Yuan, B. Van de Moortèle, T. Epicier, Accurate post-mortem alignment for Focused Ion Beam and Scanning Electron Microscopy (FIB-SEM) tomography, Ultramicroscopy. 228 (2021). https://doi.org/10.1016/j.ultramic.2021.113265.

[125] F. Long, D. Kerr, G. Domizzi, Q. Wang, M.R. Daymond, Microstructure characterization of a hydride blister in Zircaloy-4 by EBSD and TEM, Acta Mater. 129 (2017) 450–461. https://doi.org/10.1016/j.actamat.2017.03.016.

[126] H. Muta, R. Nishikane, Y. Ando, J. Matsunaga, K. Sakamoto, S. Harjo, T. Kawasaki, Y. Ohishi, K. Kurosaki, S. Yamanaka, Effect of hydrogenation conditions on the microstructure and mechanical

properties of zirconium hydride, J. Nucl. Mater. 500 (2018) 145–152. https://doi.org/10.1016/j.jnucmat.2017.12.027.

[127] W. Qin, N.A.P. Kiran Kumar, J.A. Szpunar, J. Kozinski, Intergranular δ-hydride nucleation and orientation in zirconium alloys, Acta Mater. 59 (2011) 7010–7021. https://doi.org/10.1016/j.actamat.2011.07.054.

[128] R.M. Birch, J.O. Douglas, T. Ben Britton, Characterization of local deformation around hydrides in Zircaloy-4 using conventional and high angular resolution electron backscatter diffraction, Mater. Charact. 202 (2023) 112988. https://doi.org/10.1016/j.matchar.2023.112988.

[129] A. Winkelmann, C. Trager-Cowan, F. Sweeney, A.P. Day, P. Parbrook, Many-beam dynamical simulation of electron backscatter diffraction patterns, Ultramicroscopy. 107 (2007) 414–421. https://doi.org/10.1016/j.ultramic.2006.10.006.

[130] Oxford Instruments, Electron Backscatter Diffraction (EBSD) Pattern formation, EBSD.Com. (2024). https://ebsd.com/ebsd-explained/pattern-formation.

[131] Oxford Instrument, What information does Electron Backscatter Diffraction (EBSD) provide?, (2024). https://www.ebsd.com/ebsd-applications/what-information-does-ebsd-provide.

[132] T.B. Britton, J. Jiang, Y. Guo, A. Vilalta-Clemente, D. Wallis, L.N. Hansen, A. Winkelmann, A.J. Wilkinson, Tutorial: Crystal orientations and EBSD - Or which way is up?, Mater. Charact. 117 (2016) 113–126. https://doi.org/10.1016/j.matchar.2016.04.008.

[133] Oxford Instruments, Calibrating an Electron Backscatter Diffraction (EBSD) system, (2024). https://www.ebsd.com/ebsd-explained/calibrating-an-ebsd-system.

[134] J. Basinger, D. Fullwood, J. Kacher, B. Adams, Pattern center determination in electron backscatter diffraction microscopy, Microsc. Microanal. 17 (2011) 330–340. https://doi.org/10.1017/S1431927611000389.

[135] A.J. Wilkinson, Methods for determining elastic strains from electron backscatter diffraction and electron channelling patterns, Mater. Sci. Technol. 13 (1997) 79–84. https://doi.org/10.1179/mst.1997.13.1.79.

[136] K.Z. Troost, P. Van Der Sluis, D.J. Gravesteijn, Microscale elastic-strain determination by backscatter

Kikuchi diffraction in the scanning electron microscope, Appl. Phys. Lett. 62 (1993) 1110–1112. https://doi.org/10.1063/1.108758.

[137] A.J. Wilkinson, D. Randman, Determination of elastic strain fields and geometrically necessary dislocation distributions near nanoindents using electron back scatter diffraction, Philos. Mag. 90 (2010) 1159–1177. https://doi.org/10.1080/14786430903304145.

[138] A.J. Wilkinson, G. Meaden, D.J. Dingley, High resolution mapping of strains and rotations using electron backscatter diffraction, Mater. Sci. Technol. 22 (2006) 1271–1278. https://doi.org/10.1179/174328406X130966.

[139] A.J. Wilkinson, G. Meaden, D.J. Dingley, High-resolution elastic strain measurement from electron backscatter diffraction patterns: New levels of sensitivity, Ultramicroscopy. 106 (2006) 307–313. https://doi.org/10.1016/j.ultramic.2005.10.001.

[140] P.S. Karamched, A.J. Wilkinson, High resolution electron back-scatter diffraction analysis of thermally and mechanically induced strains near carbide inclusions in a superalloy, Acta Mater. 59 (2011) 263–272. https://doi.org/10.1016/j.actamat.2010.09.030.

[141] T.B. Britton, A.J. Wilkinson, High resolution electron backscatter diffraction measurements of elastic strain variations in the presence of larger lattice rotations, Ultramicroscopy. 114 (2012) 82–95. https://doi.org/10.1016/j.ultramic.2012.01.004.

[142] J. Jiang, T.B. Britton, A.J. Wilkinson, Measurement of geometrically necessary dislocation density with high resolution electron backscatter diffraction: Effects of detector binning and step size, Ultramicroscopy. 125 (2013) 1–9. https://doi.org/10.1016/j.ultramic.2012.11.003.

[143] T.B. Britton, A.J. Wilkinson, Measurement of residual elastic strain and lattice rotations with high resolution electron backscatter diffraction, Ultramicroscopy. 111 (2011) 1395–1404. https://doi.org/10.1016/j.ultramic.2011.05.007.

[144] T.B. Britton, J. Jiang, R. Clough, E. Tarleton, A.I. Kirkland, A.J. Wilkinson, Assessing the precision of strain measurements using electron backscatter diffraction - part 1: Detector assessment, Ultramicroscopy. 135 (2013) 126–135. https://doi.org/10.1016/j.ultramic.2013.08.005.

[145] T.B. Britton, J. Jiang, R. Clough, E. Tarleton, A.I. Kirkland, A.J. Wilkinson, Assessing the precision of

strain measurements using electron backscatter diffraction - Part 2: Experimental demonstration, Ultramicroscopy. 135 (2013) 136–141. https://doi.org/10.1016/j.ultramic.2013.08.006.

[146] C. Maurice, J.H. Driver, R. Fortunier, On solving the orientation gradient dependency of high angular resolution EBSD, Ultramicroscopy. 113 (2012) 171–181. https://doi.org/10.1016/j.ultramic.2011.10.013.

[147] J.F. Nye, Some geometrical relations in dislocated crystals, Acta Metall. 1 (1953) 153–162. https://doi.org/10.1016/0001-6160(53)90054-6.

[148] Y. Guo, D.M. Collins, E. Tarleton, F. Hofmann, A.J. Wilkinson, T. Ben Britton, Dislocation density distribution at slip band-grain boundary intersections, Acta Mater. 182 (2020) 172–183. https://doi.org/10.1016/j.actamat.2019.10.031.

[149] T.B. Britton, H. Liang, F.P.E. Dunne, A.J. Wilkinson, The effect of crystal orientation on the indentation response of commercially pure titanium: Experiments and simulations, Proc. R. Soc. A Math. Phys. Eng. Sci. 466 (2010) 695–719. https://doi.org/10.1098/rspa.2009.0455.

[150] A.J. Wilkinson, E. Tarleton, A. Vilalta-Clemente, J. Jiang, T.B. Britton, D.M. Collins, Measurement of probability distributions for internal stresses in dislocated crystals, Appl. Phys. Lett. 105 (2014). https://doi.org/10.1063/1.4901219.

[151] J. Jiang, T. Benjamin Britton, A.J. Wilkinson, Evolution of intragranular stresses and dislocation densities during cyclic deformation of polycrystalline copper, Acta Mater. 94 (2015) 193–204. https://doi.org/10.1016/j.actamat.2015.04.031.

[152] A. Koko, T.H. Becker, E. Elmukashfi, N.M. Pugno, A.J. Wilkinson, T.J. Marrow, HR-EBSD analysis of in situ stable crack growth at the micron scale, J. Mech. Phys. Solids. 172 (2023) 105173. https://doi.org/10.1016/j.jmps.2022.105173.

[153] D. Wallis, L.N. Hansen, T. Ben Britton, A.J. Wilkinson, Dislocation Interactions in Olivine Revealed by HR-EBSD, J. Geophys. Res. Solid Earth. 122 (2017) 7659–7678. https://doi.org/10.1002/2017JB014513.

[154] R.M. Birch, J.O. Douglas, T. Ben Britton, Characterization of local deformation around hydrides in Zircaloy-4 using conventional and high angular resolution electron backscatter diffraction Keywords,

(n.d.) 1–37.

[155] E.S. Fisher, C.J. Renken, Single-crystal elastic moduli and the hcp → bcc transformation in Ti, Zr, and Hf, Phys. Rev. 135 (1964). https://doi.org/10.1103/PhysRev.135.A482.

[156] P.F. Weck, E. Kim, V. Tikare, J.A. Mitchell, Mechanical properties of zirconium alloys and zirconium hydrides predicted from density functional perturbation theory, Dalt. Trans. 44 (2015) 18769–18779. https://doi.org/10.1039/c5dt03403e.

[157] P.A.T. Olsson, A.R. Massih, J. Blomqvist, A.M. Alvarez Holston, C. Bjerkén, Ab initio thermodynamics of zirconium hydrides and deuterides, Comput. Mater. Sci. 86 (2014) 211–222. https://doi.org/10.1016/j.commatsci.2014.01.043.

[158] W. Zhu, R. Wang, G. Shu, P. Wu, H. Xiao, First-principles study of different polymorphs of crystalline zirconium hydride, J. Phys. Chem. C. 114 (2010) 22361–22368. https://doi.org/10.1021/jp109185n.

[159] Dantec Dynamics, Measurement Principles of DIC, (2024). https://www.dantecdynamics.com/solutions/stress-strain-espi-dic/solid-mechanics-dic/measurement-principles-of-dic/.

[160] J. Bair, M. Asle, M. Tonks, A review on hydride precipitation in zirconium alloys, J. Nucl. Mater. 466 (2015) 12–20. https://doi.org/10.1016/j.jnucmat.2015.07.014.

[161] M. Ma, M. he Li, Y. biao Tan, H. Yuan, W. chang Liu, Microstructure and texture evolution in commercial-purity Zr 702 during cold rolling and annealing, Int. J. Miner. Metall. Mater. 21 (2014) 785–795. https://doi.org/10.1007/s12613-014-0972-z.

[162] A.J. de O. Zimmermann, A.F. Padilha, Rolling and recrystallization behavior of pure zirconium and zircaloy-4, Rev. Mater. 24 (2019). https://doi.org/10.1590/S1517-707620190003.0767.

[163] J. Gong, T. Benjamin Britton, M.A. Cuddihy, F.P.E. Dunne, A.J. Wilkinson, (a) Prismatic, (a) basal, and (c+a) slip strengths of commercially pure Zr by micro-cantilever tests, Acta Mater. 96 (2015) 249–257. https://doi.org/10.1016/j.actamat.2015.06.020.

[164] J. Chen, S.J. Bull, On the relationship between plastic zone radius and maximum depth during nanoindentation, Surf. Coatings Technol. 201 (2006) 4289–4293. https://doi.org/10.1016/j.surfcoat.2006.08.099.

[165] A. Akhtar, A. Teghtsoonian, Plastic deformation of zirconium single crystals, Acta Metall. 19 (1971) 655–663. https://doi.org/10.1016/0001-6160(71)90019-8.

[166] A. Akhtar, Basal slip in zirconium, Acta Metall. 21 (1973) 1–11. https://doi.org/10.1016/0001-6160(73)90213-7.

[167] A. Lodh, P. Pant, G. Kumar, K. V. Mani Krishna, R. Tewari, I. Samajdar, Orientation-dependent solid solution strengthening in zirconium: a nanoindentation study, J. Mater. Sci. 55 (2020) 4493–4503. https://doi.org/10.1007/s10853-019-04280-3.

[168] S. Pathak, S.R. Kalidindi, N.A. Mara, Investigations of orientation and length scale effects on micromechanical responses in polycrystalline zirconium using spherical nanoindentation, Scr. Mater. 113 (2016) 241–245. https://doi.org/10.1016/j.scriptamat.2015.10.035.

[169] M.A. Vicente Alvarez, J.R. Santisteban, G. Domizzi, J. Almer, Phase and texture analysis of a hydride blister in a Zr-2.5%Nb tube by synchrotron X-ray diffraction, Acta Mater. 59 (2011) 2210–2220. https://doi.org/10.1016/j.actamat.2010.12.024.

[170] O. Zanellato, M. Preuss, J.Y. Buffiere, F. Ribeiro, A. Steuwer, J. Desquines, J. Andrieux, B. Krebs, Synchrotron diffraction study of dissolution and precipitation kinetics of hydrides in Zircaloy-4, J. Nucl. Mater. 420 (2012) 537–547. https://doi.org/10.1016/j.jnucmat.2011.11.009.

[171] H. Chan, S.G. Roberts, J. Gong, Micro-scale fracture experiments on zirconium hydrides and phase boundaries, J. Nucl. Mater. 475 (2016) 105–112. https://doi.org/10.1016/j.jnucmat.2016.03.026.

[172] H.E. Weekes, V.A. Vorontsov, I.P. Dolbnya, J.D. Plummer, F. Giuliani, T.B. Britton, D. Dye, In situ micropillar deformation of hydrides in Zircaloy-4, Acta Mater. 92 (2015) 81–96. https://doi.org/10.1016/j.actamat.2015.03.037.

[173] N.A.P. Kiran Kumar, J.A. Szpunar, Z. He, Preferential precipitation of hydrides in textured zircaloy-4 sheets, J. Nucl. Mater. 403 (2010) 101–107. https://doi.org/10.1016/j.jnucmat.2010.06.005.

[174] F. Li, S. Li, G. Liu, X. Chen, Y. Wang, Formation and characterization of circular δ-hydride in Zircaloy-4 under ion irradiation, J. Nucl. Mater. 513 (2019) 1–7. https://doi.org/10.1016/j.jnucmat.2018.10.042.

[175] A.T.W. Barrow, C. Toffolon-Masclet, J. Almer, M.R. Daymond, The role of chemical free energy and

elastic strain in the nucleation of zirconium hydride, J. Nucl. Mater. 441 (2013) 395–401. https://doi.org/10.1016/j.jnucmat.2013.06.013.

[176] S.J. Oh, C. Jang, J.H. Kim, Y.H. Jeong, Microstructure and hydride embrittlement of zirconium model alloys containing niobium and tin, Mater. Sci. Eng. A. 528 (2011) 3771–3776. https://doi.org/10.1016/j.msea.2011.01.093.

[177] Y. Choi, J.W. Lee, Y.W. Lee, S.I. Hong, Hydride formation by high temperature cathodic hydrogen charging method and its effect on the corrosion behavior of Zircaloy-4 tubes in acid solution, J. Nucl. Mater. 256 (1998) 124–130. https://doi.org/10.1016/S0022-3115(98)00180-9.

[178] M.L. Vanderglas, Y.J. Kim, Stresses due to volumetric expansion of zirconium hydride inclusions, Int. J. Press. Vessel. Pip. 22 (1986) 177–196. https://doi.org/10.1016/0308-0161(86)90116-X.

[179] R.N. Singh, R. Kishore, T.K. Sinha, S. Banerjee, B.P. Kashyap, Stress field estimation around a semi-constrained inclusion and its validation by interpreting hydride platelet orientation around a blister in a Zr-2.5Nb alloy, Mater. Sci. Eng. A. 339 (2003) 17–28. https://doi.org/10.1016/S0921-5093(02)00115-6.

[180] A. Hellouin De Menibus, Q. Auzoux, O. Dieye, P. Berger, S. Bosonnet, E. Foy, V. Macdonald, J. Besson, J. Crépin, Formation and characterization of hydride blisters in Zircaloy-4 cladding tubes, J. Nucl. Mater. 449 (2014) 132–147. https://doi.org/10.1016/j.jnucmat.2014.03.006.

[181] M. J.W., Christian, S., Deformation Twinning, Prog. Mater. Sci. 39 (1995) 1–157. https://doi.org/10.1016.

[182] R.B. Russell, On the Zr-Hf System, J. Appl. Phys. 24 (1953) 232–233. https://doi.org/10.1063/1.1721254.

[183] S. Yamanaka, K. Yamada, K. Kurosaki, M. Uno, K. Takeda, H. Anada, T. Matsuda, S. Kobayashi, Characteristics of zirconium hydride and deuteride, J. Alloys Compd. 330–332 (2002) 99–104. https://doi.org/10.1016/S0925-8388(01)01448-7.

[184] Y.J. Jia, I.J. Beyerlein, W.Z. Han, Precipitation characteristics and distributions of subsurface hydrides in zirconium, Acta Mater. 216 (2021) 117146. https://doi.org/10.1016/j.actamat.2021.117146.

[185] G.J.C. Carpenter, The precipitation of γ-zirconium hydride in zirconium, Acta Metall. 26 (1978) 1225–1235. https://doi.org/10.1016/0001-6160(78)90006-8.

[186] S. Wang, F. Giuliani, T. Ben Britton, Microstructure and formation mechanisms of δ-hydrides in variable grain size Zircaloy-4 studied by electron backscatter diffraction, Acta Mater. 169 (2019) 76–87. https://doi.org/10.1016/j.actamat.2019.02.042.

[187] S. Arsene, J. Bai, P. Bompard, Hydride Embrittlement and Irradiation Effects on the Hoop Mechanical Properties of Pressurized Water Reactor (PWR) and Boiling-Water Reactor (BWR) Zircaloy Cladding Tubes: Part III., Metall. Mater. Trans. A. 34 (2003) 579–588.

[188] Y. Liu, Q. Peng, W. Zhao, H. Jiang, Hydride precipitation by cathodic hydrogen charging method in zirconium alloys, Mater. Chem. Phys. 110 (2008) 56–60. https://doi.org/10.1016/j.matchemphys.2007.12.028.

[189] R.W. T., S. W., Dislocation Models of Crystal Grain Boundaries, Phys. Rev. 78 (1950) 275.

[190] K. V. Mani Krishna, A. Sain, I. Samajdar, G.K. Dey, D. Srivastava, S. Neogy, R. Tewari, S. Banerjee, Resistance to hydride formation in zirconium: An emerging possibility, Acta Mater. 54 (2006) 4665–4675. https://doi.org/10.1016/j.actamat.2006.06.004.

[191] H.E. Weekes, N.G. Jones, T.C. Lindley, D. Dye, Hydride reorientation in Zircaloy-4 examined by in situ synchrotron X-ray diffraction, J. Nucl. Mater. 478 (2016) 32–41. https://doi.org/10.1016/j.jnucmat.2016.05.029.

[192] L. Reali, D.S. Balint, M.R. Wenman, Dislocation modelling of the plastic relaxation and thermal ratchetting induced by zirconium hydride precipitation, J. Mech. Phys. Solids. 167 (2022) 104988. https://doi.org/10.1016/j.jmps.2022.104988.

[193] A.T. Motta, L.Q. Chen, Hydride formation in zirconium alloys, Jom. 64 (2012) 1403–1408. https://doi.org/10.1007/s11837-012-0479-x.

[194] G.J. Field, J.T. Dunn, B.A. Cheadle, Analysis of the Pressure Tube Failure at Pickering NGS “A” Unit 2 Nuclear Systems Department, Can. Metall. Q. 24 (1985) 181–188. https://doi.org/10.1179/cmq.1985.24.3.181.

[195] N.P. Company, C. River, N. Laboratories, M. Division, DELAYED HYDROGEN EMBRITTLEMENT IN Zr-2.5 C.J. SIMPSON * and C.E. ELLS wt % Nb, Fuel. 52 (1974) 289–295.

[196] J. Blaber, B. Adair, A. Antoniou, Ncorr: Open-Source 2D Digital Image Correlation Matlab Software,

Exp. Mech. 55 (2015) 1105–1122. https://doi.org/10.1007/s11340-015-0009-1.

[197] C.M. Silva, F. Ibrahim, E.G. Lindquist, J.W. McMurray, C.D. Bryan, Brittle nature and the related effects of zirconium hydrides in Zircaloy-4, Mater. Sci. Eng. A. 767 (2019) 138396. https://doi.org/10.1016/j.msea.2019.138396.

[198] D. Lunt, T. Busolo, X. Xu, J. Quinta da Fonseca, M. Preuss, Effect of nanoscale α2 precipitation on strain localisation in a two-phase Ti-alloy, Acta Mater. 129 (2017) 72–82. https://doi.org/10.1016/j.actamat.2017.02.068.

[199] A. Orozco-Caballero, D. Lunt, J.D. Robson, J. Quinta da Fonseca, How magnesium accommodates local deformation incompatibility: A high-resolution digital image correlation study, Acta Mater. 133 (2017) 367–379. https://doi.org/10.1016/j.actamat.2017.05.040.

[200] F. Di Gioacchino, J. Quinta da Fonseca, Plastic Strain Mapping with Sub-micron Resolution Using Digital Image Correlation, Exp. Mech. 53 (2013) 743–754. https://doi.org/10.1007/s11340-012-9685-2.

[201] M. Kerr, M.R. Daymond, R.A. Holt, J.D. Almer, Strain evolution of zirconium hydride embedded in a Zircaloy-2 matrix, J. Nucl. Mater. 380 (2008) 70–75. https://doi.org/10.1016/j.jnucmat.2008.07.004.

[202] S. Mahajan, D.F. Williams, Deformation Twinning in Metals and Alloys, Int. Metall. Rev. 18 (1973) 43–61. https://doi.org/10.1179/imtlr.1973.18.2.43.

[203] V. Tong, E. Wielewski, B. Britton, Characterisation of slip and twinning in high rate deformed zirconium with electron backscatter diffraction, (2018) 1–45. http://arxiv.org/abs/1803.00236.

[204] H.L. Yang, S. Kano, L.J. Chai, J.J. Shen, Z.S. Zhao, J. McGrady, Z.G. Duan, H. Abe, Interaction between slip and {101¯2} tensile twinning in Zr alloy: Quasi in situ electron backscatter diffraction study under uniaxial tensile test, J. Alloys Compd. 782 (2019) 659–666. https://doi.org/10.1016/j.jallcom.2018.12.190.

[205] T. Pardoen, Y. Brechet, Influence of microstructure-driven strain localization on the ductile fracture of metallic alloys, Philos. Mag. 84 (2004) 269–297. https://doi.org/10.1080/14786430310001610366.

[206] S. Wang, F. Giuliani, T. Ben Britton, Slip–hydride interactions in Zircaloy-4: Multiscale mechanical testing and characterisation, Acta Mater. 200 (2020) 537–550. https://doi.org/10.1016/j.actamat.2020.09.038.

[207] S. Wang, S. Kalácska, X. Maeder, J. Michler, F. Giuliani, T. Ben Britton, The effect of δ-hydride on the micromechanical deformation of a Zr alloy studied by in situ high angular resolution electron backscatter diffraction, Scr. Mater. 173 (2019) 101–105. https://doi.org/10.1016/j.scriptamat.2019.08.006.